AEROSOL WET SCAVENGING AND CLOUD PROCESSING OF AEROSOLS IN A GLOBAL CLIMATE MODEL

by

Betty Croft

Submitted in partial fulfillment of the requirements
for the degree of Doctor of Philosophy

at

Dalhousie University
Halifax, Nova Scotia
January 2011

DALHOUSIE UNIVERSITY

DEPARTMENT OF PHYSICS AND ATMOSPHERIC SCIENCE

The undersigned hereby certify that they have read and recommend to the Faculty of Graduate Studies for acceptance a thesis entitled "Aerosol Wet Scavenging and Cloud Processing of Aerosols in a Global Climate Model" by Betty Croft in partial fulfillment of the requirements for the degree of Doctor of Philosophy.

Dated: January 28, 2011

External Examiner: Peter Adams

Research Supervisors: Ulrike Lohmann

Randall Martin

Examining Committee: Ian Folkins

Examining Committee: Glen Lesins

Departmental Representative: Jeff Pierce

DALHOUSIE UNIVERSITY

DATE: January 28, 2011

AUTHOR: Betty Croft

TITLE: Aerosol Wet Scavenging and Cloud Processing of Aerosols in a Global Climate Model

DEPARTMENT: Department of Physics and Atmospheric Science

DEGREE: Ph.D. CONVOCATION: May YEAR: 2011

Signature of Author

To my immediate and extended family, for your enthusiastic support during this project, for your companionship in accompanying me on my various travels to attend conferences and meetings, and for giving of your time to help with child-care

To my husband, Paul Croft, my greatest encouragement and support

To my children, Matthew and Sophia Croft, my pride and joy, you always make me smile

To my extended family, my village, (and yes it does take a village!)

Cyril and Sarah Carlin

Muriel and Arthur Croft

Marilyn and Bill Parsons

Brent and Judy Baxter

Rob Carlin and Chris Paci

Table of Contents

List of Tables

List of Figures

Abstract

Clouds strongly influence three-dimensional aerosol distributions by 1) wet scavenging and subsequent deposition to the earth's surface, and 2) processing and subsequent release to the atmosphere by evaporation processes. In this study, physically detailed size-dependent representations of below-cloud and in-cloud scavenging for mixed phase clouds are introduced into the ECHAM5-HAM global climate model. As well, a stratiform cloud aerosol processing scheme is extended to convective clouds.

Below-cloud impaction scavenging is found to contribute strongly to the global and annual mean mass deposition for sulfate (14%), black carbon (13%), particulate organic matter (10%), sea salt (23%), and dust (24%). The modeled global mean aerosol optical depth, and sea salt burden are reduced by about 15% for the more vigorous size-dependent parameterization of below-cloud scavenging by rain and snow.

In stratiform clouds, aerosol mass is found to be primarily (>90%) scavenged by cloud nucleation processes for all aerosol species, except for dust (50%). Uncertainties in the representation of in-cloud scavenging processes change the predicted annual, global mean aerosol mass burdens by 20 to 30%, and change the predicted aerosol mass concentrations by up to one order of magnitude in the middle troposphere where mixed phase clouds exist. Closer agreement with observations of black carbon profiles from aircraft is found for the new in-cloud scavenging scheme.

Convective and stratiform clouds contribute about equally to the global, annual mean aerosol processing, but wet deposition is primarily attributed to stratiform clouds (75%). Sulfate and carbonaceous aerosols undergo 1-3 cloud cycles before deposition. Aerosol burdens and optical depth (AOD) increase by a factor of 3-5 with the explicit representation of cloud/precipitation evaporation. Revised sea salt emissions and more vigorous in-cloud impaction scavenging reduce the AOD by a factor of three to give closer agreement with satellite retrievals. Observed marine boundary layer accumulation mode size distributions, and vertically integrated aerosol size distributions from AERONET observations are more closely approximated with the aerosol processing scheme than for the standard ECHAM5-HAM.

List of Abbreviations and Symbols Used

Symbol	Units	Description
AEROCOM		Aerosol Intercomparison Project
AERONET		Aerosol Robotics Network
AI		insoluble accumulation mode
AOD	-	aerosol optical depth
ARC-PAC		NOAA Aerosol Radiation and Cloud Processes affecting Arctic Climate
ARC-TAS		NASA Arctic Research of the Composition of the Troposphere from Aircraft and Satellites
AS		internally mixed/soluble accumulation mode
AVE-Houston		NASA Houston Aura Validation Experiment
BC		black carbon
BCS		below-cloud scavenging
C_i	kg kg$^-$1	grid-box mean mixing ratio of i^{th} tracer
C_i^{amb}	kg kg$^-$1	ambient mixing ratio of i^{th} tracer in cloud-free air
C_{ice}	kg kg$^-$1	cloud ice water mixing ratio
C_{liq}	kg kg$^-$1	cloud liquid water mixing ratio
CAPE	J	convective available potential energy
CARB		NASA initiative in collaboration with California Air Resources Board
CC	-	cloud cover
CCN		cloud condensation nuclei
CD		stratiform in-droplet mode
CDCV		convective in-droplet variable
CDNC	cm^{-3}	cloud droplet number concentration
CI		insoluble coarse mode
CN		condensation nuclei
CR-AVE		NASA Costa Rico Aura Validation Experiment
CS		internally mixed/soluble coarse mode
CTL		control simulation
CTM		chemical transport model
Conv.		convective
D	m^2 s^{-1}	diffusion coefficient
D_g	m^2 s^{-1}	diffusivity coefficient for gas in air
D_m	cm	characteristic length for rimed particles

D_p	μm, mm	droplet diameter
DMS		dimethyl sulfide
DU		dust
E		collision efficiency
ECHAM5		Fifth generation GCM developed at the Max-Planck Institute in Hamburg, Germany
ECMWF		European Centre for Medium-Range Weather Forecasts
e	Pa	ambient vapor pressure
$e_{w,s}$	Pa	saturation vapor pressure over water
F_N	m^{-3}	cumulative lognormal size distribution
F^r	kg m^{-2} s^{-1}	rain flux
F^s	kg m^{-2} s^{-1}	snow flux
$\overline{f_a}$	-	mean ventilation coefficient
f^{cl}	-	cloudy fraction of grid-box
f^{liq}	-	liquid fraction of cloud water
f^{ice}	-	ice fraction of cloud water
f^{precip}	-	fraction of grid-box affected by precipitation
GCM		global climate model, general circulation model
g	m s^{-2}	acceleration due to gravity
HAM		Hamburg Aerosol Module
HASP		High Altitude Sampling Program
IC		stratiform in-crystal mode
ICCV		convective in-crystal variable
ICNC	cm^{-3}	ice crystal number concentration
ICS		in-cloud scavenging
ISCCP		International Satellite and Cloud Climatology Project
IWP	g m^{-2}	ice water path
K	m^3 s^{-1}	collection kernel
K_c	m s^{-1}	mass transfer coefficient
KI		insoluble Aitken mode
KS		internally mixed/soluble Aitken mode
LCF	W m^{-2}	longwave cloud forcing
LS		large-scale (stratiform)
LW_{allsky}	W m^{-2}	all sky outgoing longwave radiation
LW_{clr}	W m^{-2}	clear sky outgoing longwave radiation

LWP	g m^{-2}	liquid water path
M	kg	mass of snow crystal
MF_{up}	kg m^{-2} s^{-1}	updraft mass flux
MISR		Multi-angle Imaging Spectroradiometer
MODIS		Moderate Resolution Imaging Spectroradiometer
M_s	kg mol^{-1}	molecular weight of solute
M_w	kg mol^{-1}	molecular weight of water
m	kg	aerosol mass
$m_{x,j}$	kg kg^{-3}	aerosol mass concentration of species x in mode j
$m_{x,CDCV}$	kg kg^{-3}	aerosol mass concentration of species x in convective cloud droplets
$m_{x,ICCV}$	kg kg^{-3}	aerosol mass concentration of species x in convective cloud ice crystals
N	m^{-3}	total aerosol number concentration
$N_{>25nm}$	cm^{-3}	aerosol number concentration in soluble modes with radius larger than 25 nm
$N_{>35nm}$	cm^{-3}	aerosol number concentration in soluble modes with radius larger than 35 nm
$N_{act,j}$	m^{-3}	number of aerosols activated in j^{th} mode
N_d	m^{-3}	cloud droplet number concentration
N_i	m^{-3}	ice crystal number concentration
N_j	cm^{-3}	aerosol number concentration in j^{th} mode
$N_{j>35nm}$	cm^{-3}	aerosol number concentration in j^{th} mode with radius larger than 35 nm
$N_{j,k}$	cm^{-3}	aerosol number concentration in j^{th} mode at k^{th} model vertical level
$N_{j,scav}$	cm^{-3}	number of aerosols scavenged from j^{th} mode
N_{Re}	-	Reynold's number
N_l	m^{-3}	cloud droplet number concentration
N_i	m^{-3}	ice crystal number concentration
NASA		National Aeronautics and Space Administration
NOAA		National Oceanic and Atmospheric Administration
NS		nucleation soluble mode
n	m^{-3} μm^{-1}	aerosol number concentration
OBS		observations

OC		organic carbon
PEM		NASA Pacific Exploratory Mission
POM		particulate organic matter
Pe	-	Peclet number
P_{form}	kg kg^{-1} s^{-1}	rate of precipitation formation
PF_{conv}	-	convective precipitating fraction
p_k	hPa	pressure at k^{th} model vertical level
ppm	-	parts per million
Q^{liq}	kg kg^{-1} s^{-1}	summed conversion rate of cloud liquid to precipitation
Q^{ice}	kg kg^{-1} s^{-1}	summed conversion rate of cloud ice to precipitation
$\overline{Q}_{BFevap}$	cm^{-3} s^{-1}	droplet evaporation rate due to Bergeron-Findeisen process
$\overline{Q}_{coll,j}$	cm^{-3} s^{-1}	droplet-aerosol collision rate for j^{th} mode
$\overline{Q}_{colli,j}$	cm^{-3} s^{-1}	ice crystal-aerosol collision rate for j^{th} mode
$\overline{Q}_{evap}$	cm^{-3} s^{-1}	droplet evaporation rate
$\overline{Q}_{frz}$	cm^{-3} s^{-1}	droplet freezing rate
$\overline{Q}_{nuc}$	cm^{-3} s^{-1}	droplet nucleation rate
$\overline{Q}_{rain}$	g m^{-3}	rain formation
$\overline{Q}_{snow}$	g m^{-3}	snow formation
$\overline{Q}_{sub}$	cm^{-3} s^{-1}	crystal sublimation rate
q_l	g m^{-3}	liquid water mass concentration
q_i	g m^{-3}	ice water mass concentration
R	J mol^{-1} K^{-1}	universal gas constant
R	mm hr^{-1}	rainfall rate
R_{liq}	m	radius of cloud droplet
R_{ice}	m	radius of ice crystal
R_{snow}	m	radius of snow crystal
Re	-	Reynold's number
R_i	-	prescribed in-cloud scavenging ratio for the i^{th} mode
R_i, nuc	-	in-cloud nucleation scavenging ratio for the i^{th} mode
R_i, imp	-	in-cloud impaction scavenging ratio for the i^{th} mode

R_i^r	m^{-2} kg $^{-1}$ s^{-1}	below-cloud scavenging coefficient for rain and for i^{th} tracer, normalized by rain flux
R_i^s	m^{-2} kg $^{-1}$ s^{-1}	below-cloud scavenging coefficient for snow and for i^{th} tracer,normalized by snow flux
R_p	μm, mm, m	droplet radius
r	nm, μm, m	aerosol radius
r_b	nm, μm, m	radius of larger collision partner
r_{dry}	nm, μm, m	dry aerosol radius
$r_{j,crit}$	nm, μm, m	critical aerosol radius for j^{th} mode
r_p	nm, μm, m	aerosol radius
r_{pm}	nm, μm, m	aerosol median radius
$\overline{r}_{pg}$	nm, μm, m	geometric mean aerosol radius
r_s	nm, μm, m	radius of smaller collision partner
$r_{wet,j,k}$	m	aerosol count median wet radius for the j^{th} mode and k^{th} model vertical level
S		sulfur
SCF	W m^{-2}	shortwave cloud forcing
SO_2		sulfur dioxide
SO_4		sulfate
SS		sea salt
SU		sulfate
SW_{allsky}	W m^{-2}	all sky outgoing shortwave radiation
SW_{clr}	W m^{-2}	clear sky outgoing shortwave radiation
Sc	-	Schmidt number
St	-	Stokes number
Strat.		Stratiform
T	K , °C	temperature
TOVS		TIROS Operational Vertical Sounder
TKE		turbulent kinetic energy
TRACE-P		NASA Transport and Chemical Evolution over the Pacific experiment
t	s	time
U_t	m s^{-1}	terminal velocity
V_s	m s^{-1}	Stokes flow velocity
V_∞	m s^{-1}	terminal velocity
$V_{\infty,b}$	m s^{-1}	terminal velocity of larger collision partner
$V_{\infty,s}$	m s^{-1}	terminal velocity of smaller collision partner
v_{up}	m s^{-1}	updraft velocity

WD		wet deposition
y_c	nm, μm	radius of aerosol grazing trajectory
ZSZ		zero scavenging zone
Greek Letters		
Δ		difference
η_a	kg m^{-1} s^{-1}	dynamic (absolute) viscosity of air
Λ	s^{-1}	impaction scavenging coefficient
Λ_m	s^{-1}	impaction scavenging coefficient for number
Λ_n	s^{-1}	impaction scavenging coefficient for mass
λ_a	m	mean free path of air molecules
ν	m^2 s^{-1}	kinematic viscosity of air
ρ_a	kg m^{-3}	air density
ρ_p	kg m^{-3}	aerosol density
ρ_w	kg m^{-3}	water density
σ	N m^{-1}	water surface tension
σ_g		geometric standard deviation
ω	m s^{-1}	updraft velocity
$\overline{\omega}$	m s^{-1}	large scale vertical velocity

Acknowledgements

The constructive suggestions, and insightful comments of my two co-supervisors, Drs. Ulrike Lohmann and Randall Martin have been invaluable during the course of this PhD project. I have truly enjoyed collaborating with both of you! I have appreciated your ongoing input, encouragement, and ideas about the most fruitful research directions to pursue during the course of this project. I am grateful to you, Ulrike for developing the original concepts for this project, and for being willing to continue to supervise and support this project despite our geographic separation. Your financial support for my seven visits to ETH Zurich is sincerely appreciated. I found these visits with you, collaborations with colleagues there, and attendance at your annual group retreats to be of fundamental support in the development of this project. I am also thankful to Randall Martin for your ongoing financial support for this project, which was as a supplement to the financial assistance that was also gratefully received from the National Science and Engineering Research Council of Canada (NSERC CGS-D2) and Killam Trusts Foundation of Canada scholarships, and the NSERC financial supplements provided by the Canadian Meteorological and Oceanographic Society, and Meteorological Service of Canada.

I would also like to express my sincere thanks to my co-authors, Drs. Johann Feichter, Philip Stier, Sabine Wurzler, Corinna Hoose, Sylvaine Ferrachat, Rebekka Posselt, Ulla Heikkilä and my fellow PhD student, Aaron van Donkelaar. Each one you has entertained my numerous questions, and engaged in productive discussions, which have helped to refine this work. Your input, comments, and suggestions related to this research are gratefully appreciated. I have enjoyed this opportunity to work with each of you.

Additionally, I would like to acknowledge Drs. Jeff Pierce, Lyatt Jaeglé, Declan O'Donnell, Jan Kazil, Philipp Reuter, and Dorothy Koch for their productive discussions. Thanks also to Dorothy Koch and the following groups associated with providing aircraft data: NOAA at UC Boulder (David Fahey), University of Tokyo (Y. Kondo), and University of Hawaii (T. Clarke). Thanks to Aaron van Donkelaar

for providing aerosol optical depth data used for this project. I would also like to thank Luis Ladino, who is currently a PhD student at ETH Zurich, for his discussions and insights into this work from an experimental perspective. Thanks also to the four anonymous reviewers who reviewed the manuscripts that are presented as the second and third chapters of this thesis. Finally, I also thank the AERONET Principal Investigators and their staff for establishing and maintaining the 48 sites used in this investigation, and thanks to CSCS for computing time.

Chapter 1

Introduction

1.1 Our Warming Planet

Over the past one hundred years (1905-2005), the global mean earth surface temperature has increased by 0.76 °C; and over the last 50 years, the warming rate is 0.13 °C per decade [Solomon et al., 2007]. There is now a very high level of confidence that the global average net effect of human activities since 1750 has been one of warming. The earth's atmosphere plays a key role in modulating the earth's surface temperature. Without an atmosphere, the global mean surface temperature of the earth would be about 255 K, as opposed to the current 288 K. Thus, the knowledge of atmospheric processes is crucial towards understanding the response of our earth system to anthropogenic activities.

Unknowingly at first, mankind embarked on a global experiment in climate modification. At the present-day, society is becoming increasingly aware of these anthropogenic climate changes, and increased efforts are being devoted towards understanding and controlling these changes. This current work contributes towards the understanding of certain atmospheric processes related to aerosol and cloud interactions. The Intergovernmental Panel on Climate Change [Solomon et al., 2007] identified that the full range of processes related to the modification of cloud properties by aerosols (airborne particles) are not well understood. They are a key uncertainty in our understanding of climate change.

The earth's climate system is composed of several sub-systems, including the atmosphere, hydrosphere (oceans, rivers, and lakes), cryosphere (sea ice, ice sheets and glaciers), biosphere, and land surface. Radiation from the sun powers this system. The interactions within, and between these various subsystems are complex. This makes the understanding and prediction of climate change a challenging problem. Climate change can be driven by a variety of factors including the anthropogenic

(human-induced) changes in the emissions of gases and particles to the atmosphere, changes to the land surface, and natural changes such as fluctuations in solar irradiance. A dominant factor in the current climate change is the emission of carbon dioxide. The atmospheric concentration of carbon dioxide has increased from a pre-industrial value of 280 ppm to 379 ppm in the present day. Carbon dioxide is an important greenhouse gas, which absorbs out-going terrestrial radiation and warms the earth's surface. However, the problem of global warming is much more than a carbon dioxide problem. The following sections give a brief introduction to the atmosphere, and processes that are relevant towards understanding the subsequent chapters.

1.2 Earth's Atmosphere

The earth's atmosphere is generally considered as being divided into four layers, the troposphere, stratosphere, mesosphere, and thermosphere. The troposphere extends from the earth's surface up to 10 - 15 km. Temperature decreases with height in this layer. The processes examined in this study occur in this layer.

1.2.1 Gases

The atmosphere of the earth is a mixture of gases and particles. The primary gases are N_2 and O_2, which account for 78 and 21%, respectively, of the total volume of the atmosphere. The remaining 1% is mainly argon, but there are numerous, important trace gases. The trace gases include compounds of sulfur, nitrogen, carbon, and halogens, as well as ozone. The greenhouse gases are trace gases, including water vapor, carbon dioxide, methane, ozone and nitrous oxide. These gases absorb out-going terrestrial radiation and thereby keep the surface of the earth warmer. The atmospheric gases participate in physical and chemical cycles during their residence time in the atmosphere. Sources of these gases include biological and volcanic activity, radioactive decay, human industrial activity, and also chemical production in the atmosphere. Eventually, all gases are removed from the atmosphere by dry and wet deposition processes; but their lifetimes can vary from seconds to millions of years for nitrogen and the noble gases [Seinfeld and Pandis, 1998]. The major greenhouse

Table 1.1: Global mean aerosol and aerosol precursor emissions (Tg yr^{-1}, except Tg S yr^{-1} for sulfur species).

Species	Source	Reference	Tg yr^{-1}
SO_2	Volcanoes	Andres and Kasgnoc [1998] Halmer et al. [2002]	14.6
	Vegetation Fires	van der Werf et al. [2003]	2.1
	Industry, Fossil Fuel, Bio-fuels	Cofala et al. [2005]	54.2
DMS	Marine Biosphere	Kettle and Andreae [2000] Nightingale et al. [2000]	23.4
	Terrestrial Biosphere	Pham et al. [1995]	0.3
Black Carbon	Vegetation Fires	van der Werf et al. [2003]	3.0
	Fossil Fuels	Bond et al. [2004]	3.0
	Bio-fuels	Bond et al. [2004]	1.6
Organic Matter	Biogenic	Guenther et al. [1995]	19.1
	Vegetation Fires	van der Werf et al. [2003]	34.7
	Fossil Fuels	Bond et al. [2004]	3.4
	Bio-fuels	Bond et al. [2004]	9.1
Sea Salt	Wind-driven	Schultz et al. [2004]	5350
Dust	Wind-driven	Tegen et al. [2002]	330

gases have lifetimes of many years, except for water vapor (close to one week), and tropospheric ozone (days to weeks).

1.2.2 Aerosols

Aerosols are the particulate matter that is suspended in the atmosphere. Primary aerosols are emitted directly from the surface, and include sea salt, dust, sulfate, black carbon and particulate organic matter. Secondary aerosols are produced within the atmosphere by the oxidation of gaseous precursors, and include sulfate from SO_2, organic matter from semi-volatile organic compounds and nitrates from NO_x emissions. There are considerable uncertainties in the estimates of global emission inventories. Table 1.1 shows the annual and global mean present-day aerosol emission inventory used for this study. Recent work by Heald et al. [2010] suggests that our inventory may under-estimate organic aerosol by about a factor of two.

Atmospheric aerosols have an important role in the climate system since they

scatter and absorb incident solar radiation. These are termed the direct aerosol effects [Charlson et al., 1992]. Black carbon and dust absorb solar radiation and have a warming influence, particularly over high albedo surfaces [Chylek and Wong, 1995], whereas the other aerosol species scatter solar radiation and have a cooling effect on climate. Additionally, aerosols act as the nuclei for the formation of cloud droplets and ice crystals. In this latter role, the aerosols can modify cloud properties and precipitation, and thus indirectly influence the earth's radiation budget. These are the indirect aerosol effects [Twomey, 1991, Lohmann and Feichter, 2005]. Clouds are important components of the climate system since they scatter and absorb both solar and terrestrial radiation.

The size spectrum of aerosols is described with a size distribution function. The lognormal distribution is one of the most commonly used functions. This is given by

$$\frac{dN}{d\ln r} = \frac{N}{\sqrt{2\pi}\ln\sigma_g}\exp\Big(-\frac{(\ln r - \ln \overline{r}_{pg})^2}{2\ln^2\sigma_g}\Big) \tag{1.1}$$

where N is the total aerosol number concentration, r is the aerosol radius, $\overline{r}_{pg}$ and σ_g are parameters of the lognormal distribution, the geometric mean aerosol radius and the geometric standard deviation, respectively. The natural aerosol spectrum is typically multi-modal. Thus, a superposition of two or more lognormal modes is needed to describe natural aerosol spectra [Vignati et al., 2004, Stier et al., 2005]. Typical aerosol size ranges for these modes are: 1) nucleation (radius $<$5 nm) 2) Aitken (radius 5 - 50 nm) 3) accumulation (radius 50 - 500 nm), and 4) coarse (radius $>$ 500 nm).

Aerosols can be considered as externally or internally mixed. If each aerosol particle in a sample consists of one chemical compound, but that composition varies between aerosol particles, we consider those aerosols to be externally mixed. If the aerosols in a sample each contain a similar distribution of chemical compounds, then those aerosols are said to be internally mixed. Aerosols that have been in the atmosphere for longer periods of time (aged aerosols) typically are internally mixed since they have coagulated with other aerosols, or had additional chemical compounds condense upon them. The mixing state of aerosols is important since internally mixed aerosols are generally more soluble than certain externally mixed species such as black carbon, primary organic matter and dust. The solubility of an aerosol will determine

how readily that aerosol can take up water vapor and act as a nucleus for condensation of a cloud droplet or ice crystal [Pruppacher and Klett, 1997, Seinfeld and Pandis, 1998].

1.2.3 Aerosol-Cloud Interactions

Aerosols that contain some fraction of soluble material will take up water and grow in size in moist air. The Köhler equation [Köhler, 1936] is used to describe the equilibrium size of an aerosol particle as a function of the supersaturation (the ratio of the ambient to the saturation vapor pressure). For the case of an aqueous solution drop [Pruppacher and Klett, 1997], this equation is given as

$$\frac{e}{e_{w,s}} = 1 + \frac{A}{r} - \frac{B}{r^3} \tag{1.2}$$

where

$$A = \frac{2\sigma M_w}{RT\rho_w} \tag{1.3}$$

and

$$B = \frac{3m_s M_w}{4\pi M_s \rho_w}. \tag{1.4}$$

e is the ambient vapor pressure at the particle surface, $e_{w,s}$ is the saturation vapor pressure such that the net flux of water molecules at the drop's surface would be zero, r is the wet aerosol radius, σ is the surface tension, and ρ_w is the density of water. M_w and M_s are the molecular weights of water and of the solute, respectively and T is the temperature and R is the universal gas constant. The second term in Eqn. 1.2 is commonly called the curvature (Kelvin) term and indicates that smaller aerosols require greater supersaturation to be in equilibrium with the environment. The last term is the solution (Raoult's) term, which indicates that the equilibrium vapor pressure is lower over droplets that contain more relatively more soluble material. Figure 1.1 shows the equilibrium size for a wet 10^{-16} g NaCl aerosol. There is competition between the curvature and solution terms, which results in a maximum in the Köhler curve for a certain wet aerosol radius depending on the solute mass, and temperature. Aerosols that take up water more readily than others are said to be more hygroscopic.

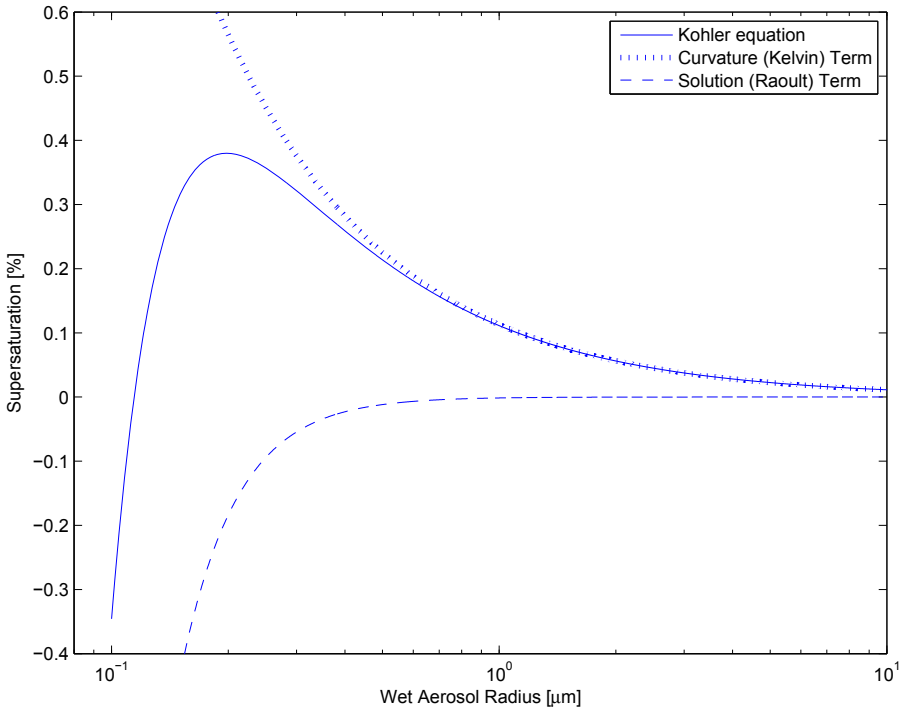

Figure 1.1: Equilibrium aerosol wet radius as a function of supersaturation for a 10^{-16} g NaCl aerosol, and the separate curvature and solution terms.

If the number of aerosols in the atmosphere is increased, such as in the case of anthropogenic pollution, there are more aerosols to compete for the available water vapor. As a result, the cloud droplets that form will tend to be smaller and more numerous than for a pristine case with lower aerosol numbers. Thus, clouds that form in polluted regions with higher aerosol concentrations tend to be more reflective of solar radiation due to the more numerous and smaller cloud droplets than for a cloud that forms in cleaner conditions. This effect is called the first aerosol indirect effect or Twomey effect [Twomey, 1991]. The Intergovernmental Panel on Climate Change in the most recent Fourth Assessment Report (2007) states that relative to pre-industrial times, the radiation balance has been perturbed by between -0.3 and -1.8 W m^{-2} due to the Twomey effect [Solomon et al., 2007]. However, due to the complexity of the processes involved, there is low level of scientific understanding associated with this estimate. This motivates the need for ongoing research into the field of cloud-aerosol interactions. There is a slightly better (moderate to low) level

of scientific understanding associated with estimates of the perturbation of the global radiation balance since pre-industrial times due to the direct effect of aerosols (-0.1 to -0.9 W m^{-2}) [Solomon et al., 2007].

In addition to the first indirect effect, there are a variety of other ways that aerosols can modify cloud properties [Lohmann and Feichter, 2005]. 1) The cloud lifetime effect refers to the delayed onset of precipitation, and increased cloud lifetime that is expected in the case of smaller and more numerous cloud droplets or ice crystals. This occurs since the relative size and number of cloud hydrometeors influences the rate of collision and coalescence of those hydrometeors, which in turn strongly controls the development of precipitation. This effect was first hypothesized by Albrecht [1989] and is also sometimes called the Albrecht or second indirect effect. However, newer studies did not find evidence for an increased lifetime, but suggest that the smaller droplets evaporate more readily [Jiang et al., 2006]. 2) The thermodynamic effect is the delay of freezing in clouds that have more numerous and smaller droplets. Particularly for convective clouds, if small droplets are more numerous, this delays the onset of warm rain formation, and delays freezing. As a result, freezing and latent heat release occur at higher altitudes in the cloud. This invigorates the convection [Rosenfeld and Woodley, 2000, Khain et al., 2001, 2005]. The net impacts on precipitation, and on cloud radiative effects for this process are still not conclusively determined. 3) The glaciation indirect effect [Lohmann, 2002] refers to the increase in precipitation production efficiency in the case of more numerous ice nuclei since a cloud that glaciates more readily will produce precipitation more readily. 4) Finally, the riming indirect effect is the reduced riming efficiency that occurs in mixed liquid and ice phase clouds due to smaller droplets [Borys et al., 2003]. Riming refers to the collision of droplets with crystals in clouds that contain both droplets and crystals, and the subsequent freezing of the droplets onto the crystal surface. Cloud droplets that are smaller and more numerous have a smaller riming efficiency and this reduces the rate of production of snow in polluted clouds. Thus, aerosols modify cloud properties by several mechanisms.

1.2.4 Radiation Budget

Clouds and aerosols strongly influence the earth's radiation budget. In an equilibrium climate, the input of solar radiation to the earth-atmosphere system is exactly balanced by outgoing longwave radiation. However, the earth is currently gradually warming; and there is a current imbalance of about +0.85 W m^{-2} [Hansen et al., 2005, Trenberth et al., 2009]. The incoming solar radiation is reflected by the atmosphere, clouds and surface. The remainder is absorbed by the atmosphere, and at the surface. The surface emits outgoing longwave radiation that is absorbed and re-emitted by the atmosphere and clouds. There are also fluxes of sensible heat from the surface, and latent heat release associated with the phase changes of water in the atmosphere. Current estimates of the global radiation budget considering all of these properties, and based on satellite retrievals are summarized by Trenberth et al. [2009].

As we have seen in the previous section, aerosols influence cloud radiative properties. The shortwave cloud forcing (SCF) at the top of the atmosphere [Ramanthan et al., 1989] is defined as

$$SCF = SW_{clr} - SW_{allsky} \tag{1.5}$$

where SW_{clr} is the outgoing shortwave radiation in the case of no clouds, and SW_{allsky} is the outgoing shortwave radiation considering a sky that includes clouds. The loss of shortwave radiation to space is greater when clouds are included, and thus the SCF is negative. Clouds have a net cooling effect in terms of shortwave radiation. The longwave cloud forcing (LCF) at the top of the atmosphere [Ramanthan et al., 1989] is given as

$$LCF = LW_{clr} - LW_{allsky} \tag{1.6}$$

where LW_{clr} and LW_{allsky} are the outgoing longwave radiation at the top of the atmosphere for clear sky only and including clouds, respectively. The outgoing longwave radiation is reduced since clouds absorb longwave radiation and re-emit at lower temperature. This is particularly true for high-level clouds. The global and annual mean SCF and LCF cloud forcing are estimated from satellite retrievals as -50 W m^{-2}, and 30 W m^{-2}, respectively [Kiehl and Trenberth, 1997]. Additionally, clouds influence the global radiation budget due to water phase changes, which release latent heat associated with the condensation of water vapor, and freezing. To summarize, the

net effect of aerosols and clouds on the climate system is believed to be in opposition to the warming effects of greenhouse gases, but the level of scientific understanding is low to moderate [Solomon et al., 2007].

1.2.5 Wet Scavenging and Cloud Processing of Aerosols

In the previous sections, we have seen that aerosols influence clouds and precipitation processes. Conversely, clouds and precipitation also influence the physical and chemical properties of aerosols. Wet scavenging of aerosols refers to the processes that incorporate aerosols into cloud hydrometeors and precipitation. This can ultimately lead to the removal of aerosols from the atmosphere as the aerosol-laden precipitation falls to the earth's surface. Early interest in wet scavenging processes developed with the advent of nuclear bomb testing in the 1950s since the rates of removal of radio-active debris from the atmosphere became a concern [Greenfield, 1957]. Later interest continued with concern about acid rain in the 1970s and 1980s [Grover and Pruppacher, 1977, Wang et al., 1978, Slinn, 1984]. Aerosols may be incorporated in clouds and precipitation by two primary mechanisms 1) by acting as a cloud condensation or ice nucleus for the formation of a cloud droplet or ice crystal, respectively, which may then grow to precipitation size (nucleation scavenging) and 2) by colliding with cloud hydrometeors or precipitation (impaction scavenging). Wet scavenging accounts for a large fraction of the global and annual mean removal of aerosols from the atmosphere, and strongly controls three-dimensional aerosol distributions. Thus, understanding these processes is relevant towards understanding the role of aerosols in the climate system [Rasch et al., 2000, Textor et al., 2006].

Pioneering work in the field of impaction scavenging was conducted by Greenfield [1957]. We use the term collision efficiency to refer to the efficiency that falling particles of different sizes collide with each other. Considering the dimensions of the colliding partners, the collision efficiency is defined as the ratio of the actual collision cross-section to the geometric cross-section. For spherical particles, the collision efficiency is

$$E = \frac{y_c^2}{(r_1 + r_2)^2} \tag{1.7}$$

where y_c is a radius of the grazing trajectory and r_1 and r_2 are the radius of the

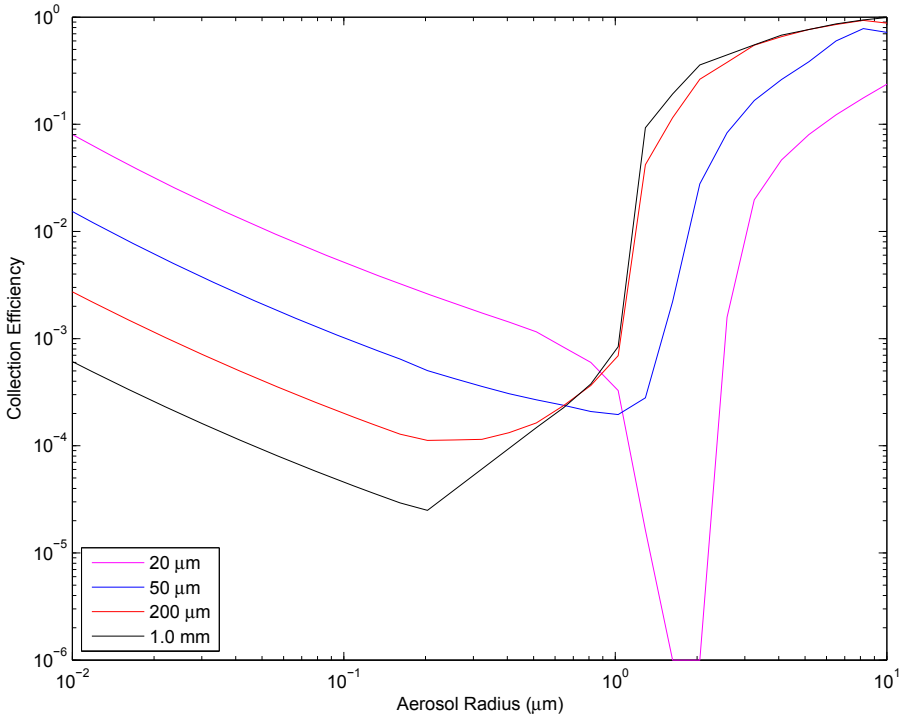

Figure 1.2: Collision efficiency for drop-aerosol collisions as a function of aerosol radius and collector rain drop size

2 collision partners, representing the geometric cross-section. Figure 1.2 shows an example of collision efficiency as a function of aerosol size for a variety of drop sizes. There are a variety of forces involved in this problem. As a result of this interplay of forces, Greenfield [1957] found that there is a minimum aerosol size (generally, the accumulation mode) that is least efficiently collected by cloud and precipitation hydrometeors. With decreasing aerosol size in the submicron size range, Brownian motion increases the collision efficiency. For aerosols about one micron in radius and larger, inertial forces cause the collision efficiency to increase with increasing aerosol size. The collision efficiency minimum is commonly referred to as the 'Greenfield Gap'. Investigations have also been conducted for collision efficiencies for crystal-aerosol collisions [Pitter, 1977, Martin et al., 1980, Murakami et al., 1985, Miller and Wang, 1989, Sauter and Wang, 1989, Miller and Wang, 1991, Song and Lamb, 1994, Bell and Saunders, 1995, Wang and Lin, 1995]. One important feature shown by Fig. 1.2 is that the collision efficiency ranges over several orders of magnitude for aerosols

in the Aitken, accumulation and coarse mode size ranges. This motivates the need for physically detailed representations of the collision scavenging process in models that simulate this process.

For aerosols near the Greenfield gap size, other forces can more strongly influence the collision efficiency. This includes phoretic effects (thermophoresis and diffusiophoresis), electrical and turbulent effects. Thermophoretic effects enhance the collision efficiency when a hydrometeor is evaporating. Evaporative cooling at the collector's surface produces a temperature gradient between the hydrometeor surface and the ambient air, which induces aerosol motion towards the collector [Grover and Pruppacher, 1977, Wang et al., 1978]. The collision efficiency increases as the ambient relative humidity decreases. Diffusiophoresis refers to aerosol motions induced by concentration gradients in gaseous mixture [Pruppacher and Klett, 1997]. For the systems of interest here, water vapor gradients induce aerosol motion in the same direction as the vapor flux. Thus, thermophoresis and diffusiophoresis have opposing effects on the collision efficiency, but the thermophoretic effects are generally of larger magnitude. If the collision partner have opposing charges, this will also increase the collision efficiency [Wang et al., 1978, Tinsley et al., 2006]. Similarly, turbulence can enhance the collision efficiency relative to that for laminar flow [Vohl et al., 1999]. Collection efficiency is the product of the collision efficiency and the coalescence efficiency. The coalescence efficiency is the probability that aerosols that have collided with each other will coalesce. Coalescence efficiencies are commonly assumed to be unity for collisions between aerosols and atmospheric hydrometeors [Pruppacher and Klett, 1997]. Thus, collision efficiencies and collection efficiencies are commonly treated as being identical.

Nucleation scavenging depends on the aerosol size, and additionally on the chemical composition, as described by the Köhler equation [Köhler, 1936] in the previous section. Internally mixed particles that contain some soluble material will nucleate cloud droplets more readily than insoluble dust and carbonaceous aerosols, which do not nucleate cloud droplets at typical atmospheric supersaturations [Lin and Leaitch, 1997, Lohmann et al., 2007, Lohmann, 2008]. The ice nucleating ability of various

aerosol species is the ongoing subject of research, but generally dust and black carbon are considered as species with the ability to nucleate ice crystals [Young, 1974, Cotton et al., 1986, Pruppacher and Klett, 1997, Diehl and Wurzler, 2004, Lohmann and Diehl, 2006].

Cloud processing refers to the set chemical and physical processes that modify aerosols as they as pass through clouds. Various chemical reactions occur in cloud droplets, which can ultimately produce aerosols. Oxidation of sulfur dioxide by ozone and hydrogen peroxide in cloud droplets are important pathways for the production of sulfate aerosols [Feichter et al., 1996]. Additionally, organic aerosols are produced by the in-droplet oxidation of organic compounds [Blando and Turpin, 2000, Kanakidou et al., 2005, Kroll and Seinfeld, 2008, Hallquist et al., 2009]. Also, within cloud droplets and ice crystals, insoluble aerosols are mixed with soluble species. As the droplets (crystals) evaporate (sublimate), the insoluble aerosols are coated with soluble material [Wurzler et al., 2000, Crumeyrolle et al., 2008, Hoose et al., 2008a,b]. Thus, the passage through clouds increases the fraction of aerosols which may nucleate droplets and crystals at a subsequent point in time. Additionally, cloud processing modifies aerosol size distributions. Often there is more than one aerosol in a droplet or crystal, and when the hydrometeor evaporates, the aerosols coagulate together to produce one larger aerosol. These processes contribute towards the aging of aerosols. An aged aerosol is an aerosol than has resided in the atmosphere long enough to become mixed with other aerosol species.

1.3 Global Climate Models - The ECHAM5-HAM GCM

As the previous sections have pointed out, there are many non-linear processes involved in aerosol-cloud-precipitation interactions. Also, there are many feedbacks between these processes. As a result, models are valuable tools for understanding how changes in certain aspects of the climate system may influence the state of the entire system. Global climate models (GCMs) are used to represent the entire earth-atmosphere-ocean system. For this study we use the ECHAM5 GCM [Roeckner et al., 2003].

GCMs are different from other global models, such as the weather forecast models and chemical transport models. Weather forecast models rely strongly on initial conditions. A small change in the initial conditions can cause the model solutions to diverge widely after several days of model integrations. For this reason, weather forecasts can only be extended a few days into the future since a complete description of the global initial conditions is impossible. This is often termed the 'butterfly' effect. A small change in the initial conditions, such as butterfly's moving wings can cause solutions for the equations of motion to diverge. Conversely, a climate model depends strongly on boundary conditions. This includes detailed descriptions of the surface type, typography and albedo, radiation inputs to the system, and sea surface temperatures (in the case that an ocean model is not coupled to the atmospheric model). The boundary conditions keep the model constrained such that typical monthly mean conditions are predicted for each GCM grid box. Due to computational constraints, the typical size grid box size of a GCM is generally larger than for a weather forecast model (a few hundreds of km and a few tens of kilometers, respectively). A chemical transport model (CTM) also differs from a GCM. A CTM uses assimilated, as opposed to prognosed, meteorological fields such that the emphasis is on detailed representations of the atmospheric chemistry and composition.

The ECHAM5-HAM GCM, used for this study, is the fifth generation atmospheric GCM developed at the Max-Planck Institute for Meteorology [Roeckner et al., 2003], and evolved from the model of the European Centre for Medium Range Weather Forecasting (ECMWF). The model solves prognostic equations for atmospheric motion (vorticity and divergence), temperature and surface pressure using spheric harmonics with triangular truncation. Water vapor, cloud liquid and ice water are also prognostic variables and are transported using a semi-Lagrangian scheme [Lin and Rood, 1996]. The solar radiation scheme has 6 spectral bands [Cagnazzo et al., 2007] and the infrared has 16 spectral bands [Mlawer et al., 1997, Morcrette et al., 1998]. The GCM is coupled to the Hamburg Aerosol Module (HAM), which is a detailed aerosol microphysics scheme [Stier et al., 2005] that considers five aerosol species. The aerosols are described as the superposition of seven lognormal modes. There are four soluble/internally mixed modes in the size ranges of nucleation (NS), Aitken (KS),

accumulation (AS) and coarse (CS), and three insoluble modes (Aitken (KI), accumulation (AI), and coarse (CI)). The mass of each species and the aerosol number for each of the seven modes are prognostic tracers in the model.

1.4 Goals of this Present Work

The preceding sections have given a brief introduction, and provide the background necessary to understand this work, and to put this project into context. This section outlines the motivation for conducting the project. The ultimate goal of this work is to make a contribution towards the understanding of aerosol-cloud-precipitation interactions in the climate system. Since there is a low level of scientific understanding with respect to aerosol-cloud-precipitation interactions [Solomon et al., 2007], there is a low level of confidence in predictions about the extent that aerosols and clouds can moderate the warming associated with future increases in greenhouse gas concentrations.

Models are useful tools to predict future climate change since many non-linear and coupled feedback processes are involved. Examination of simulations of present-day aerosol and cloud three-dimensional distributions allows us to examine and identify the aspects of our knowledge, which need further research. This project uses one of the world-leading global aerosol-climate models (ECHAM5-HAM), and examines the performance of the wet scavenging and cloud processing schemes for simulations of our present-day climate. Physically detailed representations of these processes are developed and introduced into the GCM.

Wet scavenging processes strongly influence three-dimensional aerosol distributions. However, these processes are represented with a variety of approaches between global models. This contributes to considerable differences in the predicted aerosol distributions [Rasch et al., 2000, Textor et al., 2006]. Koch et al. [2009] showed that vertical profiles of predicted black carbon concentrations differed by up to 2 orders of magnitude between global models. This study investigates the extent that the representation of wet scavenging and cloud processing can contribute to these differences. Wet scavenging processes are generally represented in global models with either 1) prescribed fractions or 2) a scheme that links the scavenging more explicitly with the

cloud microphysics. The standard ECHAM5-HAM model uses prescribed fractions to represent the wet scavenging processes both below and in clouds. This approach is typical of many global models [Barth et al., 2000, Chin et al., 2000, Takemura et al., 2002, Stier et al., 2005, Tie et al., 2005]. Since wet scavenging is a size-dependent process, the scavenging rates can vary over several orders of magnitude for the nucleation, Aitken, accumulation and coarse size ranges. Prescribed scavenging fractions can not capture this intra-modal variability. With the recent development of models that predict aerosol size [Stier et al., 2005], a more physically detailed representation of the size-dependency of the wet processes is now possible. The goals of the first of the three sub-projects conducted for this project are to 1) introduce a size-dependent representation of below-cloud impaction scavenging by both rain and snow into the ECHAM5-HAM model, 2) evaluate the impact of these changes on the predicted aerosol distributions, and 3) evaluate the model performance in comparison with observations. Finally, 4) this project can provide useful guidance to other global models in regard to the performance of prescribed scavenging fraction schemes relative to more physically detailed approaches.

The second sub-project of this work focuses on in-cloud scavenging. In-cloud scavenging is also commonly treated with prescribed fractions to represent the uptake of aerosols in to cloud hydrometeors [Stier et al., 2005]. Alternatively, there may be a more explicit link to the cloud microphysics of the model [Adams and Seinfeld, 2002, Gong et al., 2003, Tost et al., 2006]. The goals of this project are to 1) introduce an explicit representation of the size dependence of the in-cloud impaction scavenging into the ECHAM5-HAM model (based on the size of the aerosol and cloud hydrometeors, and also on the cloud droplet and ice crystal number concentrations), and 2) develop a new parameterization of the processes of nucleation scavenging, which depends on the size and composition of the aerosols. With these developments, the relative importance of nucleation and impaction scavenging in the global removal of aerosols from the atmosphere can be quantified. 3) This will allow an examination of how uncertainties in the representation of in-cloud scavenging processes contribute to differences in predicted aerosol vertical profiles of concentrations and deposition.

4) Based on this work, guidelines can be provided to global modelers about the representation of in-cloud scavenging, and the strengths and weaknesses of the various approaches for representing these processes. Finally, 5) this work can identify those processes that need future research both through modeling, laboratory and field studies.

The final part of this project addresses the cloud processing of aerosols. Cloud processing and wet scavenging are the two primary ways that clouds can influence aerosol size distributions. While wet scavenging focuses on the removal of aerosols from the atmosphere, cloud processing focuses on the passage of aerosols through clouds followed by release to the atmosphere by evaporation. Evaporation processes are very important in the atmosphere. Pruppacher and Jaenicke [1995] and Hoose et al. [2008a] showed that in the annual and global mean, about 85% of clouds will evaporate, as opposed to dissipating by precipitation. The goals of this final part of the project include 1) to extend the stratiform cloud processing approach of Hoose et al. [2008a,b] to convective clouds. There are a limited number of other global models that make an explicit representation of cloud processing of aerosols [Jones et al., 2001, Easter et al., 2004, Koch et al., 2006]. The treatment of Hoose et al. [2008a,b] is unique in that the aerosol mass in droplet and in crystals are treated as separate prognostic variables in the model. The recent development of the double-moment convective cloud microphysics scheme of Lohmann [2008] makes an extension of this approach possible for convective clouds.

A further goal of this final sub-project is 2) to conduct an examination of the relative importance of aerosol cycling through convective versus stratiform clouds from a global perspective. Early work by Pruppacher and Jaenicke [1995] found that an aerosol remote to source has cycled through clouds about 3 times. Hoose et al. [2008a] showed that in the global, and annual mean, stratiform cloud processing contributes to less than 1 cycle through clouds. Thus, convective cloud processing is expected to contribute significantly to the cycling of aerosols through clouds. Earlier modeling and field studies have shown that processing by convective clouds can strongly modify aerosol size distributions and hygroscopicity (the tendency of an aerosol to take up water) [Wurzler et al., 2000, Ekman et al., 2006, Crumeyrolle et al., 2008]. The

final goal of this third sub-project is 3) to quantify the extent that an explicit representation of convective processing of aerosols modifies predicted three-dimensional aerosol distributions, and to examine the relative importance of these processes for convective as compared to stratiform clouds. This work provides guidance to other modelers about the relevance of the inclusion of cloud processing in global models.

Chapter 2

Aerosol Size-Dependent Below-Cloud Scavenging by Rain and Snow in the ECHAM5-HAM

Authors: B. Croft[1], U. Lohmann[2], R. V. Martin[1,3], P. Stier[4], S. Wurzler[5], J. Feichter[6], R. Posselt[7], and S. Ferrachat[2]

[1]Department of Physics and Atmospheric Science, Dalhousie University, Halifax, Canada
[2]Institute of Atmospheric and Climate Science, ETH Zurich, Zurich, Switzerland
[3]Harvard-Smithsonian Center for Astrophysics, Cambridge, USA
[4]Atmospheric, Oceanic, and Planetary Physics, University of Oxford, Oxford, UK
[5]Landesamt fur Natur, Umwelt und Verbraucherschutz NRW (LANUV), Recklinghausen, Germany
[6]Max Planck Institute for Meteorology, Hamburg, Germany
[7]Federal Office of Meteorology and Climatology MeteoSwiss, Zurich, Switzerland

Article published in Atmospheric Chemistry and Physics, 9, 4653-4675, 2009.
All text, figures, tables, and presented results were contributed by the first author, B. Croft, with the exception of Tables 2.2 and 2.3, and observational data (sources are referenced in the text).

2.1 Abstract

Wet deposition processes are highly efficient in the removal of aerosols from the atmosphere, and thus strongly influence global aerosol concentrations, and clouds, and their respective radiative forcings. In this study, physically detailed size-dependent below-cloud scavenging parameterizations for rain and snow are implemented in the ECHAM5-HAM global aerosol-climate model. Previously, below-cloud scavenging by

rain in the ECHAM5-HAM was simply a function of the aerosol mode, and then scaled by the rainfall rate. The below-cloud scavenging by snow was a function of the snowfall rate alone. The global mean aerosol optical depth, and sea salt burden are sensitive to the below-cloud scavenging coefficients, with reductions about 15% when the more vigorous size-dependent below-cloud scavenging by rain and snow is implemented. The inclusion of a prognostic rain scheme significantly reduces the fractional importance of below-cloud scavenging since there is higher evaporation in the lower troposphere, increasing the global mean sea salt burden by almost 15%. Thermophoretic effects are shown to produce increases in the global and annual mean number removal of Aitken size particles of about 10%, but very small increases (about 1%) in the global mean below-cloud mass scavenging of carbonaceous and sulfate aerosols. Changes in the assumptions about the below-cloud scavenging by rain of particles with radius smaller than 10 nm do not cause any significant changes to the global and annual mean aerosol mass or number burdens, despite a change in the below-cloud number removal rate for nucleation mode particles by about five-fold. Annual and zonal mean nucleation mode number concentrations are enhanced by up to 30% in the lower troposphere with the more vigourous size-dependent below-cloud scavenging. Closer agreement with different observations is found when the more physically detailed below-cloud scavenging parameterization is employed in the ECHAM5-HAM model.

2.2 Introduction

Atmospheric aerosols significantly influence climate since they both reflect and absorb radiation (direct effects), and modify cloud properties (indirect radiative effects) [Twomey, 1991, Charlson et al., 1992]. A general circulation model (GCM) must correctly quantify the global 3-dimensional distribution of the various aerosol species in order to accurately predict climate. Global aerosol distributions are strongly controlled by the rate of removal of aerosols from the atmosphere by wet scavenging processes [Rasch et al., 2000], and these processes are represented with a great diversity between models [Textor et al., 2006]. To date, the below-cloud scavenging coefficients in the ECHAM5-HAM model have been a function of the aerosol mode

(nucleation, Aitken, accumulation and coarse), and then scaled by the precipitation flux. However, in reality these scavenging coefficients can vary over one or two orders of magnitude within any given size mode [Greenfield, 1957, Wang et al., 1978]. This variability is due to a variety of physical processes, including an interplay of Brownian motion, and inertial impaction that produces a scavenging minimum for aerosols about 0.1 μm in radius.

Previous modeling studies have implemented size-dependent below-cloud scavenging parameterizations for rain into regional and global models [Gong et al., 1997, Tost et al., 2006, Henzing et al., 2006]. Tost et al. [2006] assumed a mean raindrop size as opposed to introducing a raindrop size distribution. Observational studies [Andronache, 2003, Andronache et al., 2006] have shown that below-cloud scavenging does depend on the aerosol and raindrop distribution. In this study, we include both the aerosol and raindrop distributions in the parameterization of the below-cloud scavenging coefficients, and investigate the deposition budgets for sulfate, black carbon, particulate organic matter, sea salt, and dust, and the 3-dimensional distributions of these aerosols in global simulations with the ECHAM5-HAM model. Since the ECHAM5-HAM model predicts the median radius of the log-normal distribution for each of seven aerosol modes, the detailed dependency of below-cloud scavenging on aerosol size can be included in the model.

Below-cloud scavenging by snow is more difficult to represent in models since more assumptions about the size and the shape of the crystals are required in order to estimate the collection efficiency of the snow. Previous global studies have typically used fixed mean below-cloud scavenging coefficients that are scaled by the snow flux [Stier et al., 2005, Tost et al., 2006]. Gong et al. [1997] did apply an aerosol size-dependent below-cloud scavenging parameterization for snow following Slinn [1984] into a regional model for sea salt. This study uses a similar parameterization, following Slinn [1984] and Dick [1990] but extends the approach to global simulations of five aerosol species.

The goal of this study is to investigate the impacts of below-cloud scavenging parameterizations for both rain and snow on the vertical profiles of aerosol mass and

number in the framework of a global model. For this study, we use the term below-cloud scavenging since the aerosol impaction scavenging by rain and snow is examined only below cloud base. We will consider the impacts of these parameterizations on global aerosol deposition, burdens, concentrations, and also on cloud properties, cloud radiative properties, and precipitation. Section 2.3 provides an overview of the ECHAM5-HAM model, and presents the collection efficiencies and below-cloud scavenging coefficients required for the aerosol size-dependent below-cloud scavenging parameterizations. Section 2.4 presents the results and discussion, comparing the various aerosol size-dependent below-cloud scavenging parameterizations in terms of their impacts on aerosol wet deposition, burdens, vertical profiles of aerosol mass and number concentrations, and clouds. Section 2.5 is the summary and conclusions.

2.3 Model Description

ECHAM5 is a fifth generation atmospheric general circulation model (GCM) developed at the Max-Planck Institute for Meteorology [Roeckner et al., 2003], and evolved from the model of the European Centre for Medium Range Weather Forecasting (ECMWF). The model solves prognostic equations for vorticity, divergence, temperature and surface pressure using spheric harmonics with triangular truncation. Water vapor, cloud liquid water and ice are transported using a semi-Lagrangian scheme [Lin and Rood, 1996]. Prognostic equations for cloud water and ice follow Lohmann et al. [2007]. The model includes the cirrus scheme of Lohmann and Kärcher [2002]. Convective clouds, and transport are based on the mass-flux scheme of Tiedtke [1989] with modifications following Nordeng [1994]. The solar radiation scheme has 6 spectral bands [Cagnazzo et al., 2007] and the infrared has 16 spectral bands [Mlawer et al., 1997, Morcrette et al., 1998]. The GCM is coupled to the Hamburg Aerosol Model (HAM), which is described in detail in Stier et al. [2005]. The aerosols are represented by seven log-normal modes, 4 internally mixed/soluble modes (nucleation (NS), Aitken (KS), accumulation (AS), and coarse (CS)) and 3 insoluble modes (Aitken (KI), accumulation (AI),and coarse (CI)). The median radius for each mode is calculated from the aerosol mass and number distributions in each mode. Aerosol mass and number are transferred between the modes by the processes of sulfuric acid

condensation, and also coagulation between aerosols. All results presented in this study are from a one year simulation, following a three months spin-up period, and are nudged towards the meteorological conditions of the year 2001. The nudging approach, combined with aerosol-radiation de-coupling, was chosen in order to have the same dust and sea salt emissions in all simulations. We chose the year 2001 since that was a neutral year for the El Nino Southern Oscillation. The natural emissions of sea salt, dust, and DMS from the oceans are calculated on-line, based on the meteorology of the model. Emissions for all other aerosol species are taken from the AEROCOM emission inventory, and are representative for the year 2000 [Dentener et al., 2006b]. The aerosol emissions and the removal processes of in-cloud scavenging, sedimentation, and dry deposition are described in detail in Stier et al. [2005].

2.3.1 Below-Cloud Scavenging Parameterizations

Current below-cloud scavenging parameterization

The below-cloud scavenging parameterization in the control (CTL) simulation of the ECHAM5-HAM model follows Stier et al. [2005]. The below-cloud scavenging coefficients are a function of the aerosol mode, and are scaled by the respective rain, or snow flux in each model layer. These coefficients are shown in Table 2.1, and for rain assume a fixed rain drop diameter of 4 mm, and a lognormal aerosol distribution, following Fig. 20.15 in Seinfeld and Pandis [1998]. The tracer tendency due to below-cloud scavenging is

$$\overline{\frac{\Delta C_i}{\Delta t}} = C_i^{\mathrm{amb}} f^{\mathrm{precip}} (R_i^r F^r + R_i^s F^s) \tag{2.1}$$

where C_i^{amb} is the ambient mixing ratio of the ith tracer in the cloud-free air. F^r and F^s are the fluxes of rain and snow, respectively. f^{precip} is the fraction of the grid box affected by precipitation. R_i^r and R_i^s are the below-cloud scavenging coefficients normalized by the precipitation flux for rain and snow, respectively.

New Below-Cloud Scavenging Parameterization for Rain

The more physically detailed size-dependent below-cloud scavenging parameterization for rain used in all model simulations except CTL does not assume a fixed collector

Table 2.1: Prescribed below-cloud scavenging coefficients ($m^2\ kg^{-1}$) as a function of aerosol mode, for the four internally mixed/soluble modes, nucleation (NS), Aitken (KS), accumulation (AS), coarse (CS), and the three insoluble modes, Aitken (KI), accumulation (AI), and coarse (CI).

	Rain	Snow
NS	5 x 10^{-4}	5 x 10^{-3}
KS	1 x 10^{-4}	5 x 10^{-3}
AS	1 x 10^{-3}	5 x 10^{-3}
CS	1 x 10^{-1}	5 x 10^{-3}
KI	1 x 10^{-4}	5 x 10^{-3}
AI	1 x 10^{-3}	5 x 10^{-3}
CI	1 x 10^{-1}	5 x 10^{-3}

drop size, but instead assumes that the raindrops follow the distribution of Marshall and Palmer [1948],

$$N(D_p) = n_o \exp(-\Lambda D_p) \tag{2.2}$$

where

$$\Lambda = 4.1 R^{-0.21} \tag{2.3}$$

and n_o is $8{\times}10^3\,\mathrm{m}^{-3}\,\mathrm{mm}^{-1}$, and D_p is the drop diameter in mm, and R is the rainfall rate in $\mathrm{mm\,hr}^{-1}$.

The below-cloud scavenging coefficients as a function of aerosol size (r_p) are given by

$$\Lambda(r_p) = \int_0^\infty \pi R_p^2 U_t(R_p) E(R_p, r_p) N(R_p) dR_p \tag{2.4}$$

following Slinn [1984]; Pruppacher and Klett [1997] and Seinfeld and Pandis [1998], where $E(R_p, r_p)$ is the collection efficiency as a function of the drop and aerosol radii, R_p and r_p, respectively, and $U_t(R_p)$ is the drop's terminal velocity.

The collection efficiencies used in this study are compiled in a look-up table as a function of aerosol and collector drop size from the sources that are outlined in Table 2.2. The collection efficiency due to Brownian diffusion follows Young [1993] and is

$$E_{\text{Brownian}} = \frac{4 r_b D \overline{f_a}}{(r_s + r_b)^2 |V_{\infty,b} - V_{\infty,s}|} \tag{2.5}$$

where D is the diffusion coefficient for small particles and $\overline{f_a}$ is the ventilation coefficient. The terminal velocities, $V_{\infty,b}$ and $V_{\infty,s}$ for the collector and aerosol particles,

Table 2.2: Collision efficiencies as a function of the radii of the bigger and smaller collision partners, r_b and r_s, respectively.

r_b (μm)	r_s (μm)	collision efficiency
r_b>300	r_s>10	1.
300≥r_b>10	r_s>10	modified tables from Hall [1980] (see Table 2.3) and grid square method with bilinear interpolation
r_b>300	10≥r_s>0.2	values interpolated between Brownian diffusion and Wang et al. [1978] data using logarithmic interpolation
300≥r_b>42	10≥r_s>0.2	values from Wang et al. [1978], Fig. 4, curves 4-D and grid square method with bilinear interpolation
42≥r_b>10	10≥r_s>0.5	values interpolated between Brownian diffusion, modified Hall table and Wang et al. [1978] data using grid square method with bilinear interpolation
42≥r_b>10	0.5≥r_s>0.2	Brownian diffusion
r_b≤10	10≥r_s>0.5	values interpolated between Brownian diffusion, modified Hall table and Wang et al. [1978] data using logarithmic interpolation
r_b≤10	0.5≥r_s>0.2	Brownian diffusion
all values of r_b	$r_s \leq 0.2$	Brownian diffusion

respectively, are dependent on particle size. For particles of radius, r <10 μm, the terminal velocity is

$$V_\infty = (1 + \frac{1.26\lambda_a}{r})V_s \tag{2.6}$$

where V_s is the Stokes flow velocity and λ_a is the mean free path of air molecules. For particles of radius 10≤r<500 μm,

$$V_\infty = \frac{\eta_a N_{Re}}{2\rho_a r} \tag{2.7}$$

is the terminal velocity where η_a and ρ_a are the dynamic viscosity and density of air, respectively, and N_{Re} is the Reynolds number [Beard and Pruppacher, 1969]. Finally for the case where r≥500 μm, the terminal velocity is given by the empirical approach for deformed drops based on Gunn and Kinzer [1949], Garner and Lihou [1965], and Beard [1976].

The modified Hall table, which is referred to in Table 2.2 is shown in Table 2.3. These values are from Hall [1980] except for collector drop radii ≤30 μm new efficiencies were generated by averaging from the values in Lin and Lee [1975], Schlamp et al.

Table 2.3: Collision efficiencies from Hall [1980] and modified for drop radii $\leq 30\,\mu$m. The bigger and smaller collision partners are r_b (μm) and r_s (μm), respectively.

r_b	300	200	150	100	70	60	50	40	30	20	10
r_s/r_b											
0.05	0.97	0.87	0.77	0.5	0.18	0.05	0.005	0.001	0.0001	0.0001	0.0001
0.10	1.0	0.96	0.93	0.79	0.56	0.43	0.40	0.07	0.002	0.0001	0.0001
0.15	1.0	0.98	0.97	0.91	0.80	0.64	0.60	0.28	0.02	0.005	0.0001
0.20	1.0	1.0	0.97	0.95	0.88	0.77	0.70	0.50	0.04	0.015	0.013
0.25	1.0	1.0	1.0	0.95	0.90	0.84	0.78	0.62	0.085	0.023	0.016
0.30	1.0	1.0	1.0	1.0	0.91	0.87	0.83	0.68	0.17	0.032	0.02
0.35	1.0	1.0	1.0	1.0	0.94	0.89	0.86	0.74	0.27	0.043	0.024
0.40	1.0	1.0	1.0	1.0	0.95	0.90	0.88	0.78	0.40	0.054	0.028
0.45	1.0	1.0	1.0	1.0	0.96	0.91	0.90	0.80	0.50	0.065	0.031
0.50	1.0	1.0	1.0	1.0	0.97	0.91	0.90	0.80	0.53	0.075	0.034
0.55	1.0	1.0	1.0	1.0	0.98	0.91	0.90	0.80	0.54	0.081	0.035
0.60	1.0	1.0	1.0	1.0	0.98	0.91	0.90	0.78	0.54	0.084	0.036
0.65	1.0	1.0	1.0	1.0	0.98	0.91	0.89	0.77	0.54	0.082	0.037
0.70	1.0	1.0	1.0	1.0	0.99	0.92	0.88	0.76	0.53	0.078	0.037
0.75	1.0	1.0	1.0	1.0	1.0	0.93	0.88	0.77	0.51	0.07	0.037
0.80	1.0	1.0	1.0	1.0	1.05	0.95	0.89	0.77	0.48	0.06	0.037
0.85	1.0	1.0	1.0	1.0	1.10	1.0	0.92	0.78	0.46	0.05	0.036
0.90	1.0	1.0	1.0	1.0	1.3	1.03	1.01	0.79	0.43	0.042	0.034
0.95	1.0	1.0	1.0	1.0	2.0	1.7	1.3	0.95	0.44	0.035	0.032
1.00	1.0	1.0	1.0	1.0	4.0	3.0	2.3	1.4	0.52	0.027	0.027

[1976] and Klett and Davis [1973]. The final assumption is that all collisions result in collection. Thus, the coagulation efficiency is assumed to be unity.

Examples of the collection efficiencies for certain collector partner sizes are shown in Fig. 2.1. Aerosols with radii less than about $0.1\,\mu$m are more efficiently collected due to their Brownian motion, and larger aerosols are more efficiently collected due to their inertia. Thus, there is a minimum collection efficiency for particle radius about $0.1\,\mu$m, as first presented by Greenfield [1957], which is often called the Greenfield gap. Aerosols in this size range are most readily swept around the falling drop. Equations to parameterize these collection efficiencies do exist [Slinn, 1984, Jung and Lee, 1998]. These equations parameterize the collection efficiency due to the processes of Brownian diffusion, interception, and inertial impaction. One advantage of our approach is that the code can be readily modified to introduce tables that

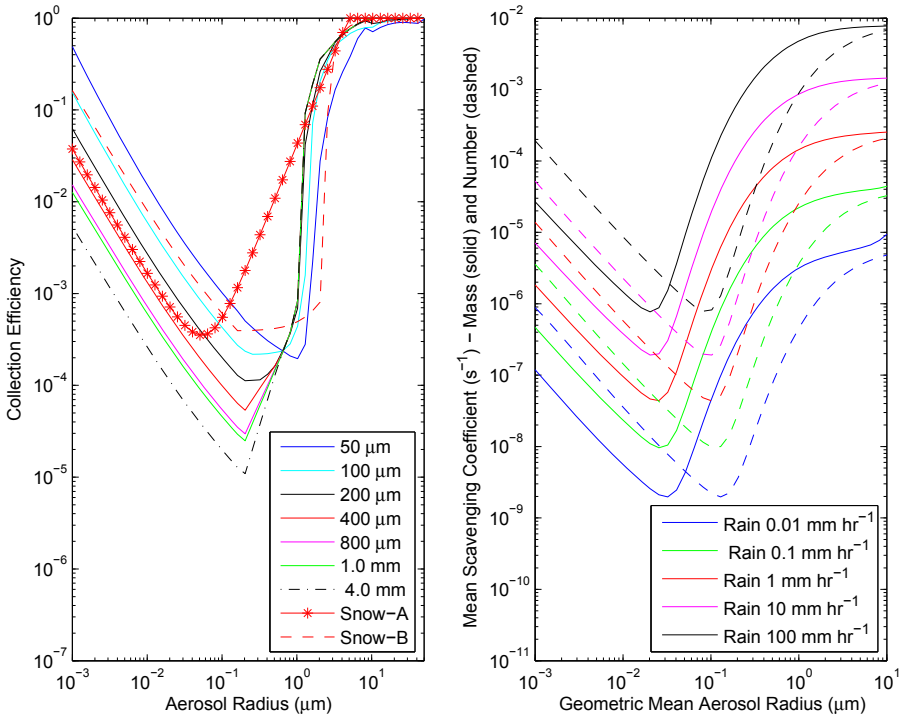

Figure 2.1: Collision efficiency for raindrop-aerosol collisions as a function of aerosol radius and collector rain drop size is shown on the left panel. Also on the left is the snow-aerosol collision efficiency (Snow A: Dick, 1990; Snow B: Slinn, 1984). Coagulation efficiency is assumed to be unity. Mean mass (solid lines) and number (dashed lines) below-cloud scavenging coefficients (s^{-1}) as a function of aerosol modal radius and rainfall rate are shown on right panel.

include the effects of thermophoresis, as has been done in this study, or additionally turbulence or electric charge, and the approach can be more readily extended over a wider range of size of collision partners, such as for in-cloud impaction scavenging.

To obtain the mean below-cloud scavenging coefficients for the mass distributions as a function of aerosol median diameter, $\Lambda_m(r_{pm})$, a second integration over the aerosol size distribution $n(r_p)$ is done,

$$\Lambda_m(r_{pm}) = \frac{\int_0^\infty \Lambda(r_p) r_p^3 n(r_p) dr_p}{\int_0^\infty r_p^3 n(r_p) dr_p}. \tag{2.8}$$

Similarly, the mean below-cloud scavenging coefficients for the number distributions

are,

$$\Lambda_n(r_{pm}) = \frac{\int_0^\infty \Lambda(r_p) n(r_p) dr_p}{\int_0^\infty n(r_p) dr_p}. \tag{2.9}$$

The resulting mass and number distribution scavenging coefficients are shown in Fig. 2.1. These coefficients have a minimum for aerosol sizes about 0.1 μm due to the collection efficiency minimum. Scavenging coefficients are higher for higher rainfall rates. A look-up table of these scavenging coefficients as a function of aerosol size and rainfall flux is used in the model. These coefficients are applied as $R_i^r F^r$ in Eqn. 2.1.

Figure 2.2 shows how the assumption of an exponential raindrop distribution as opposed to assuming all the raindrops are either 0.4 mm or 4.0 mm can give differences in the below-cloud scavenging coefficients of more than an order of magnitude. The differences in the scavenging coefficients, assuming various exponential distributions for drizzle, thunderstorm and the standard Marshall-Palmer distribution, are not as great as the difference in the coefficients if all the raindrops are assumed to be one size. The exponential raindrop distributions generally give coefficients that are between the coefficients for unimodal 0.4 and 4.0 mm raindrops, except for the scavenging of ultrafine particles, which is greatest in the case of drizzle. The exponential distributions are from Joss and Waldvogel [1969]. The equations for the scavenging coefficients assuming unimodal raindrops are given in Seinfeld and Pandis [1998]. For mass scavenging of aerosols with radii over 50 nm, all coefficients shown in Fig. 2.2 exceed those used by Stier et al. [2005] by up to 2 orders of magnitude.

Figure 2.3 shows how these scavenging coefficients are influenced by lower relative humidity. Based on the collection efficiencies of Wang et al. [1978], the mean mass and number scavenging coefficients have been re-calculated. Decreasing relative humidity increases scavenging in the Greenfield gap since the evaporating raindrops are cooler at the surface, and this sets up a thermal gradient that induces motion of the aerosols towards the cooler raindrop surface. Away from the Greenfield gap, other physical processes such as Brownian motion and inertial impaction dominate the collection, and so the influence of relative humidity is less pronounced. This is particularly evident at lower rainfall rates.

Andronache et al. [2006] found that observed scavenging coefficients for ultrafine

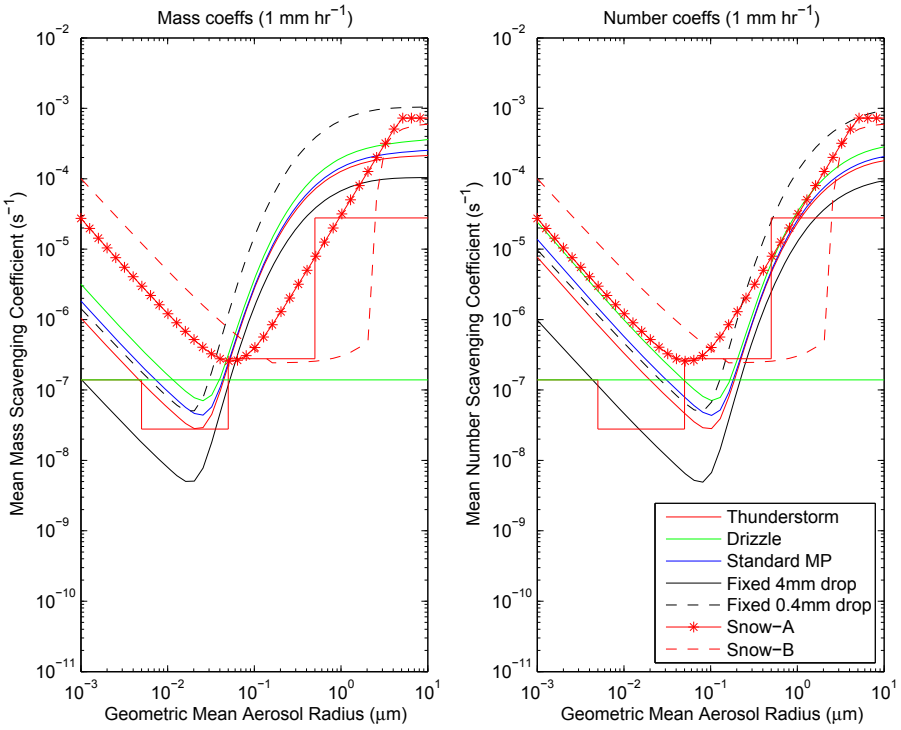

Figure 2.2: Mean below-cloud scavenging coefficients for a precipitation rate of $1\,\mathrm{mm\,hr^{-1}}$, assuming exponential distributions for thunderstorm, drizzle, and the standard Marshall Palmer. Also, assuming unimodal distributions for raindrop radii of 4 mm and 0.4 mm, and a fixed snow crystal radius. Mass scavenging coefficients are on left panel and number scavenging coefficients are on the right panel. Red and green steps: modal coefficients of Stier et al. [2005] for rain and snow, respectively.

particles exceeded model calculations for below-cloud scavenging based on Brownian motion, interception, and typical phoretic and charge effects. Here, we present two sensitivity studies for the below-cloud scavenging of particles with radius smaller than 10 nm, and investigate the impact on global aerosol concentrations and deposition. Figure 2.4 shows the scavenging coefficients for the extreme assumption that the collection efficiency is zero for ultra-fine particles that are smaller than 10 nm in radius. These coefficients are used in the sensitivity study BCS2-ULOW. As an additional sensitivity test, we assume that the collection of particles smaller than 10 nm radius can be described by the mass transfer coefficient, K_c, for the transfer of a

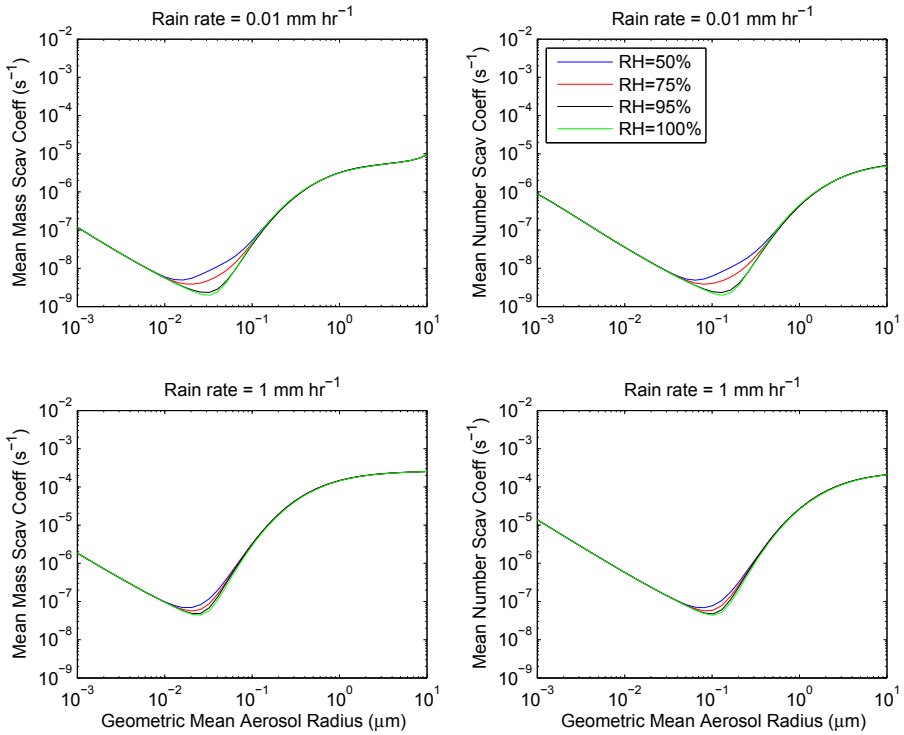

Figure 2.3: Mean below-cloud mass and number scavenging coefficients for rain with thermophoretic effects included for relative humidities of 50%, 75%, 95% and 100%, and for rainfall rates of 0.01 and 1 mm hr^{-1}.

gaseous molecule to a falling rain drop [Seinfeld and Pandis, 1998].

$$K_c = \frac{D_g}{2R_p}\left(2 + 0.6\left(\frac{2R_pU_t}{\nu}\right)^{1/2}\left(\frac{\nu}{D_g}\right)^{1/3}\right) \tag{2.10}$$

where D_g is the diffusivity coefficient for the gas in air (cm^2 s^{-1}), ν is the kinematic viscosity (cm^2 s^{-1}), U_t is the terminal velocity of the falling rain drop, and R_p is the rain drop radius. We assume that the particles behave as the gas water vapor. The mass transfer coefficients are used in place of $U_t(R_p)E(R_p, r_p)$ in Eqn. 2.4, and the mean mass and number scavenging coefficients are found following Eqns. 2.8 and 2.9. For aerosol particles about 10 nm in radius, the mean mass and number scavenging coefficients are increased by about two orders to magnitude for this assumption. These coefficients are used in the sensitivity simulation BCS2-UHIGH.

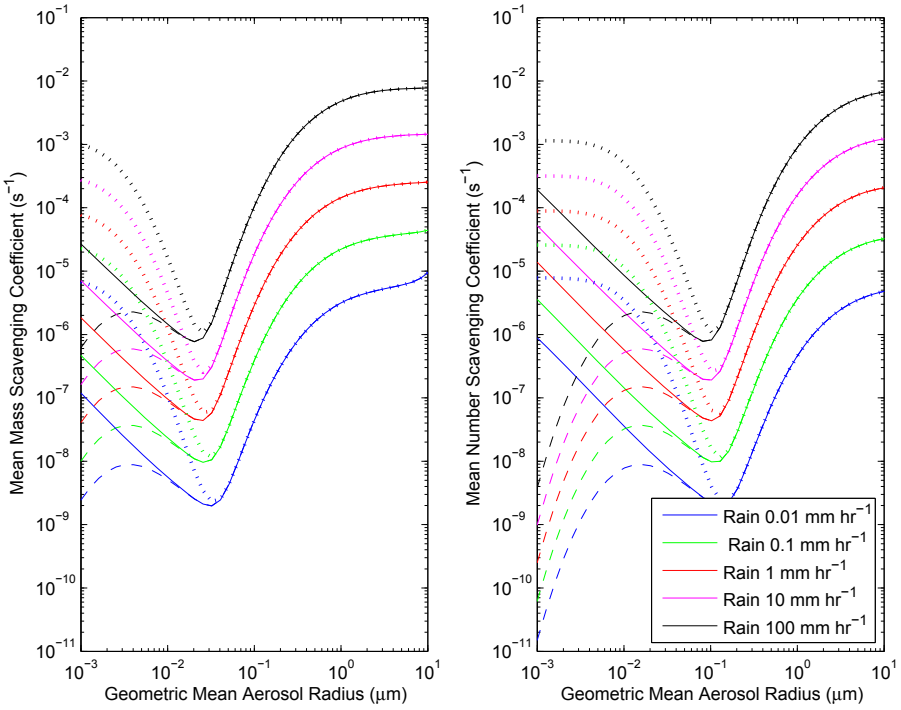

Figure 2.4: Mean below-cloud mass and number scavenging coefficients for rain, assuming the standard Marshall-Palmer raindrop distribution for five rainfall rates, and for three assumptions about the collection of particles with radius smaller than 10 nm: collection due to Brownian motion (solid lines), zero collection efficiency (dashed lines), and collection behavior similar to an irreversibly soluble gas (dotted lines).

New Below-Cloud Scavenging Parameterization for Snow

For the below-cloud scavenging by snow, the CTL simulation of the ECHAM5-HAM follows Eqn. 2.1 and the value of R_i^s is fixed at $0.005\,\mathrm{m^2\,kg^{-1}}$ for all aerosol modes. To make the below-cloud scavenging by snow depend on the aerosol size, a size-dependent collection efficiency for snow is required. Following Dick [1990] the collection efficiency is

$$E = \frac{mU_t}{6\pi r\eta R} + 4Pe^{-1}(1 + 0.4Re^{1/6}Pe^{1/3}) \tag{2.11}$$

where m is the aerosol particle mass, U_t is the terminal velocity of the snow crystals, r is the radius of the aerosol particles, η is the absolute viscosity of air, R_{snow} is the radius of the snow crystals, Re is the Reynold's number and Pe is the Peclet number. Following Dick [1990], we assume that all snow crystals are 30 μg in mass and have a

radius of 0.5 mm and fall at a terminal velocity of 80 cm s^{-1}. The Reynold's number is

$$Re = \frac{\rho_a R_{snow} U_t}{\eta} \tag{2.12}$$

where ρ_a is the air density. The Peclet number is

$$Pe = \frac{2R_{snow} U_t}{D} \tag{2.13}$$

where D is the aerosol diffusivity. Again following Dick [1990], the scavenging coefficient normalized by the precipitation flux is the collection efficiency multiplied by the cross-sectional area of a snow crystal divided by the snow crystal mass M,

$$R^s(r) = \frac{\pi R_{snow}^2}{M} E \tag{2.14}$$

As an alternative, the collection efficiency equation of Slinn [1984] may be used. The collection efficiency for snow is given by,

$$E(r) = \left(\frac{1}{Sc}\right)^{\alpha} + \left(1 - \exp\left(-(1 + Re_{\lambda}^{1/2})\right)\right)\frac{r^2}{\lambda^2} + \left(\frac{St - S_*}{St - S_* + \frac{2}{3}}\right)^{3/2} \tag{2.15}$$

where Sc is the Schmidt number, Re is the Reynold's number and St is the Stokes number and r is the aerosol size. The parameter S_* is given as

$$S_* = \frac{12/10 + (1/12)\ln(1 + Re)}{1 + \ln(1 + Re)} \tag{2.16}$$

where Re is the Reynold's number. The parameters α and λ depend on the type of snow crystals. For this study, the crystals were assumed to be rimed crystals, and thus α and λ were fixed at 100 μm and 2/3, respectively. Following Slinn [1984], the scavenging coefficient as a function of aerosol size r, and normalized by the snow fall rate is given by,

$$R^s(r) = \frac{\gamma E(r)}{D_m} \tag{2.17}$$

where D_m is a characteristic length of 2.7×10^{-3} cm for rimed particles and γ is a fixed parameter of order unity (0.6). Figure 2.1 shows the collection efficiencies for snow from both Dick [1990] (Snow-A) and Slinn [1984] (Snow-B). Figure 2.2 shows how these scavenging coefficients for snow compare to the fixed coefficient for a precipitation rate of 1 mm hr^{-1}, which is shown as the horizontal green line. The conversion

from precipitation flux was made by assuming the snow density was 0.1 of the water density. These size dependent scavenging coefficients for snow are higher than the coefficients used in the CTL simulation by a few orders of magnitude, particularly for the nucleation and coarse modes. The scavenging minimum is at a different radius and has a different width for the two parameterizations. This is due to differences in the assumptions about the morphology of the snow particles, similar to that presented by Miller and Wang [1991] and Feng [2009]. This study has implemented the coefficients of Slinn [1984]. The parameterization of below-cloud scavenging by snow is difficult since there are many assumptions to be made about the snow crystal properties. While our assumptions are reasonable, there remains considerable uncertainty since the variability in the size and shape of the snow crystals is neglected.

All below-cloud scavenging parameterizations require a representation of the precipitation fraction. The stratiform precipitating fraction is found starting from the top layer of the model and descending the vertical column. The precipitation fraction is set to the cloud fraction in the first precipitating layer. Thereafter, the precipitating fraction remains the same in subsequent layers until the amount of precipitation formed in any layer exceeds the amount of precipitation formed in the overlying layers. In the latter case, the precipitation fraction is set to the cloud fraction of that layer and so forth down the vertical column. The precipitation fraction is further adjusted if the cloud fraction exceeds the precipitating fraction from the overlying layer, but the precipitation generated in that layer does not exceed that from overlying layers. In this case, the new precipitation fraction is the weighted sum of the precipitation fraction and precipitation generated from the over-lying layers, and the cloud fraction and precipitation generated in the given layer. In all simulations except BCS2-CPF, the convective precipitation fraction in the kth model layer is,

$$PF_{\text{conv}}(k) = \frac{MF_{\text{up}}}{v_{\text{up}}(k)\rho_{\text{air}}(k)} \tag{2.18}$$

where MF_{up} is the updraft mass flux, $v_{\text{up}}(k)$ is a prescribed updraft velocity ($2\,\text{m}\,\text{s}^{-1}$), and ρ_{air} is the air density. Since below-cloud scavenging is parameterized to occur only in completely clear layers, this might under-estimate the scavenging because $PF_{\text{conv}}(k)$ is likely to be lower in cloud-free layers than in cloudy layers. Thus, in the sensitivity simulation, BCS2-CPF, the convective precipitating fraction is found

Table 2.4: The simulations presented in this study are summarized in this table.

Simulation	Description
CTL	Control simulation using prescribed rain and snow below-cloud scavenging coefficients from Table 2.1
BCS1	Prescribed scavenging coefficients for rain replaced by size-dependent rain scavenging
BCS2	Same as BCS1 but prescribed scavenging coefficients for snow replaced by size-dependent snow scavenging
BCS2-M0.4	Same as BCS2 but assumes all raindrops are 0.4 mm
BCS2-M4.0	Same as BCS2 but assumes all raindrops are 4.0 mm
BCS2-PR	Same as BCS2 but implements the Posselt and Lohmann [2008] prognostic rain scheme
BCS2-CPF	Same as BCS2 but revised convective precipitation fraction
BCS2-T	Same as BCS2 but includes thermophoretic effects
BCS2-ULOW	Same as BCS2 but assumes zero collection of ultra-fine particles with radius < 10 nm
BCS2-UHIGH	Same as BCS2 but assumes ultra-fine particles with radius < 10 nm are scavenged like an irreversibly soluble gas

using a maximum overlap assumption, and a precipitation-based weighting of the precipitating fractions from overlying layers. That is,

$$PF_{\text{conv}}^{\text{new}}(k) = \frac{\sum_{z=\text{ktop}}^{k} PF_{\text{conv}}(k) \cdot P_{\text{form}}(k)}{\sum_{z=\text{ktop}}^{k} P_{\text{form}}(k)} \tag{2.19}$$

where P_{form} is the precipitation formed in the kth layer.

2.4 Results and Discussion

2.4.1 Mass Deposition Budgets

Table 2.4 summarizes the model simulations. Figures 2.5 and 2.6 show the geographic distribution of the annual mean mass wet deposition of sulfate, black carbon (BC), particulate organic matter (POM), sea salt (SS) and dust (DU) for the simulation BCS2, which has size-dependent below-cloud scavenging for both rain and snow. These figures also compare the wet deposition between the BCS2 and CTL simulations. Modification to the below-cloud scavenging parameterization is shown to produce the greatest changes in the sea salt and dust wet deposition. Wet deposition

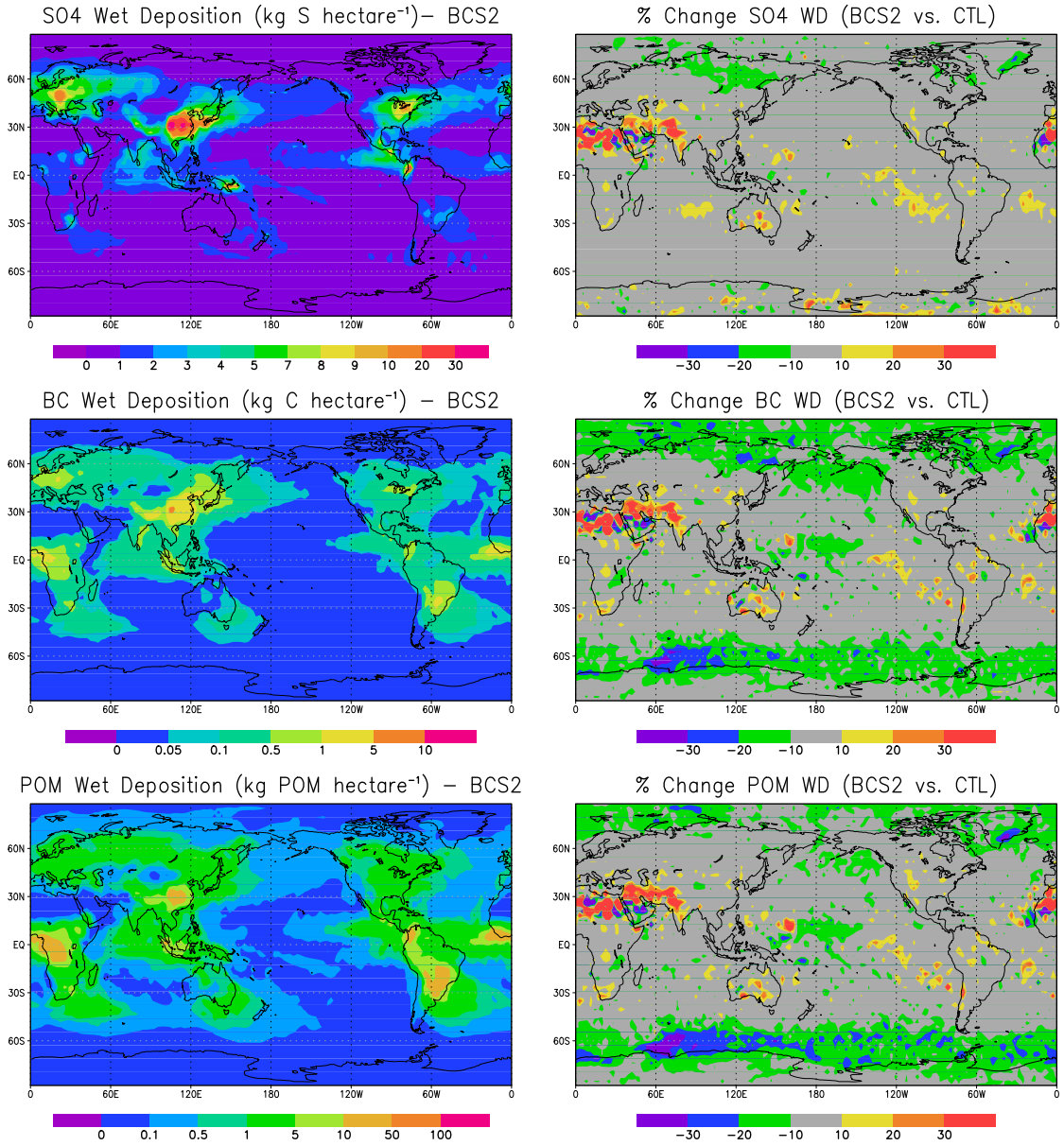

Figure 2.5: The geographic distribution of annual mean wet deposition of sulfate, black carbon and particulate organic matter for the BCS2 simulation is shown on the left panels. The percent change in the wet deposition relative to the control simulation ((BCS2-CTL)/CTL) is shown on the right panels.

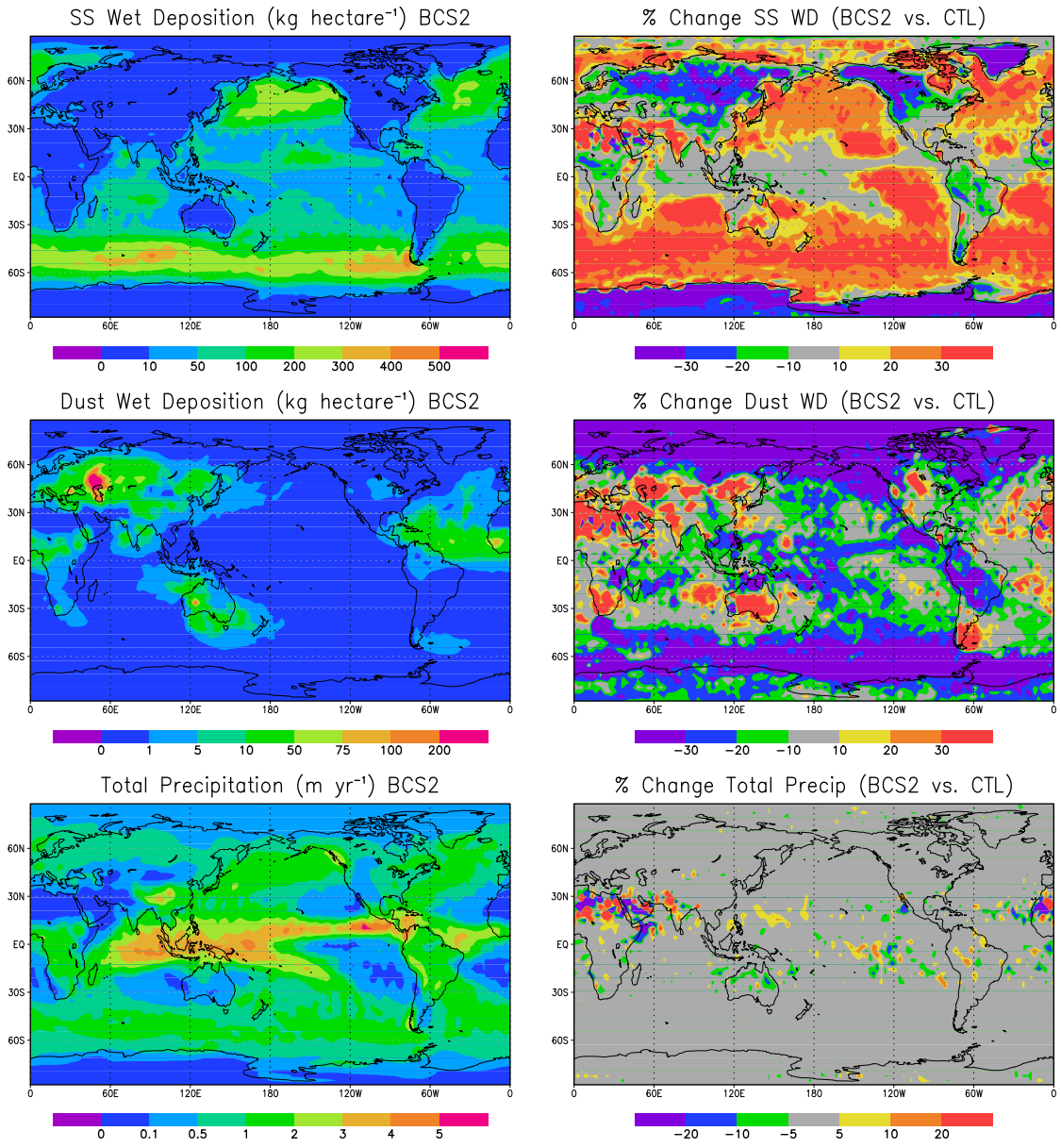

Figure 2.6: The geographic distribution of annual mean wet deposition of sea salt and dust and total precipitation for the BCS2 simulation is shown on the left panels. The percent change in the wet deposition and total precipitation relative to the control simulation ((BCS2-CTL)/CTL) is shown on the right panels.

of these aerosols is increased close to source regions for the BCS2 simulation. Henzing et al. [2006] also showed that below-cloud scavenging is an important sink for sea salt particles, about 12% of global removal, and should be included in a size-resolved parameterizations, such as was also done by Gong et al. [1997].

In terms of mass, the wet deposition of the carbonaceous aerosols and sulfate is shown to be least influenced by the below-cloud scavenging parameterization on a global scale, but there are regional changes. Unlike sea salt and dust, wet deposition is not significantly increased at the major source regions. However, in the zonal band near 20° N there is increased wet deposition. This latter feature is associated with an aerosol-precipitation feedback triggered by the below-cloud scavenging parameterizations and will be discussed further in the following sub-sections. Additionally, there is reduced wet deposition of dust and carbonaceous aerosols in the latitude band near 60° S, which is indicative of reduced poleward transport of these aerosols in response to increased wet deposition somewhat closer to their sources. To better understand whether these changes in wet deposition are due to the revised parameterizations, or due to differences in the precipitation rates, the change in total precipitation rates between the simulations BCS2 and CTL is shown in Fig. 2.6. Over the southern oceans, the precipitation is not changed by more than 5%, and so increases to the sea salt deposition here are primarly due to the new parameterizations. However, over regions of Northern Africa, and small, local regions in the tropics, there are changes to the precipitation that do contribute to the differences in the wet deposition.

Tables 2.5–2.9 present the annual and global mean mass deposition budgets for the various simulations. The annual and global mean mass removal by below-cloud scavenging is shown to be highly sensitive to the choice of below-cloud scavenging coefficients, with an increase of between one and two orders of magnitude for the BCS2 simulation as compared to the CTL simulation for the various aerosol species. The mass deposition budgets for sea salt and dust are controlled by the scavenging of the coarse mode, whereas the sulfate, black carbon, and particulate organic matter mass deposition budgets are dominated by the accumulation mode scavenging. Figure 2.2 shows that the CTL simulation uses much lower coefficients for accumulation and coarse mode mass scavenging than the other simulations with size-dependent

Table 2.5: The global and annual mean sulfate mass deposition rates (Tg S yr^{-1}) for the processes of below-cloud scavenging (BCS), in-cloud scavenging (ICS), dry deposition, and sedimentation, and sulfate burdens (Tg S), and lifetimes (days) for the model simulations. See Table 2.4 for descriptions of the simulations. The annual emission and production of sulfate is about 73.5 Tg S yr^{-1}.

Sulfate Deposition	BCS	ICS	Dry Dep	Sed	Burden	Lifetime
CTL	0.23	69.4	2.32	1.59	0.88	4.37
BCS1	7.02	63.0	2.12	1.35	0.85	4.24
BCS2	9.90	60.2	2.09	1.29	0.84	4.17
BCS2-M0.4	16.2	54.1	1.93	1.14	0.81	4.03
BCS2-M4.0	6.96	62.9	2.18	1.42	0.85	4.24
BCS2-PR	3.79	65.3	2.35	1.53	0.86	4.29
BCS2-CPF	9.99	60.1	2.08	1.28	0.84	4.17
BCS2-T	9.99	60.1	2.09	1.29	0.84	4.17
BCS2-ULOW	9.90	60.2	2.09	1.28	0.84	4.17
BCS2-UHIGH	9.90	60.2	2.08	1.29	0.84	4.17

scavenging. As a result, this low mass removal in the CTL simulation is expected. Tables 2.5–2.9 show that the mass removal by below-cloud scavenging is highly sensitive to the assumptions about the raindrop distribution with differences up to 60% between the BCS2, BCS2-M0.4 and BCS2-M4.0 simulations. Assuming all the raindrops are 0.4 mm in size gives the highest removal of mass by below-cloud scavenging. These effects occur for all aerosol species. Increases in the mass removal by below-cloud scavenging are associated with decreases in the mass removal by in-cloud scavenging. This is expected since the greater aerosol removal below cloud base allows less aerosol to be available for transport upward to the altitudes where in-cloud scavenging occurs. Sedimentation and dry mass deposition rates are also reduced in response to the lower aerosol concentrations. For sea salt, the global and annual mean fraction of mass removal by below-cloud scavenging for the simulation BCS2 (23%) is higher than that reported by Henzing et al. [2006] (12%) using the global chemistry transport model TM4, and considerably higher than for the CTL simulation (3%).

Table 2.10 shows the relative contributions of both stratiform and convective rain and snow to the total mass removal by below-cloud scavenging for all 5 aerosol species. Stratiform rain accounts for the majority of the below-cloud scavenging, about 60%

Table 2.6: Global and annual mean black carbon mass deposition rates ($\mathrm{Tg\,C\,yr^{-1}}$) for the processes of below-cloud scavenging (BCS), in-cloud scavenging (ICS), dry deposition, and sedimentation, and black carbon burdens (Tg C), and lifetimes (days) for the model simulations. See Table 2.4 for descriptions of the simulations. The annual emission of black carbon is $7.7\,\mathrm{Tg\,C\,yr^{-1}}$.

BC Deposition	BCS	ICS	Dry Dep	Sed	Burden	Lifetime
CTL	0.01	7.01	0.72	0.027	0.120	5.69
BCS1	0.68	6.35	0.70	0.025	0.119	5.64
BCS2	0.98	6.06	0.70	0.024	0.118	5.59
BCS2-M0.4	1.68	5.37	0.69	0.023	0.114	5.54
BCS2-M4.0	0.70	6.33	0.71	0.025	0.120	5.69
BCS2-PR	0.39	6.63	0.72	0.026	0.116	5.50
BCS2-CPF	0.99	6.05	0.70	0.024	0.117	5.54
BCS2-T	0.99	6.05	0.70	0.024	0.117	5.54
BCS2-ULOW	0.98	6.06	0.70	0.024	0.118	5.59
BCS2-UHIGH	0.98	6.06	0.70	0.024	0.118	5.59

for dust and up to 80% for sea salt for the simulation BCS2. Convective scavenging accounts for less than 1% of the global below-cloud removal since convective precipitation covers a much smaller fraction of the model grid boxes as compared to the stratiform precipitation. Simulation BCS2-CPF shows that an alternative to the convective precipitation fraction, as given in Eqn. 2.19, can increase the annual mean convective scavenging by 3–4 times, but the contribution to total below-cloud scavenging is still only about 1%. We have used a relatively high and fixed vertical velocity, and this contributes to relatively low convective precipitation fractions, and low convective below-cloud scavenging rates for this study. As convective parameterizations develop, and the representation of subgrid scale effects related to convective clouds is advanced, then improvements can be made to the treatment of convective below-cloud scavenging.

2.4.2 Column Mass Burdens and Lifetimes

Figures 2.7 and 2.8 show the geographic distribution of the aerosol burdens for the BCS2 simulation, and a comparison between the CTL and BCS2 simulations. The sea salt and dust burdens are reduced more by the invigorated below-cloud scavenging

Table 2.7: Global and annual mean particulate organic matter mass deposition rates ($\mathrm{Tg\,yr^{-1}}$) for the processes of below-cloud scavenging (BCS), in-cloud scavenging (ICS), dry deposition, and sedimentation, and particulate organic matter burdens (Tg), and lifetimes (days) for the model simulations. See Table 2.4 for descriptions of the simulations. The annual emission of particulate organic matter is $66.1\,\mathrm{Tg\,C\,yr^{-1}}$.

POM Deposition	BCS	ICS	Dry Dep	Sed	Burden	Lifetime
CTL	0.08	60.0	5.91	0.21	1.05	5.78
BCS1	5.11	55.1	5.87	0.20	1.03	5.69
BCS2	6.58	53.6	5.86	0.20	1.02	5.64
BCS2-M0.4	12.6	47.7	5.80	0.19	0.99	5.48
BCS2-M4.0	4.42	55.7	5.89	0.20	1.03	5.69
BCS2-PR	2.02	58.1	5.98	0.20	1.01	5.56
BCS2-CPF	6.66	53.5	5.85	0.20	1.02	5.64
BCS2-T	6.66	53.5	5.85	0.19	1.02	5.64
BCS2-ULOW	6.58	53.6	5.86	0.20	1.02	5.64
BCS2-UHIGH	6.57	53.6	5.87	0.20	1.02	5.64

than the sulfate and carbonaceous aerosol burdens. Dust burdens are changed by less than 10% near the major source regions, except for Eur-Asian dust. This is expected since dust is often emitted in regions with low precipitation, and also may be lofted above levels where below-cloud scavenging occurs. However, dust burdens are reduced poleward, and away from the major source regions by up to 30% in response to the invigorated below-cloud scavenging in the simulation BCS2. One must remember that percent changes should be interpreted by keeping in mind that in some cases the magnitude of the burden and deposition is small, such in this case for dust deposition away from source regions. However, sea salt burdens are reduced by 20–30% over the major ocean source regions in the BCS2 simulation as compared to the CTL simulation.

Tables 2.5–2.9 also present the annual and global mean aerosol burdens and lifetimes. The global and annual mean sea salt burden, and lifetime are reduced by 15–20% when the size-dependent scavenging parameterizations are implemented. The reductions for the other aerosol species are between 5–10%. Sea salt is most strongly influenced by the size-dependent below-cloud scavenging parameterizations since this aerosol species has a considerable fraction of total mass in the coarse mode, and the scavenging coefficients for this mode are greatly enhanced, by one to two orders of

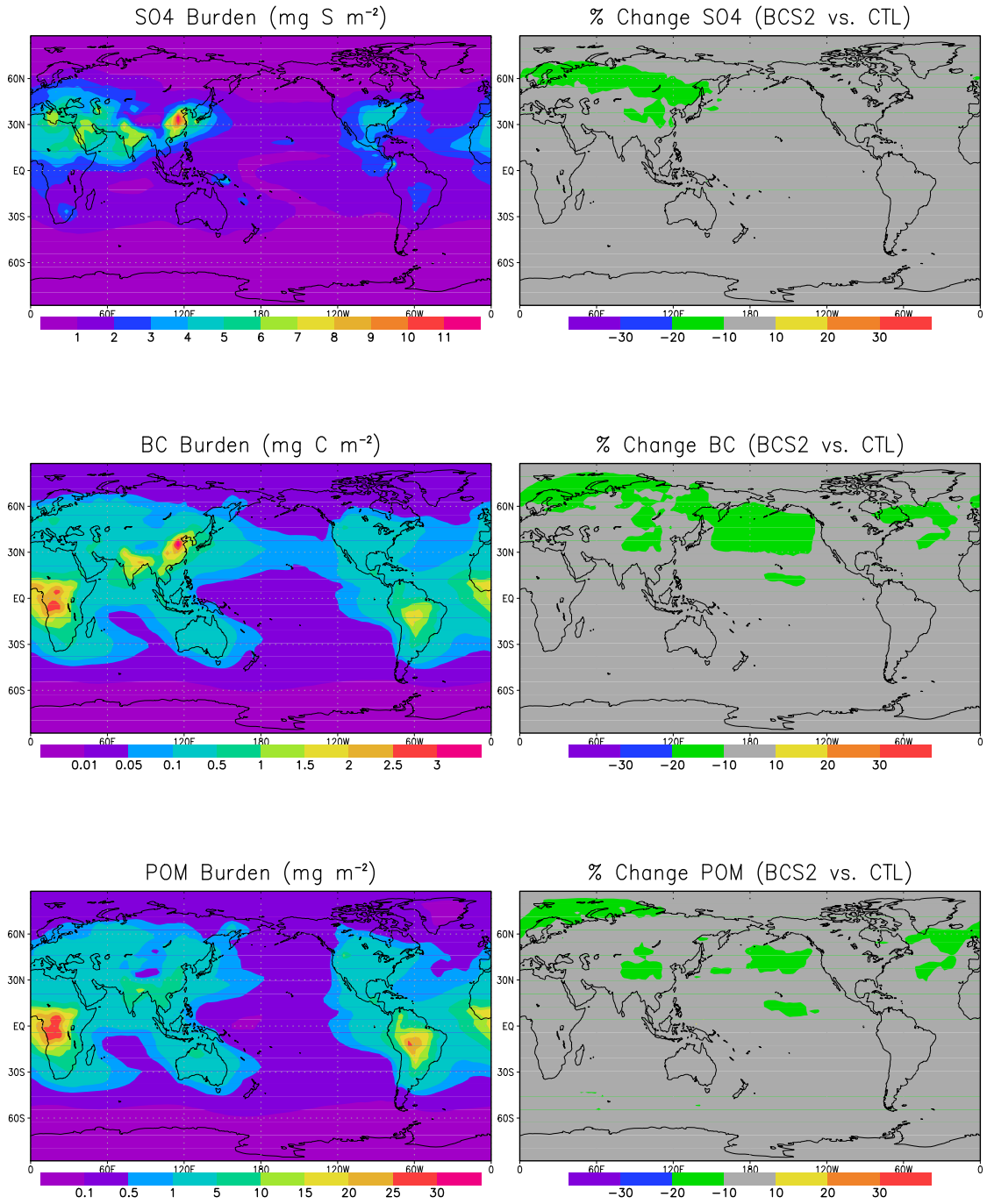

Figure 2.7: The geographic distribution of the annual mean burdens of sulfate, black carbon and particulate organic matter for the BCS2 simulation is shown on the left. The percent change relative to the CTL simulation is shown on the right.

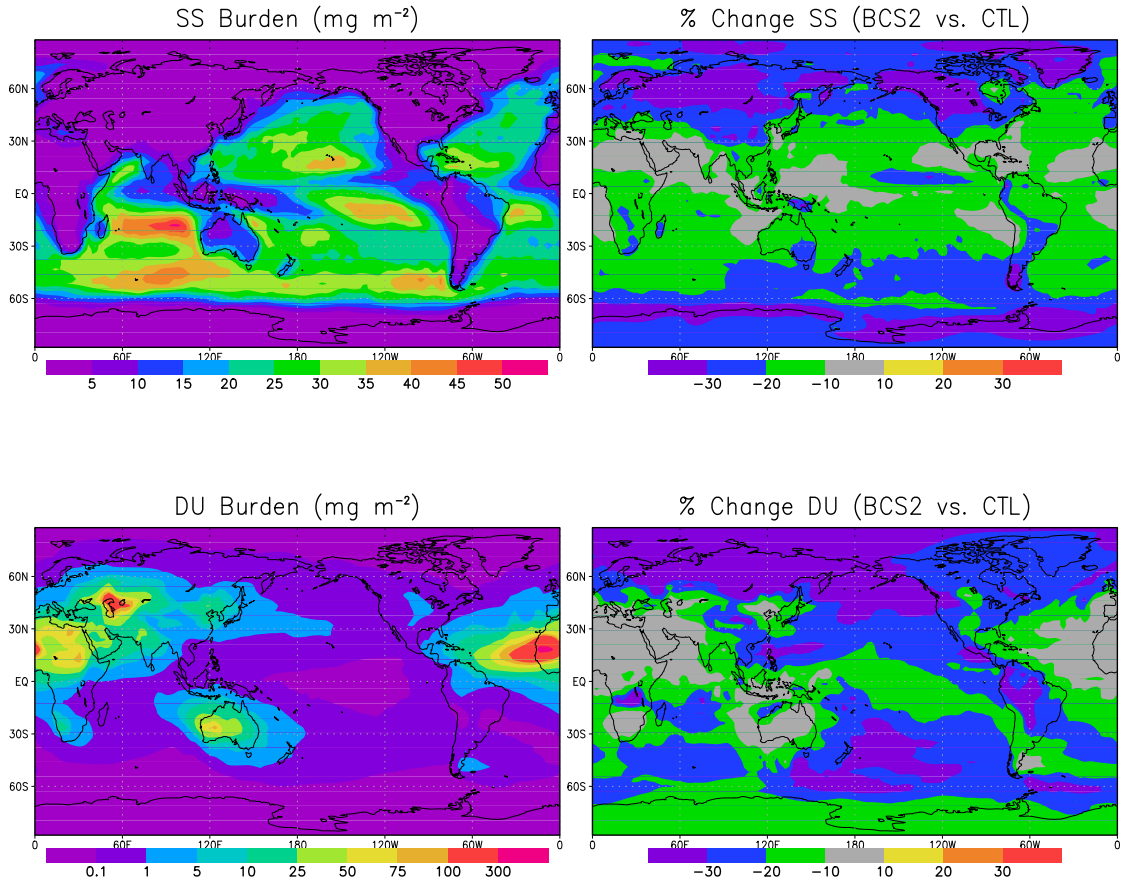

Figure 2.8: The geographic distribution of the annual mean burdens of sea salt and dust for the BCS2 simulation is shown on the left. The percent change relative to the CTL simulation is shown on the right.

Table 2.8: Global and annual mean sea salt mass deposition rates ($\mathrm{Tg\,yr^{-1}}$) for the processes of below-cloud scavenging (BCS), in-cloud scavenging (ICS), dry deposition, and sedimentation, and sea salt burdens (Tg), and lifetimes (days) for the model simulations. See Table 2.4 for descriptions of the simulations. The annual emission of sea salt is about $5350\,\mathrm{Tg\,yr^{-1}}$.

SS Deposition	BCS	ICS	Dry Dep	Sed	Burden	Lifetime
CTL	153.	2440.	1220.	1600.	9.95	0.67
BCS1	1040.	2070.	987.	1310.	8.60	0.58
BCS2	1250.	1930.	950.	1270.	8.37	0.57
BCS2-M0.4	1870.	1670.	774.	1090.	7.27	0.49
BCS2-M4.0	755.	2140.	1080.	1430.	9.21	0.62
BCS2-PR	366	2200.	1190.	1610.	9.65	0.66
BCS2-CPF	1260.	1930.	949.	1270.	8.36	0.57
BCS2-T	1250.	1930.	950.	1270.	8.38	0.57
BCS2-LOW	1250.	1930.	950.	1270.	8.37	0.57
BCS2-HIGH	1250.	1930.	950.	1270.	8.37	0.57

magnitude, as compared to the prescribed coefficients of Stier et al. [2005] (shown in Fig. 2.2). Dust also has a considerable mass in the coarse mode, but the lifetime reduction is less, 7% as opposed to 15%, for sea salt between the BCS2 and CTL simulations. This occurs since dust tends to be emitted in regions of lower precipitation, and is lofted above the altitudes of below-cloud scavenging while being aged to a soluble/mixed state, which can be scavenged by cloud nucleation processes. On the other hand, sea salt emissions are generally in regions of stratiform precipitation, and are more susceptible to removal by below-cloud scavenging shortly after emission. Figure 2.9 shows that for the BCS1 simulation, which had invigorated below-cloud scavenging by rain only, the dust and sea salt burdens are reduced by less compared to the CTL simulation than for the BCS2 simulation. Particularly poleward of 45° N and 45° S, the dust and sea salt burdens are reduced by 10 to 20% or less in the BCS1 simulation, as opposed to in excess of 20% for the BCS2 simulation.

Implementation of the prognostic stratiform rain scheme of Posselt and Lohmann [2008] in simulation BCS2-PR has the greatest impact on the annual and global mean sea salt burden. The BCS2-PR simulation is the only simulation that the rain formed in one time-step is not completely removed in that same time-step. Table 2.8 shows that the sea salt burden is increased as compared to the BCS2 simulation, and is only

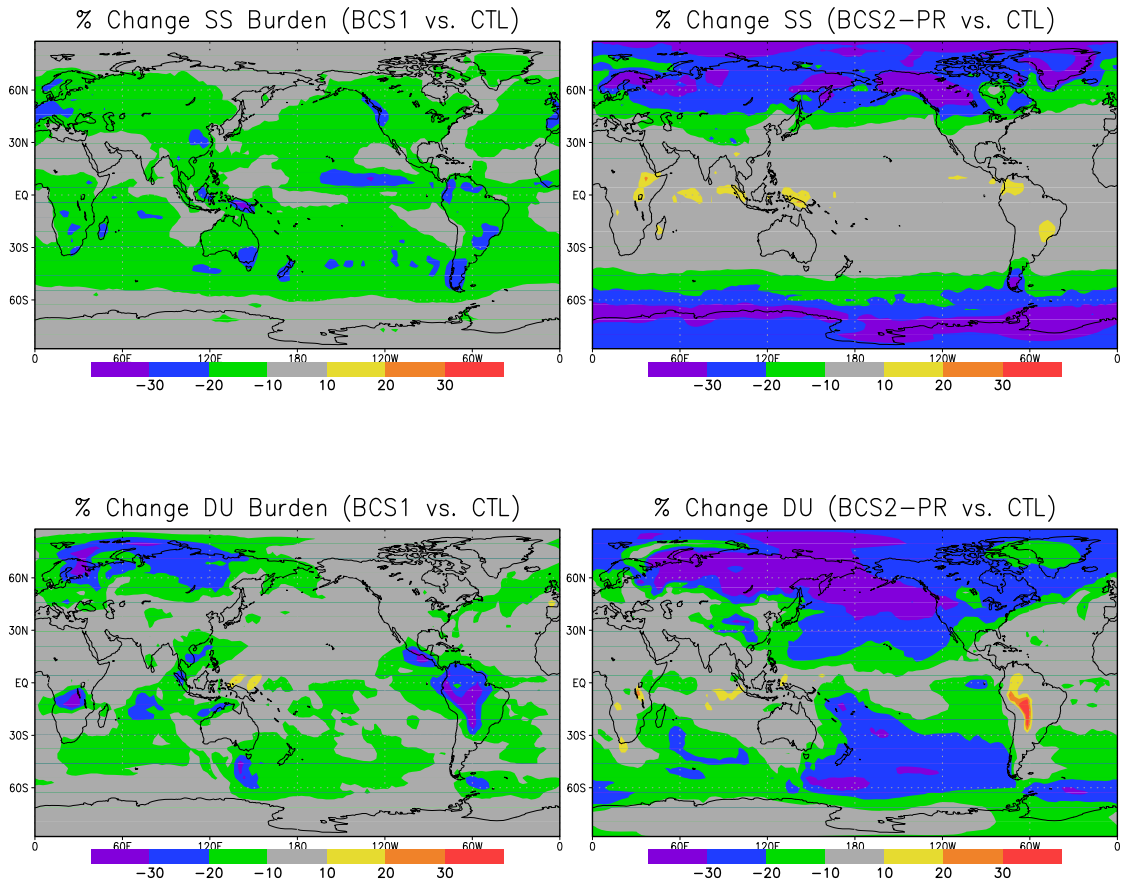

Figure 2.9: The percent change of the annual mean burdens of sea salt and dust for the BCS1 and BCS2-PR simulations relative to the CTL simulation.

Table 2.9: Global and annual mean dust mass deposition rates ($\mathrm{Tg\,yr^{-1}}$) for the processes of below-cloud scavenging (BCS), in-cloud scavenging (ICS), dry deposition, and sedimentation, and dust burdens (Tg), and lifetimes (days) for the model simulations. See Table 2.4 for descriptions of the simulations. The annual emission of dust is about $330\,\mathrm{Tg\,yr^{-1}}$.

DU Deposition	BCS	ICS	Dry Dep	Sed	Burden	Lifetime
CTL	12.7	169.	23.4	129.	3.78	4.15
BCS1	51.4	137.	21.6	124.	3.64	3.99
BCS2	78.2	113.	21.2	121.	3.52	3.86
BCS2-M0.4	101.	93.8	20.2	117.	3.39	3.72
BCS2-M4.0	60.6	123.	22.0	123.	3.62	3.97
BCS2-PR	39.2	143.	24.3	128.	3.65	4.00
BCS2-CPF	79.9	113.	21.1	121.	3.55	3.89
BCS2-T	79.2	113.	21.3	121.	3.54	3.88
BCS2-LOW	78.2	113.	21.2	121.	3.52	3.86
BCS2-HIGH	78.0	113.	21.3	121.	3.53	3.87

about 3% lower than for the CTL simulation. Similar to the other simulations with size-dependent below-cloud scavenging, the below-cloud scavenging is increased and the in-cloud scavenging is reduced for the BCS2-PR simulation relative to the CTL for all aerosol species, but the magnitude of these changes is reduced by about 50%. Figure 2.9 shows the geographic distribution of the change in the sea salt and dust burdens in the BCS2-PR simulation relative to the CTL simulation. In comparison to the BCS2 simulation, shown in Fig. 2.8, there is less reduction in the sea salt mass in the tropics and mid-latitudes. These effects occur since there is increased evaporation fluxes, particularly in the lower troposphere in the BCS2-PR simulation at these warmer latitudes. So there is more efficient release of the aerosols back to the atmosphere, reducing the mass removal by below-cloud scavenging when the prognostic rain scheme is implemented. The dust burden change for the BCS2-PR simulation, as compared to the BCS2 simulation is not as great. This is expected since dust is often lofted higher in the atmosphere prior to wet deposition, or not emitted in regions with high rainfall. Thus, the dust burden is less sensitive to the enhanced evaporation in the lower tropical troposphere in the BCS2-PR simulation.

Table 2.10: Global and annual mean deposition rates ($\mathrm{Tg\,yr^{-1}}$) for the processes of below-cloud scavenging by stratiform rain (Strat-Rain), stratiform snow (Strat-Snow), convective rain (Conv-Rain) and convective snow (Conv-Snow). The five aerosol species are sulfate (SO4), black carbon (BC), particulate organic matter (POM), dust (DU), and sea salt (SS). See Table 2.4 for descriptions of the simulations.

	Strat-Rain	Strat-Snow	Conv-Rain	Conv-Snow
SO4-CTL	0.20	0.03	0.002	<0.00001
SO4-BCS1	6.97	0.02	0.03	<0.00001
SO4-BCS2	6.97	2.93	0.03	0.001
SO4-BCS2-CPF	6.96	2.94	0.11	0.003
BC-CTL	0.006	0.005	<0.00001	<0.00001
BC-BCS1	0.68	0.004	0.003	<0.00001
BC-BCS2	0.68	0.30	0.003	0.00007
BC-BCS2-CPF	0.68	0.30	0.012	0.0002
POM-CTL	0.05	0.02	0.0006	<0.00001
POM-BCS1	5.1	0.02	0.03	<0.00001
POM-BCS2	5.1	1.4	0.03	0.0003
POM-BCS2-CPF	5.1	1.4	0.12	0.0007
DU-CTL	12.3	0.2	0.2	<0.00001
DU-BCS1	50.6	0.19	0.6	<0.00001
DU-BCS2	49.7	28.3	0.6	0.02
DU-BCS2-CPF	49.5	28.8	1.9	0.03
SS-CTL	151.	1.0	0.64	0.001
SS-BCS1	1040.	0.9	2.7	0.001
SS-BCS2	1020.	238.	2.7	0.9
SS-BCS2-CPF	1020.	238.	11.7	2.8

2.4.3 Vertical Profiles of Aerosol Mass and Number

The vertical profiles of the zonal and annual mean mass mixing ratios for the BCS2 simulation are shown in Fig. 2.10. These mixing ratios are high near their surface sources and decay with altitude, except for the sulfate production at high altitudes in the upper troposphere/lower stratosphere region. In the BCS2 simulation, there is a noted decrease in the mass of dust and sea salt in the middle and upper troposphere (up to 50%) as compared to the CTL. This is expected as the below-cloud scavenging is more vigorous in the BCS2 simulation. Again, while the percent change is large, the magnitude of the sea salt and dust burden is small in these regions of the troposphere. Nevertheless, dust acts as an ice nuclei at these levels, and so concentration changes

Table 2.11: Global and annual mean number burdens ($10^{10}\,m^{-2}$) for the 7 aerosol modes for the model simulations. See Table 2.4 for descriptions of the simulations.

Number	NS	KS	AS	CS	KI	AI	CI
CTL	18400	830.	74.4	0.46	8.58	0.032	0.068
BCS1	18430	830.	74.5	0.46	8.52	0.031	0.068
BCS2	18510	832.	74.3	0.45	8.48	0.031	0.066
BCS2-M0.4	18570	831.	74.3	0.43	8.39	0.031	0.066
BCS2-M4.0	18430	832.	74.5	0.45	8.53	0.031	0.067
BCS2-PR	18222	837.	74.8	0.46	8.20	0.031	0.066
BCS2-CPF	18470	832.	74.3	0.45	8.49	0.031	0.067
BCS2-T	18490	832.	74.5	0.45	8.49	0.031	0.066
BCS2-ULOW	18510	832.	74.3	0.45	8.48	0.031	0.066
BCS2-UHIGH	18440	831.	74.5	0.45	8.45	0.031	0.066

at these altitudes are relevant. The sulfate and carbonaceous aerosol mass is also reduced, particularly by the invigorated below-cloud scavenging by snow. However, this reduction is only up to 20% and is confined to below 5 km and poleward of 45° N and 45° S.

The vertical profiles of the aerosol number concentration for all insoluble and the coarse aerosol modes are shown in Fig. 2.11. The aerosols in the insoluble accumulation, and coarse modes are less numerous by up to 50% in the BCS2 simulation as compared to the CTL simulation, particularly at those latitudes most influenced by below-cloud scavenging by snow. Aerosols in the insoluble Aitken mode are less changed between the two simulations. Aerosols in the internally mixed/soluble Aitken and accumulation modes were changed by less than 10% between the BCS2 and CTL simulations, and so are not shown. These aerosols are more efficiently removed by in-cloud scavenging, and are less influenced by the below-cloud scavenging parameterizations. Comparing the BCS1 and CTL simulations, the changes in aerosol number were less than 10% for all aerosol modes, and are not shown.

Aerosol number burdens are shown in Table 2.11, the global and annual mean changes are less than 10%. The insoluble aerosols from all modes, and the internally mixed/soluble aerosols of the accumulation and coarse modes are less numerous in all BCS simulations as compared to the CTL simulation. Table 2.12 shows that the global and annual mean removal of soluble/internally mixed accumulation aerosol

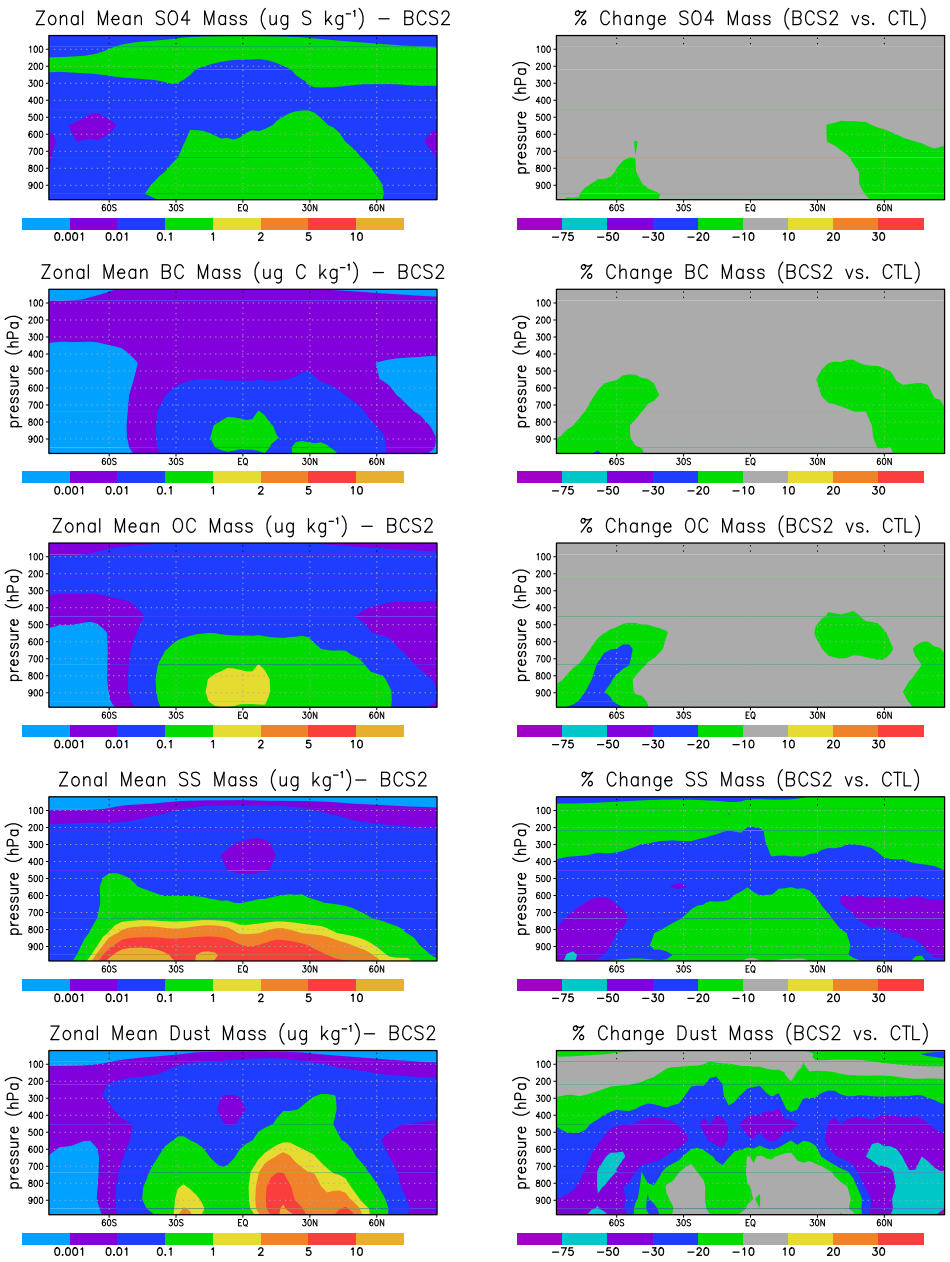

Figure 2.10: The annual and zonal mean vertical profiles of the mass mixing ratios of sulfate, black carbon, particulate organic matter, sea salt, and dust for the BCS2 simulation are shown on the left. The percent change relative to the CTL simulation for the BCS2 simulation is shown on the right.

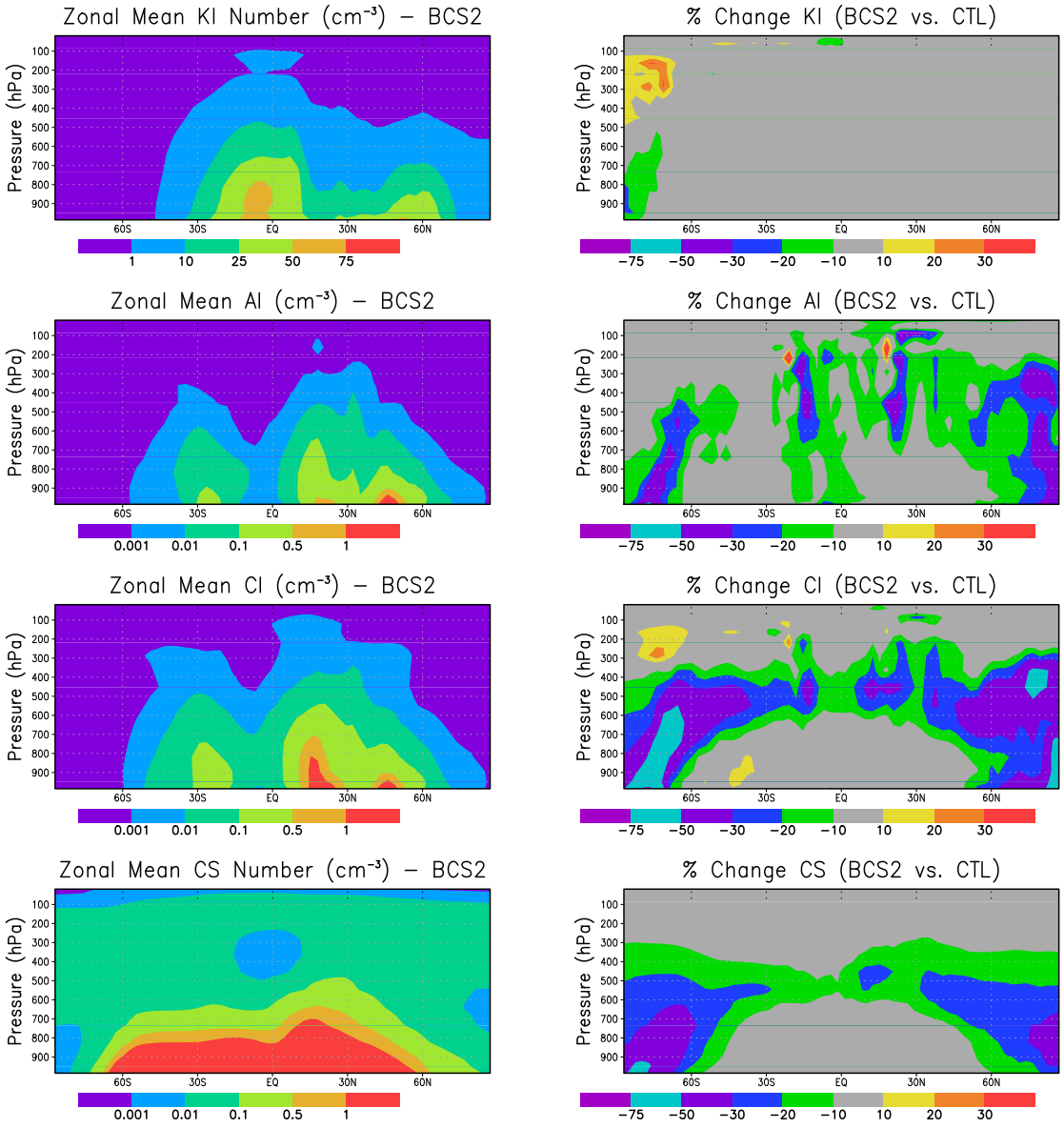

Figure 2.11: The annual and zonal mean vertical profiles of number concentration for all insoluble modes, and the internally mixed/soluble coarse mode at standard temperature and pressure for the BCS2 simulation are shown on the left. The percent change relative to the CTL simulation for BCS2 simulations is shown on the right.

Table 2.12: Global and annual mean number removal by below-cloud scavenging ($10^3\,m^{-2}\,s^{-1}$) for the 7 aerosol modes for the model simulations. See Table 2.4 for descriptions of the simulations.

Deposition	NS	KS	AS	CS	KI	AI	CI
CTL	33.8	7.2	1.2	1.6	0.41	0.002	0.09
BCS1	193.	10.0	1.1	1.9	0.61	0.002	0.10
BCS2	572.	14.6	13.5	4.3	0.84	0.007	0.21
BCS2-M0.4	699.	14.8	13.0	6.5	0.80	0.007	0.20
BCS2-M4.0	574.	12.7	13.6	3.6	0.66	0.007	0.22
BCS2-PR	660.	13.8	13.4	2.8	0.73	0.006	0.22
BCS2-CPF	758.	15.7	13.6	4.3	0.89	0.007	0.22
BCS2-T	753.	15.7	13.7	4.3	0.88	0.007	0.21
BCS2-ULOW	575.	14.6	13.5	4.3	0.84	0.007	0.21
BCS2-UHIGH	2320.	135.	13.6	4.3	6.59	0.007	0.21

number by below-cloud scavenging increases most in response to invigorated below-cloud scavenging by snow, with increases by about one order of magnitude for the BCS2 simulation compared to the CTL simulation. Inclusion of thermophoretic effects (simulation BCS2-T) most strongly influences the below-cloud scavenging of the Aitken size particles. This is expected since Aitken size aerosols lie in the Greenfield scavenging gap, and thus are most sensitive to thermophoretic effects. The global and annual mean number removal of Aitken size aerosols by below-cloud scavenging was increased by about 10% for the BCS2-T simulation compared to the BCS2 simulation. Table 2.12 shows that the enhanced ultra-fine scavenging in simulation BCS2-UHIGH gives the highest below-cloud number removal of the nucleation mode, but the number burden for this mode is slightly increased, by less than 1% relative to the CTL simulation (see Table 2.11). The nucleation mode number burden is dominated by upper tropospheric concentrations [Stier et al., 2005] that are not strongly influenced by scavenging by below-cloud scavenging processes.

To better understand the increase in the global and annual mean nucleation number burden, we present Fig. 2.12. Figure 2.12 shows the vertical profile of the fractional change in the zonal and annual mean nucleation mode number concentrations for the various simulations as compared to the CTL simulation. In the lower troposphere, as below-cloud scavenging is more vigorous we find that zonal mean nucleation

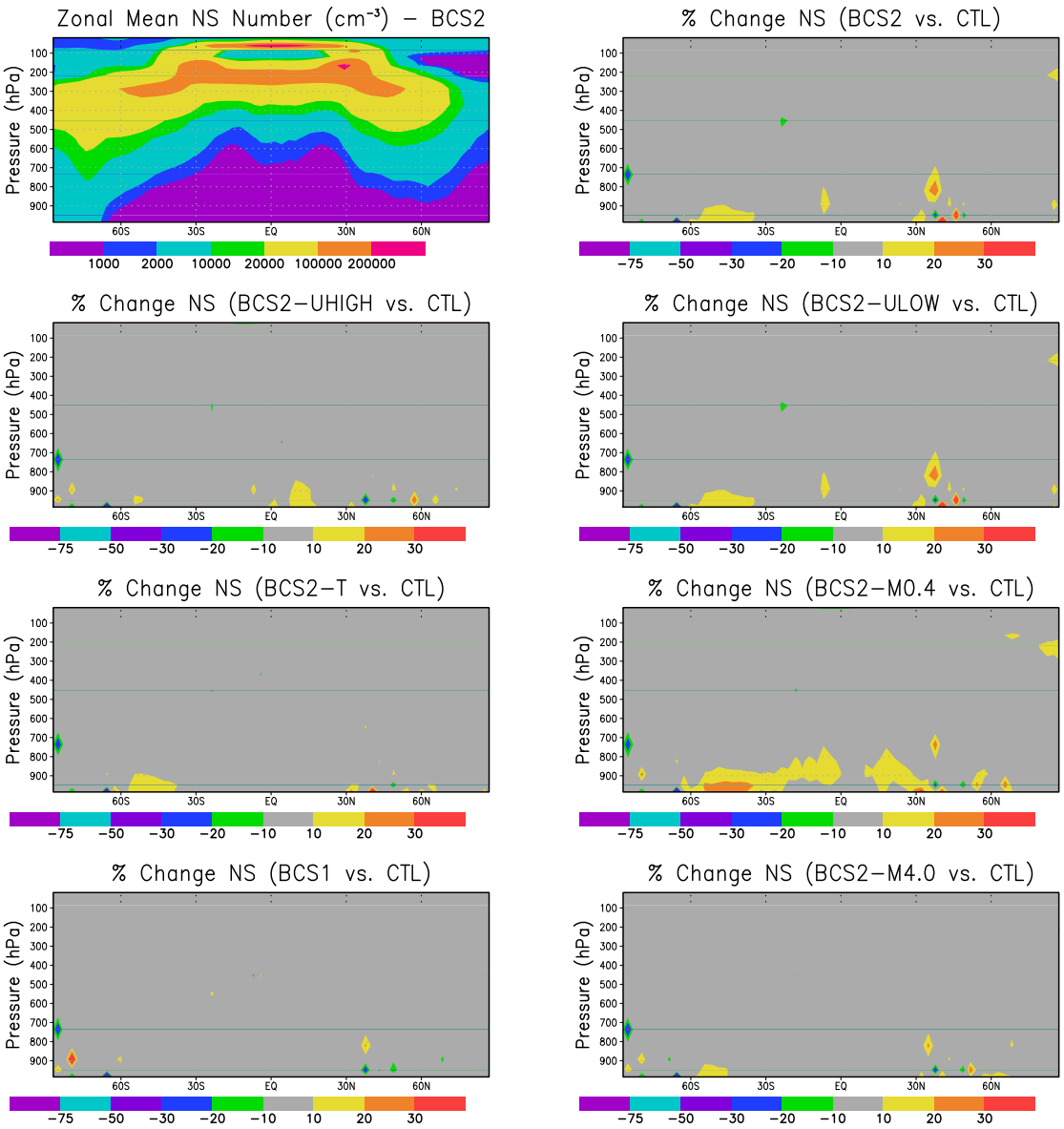

Figure 2.12: The annual and zonal mean vertical profile of nucleation mode number concentration at standard temperature and pressure, and the percent change relative to the CTL simulation for the simulations BCS2, BCS2-UHIGH, BCS2-ULOW, BCS2-T, BCS2-M0.4, BCS2-M4.0 and BCS1.

mode number concentrations are increased by up to 30%. This is expected since the more vigorous below-cloud scavenging will reduce the available condensation surfaces of the accumulation and coarse modes, and new particle formation will be enhanced, as opposed to sulfuric acid condensation on available surfaces. The competing, but less dominant factor is the higher nucleation mode below-cloud scavenging for the size-dependent simulations relative to the control, which would reduce the nucleation mode number. The lower tropospheric nucleation mode number concentrations have the greatest increase for the simulation BCS2-M0.4, which had the strongest scavenging of the accumulation and coarse modes. This is particularly evident over the southern oceans. For the simulation BCS2-UHIGH, the invigorated scavenging of particles less than 10 nm has reduced the magnitude of this effect over the southern oceans. Unfortunately, our simulations did not diagnose vertical profiles of new particle nucleation rates. However, Fig. 2.2 shows that the size-dependent simulations use higher below-cloud scavenging coefficients for the nucleation mode relative to the CTL simulation, except for simulation BCS2-M4.0. Thus the increase in nucleation mode number can not arise from lower nucleation mode scavenging for the size-dependent scavenging simulations, but rather enhanced particle formation in the lower troposphere.

2.4.4 Impacts on Cloud Properties and Precipitation

We have seen that changes in the below-cloud scavenging parameterization can cause changes in the aerosol number vertical profiles. These effects are greatest for the insoluble aerosols, which do not act as cloud condensation nuclei in our model, but can be ice nuclei. In this section we investigate if the changes in aerosol number cause any feedback on the cloud properties. In our framework of nudged simulations, we will only see changes in the clouds that occur primarily in response to changes in the aerosol number. Changes in the clouds in response to dynamical changes will not be significant since the large-scale meteorological state of the model is nudged to the observations. Additionally, we must use caution in interpreting these feedbacks since the nudging of the meteorological state of the model can reduce the magnitude of the aerosol-cloud-precipitation feedbacks themselves. Thus, this can not be a true

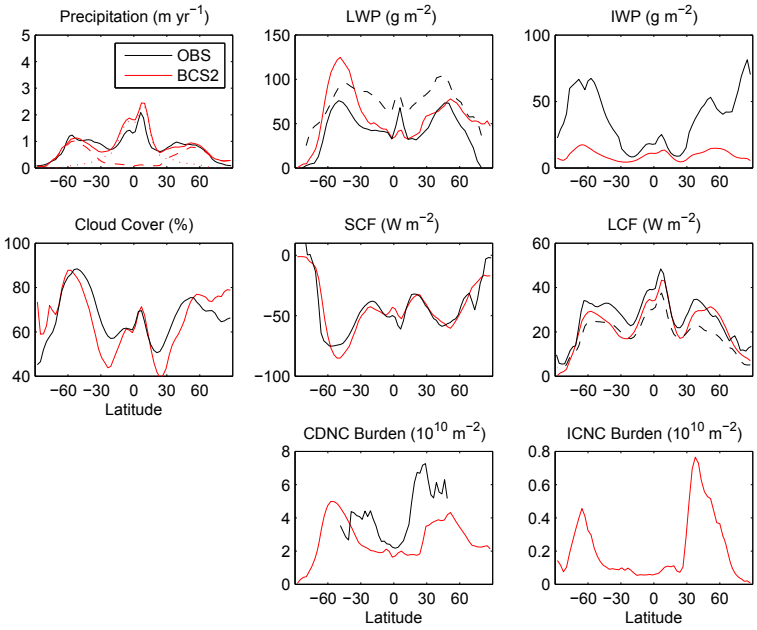

Figure 2.13: The annual and zonal mean precipitation, mean liquid water path (LWP), ice water path (IWP), cloud cover (CC), short wave cloud forcing (SCF), long wave cloud forcing (LCF), vertically integrated cloud droplet number concentration (CDNC) and vertically integrated ice crystal number concentration (ICNC) for the BCS2 simulation and observations. The sources of the observations are described in Table 2.13. For precipitation, dashed line:stratiform, dotted line:convective. For LWP observations, solid black: Weng and Grody [1994], dashed black: Greenwald et al. [1993]. For LCF, solid black: ERBE, dashed black: TOVS data. The SCF is from ERBE data.

feedback study and should not be interpreted in a broad sense. In this section we aim to investigate the extent that these aerosol-cloud feedbacks did occur in the framework of our nudged simulations.

Figure 2.13 shows the annual and zonal mean liquid and ice water paths, cloud cover, precipitation, cloud droplet and ice crystal number concentrations and cloud forcing from the BCS2 simulation and from observations. We can see that there is a reasonable agreeable with observations. The changes in these properties between the various simulations are easier to appreciate in terms of the percent change relative to the CTL simulation, which is shown in Fig. 2.14. For the BCS1 and BCS2 simulations compared to the CTL simulation, changes in the various cloud properties are 2% or

Figure 2.14: The percent change in convective and stratiform precipitation, liquid water path (LWP), ice water path (IWP), shortwave cloud forcing (SCF), longwave cloud forcing (LCF), stratiform cloud cover, vertically integrated cloud droplet number concentration (CDNC), and vertically integrated ice crystal number concentration (ICNC) relative to the CTL simulation for the BCS1 and BCS2 simulations.

less, except for the ice crystal number concentration, which fluctuates by up to 10%. Ice crystal number concentrations are sensitive to the changes in insoluble aerosol concentrations, which are influenced to a greater extent by the below-cloud scavenging parameterizations. In the zonal band near 20° N, there appears to be an invigoration of the convective precipitation of about 2%. This contibutes to the increased wet deposition near these latitudes seen in Figs. 2.5 and 2.6. This regionally increased precipitation is also shown on Fig. 2.6.

Table 2.13: Global and annual mean liquid water path (LWP) ($\mathrm{kg\,m^{-2}}$), ice water path (IWP) ($\mathrm{kg\,m^{-2}}$), cloud cover (CC), precipitation, cloud droplet number concentration (N_d) ($\mathrm{cm^{-3}}$), and ice crystal number concentration (N_i)($\mathrm{cm^{-3}}$). LWP observations are from SSM/I [Greenwald et al., 1993, Weng and Grody, 1994, Ferraro et al., 1996]. IWP has been derived from ISCCP [Storelvmo et al., 2008]. Total cloud cover is from ISCCP [Rossow and Schiffer, 1999] and total precipitation is from the Global Precipitation DataSet. Observations of N_d are from ISCCP [Han et al., 1998].

	LWP	IWP	CC	Precip	N_d	N_i	AOD
OBS	49–84		62–67	2.64–2.7	4		0.15
MODIS/TOVS	94–109		65–67				0.18–0.19
CTL	66.7	9.42	61.7	2.88	2.56	0.199	0.161
BCS1	66.6	9.42	61.6	2.88	2.56	0.202	0.148
BCS2	66.7	9.43	61.6	2.88	2.58	0.204	0.143
BCS2-M0.4	66.7	9.44	61.6	2.88	2.59	0.206	0.129
BCS2-M4.0	66.8	9.43	61.7	2.88	2.57	0.202	0.151
BCS2-PR	49.8	9.29	61.6	2.87	2.17	0.180	0.151
BCS2-CPF	66.8	9.44	61.6	2.88	2.58	0.205	0.143
BCS2-T	66.7	9.44	61.6	2.88	2.57	0.204	0.143
BCS2-ULOW	66.7	9.43	61.6	2.88	2.58	0.204	0.143
BCS2-UHIGH	66.4	9.42	61.6	2.88	2.56	0.201	0.143

Table 2.13 shows the annual and global mean cloud liquid and ice water paths, precipitation, cloud droplet, and ice crystal number concentrations. Invigorated below-cloud scavenging by snow in the BCS2 simulations as compared to the CTL simulations is associated with very small, (about 1%) increases in the global and annual cloud droplet and ice crystal number concentrations, and ice water path. This is associated with a small increase in the number of internally mixed/soluble Aitken size aerosols as shown in Table 2.11. In the global mean, the longwave cloud forcing is slightly increased, but the magnitude of this change on a global scale is less than 1% and is not shown in the table. Thus, for these nudged simulations we find that changes in the aerosol number induced by different below-cloud scavenging parameterizations are not sufficient to alter the global mean cloud properties by themselves alone without feedbacks on the meteorology. Nevertheless, though the large-scale cloud properties are not strongly affected by the modified below-cloud scavenging for our simulations, there are smaller scale local events, such as over Northern Africa, that due to model non-linearities can increase and modify the climate system. These

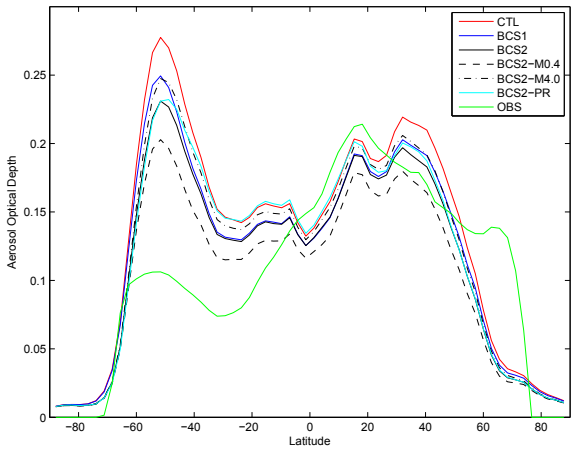

Figure 2.15: The annual and zonal mean aerosol optical depth at 550 nm from the CTL, BCS1, BCS2, BCS2-M0.4, BCS2-M4.0, and BCS2-PR simulations is shown in comparison to the composite of observations from MODIS, MISR and AERONET prepared by Kinne [2009].

small local changes in the hydrological cycle can additionally impact on dust mobilization that is dependent on recent occurrences of rainfall. These are factors that can not be completely controlled between our simulations, but contribute to differences in the aerosol wet deposition to a limited extent for our nudged simulations. While simulations with fixed cloud droplet and ice crystal number concentrations are possible, the climatology of the model deteriorates with such simulations, which is not desirable for comparisons with observations, such as in the following section.

2.4.5 Comparison with AOD and Deposition Observations

Figure 2.15 shows the annual and zonal mean aerosol optical depth (AOD) at 550 nm from a composite of MODIS (over oceans), MISR (over land), and AERONET observations [Kinne, 2009], and for the various simulations. The invigorated below-cloud scavenging produces a reduction in the AOD by about 15%. This is also shown in the global and annual mean in Table 2.13. The change in AOD between simulations is greatest in the southern hemisphere where the AOD is dominated by sea salt, which has a mass burden that is most strongly influenced by below-cloud scavenging. The used version of the ECHAM5-HAM model has a bias towards excessive sea salt AOD

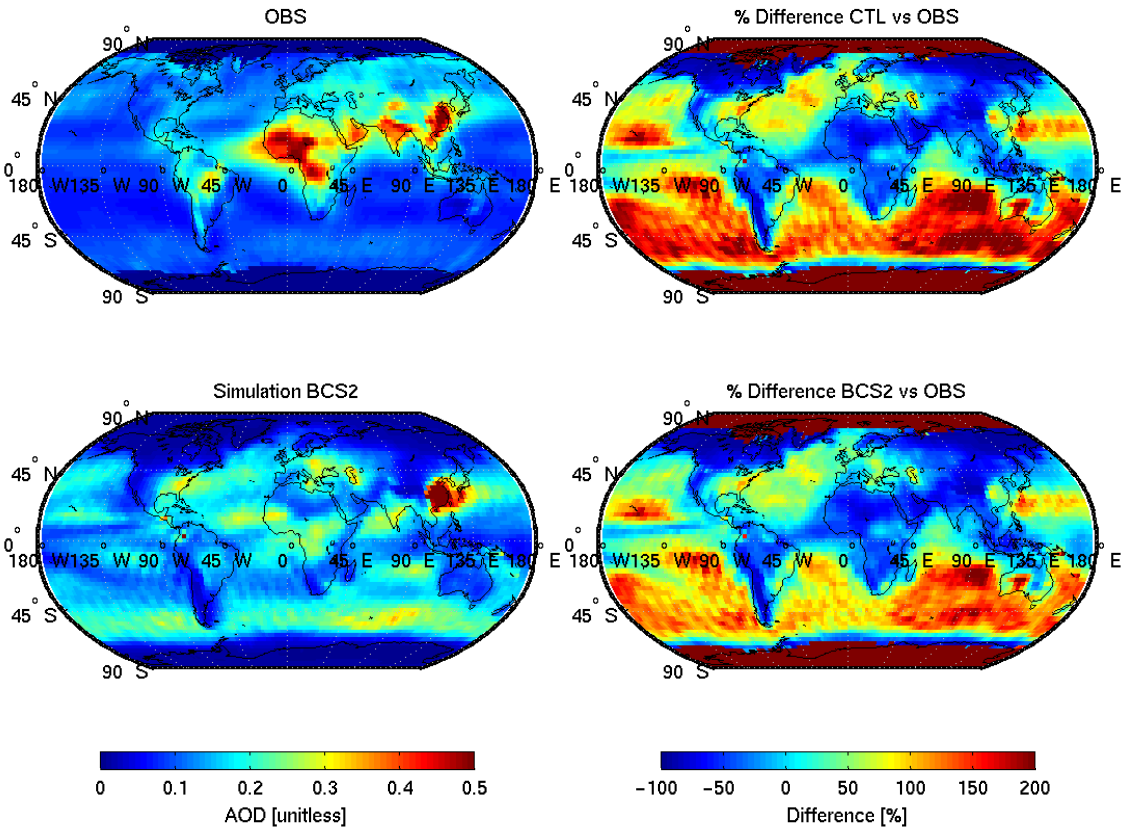

Figure 2.16: The geographic distribution of the annual mean aerosol optical depth at 550 nm for the MODIS MISR AERONET composite observations, and for the BCS2 simulation is shown on the left. On the right is the percent difference for the CTL and BCS2 simulations as compared to the observations.

that is not fully corrected by modifications to the below-cloud scavenging parameterization. However, the implementation of size-dependent below-cloud scavenging does reduce this bias. In the northern hemisphere the simulations agree more closely with the observations. Figure 2.16 shows the geographic distribution of the AOD, and a comparison with the observational composite dataset. In general, AOD is over-predicted over the oceans and under-predicted over the land. Hoose et al. [2008a] have shown that this over-prediction, particularly over the southern oceans can be corrected with improvements to the water uptake on the aerosols. A new scheme for particle growth due to ambient humidity will be available in subsequent versions of the ECHAM5-HAM and will address this issue.

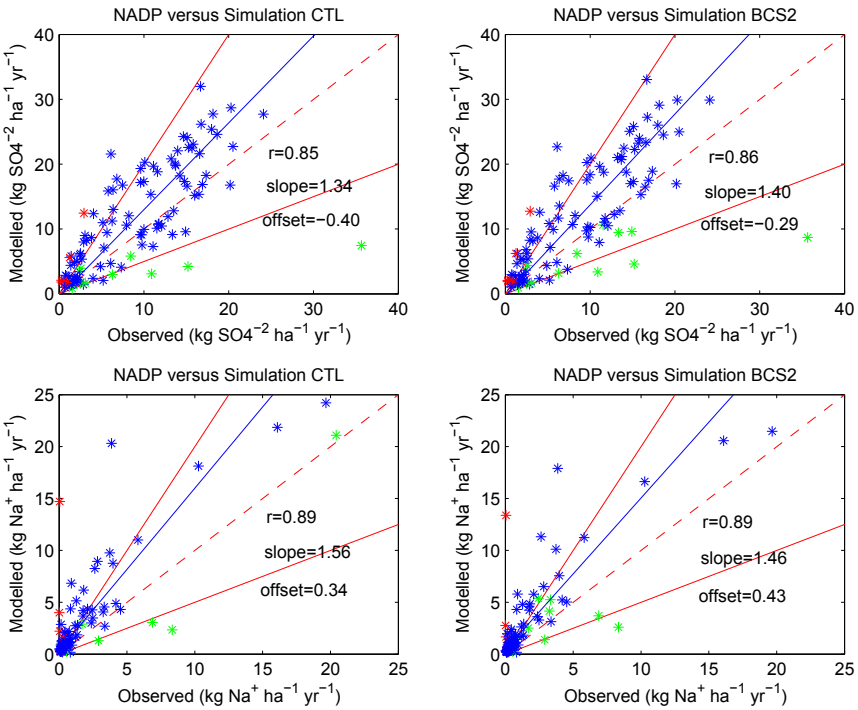

Figure 2.17: The observed annual mean sulfate deposition for 2001 ($\mathrm{kg\,SO_4^{-2}\,ha^{-1}\,yr^{-1}}$) from the National Atmospheric Deposition Program (NADP) of the United States in comparison to the CTL and BCS2 simulations is on the top 2 panels. The observed annual mean sodium ion deposition for 2001 ($\mathrm{ka\,Na^{+}\,ha^{-1}\,yr^{-1}}$) from the NADP in comparison to the CTL and BCS2 simulations is on the bottom 2 panels. Red and green asterisks: Modelled precipitation over- and under-predicts observed precipitation, respectively, by a factor of two or greater, and excluded from statistics.

Figure 2.17 compares the annual mean wet deposition of sulfate and sodium ions from the National Atmospheric Deposition Program of the United States with the simulations BCS2 and CTL. We assume that sea salt is the only source for sodium ions. For sulfate and sodium ions, both simulations give similar agreement with the observations. A similar agreement with observations was also found for all the remaining simulations that we conducted in this study (not shown). However, a more physically detailed below-cloud scavenging parameterization is desirable in global models, and our results show that the implementation of such a parameterization gives very reasonable results.

2.5 Summary and Conclusions

This study has examined the impacts of below-cloud scavenging parameterizations for rain and snow on global and annual mean vertical profiles of aerosol concentrations, and the geographic distribution of aerosol burdens and wet deposition. The aerosol species most sensitive to changes in the below-cloud scavenging parameterizations was sea salt. The global and annual mean sea salt burden was shown to change by about 15% depending on the parameterization used. Sea salt and dust mass burdens were found to be sensitive to the below-cloud scavenging coefficients used for the coarse mode scavenging. These coarse mode coefficients were shown to vary over several orders of magnitude depending on whether the rain drops are assumed to be unimodal and 0.4 or 4.0 mm in diameter, or having an exponential distribution. Thermophoretic effects were shown to produce increases in the global and annual mean below-cloud number removal of Aitken size particles of about 15%, but very small increases (about 1%) in the global below-cloud mass scavenging of carbonaceous and sulfate aerosols. Annual and zonal mean nucleation mode number concentrations were enhanced by up to 30% in the lower troposphere for the more vigorous size-dependent below-cloud scavenging since there was a reduction in the available condensation surface from the accumulation and coarse modes. Between the various below-cloud scavenging parameterizations, the global mean cloud properties did not change significantly since the internally mixed/soluble Aitken and accumulation mode number concentrations were changed by less than 10%.

Future work should be directed towards improving our understanding of the below-cloud scavenging by snow, and developing more physically detailed representations of this process in global models. Changes to the parameterization of the below-cloud scavenging by snow was found to change the insoluble accumulation and coarse aerosol number concentrations by up to 50% poleward of 45° N and 45° S. Additionally, in this study we assumed that all of the snow was the same size and shape, which does affect the below-cloud scavenging efficiency. The impact of these factors on a global scale requires further investigation. We also did not implement a prognostic scheme for the treatment of snowfall in the model, which may be even more important than prognostic rain since fall velocities for snow are generally smaller than for rain. Ultimately, more physically based parameterizations of the below-cloud scavenging by both rain and snow in global climate models will improve confidence in our estimates of the direct and indirect radiative forcing of aerosols.

2.6 Acknowledgements

The authors thank Jan Kazil, Corinna Hoose, and two anonymous reviewers for their helpful comments and discussions. We are also grateful to the National Science and Engineering Research Council of Canada and Killam Trusts Foundation of Canada for financial support, and to ETH Zurich for computing time.

Chapter 3

Influences of In-Cloud Scavenging Parameterizations on Aerosol Concentrations and Wet Deposition in ECHAM5-HAM

Authors: B. Croft[1], U. Lohmann[2], R. V. Martin[1,3], P. Stier[4], S. Wurzler[5], J. Feichter[6], C. Hoose[7], U. Heikkilä[8], A. van Donkelaar[1], and S. Ferrachat[2]

[1]Department of Physics and Atmospheric Science, Dalhousie University, Halifax, Canada
[2]Institute of Atmospheric and Climate Science, ETH Zurich, Zurich, Switzerland
[3]Harvard-Smithsonian Center for Astrophysics, Cambridge, USA
[4]Atmospheric, Oceanic, and Planetary Physics, University of Oxford, Oxford, UK
[5]Landesamt fur Natur, Umwelt und Verbraucherschutz NRW (LANUV), Recklinghausen, Germany
[6]Max Planck Institute for Meteorology, Hamburg, Germany
[7]Department of Geosciences, University of Oslo, Oslo, Norway
[8]Bjerknes Centre for Climate Research, Bergen, Norway

Article published in Atmospheric Chemistry and Physics, 10, 1511-1543, 2010.
All text, figures, tables, and presented results were contributed by the first author, B. Croft, with the exception of observational data (sources are referenced in the text).

3.1 Abstract

A diagnostic cloud nucleation scavenging scheme, which determines stratiform cloud scavenging ratios for both aerosol mass and number distributions, based on cloud

droplet, and ice crystal number concentrations, is introduced into the ECHAM5-HAM global climate model. This scheme is coupled with a size-dependent in-cloud impaction scavenging parameterization for both cloud droplet-aerosol, and ice crystal-aerosol collisions. The aerosol mass scavenged in stratiform clouds is found to be primarily (>90%) scavenged by cloud nucleation processes for all aerosol species, except for dust (50%). The aerosol number scavenged is primarily (>90%) attributed to impaction. 99% of this impaction scavenging occurs in clouds with temperatures less than 273 K. Sensitivity studies are presented, which compare aerosol concentrations, burdens, and deposition for a variety of in-cloud scavenging approaches: prescribed fractions, a more computationally expensive prognostic aerosol cloud processing treatment, and the new diagnostic scheme, also with modified assumptions about in-cloud impaction and nucleation scavenging. Our results show that while uncertainties in the representation of in-cloud scavenging processes can lead to differences in the range of 20-30% for the predicted annual, global mean aerosol mass burdens, and about 50% for accumulation mode aerosol number burden, the differences in predicted aerosol mass concentrations can be up to one order of magnitude, particularly for regions of the middle troposphere with temperatures below 273 K where mixed and ice phase clouds exist. Different parameterizations for impaction scavenging changed the predicted global, annual mean number removal attributed to ice clouds by seven-fold, and the global, annual dust mass removal attributed to impaction by two orders of magnitude. Closer agreement with observations of black carbon profiles from aircraft (increases about one order of magnitude for mixed phase clouds), mid-troposphere ^{210}Pb vertical profiles, and the geographic distribution of aerosol optical depth is found for the new diagnostic scavenging scheme compared to the prescribed scavenging fraction scheme of the standard ECHAM5-HAM. The diagnostic and prognostic schemes represent the variability of scavenged fractions particularly for submicron size aerosols, and for mixed and ice phase clouds, and are recommended in preference to the prescribed scavenging fractions method.

3.2 Introduction

Atmospheric aerosols significantly influence climate since they both reflect and absorb radiation (direct effects), and modify cloud properties (indirect radiative effects) [Twomey, 1991, Charlson et al., 1992]. Aerosols enter cloud droplets, or ice crystals by the nucleation process when they act as cloud condensation, or ice nuclei, and secondly by the process of impaction with the cloud droplets or ice crystals [Pruppacher and Klett, 1997]. A fraction of these droplets and crystals will then grow into precipitation particles that are removed from the atmosphere. Global climate models (GCMs) must accurately represent these nucleation and impaction processes that incorporate aerosols into cloud droplets and ice crystals in order to predict reasonable three-dimensional aerosol distributions, and deposition. Differences in aerosol prediction between global models have been attributed in part to differences in the representation of these removal processes [Textor et al., 2006].

This study will present a comparison between the variety of treatments for in-cloud nucleation and impaction scavenging that have been implemented in global models, including prescribed fractions, and diagnostic and prognostic treatments for the in-droplet and in-crystal aerosols. Using the ECHAM5-HAM GCM, we will examine the strengths and weaknesses of the various parameterization and investigate whether uncertainties in in-cloud scavenging parameterizations lead to any significant differences in predicted aerosol concentrations, burdens and deposition. Earlier work by Ghan and Easter [2006] showed that a diagnostic scheme under-predicted global mean aerosol burdens by 20% as compared to a prognostic representation of the in-droplet aerosols. However, that study did not explore the bias of using prescribed scavenging fractions, and did not examine sensitivities related to the scavenging of aerosols by ice crystals as we will do for this study.

Prescribed aerosol scavenging fractions have traditionally been implemented in many GCMs, including ECHAM5-HAM, and some models have simply assumed that 100% of the aerosol in a cloud is scavenged into the cloud droplets and ice crystals [e.g., Barth et al., 2000, Chin et al., 2000, Takemura et al., 2002, Stier et al., 2005, Tie et al., 2005]. This approach is desirable for the low computational expense. Other global models use diagnostic in-cloud scavenging schemes, which diagnose the

total aerosol scavenged fraction at each model time-step based on selected parameters related to cloud droplet and ice crystal nucleation and impaction processes, such as the supersaturation, updraft speed, and aerosol size and composition [e.g., Adams and Seinfeld, 2002, Gong et al., 2003]. By the term diagnostic, we mean that the total aerosol fraction scavenged into the cloud droplets and ice crystals is diagnosed at each model time-step, and unlike in a prognostic scavenging scheme, aerosol in-droplet and in-crystal concentrations are not passed between model time-steps. Prognostic aerosol cloud processing schemes have also been recently developed, which do pass aerosol in-droplet, and in-crystal aerosol concentrations between model time-steps [e.g., Ghan and Easter, 2006, Hoose et al., 2008a,b]. In this study, we introduce a new diagnostic aerosol scavenging scheme into the ECHAM5-HAM, and compare with additional simulations that treat in-cloud scavenging either by the prescribed fractions, or with the prognostic scheme of Hoose et al. [2008a,b].

Our new diagnostic scavenging scheme includes a physically detailed size-dependent parameterization of in-cloud impaction scavenging. This will allow us to examine the relative contributions of the nucleation and impaction scavenging processes to total in-cloud scavenging in the global context. Jacobson [2003] found for a one-dimensional study that aerosol mass was primarily scavenged by nucleation, whereas aerosol number was primarily scavenged by impaction processes. Recently, Baumgardner et al. [2008] have suggested that for black carbon, scavenging by ice crystals is dominated by impaction as opposed to nucleation processes.

Currently, the representation of impaction scavenging varies considerably between global models, and is a source of uncertainty in the in-cloud scavenging parameterizations. Some global models include impaction scavenging implicitly in the prescribed scavenging ratios [Stier et al., 2005]. Other models have an explicit impaction scavenging parameterization. For example, Gong et al. [2003] used a parameterized equation as a function of the mean cloud droplet and aerosol radii, and cloud droplet number concentration. Hoose et al. [2008a,b] used prescribed collection kernels for each aerosol mode of ECHAM5-HAM. In this study, we compare the prescribed kernel approach of Hoose et al. [2008a,b] with our physically detailed size-dependent cloud droplet-aerosol, and ice crystal-aerosol impaction scavenging parameterization, and

additional sensitivity simulations that have zero impaction scavenging. Our new physically detailed parameterization selects mean mass and number impaction scavenging coefficients from a look-up table as a function of mean cloud droplet radius (assuming a gamma distribution), median radius of the lognormal aerosol mass or number distribution, and cloud droplet number concentration. This is coupled with an ice-crystal-aerosol in-cloud impaction scavenging parameterization that depends on the monodisperse ice crystal radius, ice crystal number concentration, and the median aerosol radius of the mass and number distributions. In this study, we will examine the relative uncertainty in predicted aerosol concentrations that may be attributed to either nucleation or impaction processes for all cloud temperatures.

The next section gives a description of the ECHAM5 GCM, coupled to the aerosol scheme HAM, and includes the details of the various in-cloud scavenging parameterizations. Section 3.4 summarizes the impacts of the in-cloud scavenging parameterizations on the global aerosol three-dimensional distributions and removal rates. Section 3.5 presents a comparison with observations of aerosol wet deposition, vertical profiles of black carbon concentrations, marine boundary layer size distributions, and aerosol optical depth. This also includes a sub-section on the global modeling of ^{7}Be and ^{210}Pb, which are useful as passive tracers to examine in-cloud scavenging parameterizations. Section 3.6 gives a summary and conclusions.

3.3 Model Description

ECHAM5 is the fifth generation atmospheric general circulation model (GCM) developed at the Max-Planck Institute for Meteorology [Roeckner et al., 2003], and evolved from the model of the European Centre for Medium Range Weather Forecasting (ECMWF). The model solves prognostic equations for vorticity, divergence, temperature and surface pressure using spherical harmonics with triangular truncation. Water vapor, cloud liquid and ice water are transported using a semi-Lagrangian scheme [Lin and Rood, 1996]. Additionally, for this study we have implemented the prognostic equations for cloud liquid and ice water, mass and number following Lohmann et al. [2007], and the cirrus scheme of Lohmann and Kärcher [2002]. Convective clouds, and transport are based on the mass-flux scheme of Tiedtke [1989] with modifications

following Nordeng [1994]. The solar radiation scheme has 6 spectral bands [Cagnazzo et al., 2007] and the infrared has 16 spectral bands [Mlawer et al., 1997, Morcrette et al., 1998].

The GCM is coupled to the Hamburg Aerosol Model (HAM), which is described in detail in Stier et al. [2005]. The five aerosol species (sulfate, black carbon, particulate organic matter, sea salt and dust) are represented by seven log-normal modes, 4 internally mixed/soluble modes (nucleation (NS), Aitken (KS), accumulation (AS), and coarse (CS)), and 3 insoluble modes (Aitken (KI), accumulation (AI),and coarse (CI)). The count median radius for each mode is calculated from the aerosol mass and number concentrations of each mode, which are allowed to vary independently, and with a fixed standard deviation for each mode. Aerosol mass and number are transferred between the modes by the processes of sulfuric acid condensation, and also coagulation between aerosols. All results presented in this study are from a one year simulation, following a three months spin-up period, except 6 months spin-up period for simulations with ^{210}Pb and ^{7}Be. All simulations are nudged towards the meteorological conditions of the year 2001. The nudging approach, combined with aerosol-radiation de-coupling, was chosen in order to have the same dust and sea salt emissions in all simulations. We chose the year 2001 since that was a neutral year for the El Nino Southern Oscillation. The natural emissions of sea salt, dust, and DMS from the oceans are calculated on-line, based on the meteorology of the model. Emissions for all other aerosol species are taken from the AEROCOM emission inventory, and are representative for the year 2000 [Dentener et al., 2006b]. The aerosol emissions and the removal processes of sedimentation, and dry deposition are described in detail in Stier et al. [2005]. For this study, the below-cloud scavenging parameterization of Croft et al. [2009] has been implemented. This physically detailed below-cloud impaction scavenging parameterization uses look-up tables to select scavenging coefficients that represent the collection of aerosols by rain and snow below clouds based on aerosol size and precipitation rates.

Table 3.1: In-cloud scavenging ratios for each of the seven log-normal modes of the ECHAM5-HAM dependent on the cloud type and temperature (warm: T>273.15 K, mixed: 238.15<T≤273.15 K, ice: T≤238.15 K) following Stier et al. [2005].

Mode	Warm Stratiform	Mixed Stratiform	Ice Stratiform	Convective
Nucleation Soluble (NS)	0.10	0.10	0.00	0.20
Aitken Soluble (KS)	0.25	0.40	0.10	0.60
Accumulation Soluble (AS)	0.85	0.75	0.10	0.99
Coarse Soluble (CS)	0.99	0.75	0.10	0.99
Aitken Insoluble (KI)	0.20	0.10	0.10	0.20
Accumulation Insoluble (AI)	0.40	0.40	0.10	0.40
Coarse Insoluble (CI)	0.40	0.40	0.10	0.40

3.3.1 In-Cloud Aerosol Scavenging Parameterizations

Current In-Cloud Scavenging

In the standard ECHAM5-HAM model, in-cloud scavenging ratios are prescribed for each of the seven log-normal modes. These ratios depend on the cloud temperature, distinguishing between warm, mixed and ice clouds, and also depend on the cloud type, either stratiform or convective. The cloud scavenging ratios are presented in Table 3.1. The control (CTL) simulation is conducted with these prescribed ratios of the standard ECHAM5-HAM model. The rate of change of tracer i is

$$\frac{\Delta C_i}{\Delta t} = R_i C_i f^{\mathrm{cl}} \Big(\frac{f^{\mathrm{liq}} Q^{\mathrm{liq}}}{C_{\mathrm{liq}}} + \frac{f^{\mathrm{ice}} Q^{\mathrm{ice}}}{C_{\mathrm{ice}}} \Big) \tag{3.1}$$

where R_i is the prescribed in-cloud scavenging ratio, C_i is the mixing ratio of tracer i, f^{cl} is the cloud fraction, C_{liq} and C_{ice} are the cloud liquid and ice water mixing ratios, respectively, Q^{liq} and Q^{ice} are the respective sums of the conversion rates of cloud liquid and ice to precipitation by the processes of autoconversion, accretion and aggregation, and f^{liq} and f^{ice} are the respective liquid and ice fraction of the cloud water, and Δt is the time-step. Each prescribed in-cloud scavenging ratio treats impaction scavenging implicitly together with nucleation scavenging in the current model.

New Diagnostic In-Cloud Nucleation Scavenging

For the new nucleation scavenging parameterization, the scavenging ratios for stratiform clouds are diagnosed from the cloud droplet number concentration (CDNC), and the ice crystal number concentration (ICNC). The convective in-cloud scavenging for all simulations uses the prescribed ratios given in Table 3.1, and described in detail in Stier et al. [2005]. For stratiform clouds, both the CDNC and ICNC are prognostic variables in the version of the ECHAM5-HAM model used here, and the cloud microphysics is described in detail in Lohmann et al. [2007]. In our model version, and for all simulations presented in this study, the activation of aerosol particles to form cloud droplets is parameterized using the Ghan et al. [1993] scheme. The number of activated aerosols $N_{\mathrm{act,Ghan}}$ is given by

$$N_{\mathrm{act,Ghan}} = \frac{\omega N_{>35nm}}{\omega + \beta N_{>35nm}} \tag{3.2}$$

and

$$\omega = \bar{\omega} + 0.7\sqrt{\mathrm{TKE}}\,. \tag{3.3}$$

ω is the updraft velocity, $\bar{\omega}$ is the large-scale vertical velocity, TKE is the turbulent kinetic energy, β is 0.0034 $\mathrm{cm^4\,s^{-1}}$, and $\mathrm{N}_{>35nm}$ is the total number of soluble/internally mixed aerosols with radii >35 nm.

For the new diagnostic nucleation scavenging scheme, the total number of aerosols to be scavenged into the cloud droplets and ice crystals at each time-step is the sum of the CDNC and ICNC. For clouds with temperatures >238.15 K, the liquid cloud droplets, and those frozen heterogeneously to ice crystals in our model, both originate from Ghan et al. [1993] activation scheme. Thus, we can treat the total number of droplets and crystals as the total number of aerosols scavenged by nucleation. This total number must be apportioned between the four soluble/internally mixed aerosol modes in a manner that is consistent with the activation scheme as follows,

$$N_{j,\mathrm{scav}} = (\mathrm{CDNC} + \mathrm{ICNC}) \cdot \frac{N_{j>35\,nm}}{N_{>35\,nm}} \tag{3.4}$$

where $N_{j,\mathrm{scav}}$ is the total number of aerosols to be scavenged from the jth mode, for j=NS, KS, AS, CS. $N_{j>35\,nm}$ is the aerosol number for the jth mode having radii greater than 35 nm, and $N_{>35\,nm}$ is the number of aerosols having radii greater

than 35 nm summed over all the soluble/internally mixed modes. Thus, if tracer i is a soluble/internally mixed number mixing ratio, we have the following nucleation scavenging fraction,

$$R_{i,\mathrm{nuc}} = \frac{N_{j,\mathrm{scav}}}{N_j}. \tag{3.5}$$

where N_j is the total number of aerosols in the jth mode. The insoluble modes are assumed to have nucleation scavenging ratios of zero, but the impaction scavenging ratio might not be zero.

The scavenged fraction of the mass distribution is not set equal to the scavenged fraction of the number distribution. To determine the fractional scavenging of the mass distribution, the aerosols in each mode are assumed to be scavenged progressively from the largest to the smallest size. Thus, for each mode a critical radius, $r_{j,\mathrm{crit}}$, can be determined that has exactly $N_{j,\mathrm{scav}}$ in the lognormal tail of the number distribution. The total aerosol mass to be scavenged from the jth mode is that mass of the lognormal tail that lies above $r_{j,\mathrm{crit}}$.

To calculate $r_{j,\mathrm{crit}}$, the cumulative log-normal size distribution, $F_N(r_{j,\mathrm{crit}})$, is employed, where

$$F_N(r_{j,\mathrm{crit}}) = N_j - N_{j,\mathrm{scav}} = \frac{N_j}{2} + \frac{N_j}{2}\mathrm{erf}\left(\frac{\ln(r_{j,\mathrm{crit}}/r_{\mathrm{pg}})}{\sqrt{2}\ln\sigma_g}\right) \tag{3.6}$$

and r_{pg} is the count median radius for the jth mode, σ_g is the standard deviation for the respective mode and erf refers to the error function. By taking a rational approximation to the inversion of the error function, the above equation can be solved for $r_{j,\mathrm{crit}}$. Thus, the critical radius is given by,

$$r_{j,\mathrm{crit}} = r_{\mathrm{pg}} \cdot \left(\exp\left(\sqrt{2}\ln\sigma_g \cdot \mathrm{erf}^{-1}\left(1 - \left(2 \cdot (\mathrm{CDNC} + \mathrm{ICNC}) \cdot \frac{N_{j>35\,nm}}{N_j N_{>35\,nm}}\right)\right)\right)\right) \tag{3.7}$$

where $N_{j,\mathrm{scav}}$ has been replaced the explicit expression in Eqn. 3.4. Therefore, if tracer i is a soluble/internally mixed mass mixing ratio we have the following nucleation scavenging fraction for the mass distribution,

$$R_{i,\mathrm{nuc}} = \frac{\int_{r_{j,\mathrm{crit}}}^{\infty} m_{i,j}(r_{\mathrm{p}})dr_{\mathrm{p}}}{\int_0^{\infty} m_{i,j}(r_{\mathrm{p}})dr_{\mathrm{p}}} \tag{3.8}$$

where $m_{i,j}(r_{\mathrm{p}})$ is the lognormal mass distribution for the ith aerosol species of the jth mode, and r_{p} is the aerosol radius. The lognormal mass distribution has the same

standard deviation as the number distribution for any given mode, as described in Stier et al. [2005], and the mass median radius for the lognormal distribution ($r_{\mathrm{pg,m}}$) is related to the count median radius (r_{pg}) following

$$r_{\mathrm{pg,m}} = r_{\mathrm{pg}} \cdot \exp(3 \ln^2 \sigma_g). \tag{3.9}$$

The nucleation scavenging for temperatures below 238.15 K is different, since the ice crystals originate from homogeneous freezing at these temperatures. Homogeneous freezing does not require an ice nucleus. The version of the ECHAM5-HAM model used here includes the cirrus scheme described in Lohmann and Kärcher [2002]. The total ICNC is assumed to be equal to the total number of aerosols to be scavenged, but the modes are scavenged progressively from the largest soluble/internally mixed mode (CS) to the smallest (KS), which is consistent with the homogeneous freezing parameterization of our model. As a result, the calculation of the critical radius, is only done for the mode that is found to be partially scavenged, after all larger modes are fully scavenged. The nucleation scavenging ratio is set to zero for all modes smaller than the partially scavenged mode, and for all insoluble modes.

New Size-Dependent In-Cloud Impaction Scavenging

For the aerosol-cloud droplet impaction scavenging, the mean mass scavenging coefficients, in units of inverse time, are

$$\Lambda_{\mathrm{m}}(r_{\mathrm{pg,m}}) = \frac{\int_0^\infty \Lambda(r_{\mathrm{pg,m}}) r_{\mathrm{p}}^3 n(r_{\mathrm{p}}) dr_{\mathrm{p}}}{\int_0^\infty r_{\mathrm{p}}^3 n(r_{\mathrm{p}}) dr_{\mathrm{p}}}, \tag{3.10}$$

and the mean number scavenging coefficients are

$$\Lambda_{\mathrm{n}}(r_{\mathrm{pg}}) = \frac{\int_0^\infty \Lambda(r_{\mathrm{pg}}) n(r_{\mathrm{p}}) dr_{\mathrm{p}}}{\int_0^\infty n(r_{\mathrm{p}}) dr_{\mathrm{p}}}, \tag{3.11}$$

where $n(r_{\mathrm{p}})$ is the aerosol lognormal number distribution, r_{p} is the aerosol radius, and r_{pg}, and $r_{\mathrm{pg,m}}$ are the median aerosol radius for the number and mass distribution, respectively. The scavenging coefficient $\Lambda(r_{\mathrm{pg}})$, also in units of inverse time, is defined as

$$\Lambda(r_{\mathrm{pg}}) = \int_0^\infty \pi R_{\mathrm{liq}}^2 U_{\mathrm{t}}(R_{\mathrm{liq}}) E(R_{\mathrm{liq}}, r_{\mathrm{pg}}) n(R_{\mathrm{liq}}) dR_{\mathrm{liq}} \tag{3.12}$$

where R_{liq} is the cloud droplet radii, $U_{\mathrm{t}}(R_{\mathrm{liq}})$ is the terminal velocity of the cloud droplet, $E(R_{\mathrm{liq}}, r_{\mathrm{p}})$ is the collision efficiency between the aerosol and cloud droplet, and $n(R_{\mathrm{liq}})$ is the cloud droplet number distribution, which is assumed to be a Gamma distribution. We find the collision efficiencies and terminal velocities following the approach outlined in detail in Croft et al. [2009]. Figure 3.1 shows the impaction scavenging coefficients for a CDNC of $40\,\mathrm{cm}^{-3}$ as an example. Note that for this figure, the aerosol radii are the geometric mean radii for the assumed lognormal aerosol distribution. The scavenging coefficients have a minimum for aerosol radii about $0.1\,\mu$m. For aerosols with radii smaller than $0.1\,\mu$m, Brownian motion increases their collection by the cloud droplets, whereas the inertia of larger aerosols increases their collection. At the minimum, neither of these forces is dominant. The impaction scavenging coefficients are compiled in look-up tables. Thus, if tracer i is a mass mixing ratio, the scavenging fraction for cloud droplet-aerosol impaction is

$$R_{i,\mathrm{imp,liq}} = \Lambda_{\mathrm{m}}(r_{\mathrm{pg,m}})\Delta t \tag{3.13}$$

and likewise if tracer i is a number mixing ratio, but using $\Lambda_{\mathrm{n}}(r_{\mathrm{pg}})$. Both soluble/internally mixed, and insoluble aerosol modes are scavenged similarly by impaction.

Since the ECHAM5-HAM model assumes that the ice crystals are monodisperse, we do not integrate over an ice crystal number distribution to determine the scavenging ratio. The scavenged fraction due to aerosol-ice crystal impaction is defined as

$$R_{i,\mathrm{imp,ice}} = K(R_{\mathrm{ice}}, r_{\mathrm{pg}}) \cdot \mathrm{ICNC} \cdot \Delta t \tag{3.14}$$

where ICNC is the ice crystal number concentration, and R_{ice} is the radius of the maximum dimension of the ice crystal, and r_{pg} is the median radius of the aerosol number, or mass distribution, and $K(R_{\mathrm{ice}}, r_{\mathrm{p}})$ is the collection kernel given by,

$$K(R_{\mathrm{ice}}, r_{\mathrm{pg}}) = \pi R_{\mathrm{ice}}^2 U_{\mathrm{t}}(R_{\mathrm{ice}}) E(R_{\mathrm{ice}}, r_{\mathrm{pg}}) \tag{3.15}$$

where $U_{\mathrm{t}}(R_{\mathrm{ice}})$ is the ice crystal terminal velocity and $E(R_{\mathrm{ice}}, r_{\mathrm{pg}})$ is the collection efficiency for ice crystal-aerosol collisions. The size of the monodisperse crystals is calculated depending on the ice water content and the ICNC as described in Lohmann

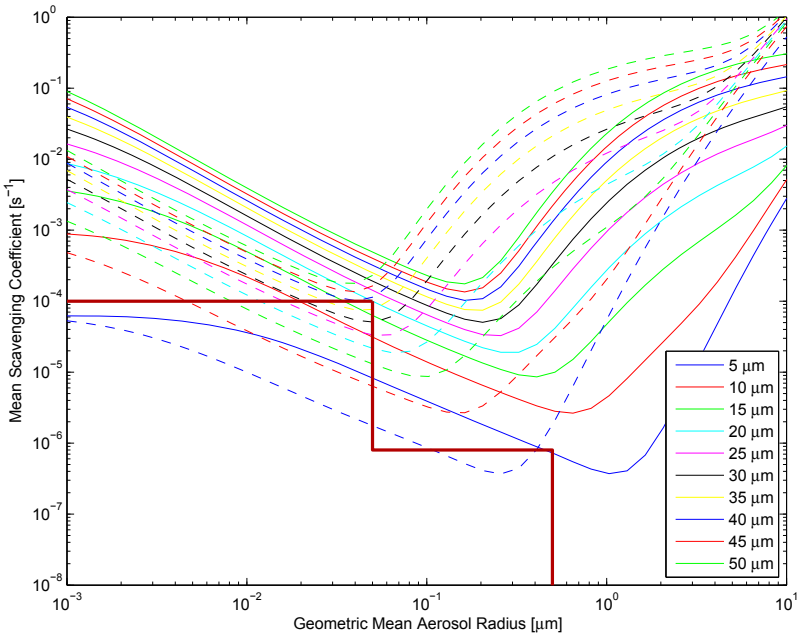

Figure 3.1: In-cloud mean mass (dashed lines) and number (solid lines) impaction scavenging coefficients (s^{-1}) as a function of geometric mean aerosol radius, for a cloud droplet number concentration of 40 cm^{-3}, and for a range of mean cloud droplet radii from 5 to 50 μm. The prescribed cloud droplet collection coefficients of Hoose et al. [2008a,b] are shown by the red thick steps.

et al. [2008]. The collection kernels are taken from Miller and Wang [1991] in units of $cm^3\,s^{-1}$ and are compiled in look-up tables in our model. For temperatures less than 238.15 K, we assume that all crystals are columns, and for temperatures greater than 238.15 K, all crystals are assumed to be plates [Lohmann et al., 2008]. There is a lack of collection data for ice crystals with radii less than about 30 μm. For these crystal sizes, we use the same collection kernels as for liquid droplets, as described in detail in Croft et al. [2009]. Ice crystals of this size are often assumed to be quasi-spherical [Spichtinger and Gierens, 2009].

Figure 3.2 shows the collection kernels for ice plates and columns for a selection of Reynold's numbers, and also for droplets with radii of 30 μm and less. In our look-up table approach, the Reynold's number is related to the size of the ice crystals following the crystal dimensions given in Martin et al. [1980], and Miller and Wang [1989]. Similar to droplets, ice crystals have a scavenging minimum, but this minimum shifts due to the various geometries of the crystals. For particle sizes near the scavenging

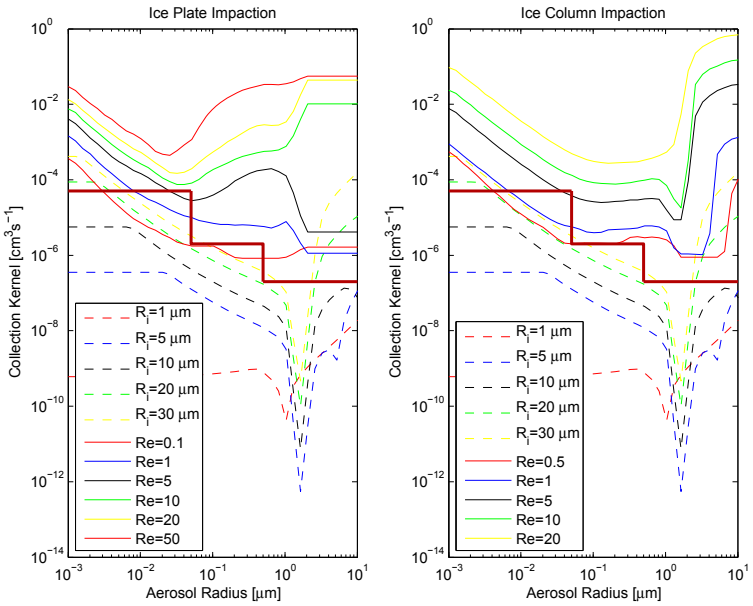

Figure 3.2: Impaction scavenging kernels (cm^3 s^{-1}) for in-cloud ice crystal-aerosol collisions as a function of aerosol radius, and ice crystal Reynold's number (Re) following Miller and Wang [1991] (solid lines), and for both columns and plates. The dashed lines are for droplet-aerosol collisions. R_i indicates collector radius. The prescribed ice crystal collection kernels of Hoose et al. [2008a,b] are shown by the red thick steps.

minimum, plates are more efficient scavengers than columns. Miller and Wang [1991] attribute this to the formation of eddies in the flow around the plate geometry, which increases their collection. There is also a zone of zero-scavenging (ZSZ) for aerosols in the 1-2 μm size range, which occurs since the sum of all forces at work results in a near-zero probability of collision between the aerosol and falling crystal. While the scavenging coefficients presented in Figs. 3.1 and 3.2 are reasonable, there are considerable uncertainties associated the parameterization of impaction scavenging. Assumptions about the collector particle size distribution, and the collection efficiency, particularly associated with thermophoretic, turbulent, and electric forces can cause the scavenging coefficients to differ by up to an order of magnitude [Wang et al., 1978, Miller and Wang, 1989]. For the parameterization of impaction scavenging of aerosols by cloud droplets, we use separate scavenging coefficients for aerosol mass and number, but we do not make this separation for ice-crystal-aerosol impaction

scavenging. This is an additional uncertainty related to the scavenging of aerosols by ice crystals that we do not address here, but that should be considered in future work.

Similar to Eqn. 3.1, the local rate of change of the tracer C_i due to in-cloud scavenging by both nucleation and impaction is

$$\frac{\Delta C_i}{\Delta t} = C_i f^{\mathrm{cl}} \Big(\frac{(R_{i,\mathrm{nuc}} + R_{i,\mathrm{imp,liq}}) f^{\mathrm{liq}} Q^{\mathrm{liq}}}{C_{\mathrm{liq}}} + \frac{(R_{i,\mathrm{nuc}} + R_{i,\mathrm{imp,ice}}) f^{\mathrm{ice}} Q^{\mathrm{ice}}}{C_{\mathrm{ice}}} \Big) \qquad (3.16)$$

where f^{liq} and f^{ice} are the respective liquid and ice water fractions of the total cloud water, f^{cl} is the cloud fraction, C_{liq} and C_{ice} are the cloud liquid and ice water content, respectively, and Q^{liq} and Q^{ice} are the respective sums of the conversion rates of cloud liquid and ice to precipitation by the processes of autoconversion, accretion and aggregation. This diagnostic scavenging approach is implemented in simulation DIAG-FULL.

Prognostic In-Cloud Scavenging

In this study, we also use the prognostic in-cloud aerosol processing scheme for stratiform clouds developed by Hoose et al. [2008a,b] (simulation PROG-AP). This scheme treats the aerosol mass and number concentrations in the cloud droplets and ice crystals as prognostic species, which are passed between model time-steps. The processes of nucleation and impaction scavenging, evaporation, sublimation, freezing and melting are represented for this parameterization. The methodology is described in detail in Hoose et al. [2008a,b]. Unlike the new diagnostic scheme, the prognostic scheme currently applies the same nucleation scavenging ratio to both the aerosol mass and number distributions for any given aerosol mode, grid box and time-step, as opposed to having separate mass and number nucleation scavenging ratios. One other difference is that the in-cloud impaction scavenging for the time being implements the prescribed kernels of Table 3.2 as opposed to the physically detailed size-dependent impaction parameterization of the new diagnostic scheme in the simulation DIAG-FULL.

Table 3.2: In-cloud impaction scavenging kernels (m^3 s^{-1}) for aerosol-droplet and aerosol-ice crystal collision for each of the seven log-normal modes of the ECHAM5-HAM following Hoose et al. [2008a,b].

Mode	Droplets	Crystals
Nucleation Soluble (NS)	2.5×10^{-12}	5.0×10^{-11}
Aitken Soluble (KS)	2.5×10^{-12}	5.0×10^{-11}
Accumulation Soluble (AS)	2.0×10^{-14}	2.0×10^{-12}
Coarse Soluble (CS)	0.0	2.0×10^{-13}
Aitken Insoluble (KI)	2.5×10^{-12}	5.0×10^{-11}
Accumulation Insoluble (AI)	2.0×10^{-14}	2.0×10^{-12}
Coarse Insoluble (CI)	0.0	2.0×10^{-13}

In-Cloud Scavenging Sensitivity Simulations

We implement several variations to the new diagnostic scheme as sensitivity tests. All simulations conducted for this study are summarized in Table 3.3. Simulation DIAG2 replaces the size-dependent in-cloud impaction parameterization of simulation DIAG-FULL with the prescribed impaction kernels of Hoose et al. [2008a,b] given in Table 3.2. DIAG2 is otherwise the same as DIAG-FULL. Simulation DIAG1 differs from simulation DIAG2 only in that the nucleation scavenging is changed such that the the mass nucleation scavenging ratios are set equal to the diagnosed number nucleation scavenging ratios. Two additional sensitivity studies are done to examine the prescribed ratio approach. 100% of the aerosols in clouds are assumed to be scavenged into the droplets or crystals for the simulation F100. This simplistic assumption has been used in global models [e.g., Barth et al., 2000]. The simulation F100-INT is similar except that 100% of the soluble/internally mixed aerosols in clouds are assumed to be cloud-borne, and 0% of the insoluble aerosol is scavenged into the cloud droplets or crystals. All of our simulations that implement scavenging by prescribed fractions treat the process of impaction implicitly together with nucleation in the prescribed fractions. To examine the relative importance of impaction, particularly related to aerosol vertical profiles, we set all in-cloud impaction scavenging to zero for the simulations DIAG-FULL-noimp and PROG-AP-noimp, which are otherwise identical to DIAG-FULL and PROG-AP, respectively.

Table 3.3: The simulations conducted for this study are summarized in this table.

Simulation	Description
CTL	Control simulation using prescribed in-cloud scavenging ratios from Table 3.1
F100	Assuming 100% of aerosols in clouds are cloud-borne for all aerosol modes
F100-INT	Assuming 100% of soluble/internally mixed aerosols in clouds are cloud-borne, and 0% of insoluble aerosols are cloud-borne
DIAG1	In-cloud nucleation scavenging ratios diagnosed from cloud droplet and ice crystal number concentrations, equating the mass with the number nucleation scavenging ratios, and using Hoose et al. [2008a,b] impaction scavenging kernels from Table 3.2
DIAG2	Same as DIAG1, but with separate mass and number nucleation scavenging ratios (see text for details)
DIAG-FULL	Same as DIAG2, but using physically detailed size-dependent in-cloud impaction scavenging coefficients, and kernels for cloud droplets and ice crystals shown in Figs. 1 and 2.
DIAG-FULL-noimp	Same as DIAG-FULL except no in-cloud impaction scavenging
PROG-AP	Prognostic stratiform aerosol processing scheme of Hoose et al. [2008a,b]
PROG-AP-noimp	Same as PROG-AP except no in-cloud impaction scavenging

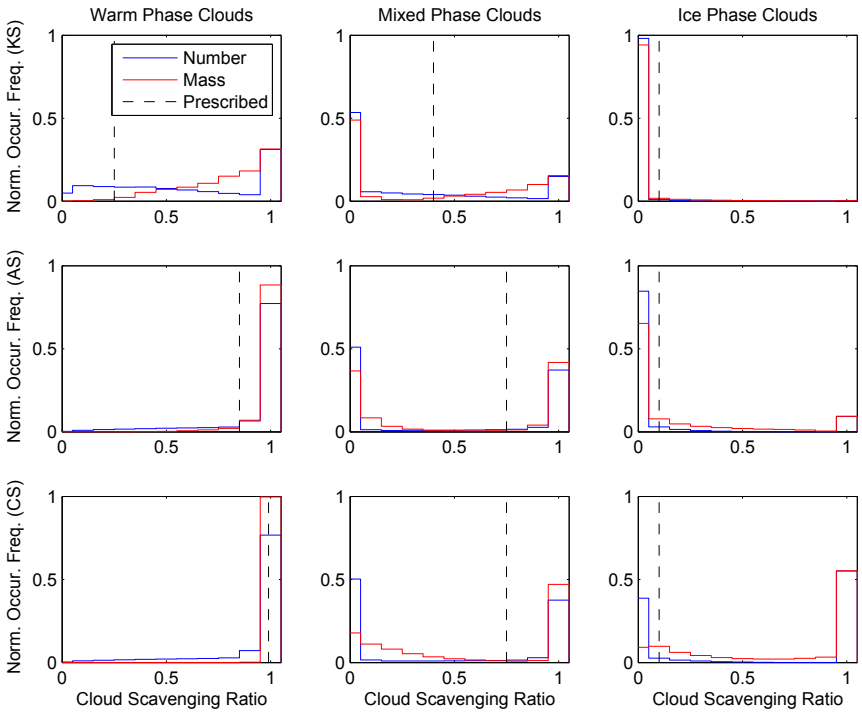

Figure 3.3: Histograms of the frequency of occurrence of the stratiform in-cloud mass and number scavenging ratios for the simulation DIAG-FULL (Table3.3), including both nucleation and size-dependent impaction scavenging for the internally mixed/soluble Aitken (KS), accumulation (AS), and coarse (CS) aerosol modes, and for warm (T>273.15 K), mixed (238.15<T≤273.15 K) and ice (T≤238.15 K) phase clouds. The dashed line indicates the prescribed ratios of Stier et al. [2005] used for the CTL simulation.

3.4 Results of the Global Simulations

3.4.1 Aerosol Scavenged Fractions

Figure 3.3 shows a frequency plot of the aerosol mass and number scavenged fractions for the DIAG-FULL simulation as compared to the prescribed ratios of Stier et al. [2005], which are implemented for the CTL simulation. Particularly for mixed phase clouds, the scavenged fractions deviate considerable from the prescribed ratios, and are <0.1 for about 50% of the occurrences for number scavenging. As the clouds glaciate, the Bergeron-Findeisen process causes rapid growth of the few ice crystals at the expense of the cloud droplets, which reduces the CDNC, and hence results in lower scavenged fractions for simulation DIAG-FULL. For warm phase clouds, the

Aitken and accumulation mode scavenged fractions for simulation DIAG-FULL are greater than the prescribed ratios for 75% of the scavenging events. For ice clouds, the scavenging of the coarse mode is greater than the prescribed ratio of 0.1 for about 60% of the scavenging occurrences, suggesting that the prescribed fraction for scavenging the coarse mode in ice clouds might be too low. Figure 3.3 also shows that the scavenged fractions for the mass distributions are higher than for the number distributions. This is physically correct since the median radii of the aerosol mass distributions are higher than for the respective number distributions, and so mass distributions should be scavenged with higher fractions. As opposed to equating the mass with the number scavenging ratios, our approach will alter the aerosol size distribution to produce smaller aerosols. The impact of in-cloud scavenging on aerosol size is examined further in the following subsection.

Figure 3.4 shows the zonal and annual mean aerosol mass scavenged into the cloud droplets and ice crystals averaged over clear and cloudy regions, comparing the simulations CTL, DIAG-FULL, and PROG-AP. The mass scavenged is greatest near the surface sources of the aerosols where warm phase clouds occur. In these regions, there are generally differences of <10% for the DIAG-FULL relative to the CTL simulation, but there are reductions of up to 50% for sulfate and sea salt scavenged mass over the southern oceans. For the PROG-AP simulation, the mass scavenged for all aerosol species in the regions of warm clouds is lower by about 50% compared to the CTL simulation. Hoose et al. [2008a] explained this is a result of the dependence of scavenged fraction on cloud history in an aerosol processing simulation. Alternatively, for the diagnostic and prescribed fraction scavenging approaches, all of the aerosol is assumed to be available for scavenging at each time-step since the in-droplet and in-crystal aerosol concentrations are not passed between model time-steps. Both the DIAG-FULL and PROG-AP simulation behave similarly in the colder regions of the troposphere where mixed and ice phase clouds occur. These more physically detailed parameterizations indicate that the mass scavenged, particularly in ice clouds, is greater by up to two-fold as compared to the mass scavenged using the prescribed scavenging fractions of the CTL simulation. This aerosol mass scavenged into the cloud droplets and ice crystals may not necessarily be removed by precipitation, since

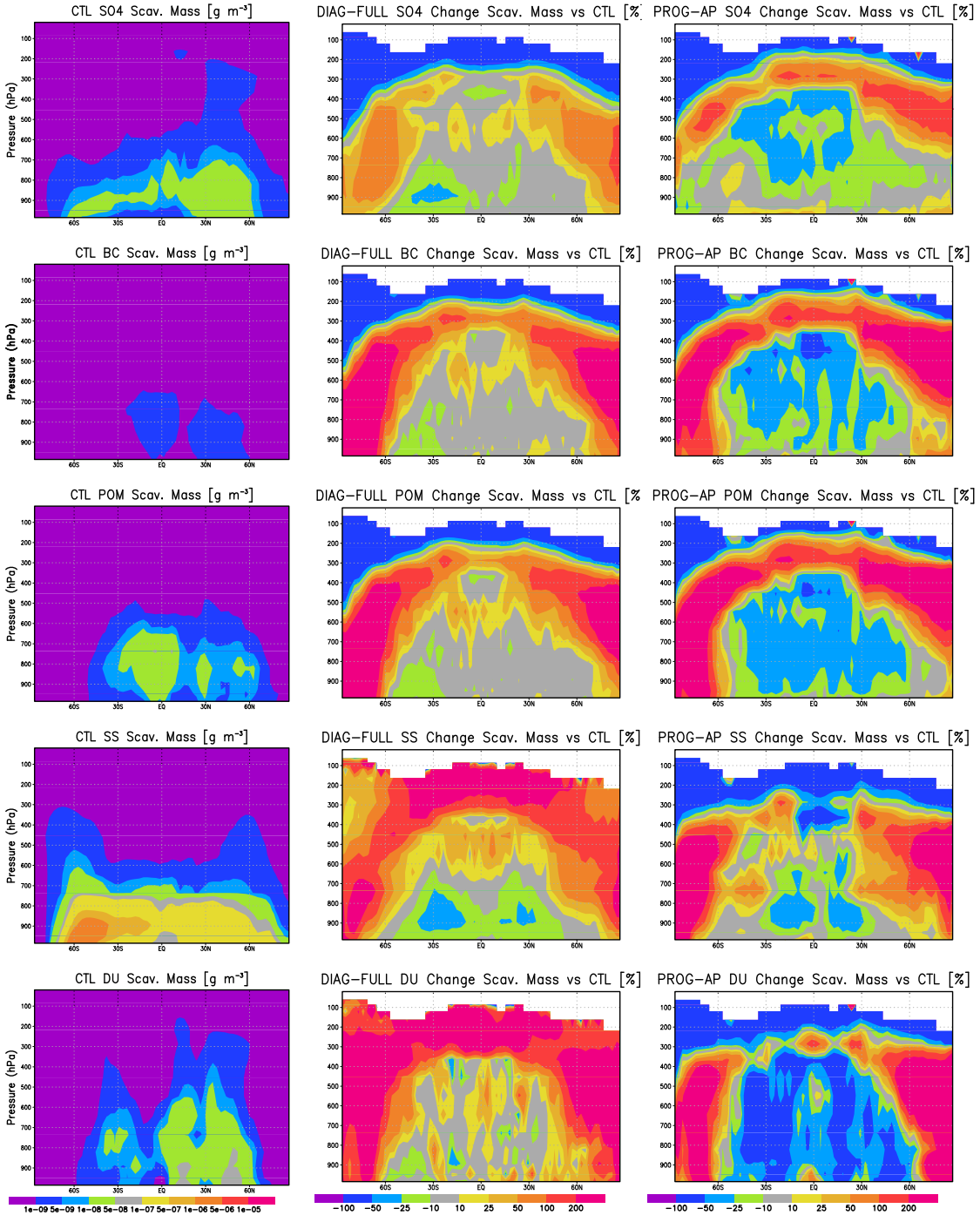

Figure 3.4: Zonal and annual mean sulfate (SO4), black carbon (BC), particulate organic matter (POM), sea salt (SS), and dust (DU) mass (g m^{-3}, except g S m^{-3} for sulfate) contained in cloud droplets and ice crystals for the simulation CTL and the percent change in these scavenged masses for the simulations DIAG-FULL and PROG-AP as compared to the CTL simulation.

the rates of formation of precipitation, and the evaporation rates also ultimately control the aerosol mass that is removed from the atmosphere.

For the simulation PROG-AP, the mass transfer rates between the interstitial and in-droplet and in-crystal modes are shown in Fig. 3.5. This figure is similar to that shown in Hoose et al. [2008a]. However, for this study we have used a more recent model version, and our dust and sea salt emissions are different with nudged meteorological conditions as compared to Hoose et al. [2008a]. Similar to Hoose et al. [2008a], cloud droplet nucleation is a dominant process for transfer to aerosol mass into the in-droplet mode. Our results differ in that collisions are shown to dominate over nucleation or freezing for transfer of aerosol into the ice crystals. This is in agreement with recent work by Baumgardner et al. [2008], who suggested that impaction scavenging might dominate over nucleation scavenging for black carbon scavenging into ice crystals. Our study also implemented the below-cloud scavenging parameterization of Croft et al. [2009], which accounts for the higher aerosol removal by below-cloud scavenging in comparison to the results in Fig. 6 of Hoose et al. [2008a]. Hoose et al. [2008a] implemented the prescribed below-cloud scavenging coefficients that are included in the standard ECHAM5-HAM model. Croft et al. [2009] show that the below-cloud scavenging with these prescribed coefficients is less vigorous than for the new physically detailed aerosol size-dependent parameterization of Croft et al. [2009]. Sensitivity tests included in Hoose et al. [2008a] also show this same comparison, and find better agreement with observations for the detailed aerosol size-dependent parameterization of Croft et al. [2009].

3.4.2 Impacts on Predicted Aerosol Size

Figure 3.6 shows the zonal and annual mean count median dry radius for the CTL simulation, and the percent difference for the simulations DIAG2 relative to DIAG1, and also for the simulations DIAG-FULL and PROG-AP relative to the CTL. As opposed to using the same nucleation scavenging ratios for the aerosol mass and number distributions (simulation DIAG1), the implementation of separate mass and number scavenging ratios gives annual and zonal mean soluble accumulation and coarse mode

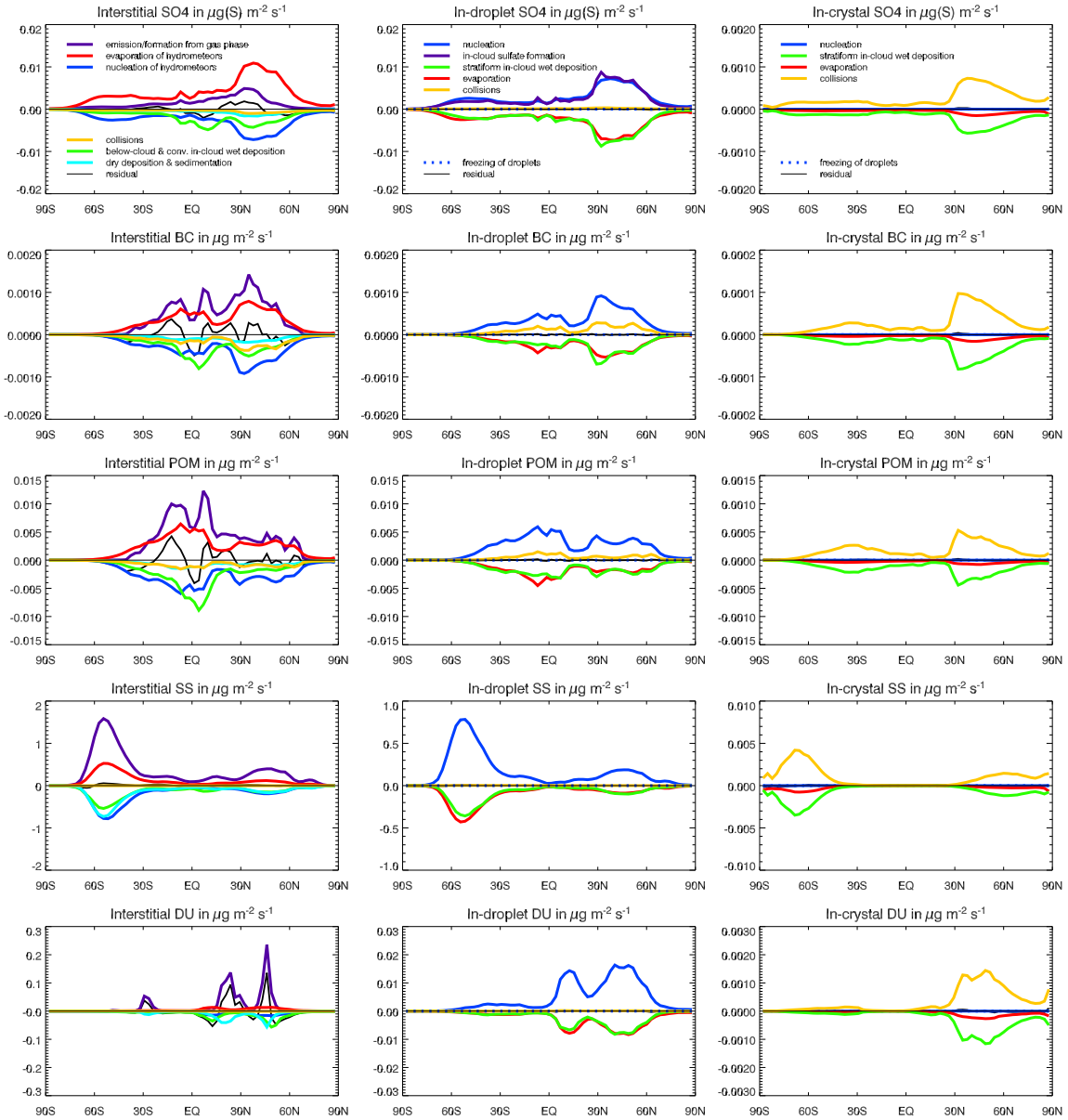

Figure 3.5: The zonal and annual mean transfer rates (μg m^{-2}s^{-1}, except μg S m^{-2}s^{-1} for sulfate) between the interstitial, in-droplet and in-crystal aerosol modes for the simulation PROG-AP due to the processes of emission/formation from gas phase, droplet and ice crystal nucleation, droplet freezing, aerosol collisions with droplets and ice crystals, below-cloud and in-cloud wet deposition, dry deposition, and sedimentation.

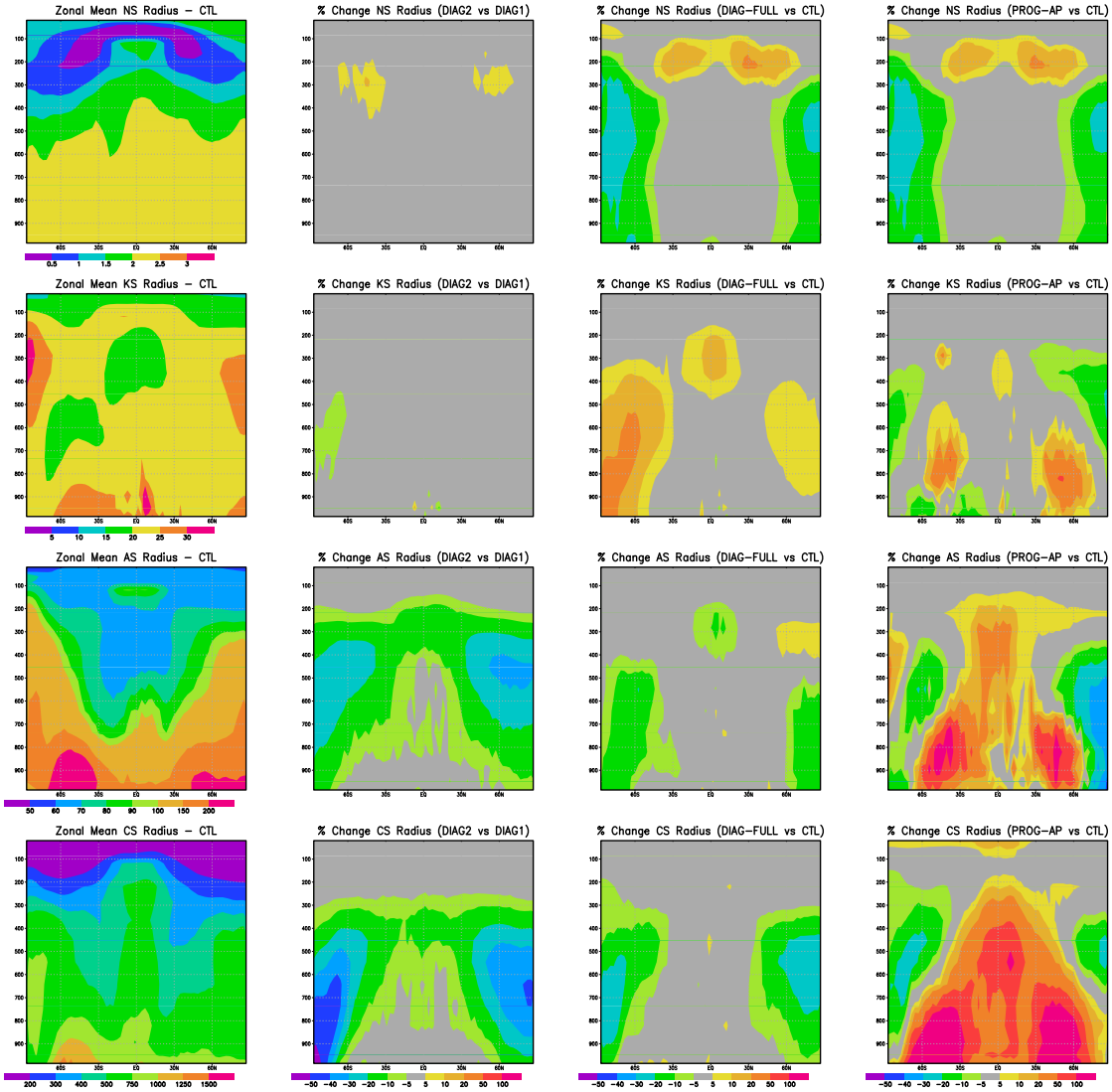

Figure 3.6: Zonal and annual mean count median dry aerosol radius (nm) for the CTL simulation for the four soluble/internally mixed modes, nucleation (NS), Aitken (KS), accumulation (AS), and coarse (CS), and the percent change of the zonal and annual mean count median aerosol radius for the simulation DIAG2 relative to the simulation DIAG1, and for DIAG-FULL and PROG-AP simulations relative to the CTL simulation.

count median radii that are smaller by up to 40% and 50%, respectively (simulation DIAG2). The regions of mixed and ice phase clouds in the middle and upper troposphere show the greatest sensitivity for the count median aerosol radius to the implementation of separate scavenging ratios for aerosol mass and number distributions. Thus, the implementation of separate mass and number nucleation scavenging ratios is worthwhile, particularly for mixed and ice phase clouds. This sensitivity is not as great for the near surface warm phase clouds since warm phase clouds had mass and number scavenging ratios of about unity for the soluble/internally mixed accumulation and coarse modes in more than 90% of the scavenging occurrences (see Fig. 3.3). Figure 3.6 shows that the soluble/internally mixed Aitken mode radius does not change by more than 10% with the implementation of separate mass and number nucleation scavenging ratios. This lower sensitivity is expected since the number of occurrences of nucleation scavenging for the soluble/internally mixed Aitken mode is about one order of magnitude smaller as compared to the larger soluble/internally mixed accumulation and coarse modes.

Figure 3.6 also shows how the zonal and annual mean count median radius is changed for the simulations DIAG-FULL and PROG-AP as compared to the CTL simulation. For the DIAG-FULL simulation, the zonal and annual mean soluble accumulation and coarse mode count median radii are reduced by up to 50% in regions of mixed and ice phase clouds, but the soluble Aitken mode radius is increased by up to 30%. Conversely, for the PROG-AP simulation the zonal and annual soluble accumulation and coarse mode radii are increased by about 100% throughout much of the lower and middle troposphere. This increased radius is typical for prognostic aerosol cloud processing simulations, which include the process of coagulation of in-droplet and in-crystal aerosols followed by evaporation or sublimation. This is associated with the release of larger aerosol particles to the atmosphere [Hoose et al., 2008a].

3.4.3 Impacts on Predicted Aerosol Mass

The zonal and annual mean aerosol mass mixing ratios comparing the simulations CTL, DIAG-FULL and PROG-AP are shown in Fig. 3.7. In comparison to the CTL simulation, both the DIAG-FULL and the PROG-AP simulations show an increase

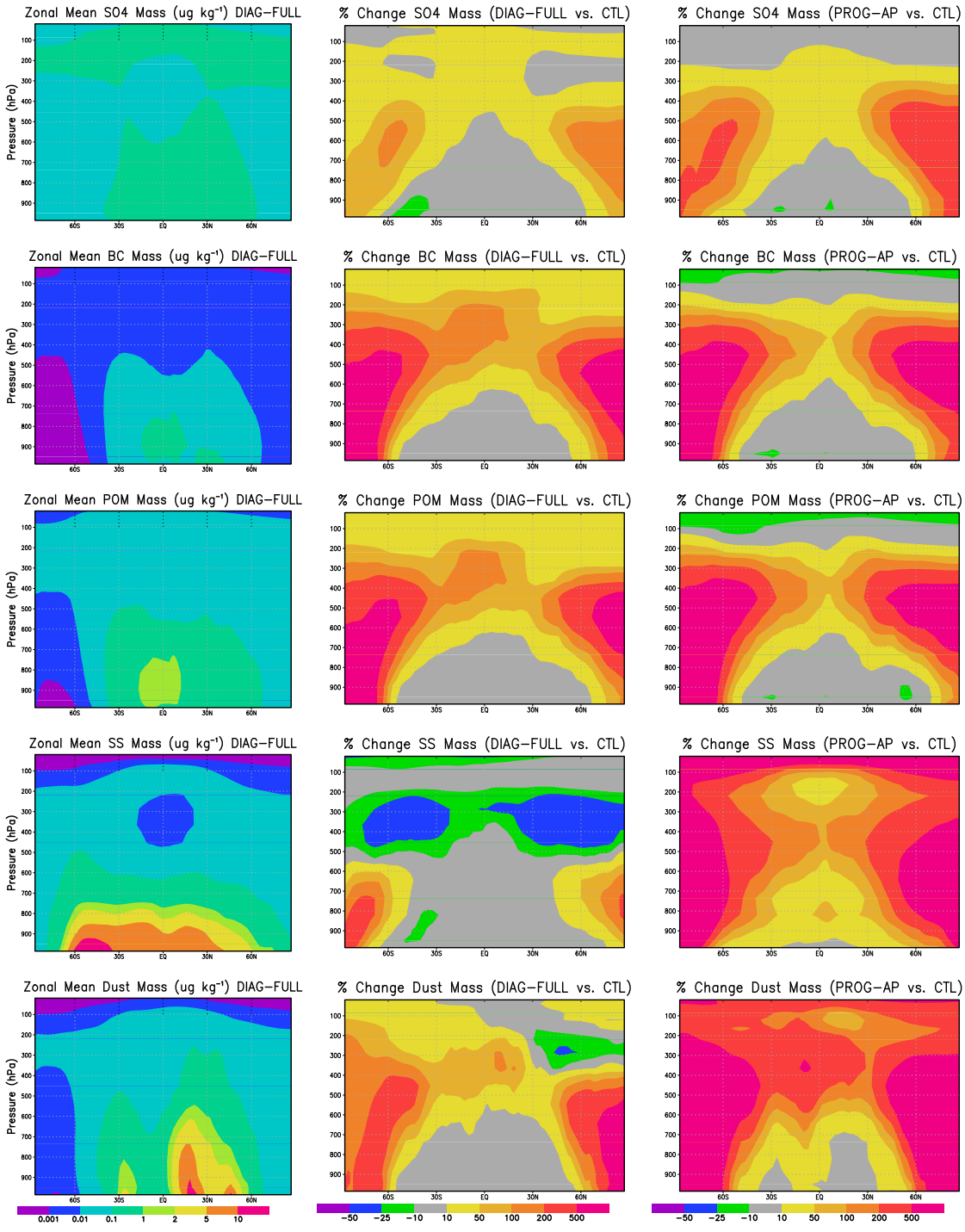

Figure 3.7: The zonal and annual mean sulfate (SO4), black carbon (BC), particulate organic matter (POM), sea salt (SS), and dust (DU) mass mixing ratios ($\mu g\,kg^{-1}$), except $\mu g\,S\,kg^{-1}$ for sulfate) for the simulation DIAG-FULL and the percent change in these masses for the simulations DIAG-FULL and PROG-AP as compared to the simulation CTL.

in dust and carbonaceous aerosol mass mixing ratios by more than five-fold, and up to two-fold for sea salt and sulfate near the middle troposphere, and towards the poles where mixed phase and ice clouds occur. Dust and carbonaceous aerosols exist partly in the insoluble modes, which are not scavenged by nucleation processes. Differences in the parameterization of impaction scavenging has a greater influence on these species. It is not intuitive whether an increase to the scavenged mass (shown in Fig. 3.4) should be associated with an increase or a decrease in the respective mass mixing ratio for any given aerosol species since there are a variety of processes, including rates of scavenging at other altitudes, evaporation, precipitation removal and transport, which interact to ultimately control the mass mixing ratio. Figure 3.4 shows that the scavenged mass was increased for all aerosol species towards the upper troposphere, but the sea salt mass mixing ratios in the upper troposphere are decreased by up to 50%, whereas for the other aerosol species, the mass mixing ratios were increased at these altitudes.

Table 3.4 presents the annual and global mean mass burdens and lifetimes for the five aerosol species, and for all the simulations conducted. The aerosol mass burdens are lower for the simulation DIAG-FULL, by 7%, 2%, 16%, and 30% for sulfate, particulate organic matter, dust, and sea salt, respectively, as compared to the PROG-AP simulation. Similarly, Ghan and Easter [2006] showed that a diagnostic scavenging scheme under-estimated aerosol burdens by about 20% as compared to a prognostic treatment of in-droplet aerosol. Aerosols are kept within the cloud droplets and ice crystals between time-steps for the prognostic aerosol processing simulation, and this affects the mass and number of aerosols available for scavenging into the cloud droplets and crystals at each time-step, and ultimately the mass distribution.

The simulation F100 allows us to compare the prescribed ratio approach of Stier et al. [2005] with the simplistic assumption that 100% of the aerosols in clouds are in the droplets and crystals. This simplistic approach has been used in global models [Barth et al., 2000]. We find that the global and annual mean aerosol mass burdens in simulation F100 are lower in comparison to the CTL simulation, by up to 10% for sulfate. The greatest mass burden difference between all simulations was 32% for the global and annual mean sea salt burden, between the F100 simulation and the

Table 3.4: Annual and global mean mass burdens (Tg, except Tg S for sulfate) and lifetimes (days) given in brackets immediately following the burdens, for the five aerosol species, and for the simulations described in Table 3.3. POM refers to particulate organic matter.

Burden (Lifetime)	Sulfate	Black Carbon	POM	Dust	Sea Salt
CTL	0.843 (4.2)	0.119 (5.6)	1.04 (5.7)	3.60 (3.9)	8.28 (0.56)
F100	0.749 (3.7)	0.109 (5.2)	0.99 (5.4)	3.40 (3.7)	7.86 (0.53)
F100-INT	0.750 (3.7)	0.116 (5.5)	1.10 (6.1)	3.77 (4.1)	7.85 (0.53)
DIAG1	0.965 (4.8)	0.133 (6.3)	1.17 (6.5)	4.10 (4.3)	8.39 (0.57)
DIAG2	0.867 (4.3)	0.122 (5.8)	1.08 (6.0)	3.93 (4.2)	7.99 (0.54)
DIAG-FULL	0.886 (4.4)	0.132 (6.3)	1.11 (6.1)	3.69 (3.9)	7.95 (0.54)
DIAG-FULL-noimp	0.991 (4.6)	0.135 (6.4)	1.13 (6.2)	3.95 (4.2)	8.01 (0.54)
PROG-AP	0.952 (4.8)	0.129 (6.1)	1.13 (6.2)	4.41 (4.6)	11.4 (0.77)
PROG-AP-noimp	1.228 (6.1)	0.186 (8.8)	1.46 (8.1)	4.78 (5.0)	12.9 (0.87)

PROG-AP simulations. Assuming that only the soluble/internally mixed aerosols are cloud-borne for the simulation F100-INT as compared to F100 does not affect the sulfate and sea salt burdens significantly, since these aerosols do not exist in the insoluble modes. However, the annual and global mean black carbon and dust burdens are higher by about 10% when none of the insoluble aerosols are allowed to be cloud-borne.

Comparing the simulations DIAG1 and DIAG2 illustrates the impact of diagnosing separate stratiform nucleation scavenging ratios for aerosol mass and number distributions. The global and annual mean mass burdens are higher by about 10% and 8% for sulfate and carbonaceous aerosols, and 5% for sea salt and dust for the simulation DIAG1 as compared to DIAG2, which diagnoses separate mass and number scavenging ratios. Thus, particularly for sulfate, diagnosing separate mass and number nucleation scavenging ratios is of importance.

Table 3.4 also includes two simulations with the in-cloud impaction processes turned off, DIAG-FULL-noimp and PROG-AP-noimp. In comparing these two simulations with DIAG-FULL and PROG-AP, respectively, impaction scavenging is found to have a greater influence on the mass burdens for the aerosol species that occur in

the submicron size modes (sulfate and carbonaceous aerosols), and for the prognostic simulations. Impaction scavenging is particularly relevant for black carbon, which has a significant mass fraction in the insoluble Aitken mode, which is not scavenged by nucleation processes. The annual and global mean sulfate, particulate organic matter, and black carbon mass burdens were reduced by 22%, 23%, and 30%, respectively, for the PROG-AP simulation as compared to PROG-AP-noimp. When the in-droplet and in-crystal aerosol concentrations are treated prognostically, impaction has a greater effect on the predicted burdens since impaction continues to add aerosols to the existing in-droplet and in-crystal concentrations over successive time-steps, unlike for DIAG-FULL simulation. To further examine the relevance of the impaction parameterization, Section 4 will present a comparison of model predictions of black carbon vertical profiles with observations.

3.4.4 Impacts on Predicted Aerosol Number

Figure 3.8 shows the geographic distribution of the ratio of the number burdens between the F100, DIAG-FULL, and PROG-AP simulations, and the CTL simulation. For the PROG-AP simulation only the interstitial number burdens are shown. The accumulation mode number burdens in the DIAG-FULL and PROG-AP simulations increase by about 2 and 5 times, respectively, as compared to the CTL in the regions of greater stratiform cloud cover, poleward of 30°. Ghan and Easter [2006] also found accumulation mode number burdens higher by up to two times towards the poles for a prognostic as compared to diagnostic in-cloud aerosol scavenging treatment. For the F100 simulation, the accumulation mode number burdens are lower by up to 20% over the regions of stratiform cloud cover in comparison to the CTL simulation. However, for the F100 simulation, the nucleation number burdens are significantly increased by up to five times over the polar regions in comparison to the CTL simulation. Despite the increased in-cloud scavenging coefficients used in F100, the reduction in surface area available for sulfate condensation on to the larger aerosol modes leads to an increase in new particle formation. The annual and global mean new particle nucleation rate was about three times greater for the F100 simulation as compared to the DIAG-FULL simulation. For the PROG-AP simulation, the interstitial coarse mode

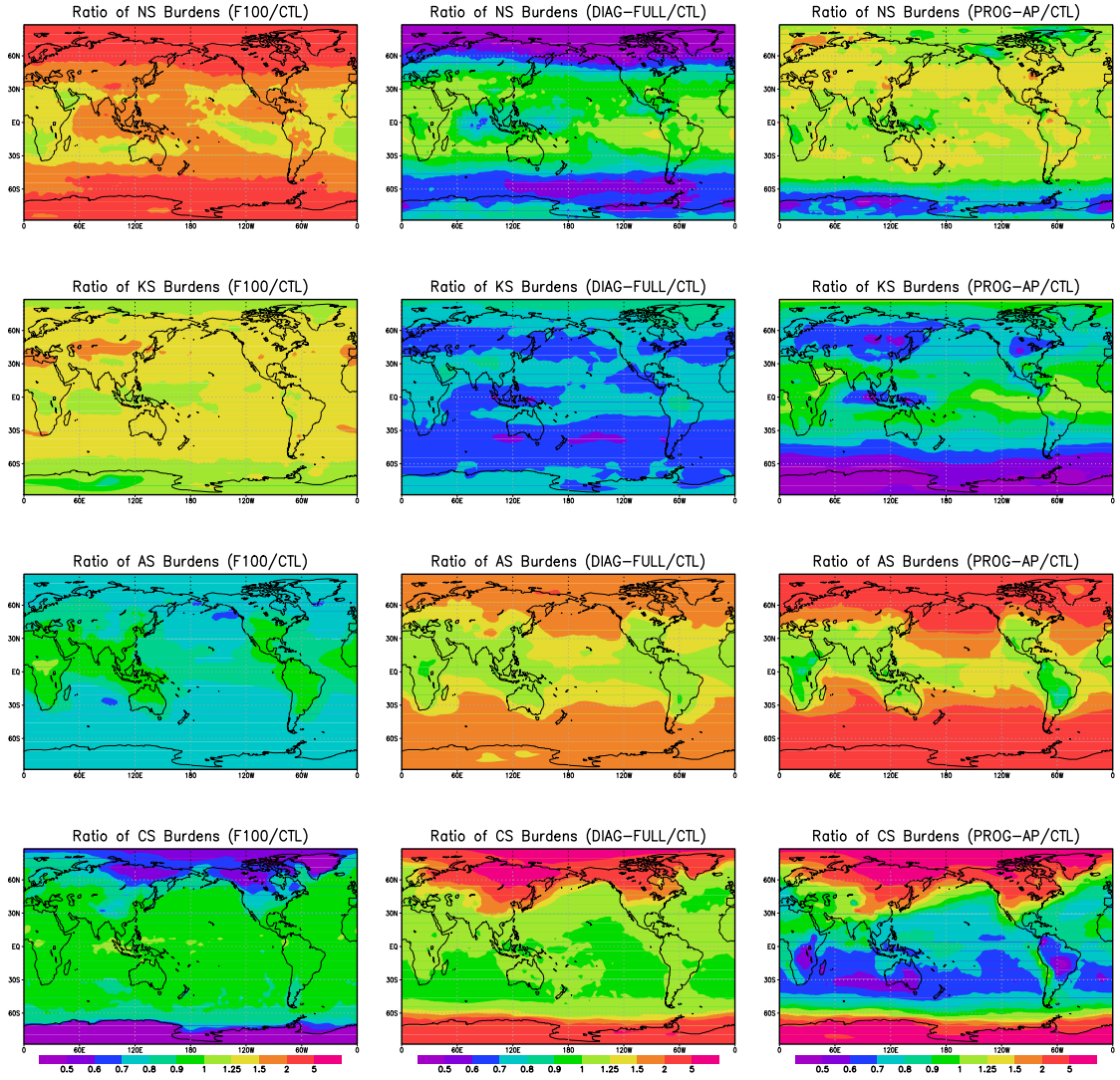

Figure 3.8: The geographic distribution of the ratio of the vertically integrated number burdens for the four soluble/internally mixed modes (nucleation (NS), Aitken (KS), accumulation (AS), and coarse (CS)) for the simulations F100, DIAG-FULL, and PROG-AP as compared to the CTL simulation. For the PROG-AP simulation, these are interstitial mode number burdens only.

is reduced by up to half over the southern oceans. This occurs since the in-droplet and in-crystal modes (not shown here) contain these aerosols.

Table 3.5 summarizes the global and annual mean number burdens for the seven standard modes of the ECHAM5-HAM. The accumulation mode number burden is increased by about 30% and 50% for the DIAG-FULL and PROG-AP simulations, respectively, relative to the CTL simulation. Ghan and Easter [2006] showed that smaller changes in global aerosol burdens (about 20%) changed the magnitude of the direct and indirect radiative forcing of aerosols on climate by considerably less than the magnitude of the current uncertainty associated with these forcings. However, since we find greater changes to the aerosol number burdens, future work should address the impact of changes of this magnitude on the direct and indirect aerosol effects predicted by our model. Comparing the number burdens for the PROG-AP and PROG-AP-noimp simulations illustrates the importance of the impaction parameterization in a global model. Without any impaction scavenging for the PROG-AP-noimp simulation, the global, annual mean accumulation number is increased by about 60%. As a consquence of this increased surface area, the number of nucleation mode particles is halved. The F100 simulation has a nucleation mode number burden that is about double that for the DIAG-FULL simulation since the surface area available for condensation on to the larger modes is reduced. Since the F100 simulation had more vigourous scavenging, the accumulation mode number is about 30% less for the F100 simulation relative to DIAG-FULL. A complete examination of the impacts of this enhanced new particle formation on modeled radiation and chemistry is beyond the scope of this paper, but should be examined in future studies. This excessive fine mode particle production in response to enhanced scavenging is of additional relevance from an air quality perspective.

3.4.5 Impacts on Predicted Aerosol Wet Deposition

The geographic distribution of wet deposition for the five aerosol species is shown in Fig. 3.9. For the species that exist only in the soluble/internally mixed modes, sea salt and sulfate, there is very little change to the geographic distribution of wet deposition for the DIAG-FULL simulation as compared to the CTL. For the DIAG-FULL

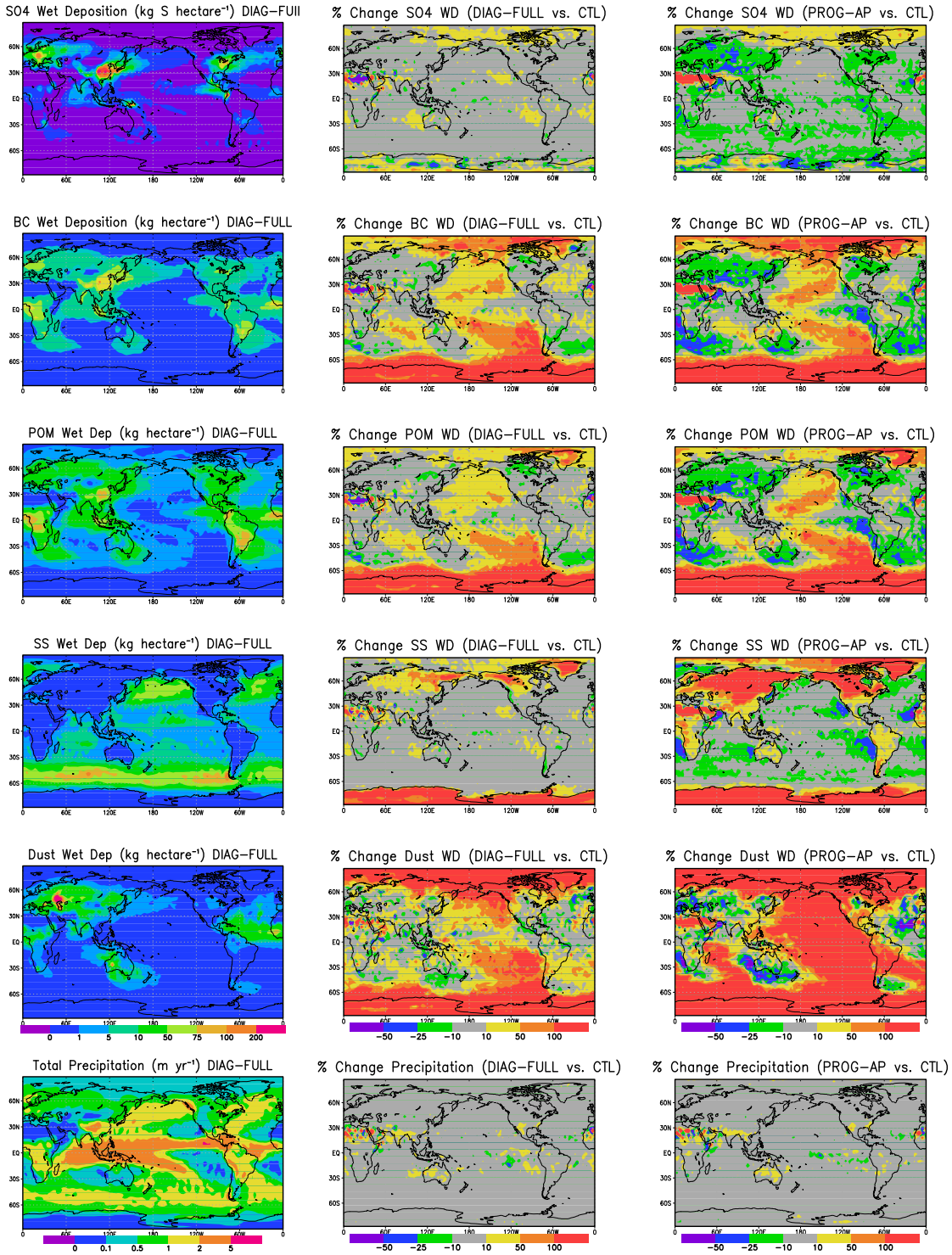

Figure 3.9: The geographic distribution of sulfate (SO4), black carbon (BC), particulate organic matter (POM), sea salt (SS) and dust annual mean wet deposition (kg hectare^{-1}, except kg S hectare^{-1} for sulfate), and total annual precipitation (m) for the DIAG-FULL simulation, and the percent change for the simulations DIAG-FULL and PROG-AP as compared to the CTL simulation.

Table 3.5: Global and annual mean number burdens (10^{10} m^{-2}) for the nine simulations and for the seven aerosol modes. CD and IC refer to the in-droplet and in-crystal modes of the prognostic simulation. Abbreviations are defined in Tables 1 and 3.

Number	NS	KS	AS	CS	KI	AI	CI	CD	IC
CTL	18800.	870.	75.1	0.441	8.29	0.031	0.068		
F100	31500.	1170.	65.9	0.414	6.84	0.028	0.063		
F100-INT	31500.	1160.	67.0	0.430	8.69	0.047	0.081		
DIAG1	17600.	668.	87.2	0.476	8.12	0.054	0.089		
DIAG2	18700.	737.	88.9	0.483	8.03	0.052	0.088		
DIAG-FULL	16700.	610.	94.2	0.470	9.21	0.047	0.083		
DIAG-FULL-noimp	15300.	604.	98.6	0.483	10.0	0.056	0.090		
PROG-AP	22500.	726.	115.	0.366	6.11	0.055	0.099	5.65	0.457
PROG-AP-noimp	10500.	605.	179.	0.375	11.2	0.069	0.116	10.5	0.683

simulation, dust and the carbonaceous aerosol wet deposition is generally changed by less than 10% close to the major source regions, but increases poleward and over the more remote oceans by about 100%. Over these more remote regions, these aerosols will have aged into the soluble/internally mixed modes, which are scavenged by cloud droplet and ice nucleation. However, the magnitude of the wet deposition is quite small in these regions. For the PROG-AP simulation, there are reductions in the wet deposition of sulfate and carbonaceous aerosols up to 25% close to the source regions. The total precipitation, which is also shown in Fig. 3.9 does not change significantly between simulations, and so these differences in wet deposition occur in response to the changes to the in-cloud scavenging parameterization, as opposed to changes to the rate of precipitation.

Aerosol Mass Deposition Budgets

Tables 3.6–3.10 summarize the deposition budgets for the five aerosol species. The simulation DIAG-FULL shows that aerosol mass removal by stratiform in-cloud scavenging is primarily by nucleation as opposed to impaction processes. Nucleation scavenging accounts for 98%, 94%, 96%, 51%, and 99% of the total deposition due

to stratiform in-cloud scavenging for sulfate, black carbon, particulate organic matter, dust, and sea salt, respectively. The remainder is due to in-cloud impaction scavenging. Below-cloud scavenging accounts for 13%, 14%, 11%, 25%, and 23% of the total annual and global mean deposition of sulfate, black carbon, particulate organic matter, dust, and sea salt, respectively for the simulation DIAG-FULL. For the DIAG-FULL simulation, in-cloud scavenging accounts for about 80% of the total removal of sulfate and carbonaceous aerosols, and close to 35% of the total removal of sea salt and dust. Stratiform, as opposed to convective, in-cloud scavenging accounts for about 65% of the total removal of sea salt and sulfate, but about 40% of the total removal of carbonaceous aerosols and dust, which have greater sources towards the tropics. Removal by warm phase nucleation (temperatures >273.15 K) is about twice that of mixed phase nucleation (temperatures between 273.15 K and 238.15 K) for sulfate and the carbonaceous aerosols, whereas for sea salt and dust these processes are about equivalent. Differences to the parameterization of the impaction scavenging process between simulations DIAG2 and DIAG-FULL, increased the annual and global mean dust and sea salt removal by impaction by about 2 orders of magnitude for the simulation DIAG-FULL. For black carbon, and particulate organic matter, the impaction scavenging is reduced by about half in DIAG-FULL as compared to DIAG2. However, since the global and annual mean aerosol mass removal is not primarily attributed to stratiform impaction processes, the global and annual mean mass burdens (see Table 3.4) change by less than 10% for all aerosol species between simulation DIAG-FULL and DIAG2.

For the simulation PROG-AP compared to the CTL simulation, the total aerosol removal by in-cloud scavenging is reduced by 20 to 25% for all aerosol species, with the greatest changes for sulfate and sea salt, with a sea salt mass burden increase of 35%. Evaporation releases considerable aerosol mass back to the atmosphere for the PROG-AP simulation. Increased aerosol burden for prognostic aerosol cloud processing simulations has been shown by Hoose et al. [2008a] and Ghan and Easter [2006]. The aerosol load that remains in the stratiform cloud droplets is not available for the convective scavenging, and so the convective in-cloud scavenging is also reduced by about 10% for sulfate. Only dust is affected in the opposite sense and the

Table 3.6: Annual mean deposition of sulfate (Tg S yr^{-1}) due to the processes of in-cloud nucleation and impaction scavenging for warm (T>273.15 K), mixed (238.15<T≤273.15 K) and ice phase (T≤238.15 K) stratiform clouds, combined nucleation and impaction scavenging for warm, mixed, and ice phase convective clouds, total in-cloud scavenging (ICS), below-cloud scavenging (BCS), dry deposition, and sedimentation. * indicates that stratiform nucleation and impaction are included together in the result shown for stratiform nucleation.

Sulfate	CTL	F100	F100 -INT	DIAG1	DIAG2	DIAG -FULL	PROG -AP
Stratiform clouds							
Warm nucleation	23.7*	24.6*	24.7*	23.6	24.6	24.4	18.9*
Mixed nucleation	13.8*	14.1*	14.2*	10.9	12.2	12.1	8.21*
Ice nucleation	0.171*	0.388*	0.388*	0.544	0.420	0.444	0.624*
Warm impaction				0.256	0.119	0.265	
Mixed impaction				0.364	0.255	0.392	
Ice impaction				0.093	0.079	0.005	
Convective clouds							
Warm	9.33	9.02	9.02	9.33	9.11	9.06	8.26
Mixed	12.4	12.0	12.0	12.9	12.3	12.4	11.2
Ice	0.72	0.70	0.70	0.78	0.73	0.77	0.70
Total ICS	60.1	60.8	61.0	58.8	59.8	59.9	48.0
Total BCS	9.67	8.96	8.91	10.9	9.97	9.91	14.9
Dry Deposition	2.02	2.00	1.98	1.94	1.91	1.89	3.72
Sedimentation	1.22	1.32	1.24	1.10	1.06	1.04	6.11

Table 3.7: Similar to Table 3.6 except for black carbon deposition (Tg yr^{-1}). * indicates that stratiform nucleation and impaction are included together in the result shown for stratiform nucleation.

Black Carbon	CTL	F100	F100 -INT	DIAG1	DIAG2	DIAG -FULL	PROG -AP
Stratiform clouds							
Warm nucleation	1.86*	2.10*	1.86*	1.49	1.61	1.75	1.39*
Mixed nucleation	1.16*	1.14*	1.17*	0.635	0.766	0.861	0.582*
Ice nucleation	0.014*	0.017*	0.031*	0.055	0.039	0.052	0.073*
Warm impaction				0.439	0.413	0.088	
Mixed impaction				0.217	0.197	0.081	
Ice impaction				0.012	0.009	0.001	
Convective clouds							
Warm	1.04	1.00	1.03	1.06	1.03	1.04	0.972
Mixed	1.86	1.79	1.87	1.92	1.85	1.94	1.77
Ice	0.121	0.116	0.122	0.126	0.121	0.132	0.121
Total ICS	6.06	6.17	6.08	5.95	6.03	5.94	4.96
Total BCS	0.980	0.886	0.955	1.09	1.02	1.09	1.53
Dry Deposition	0.706	0.684	0.711	0.687	0.687	0.701	0.828
Sedimentation	0.024	0.023	0.024	0.024	0.024	0.024	0.436

Table 3.8: Similar to Table 3.6 except for particulate organic matter (POM) deposition (Tg yr^{-1}). * indicates that stratiform nucleation and impaction are included together in the result shown for stratiform nucleation.

Organic Matter	CTL	F100	F100 -INT	DIAG1	DIAG2	DIAG -FULL	PROG -AP
Stratiform clouds							
Warm nucleation	14.9*	16.3*	15.3*	12.9	14.0	14.3	9.85*
Mixed nucleation	6.36*	6.20*	6.29*	3.94	4.66	4.83	3.14*
Ice nucleation	0.082*	0.110*	0.169*	0.376	0.277	0.318	0.476*
Warm impaction				1.71	1.53	0.417	
Mixed impaction				0.698	0.606	0.299	
Ice impaction				0.066	0.045	0.004	
Convective clouds							
Warm	10.1	9.86	9.99	10.3	10.0	10.1	9.51
Mixed	20.6	20.1	20.5	21.2	20.5	21.1	19.6
Ice	1.40	1.37	1.40	1.45	1.41	1.50	1.40
Total ICS	53.4	53.9	53.7	52.6	53.0	52.9	44.2
Total BCS	6.75	6.32	6.48	7.53	7.12	7.30	11.3
Dry Deposition	5.92	5.88	5.91	5.82	5.83	5.80	7.05
Sedimentation	0.194	0.186	0.187	0.200	0.199	0.203	3.71

Table 3.9: Similar to Table 3.6 except for dust deposition (Tg yr^{-1}). * indicates that stratiform nucleation and impaction are included together in the result shown for stratiform nucleation.

Dust	CTL	F100	F100 -INT	DIAG1	DIAG2	DIAG -FULL	PROG -AP
Stratiform clouds							
Warm nucleation	25.8*	31.5*	16.4*	15.4	16.8	15.2	10.2*
Mixed nucleation	29.5*	31.7*	17.7*	10.6	13.8	11.0	7.72*
Ice nucleation	0.308*	0.474*	1.04*	2.05	1.24	0.964	0.936*
Warm impaction				0.030	0.027	12.1	
Mixed impaction				0.191	0.172	13.6	
Ice impaction				0.088	0.085	0.002	
Convective clouds							
Warm	23.7	22.5	24.4	24.6	24.7	23.2	26.1
Mixed	34.4	32.9	36.0	37.1	36.9	35.1	39.3
Ice	2.31	2.18	2.37	2.41	2.45	2.45	2.69
Total ICS	116.	121.	97.9	92.5	96.2	114.	87.2
Total BCS	81.8	77.4	95.2	103.	99.7	86.8	104.0
Dry Deposition	21.1	20.9	21.7	22.1	22.0	21.4	23.4
Sedimentation	122.	120.	124.	126.	126.	123.	129.

Table 3.10: Similar to Table 3.6 except for sea salt (Tg yr^{-1}). * indicates that stratiform nucleation and impaction are included together in the result shown for stratiform nucleation.

Sea Salt	CTL	F100	F100 -INT	DIAG1	DIAG2	DIAG -FULL	PROG -AP
Stratiform clouds							
Warm nucleation	740.*	753.*	753.*	763.	777.	776.	494.*
Mixed nucleation	624.*	701.*	704.*	572.	622.	629.	310.*
Ice nucleation	0.41*	1.05*	1.04*	3.06	1.50	1.54	2.64*
Warm impaction				0.044	0.019	2.64	
Mixed impaction				0.096	0.056	3.53	
Ice impaction				0.001	0.0004	0.022	
Convective clouds							
Warm	285.	282.	282.	284.	280.	282.	304.
Mixed	328.	322.	321.	334.	324.	333.	371.
Ice	9.65	9.49	9.49	10.0	9.67	10.2	11.9
Total ICS	1990.	2070.	2070.	1970.	2010.	2040.	1500.
Total BCS	1240.	1200.	1200.	1290.	1260.	1250.	1530.
Dry Deposition	933.	913.	913.	915.	912.	910.	1020.
Sedimentation	1250.	1230.	1220.	1220.	1220.	1210.	1330.

convective scavenging is actually increased by a few percent. This is expected since stratiform in-cloud scavenging of dust is a less important sink compared to other removal processes, and Fig. 3.1 shows that the Hoose et al. [2008a,b] impaction scheme also scavenges coarse mode particles, such as dust, into the cloud droplets relatively inefficiently. These results point to the relevance of developing a convective aerosol processing treatment in the future that should be coupled with the stratiform aerosol processing treatment of Hoose et al. [2008a,b].

Aerosol Number Deposition Budgets

Table 3.11 shows the annual and global mean number deposition attributed to the various physical processes. The diagnostic simulations show that aerosol number scavenged in stratiform clouds is primarily attributed to impaction scavenging processes, as opposed to nucleation processes. This is in agreement with the findings of the one-dimensional study of Jacobson [2003]. For our diagnostic scavenging simulations, impaction scavenging rates for aerosol number exceed the nucleation scavenging rates by more than one order of magnitude for mixed and ice phase clouds, which account for 99% of the total number removal in stratiform clouds. This result is expected since the majority of the aerosol number is in the nucleation mode that contains aerosols that are too small to be scavenged by cloud nucleation processes, and these aerosols are most abundant in the middle and upper troposphere at the altitudes of mixed and ice phase clouds. Differences to the parameterization of impaction scavenging between simulations DIAG2 and DIAG-FULL reduced the number scavenging for ice clouds by about 7 times for the simulation DIAG-FULL. These results suggest that global modelers should give careful attention to the parameterization of impaction scavenging in predicting aerosol number scavenging in mixed and ice phase clouds. Considering all aerosol scavenging processes, in-cloud scavenging is the primary removal mechanism for aerosol number, exceeding dry deposition by up to one order of magnitude.

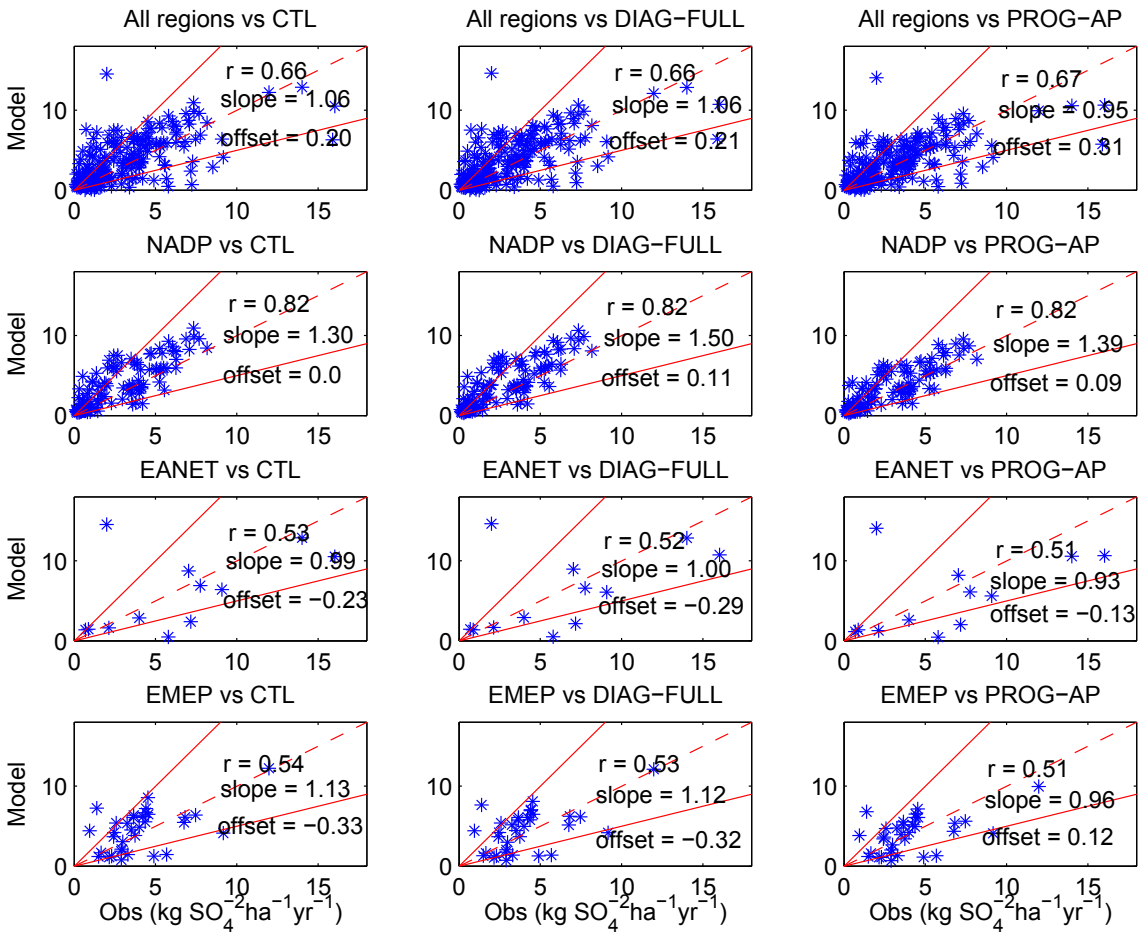

Figure 3.10: The annual mean sulfate wet deposition (kg $SO_4^{-2}ha^{-1}yr^{-1}$) grouped by regions from observations [Dentener et al., 2006a] as compared to the simulations CTL, DIAG-FULL and PROG-AP. The first row compiles data from all regions of this figure and Fig. 3.11. NADP is the National Atmospheric Deposition Program of the United States, EANET is the Acid Deposition Monitoring Network in East Asia, and EMEP is the European Monitoring and Evaluation Program.

Table 3.11: Global and annual mean aerosol number deposition (10^6 m^{-2} s^{-1}) summed over all aerosol modes. * indicates that stratiform nucleation and impaction are included together in the result shown for stratiform nucleation.

Number Dep	CTL	F100	F100-INT	DIAG1	DIAG2	DIAG-FULL
Stratiform clouds						
Warm nucleation	1.35*	21.3*	19.4*	0.61	0.64	0.56
Mixed nucleation	16.0*	259.5*	249.7*	0.49	0.53	0.44
Ice nucleation	22.7*	779.0*	777.8*	0.07	0.08	0.06
Warm impaction				1.19	1.33	0.17
Mixed impaction				6.11	8.03	6.32
Ice impaction				36.7	46.3	6.68
Total ICS	45.4	1080.	1070	48.0	59.9	16.8
Total BCS	0.62	4.02	3.90	0.41	0.46	0.30
Dry Deposition	4.86	22.2	21.4	3.06	3.20	2.56
Sedimentation	0.002	0.002	0.002	0.002	0.002	0.002

3.5 Comparison with Observations

Figures 3.10 and 3.11 show the comparison of the modeled wet deposition of sulfate with the observations compiled by Dentener et al. [2006a], and grouped according to geographic region. We do not find any statistically significant difference between the CTL, DIAG-FULL, and PROG-AP simulations in comparison to these observations. For all these simulations, the modeled deposition is within a factor of two of the observations for at least 75% of the sites. However, we must bear in mind the majority of sulfate mass, and thus the majority of the sulfate mass deposition is associated with scavenging in the near surface layers where cloud temperatures are frequently greater than 273 K. Figure 3.3 shows that the scavenged fractions for the soluble accumulation and coarse aerosol modes (containing the majority of sulfate mass) are about unity for warm phase clouds for both the CTL and DIAG-FULL simulations. Thus we would expect the simulations to compare equally well with observations for observations of sulfate wet deposition.

Figure 3.12 shows the geographic distribution of the aerosol optical depth (AOD) for the years 2001–2006, created from a combination of MODIS [Levy et al., 2007] and MISR [Diner et al., 2005, Martonchik et al., 2002] retrievals, as described in

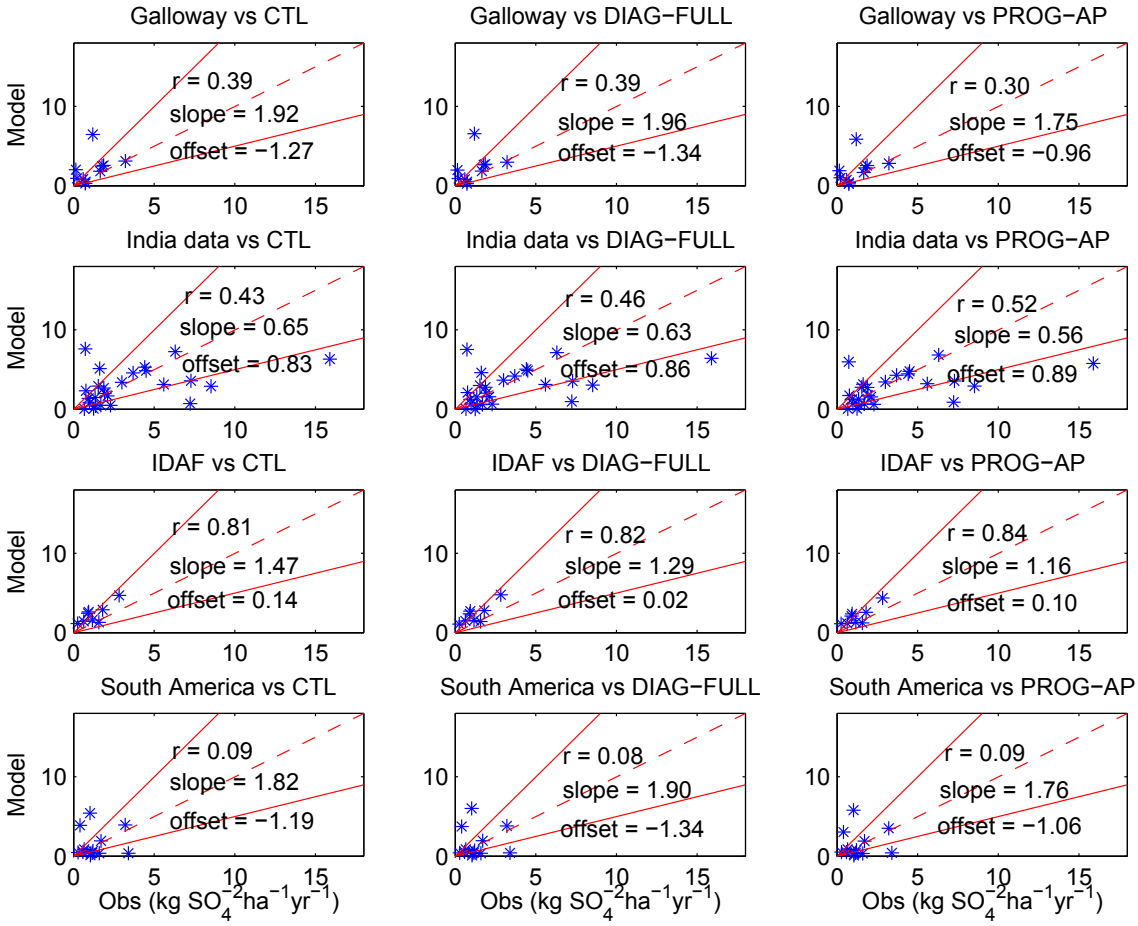

Figure 3.11: The annual mean sulfate wet deposition (kg $SO_4^{-2}ha^{-1}yr^{-1}$) grouped by regions from observations [Dentener et al., 2006a] as compared to the simulations CTL, DIAG-FULL and PROG-AP. Galloway refers to collection of sites from remote regions of primarily from the Australian and South American regions, and IDAF refers to a collection of data from Africa (Agac Debits Africa).

van Donkelaar et al. [2010]. The composite MODIS and MISR dataset is created from the ensemble of individual retrievals that exhibit little bias versus ground-based AERONET [Holben et al., 1998] AOD observations. More specifically, the accuracy of the MODIS and MISR AOD retrieval over land is evaluated relative to AERONET AOD on a monthly basis for nine land types defined using the MODIS BRDF/Albedo product at three different wavelengths (470 nm, 660 nm and 2.1 μm). Daily MODIS and MISR AOD retrievals over land types that exhibit a mean monthly bias in excess of either 0.1 or 20% are rejected. The remaining retrievals over 2001–2006 are averaged. The composite dataset is driven by MISR observations over bright surfaces where MODIS is biased [Abdou et al., 2005], and over dark surfaces by MODIS (higher temporal sampling). MODIS AOD is used over the ocean due to high sampling frequency and accuracy [Remer et al., 2005]. Annual mean AOD enhancements of >0.5 reflect a combination of mineral dust over and downwind of Africa, as well as large anthropogenic signals over India and East Asia. Sea salt contributes to moderate AOD enhancements at southern high latitudes.

Figure 3.12 also shows the geographic distribution of the ratio of the aerosol optical depth (AOD) for the simulations CTL, DIAG-FULL, and PROG-AP compared to the observational dataset. Both the DIAG-FULL and CTL simulations perform similarly. However, the number of grid points within 25% of the observations is increased by about 20% over the oceans for the DIAG-FULL simulation as compared to the CTL. The PROG-AP simulation has slightly lower AODs (10 to 20%) over the land, which improves the agreement with observations over eastern North America and eastern Europe, but the AOD is considerably over-predicted over the oceans (up to a factor of two). Hoose et al. [2008a] have shown that the agreement over the oceans can be improved with changes to the water uptake on the aerosols, which will be implemented in future versions of the ECHAM5-HAM.

Hoose et al. [2008a] showed that a prognostic in-cloud scavenging scheme modified zonal mean aerosol size distributions in the marine boundary layer to produce better agreement with the observations of Heintzenberg et al. [2000], particularly for the accumulation mode. These observations are shown in Fig. 3.13. The observations of Heintzenberg et al. [2000] are a compilation of data from different mobility, and

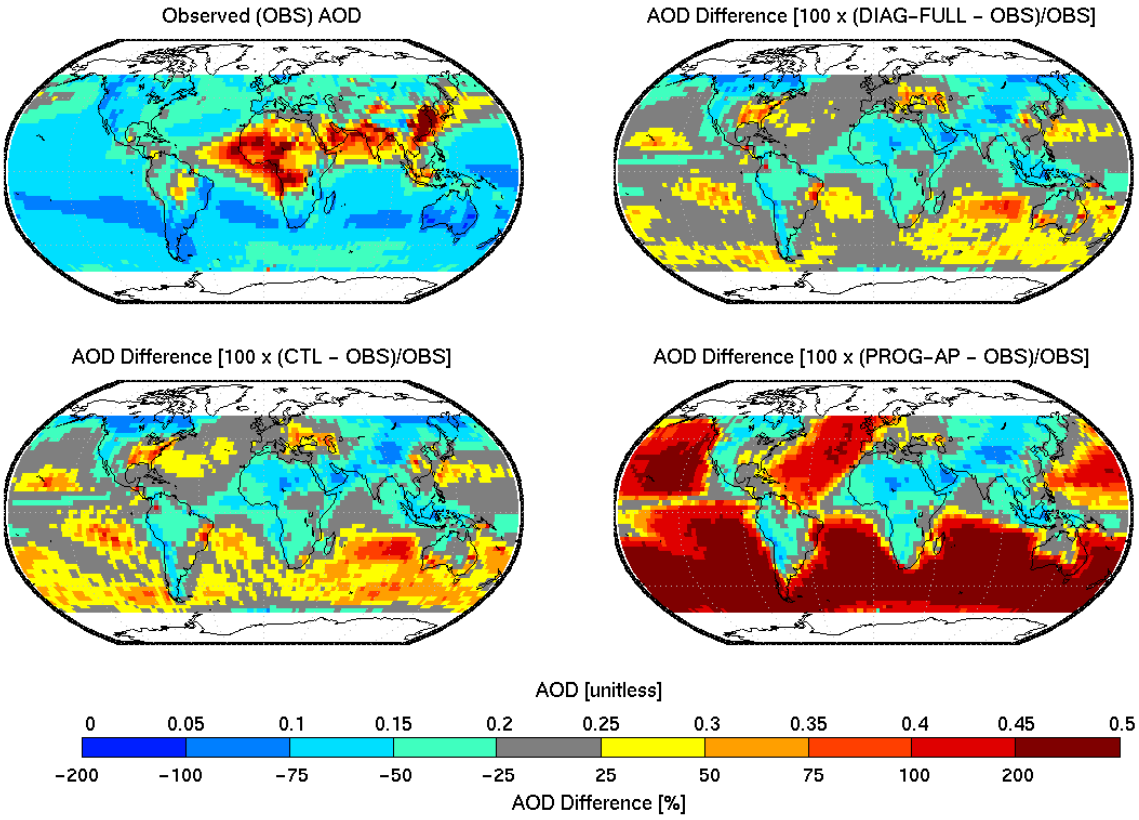

Figure 3.12: The geographic distribution of aerosol optical depth (AOD) at 550 nm from the composite MODIS, MISR, AERONET dataset compiled by van Donkelaar et al. [2010] representing the years 2001 to 2006, and the percent difference of the annual mean AOD for the simulations CTL, DIAG-FULL, and PROG-AP as compared to the observations.

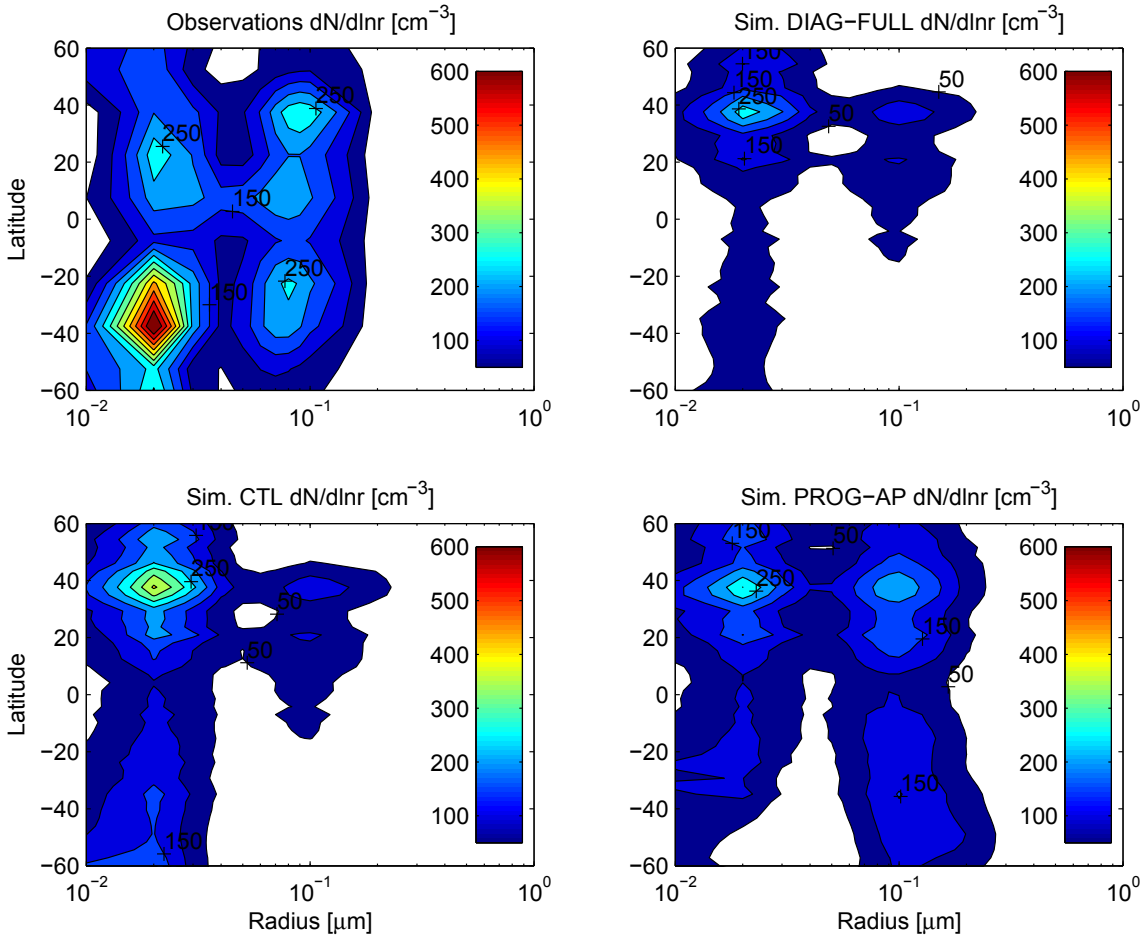

Figure 3.13: Zonal mean aerosol size distributions in the marine boundary layer for the simulations CTL, DIAG-FULL, and PROG-AP as compared to the observations of Heintzenberg et al. [2000], and similar to Fig. 8 of Hoose et al. [2008a].

aerodynamic sizing techniques, operated at relative humidities of <40%, and a multimodal lognormal distribution was fitted to the observations. The same methodology as described in Hoose et al. [2008a] was used for comparison with the simulations CTL, DIAG-FULL, and PROG-AP. Figure 3.13 shows that the DIAG-FULL simulation, unlike the PROG-AP simulation, does not modify the marine accumulation mode size distribution significantly as compared to the CTL simulation. The Aitken mode number concentrations are under-estimated by up to five times over the southern oceans for all simulations in comparison to the observations. A considerable reduction in the under-estimation could be made with changes to the treatment of new particle formation in the marine boundary layer, which will be implemented in future ECHAM versions. For the DIAG-FULL simulation, the Aitken mode numbers are reduced by half in the Southern Hemisphere relative to the CTL simulation, which is a consequence of the more vigorous scavenging in the marine boundary layer for the diagnostic scheme. Both Stier et al. [2005] and Hoose et al. [2008a] have shown that the size distributions for the ECHAM5-HAM model compare quite reasonably with observations. Accurate simulation of the aerosol size distributions in global models is also essential for the size-dependent in-cloud scavenging parameterizations to perform correctly.

Recently Koch et al. [2009] presented black carbon profiles observed from aircraft in comparison to various global models. Figures 3.14 and 3.15 compare this same aircraft data with our model simulations, CTL, DIAG-FULL, and PROG-AP. Additionally we have included two sensitivity simulations that have the in-cloud impaction processes turned off for both the diagnostic and prognostic in-cloud scavenging schemes, DIAG-FULL-noimp and PROG-AP-noimp, respectively. Figure 3.14 shows profiles from the tropics and mid-latitudes taken between the equator, and 50 °N and between 120 °E and 60 °E and averaged for the same points as shown in Koch et al. [2009, 2010]. Figure 3.15 presents profiles from the high latitudes taken between 50 °N and 80 °N and between 180 °E and 60 °E and averaged for the same points as shown in Koch et al. [2009, 2010]. These figures show that the predicted black carbon profiles, particularly in the middle troposphere differ from the observations,

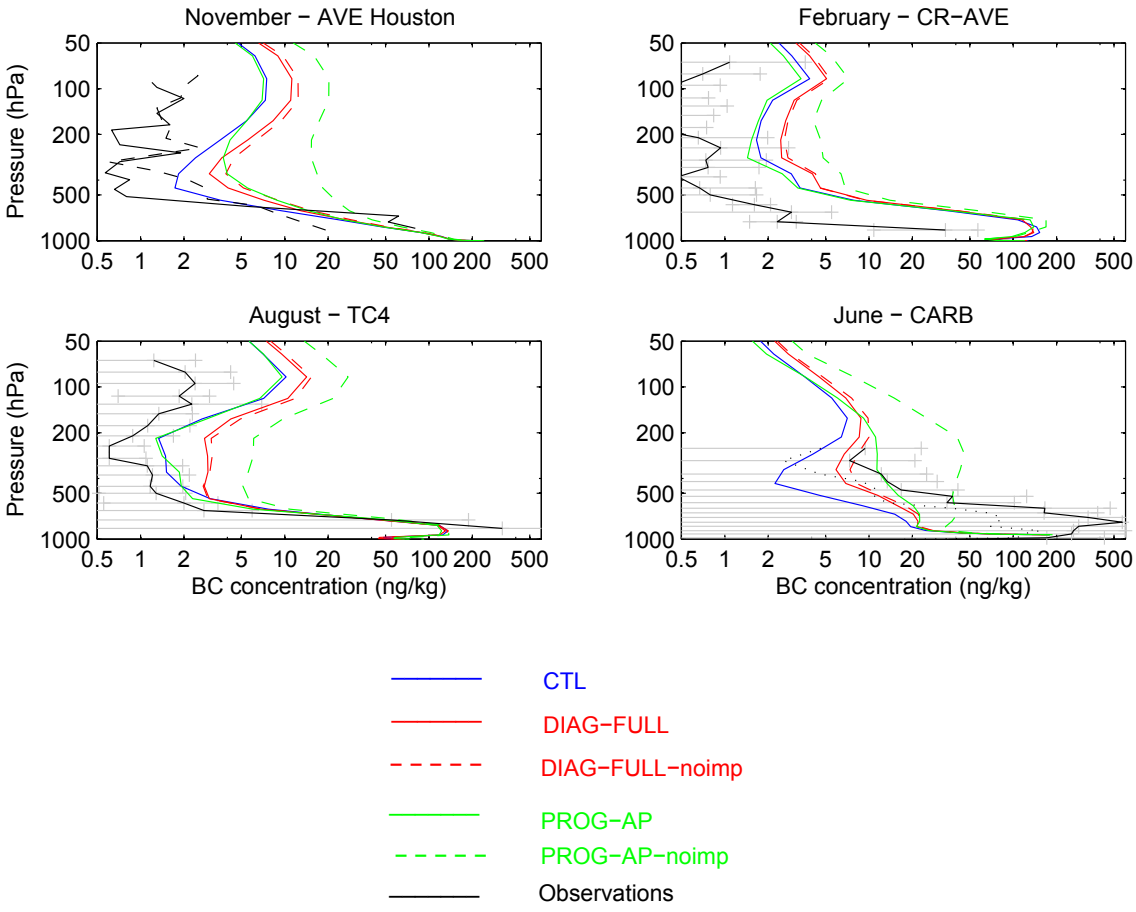

Figure 3.14: Black carbon concentrations (ng kg^{-1}) from the tropical and mid-latitude aircraft campaigns over the Americas between the equator and 50°N, and 120 °E and 60 °E, for the same locations as described in Fig. 9 of Koch et al. [2009], and for the simulations CTL, DIAG-FULL, and PROG-AP, and with no impaction scavenging for DIAG-FULL-noimp and PROG-AP-noimp. AVE-Houston: NASA Houston Aura Validation Experiment, CR-AVE: NASA Costa Rica Aura Validation Experiment, TC4: NASA Tropical Composition, Cloud, and Climate Coupling, CARB: NASA initiative in collaboration with California Air Resources Board.

and between each other, by up to two orders of magnitude depending on the treatment of in-cloud scavenging. Changes of this magnitude could influence predictions of both the direct and indirect effects of aerosols, particularly related to black carbon in the middle and upper troposphere. These effects should be investigated in future studies. For the high latitude profiles shown in Fig. 3.15, where mixed phase and ice clouds are more prevalent, the CTL simulation underestimates the concentrations by up to two orders of magnitude, and both DIAG-FULL and PROG-AP improve the agreement to within one order of magnitude. For the simulation PROG-AP, black carbon concentrations are lower by up to a factor of five, and two in the middle and upper troposphere, respectively, as compared to the simulation PROG-AP-noimp. Thus, the parameterization of impaction scavenging is particularly relevant for black carbon in mixed and ice phase clouds.

For black carbon, the parameterization of impaction scavenging is of importance since this aerosol has considerable mass in the insoluble Aitken mode, which is scavenged only by impaction processes. This parameterization also relies on the correct representation of black carbon aging to determine the correct distribution of mass between the soluble/internally mixed and insoluble modes, making prediction of black carbon concentrations challenging. For seven of the ten of the profiles presented, the black carbon profile is closer to the observations for the DIAG-FULL and PROG-AP simulations as compared to the CTL simulation (changes up to one order of magnitude), suggesting that the mixed phase prescribed scavenging fractions of the CTL simulation might be too large. For the three profiles of Fig. 3.14 that show closer agreement with observations for the prescribed coefficient scheme of the CTL simulation, the PROG-AP simulation is a better match to the observations than for the DIAG-FULL simulation.

3.5.1 Simulation of ^{210}Pb and ^{7}Be

^{7}Be and ^{210}Pb have been simulated in global models, and used as passive tracers for the validation of deposition parameterizations [e.g., Brost et al., 1991, Liu et al., 2001, Feichter et al., 1991, Koch et al., 1996, 2006]. Recently, simulation of ^{7}Be and ^{210}Pb have been introduced into the ECHAM5-HAM [Heikkilä et al., 2008, 2009]. The

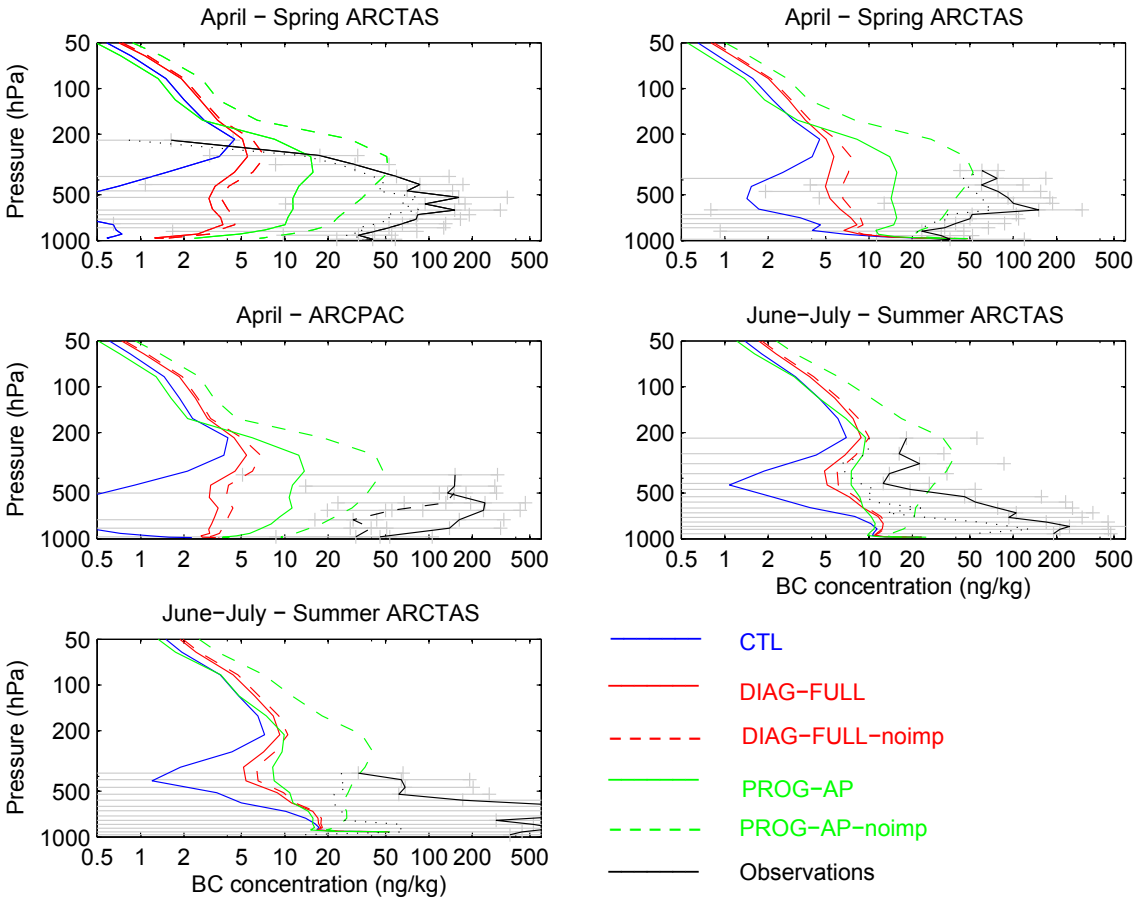

Figure 3.15: Black carbon concentrations (ng kg^{-1}) from the high latitude aircraft campaigns over the Americas between 50 °N and 80°N, and 180 °E and 60 °E, for the same locations as described in detail in Fig. 10 of Koch et al. [2009], and for the simulations CTL, DIAG-FULL, and PROG-AP, and with no impaction scavenging for DIAG-FULL-noimp and PROG-AP-noimp. ARCTAS: NASA Arctic Research of the Composition of the Troposphere from Aircraft and Satellites, ARCPAC: NOAA Aerosol Radiation and Cloud Processes affecting Arctic Climate.

methodology is described in detail in Feichter et al. [1991], Heikkilä [2007], Heikkilä et al. [2008]. The production rates for ^{7}7Be were taken from Masarik and Beer [1999]. The ^{210}Pb/radon source is from soils and was taken to be 1 atoms cm^{-2} s^{-1}, following Feichter et al. [1991], Liu et al. [2001], Koch et al. [2006]. ^{7}Be and ^{210}Pb are not explicitly distributed into the aerosol modes of the ECHAM5-HAM. However, the scavenging fractions for ^{7}Be are found by taking the ratio of the total sulfate mass scavenged to the total aerosol mass, whereas for ^{210}Pb the scavenging fractions are determined by the ratio of the total aerosol mass scavenged to the total aerosol mass. The rationale is that near the surface where ^{210}Pb is formed, particles are composed of many chemical compounds, whereas for the ^{7}Be source in the stratosphere, and upper troposphere, sulfate is the dominant chemical compound. These tracers have been coupled with the CTL and DIAG-FULL simulations.

Figure 3.16 compares the surface layer concentrations and wet deposition of these tracers for the simulations CTL and DIAG-FULL with the observations described in Heikkilä [2007], Heikkilä et al. [2008]. The comparison with observed surface layer concentrations and wet deposition is more robust for ^{210}Pb than for ^{7}Be since ^{210}Pb originates from surface sources and rarely reaches the stratosphere. ^{210}Pb has a relatively long half-life with respect to radioactive decay processes (22.4 years), but a relatively short atmospheric residence time (3–5 days) due to wet deposition processes. Conversely, the ^{7}Be source is in the upper atmosphere and ^{7}Be has a shorter half-life (few months). The longer transport path from source to the cloud levels or surface, coupled with the shorter half-life, increases the uncertainty associated with comparisons between the modeled and observed deposition and surface layer concentrations for ^{7}Be. Nevertheless, Fig. 3.16 shows that both tracers are simulated reasonably in comparison with observations of deposition and surface layer concentrations. We not find any statistically significant improvement for the DIAG-FULL scheme in comparison to the CTL. This is not unexpected since as discussed in reference to Figs. 3.10 and 3.11, the surface layer concentrations and mass deposition are strongly controlled by warm cloud scavenging processes, which do not change as significantly between the various scavenging parameterizations as does the scavenging in mixed and ice phase clouds. In making these comparisons, we must also keep in mind that the

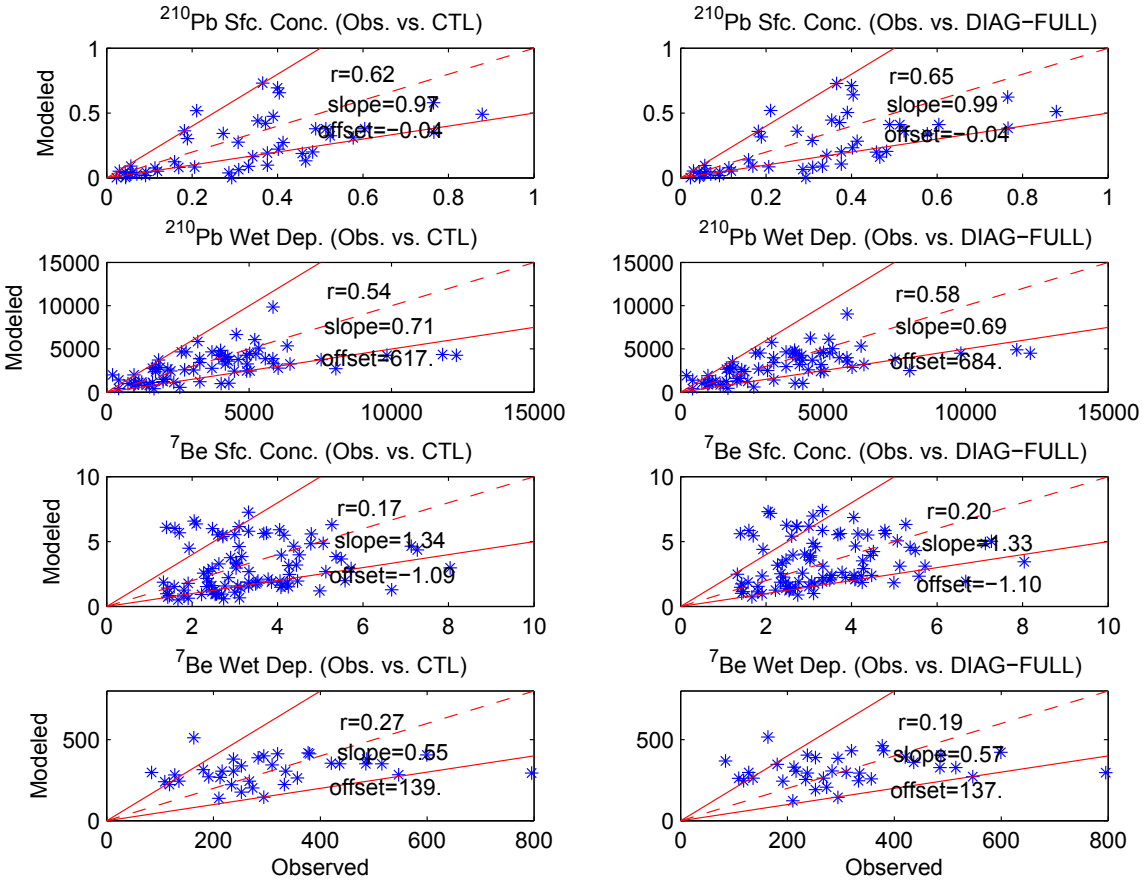

Figure 3.16: Annual mean surface layer concentrations (mBq m^{-3} at STP) and wet deposition (atoms m^{-2} s^{-1}) of ^{210}Pb and ^{7}Be from observations described in Heikkilä [2007], Heikkilä et al. [2008] compared to the simulations CTL and DIAG-FULL.

deposition observations presented do not have a global coverage as extensive as for the surface layer concentration observations. Additionally, there are uncertainties in the comparison with observations related to discrepancies between the modeled and observed meteorological conditions at the measurement sites, and the grid size of the model which does not resolve local conditions at the measurement sites. The best correlation coefficients, slope and offset parameters are for the case of ^{210}Pb surface layer concentrations. However, for both deposition and surface layer concentration, the DIAG-FULL and CTL simulations are within a factor of two of the observations at more than 75% of the sites.

Since aerosol concentrations in the middle and upper troposphere are most sensitive to differences in the parameterization of in-cloud scavenging, we present additional comparisons with observed vertical profiles of ^{210}Pb, ^{7}Be and sulfate in Figs. 3.17 and 3.18. Figure 3.17 repeats the comparisons of Liu et al. [2001] for a variety of sites in the Pacific. We have made this comparison for the same months and regions as defined in Liu et al. [2001]. Particularly for the middle latitude sites (WPML and CPML), ^{210}Pb concentrations are underestimated by the model in the middle troposphere. The new diagnostic scavenging for the simulation DIAG-FULL increases the concentrations by up to 30%, which improves the agreement. However, since these are sites that are also influenced by convective scavenging, revisions to the convective scavenging could improve the agreement further. Figure 3.18 shows that the modeled ^{210}Pb concentrations for the middle troposphere of the more northerly latitudes are most sensitive to changes to the stratiform in-cloud scavenging. There is improved agreement between the modeled annual mean, and the mean of the Kownacka [2002] multi-year (1987-1998) dataset from Poland between the altitudes of 4 and 8 km, as shown by the right hand column of Fig. 3.18. The two left hand columns of Figure 3.18 show aircraft data from the Environmental Measurement Laboratory described in detail in Heikkilä [2007]. The modeled zonal and annual mean ^{7}Be and ^{210}Pb concentrations above 15 km (shown in the two left columns) are not sensitive to the differences between our in-cloud scavenging schemes, but are shown to match well with the observations. ^{7}Be is underestimated near the tropopause as was also found by Liu et al. [2001], Koch et al. [2006], Heikkilä et al. [2008]. Figure 3.18 also

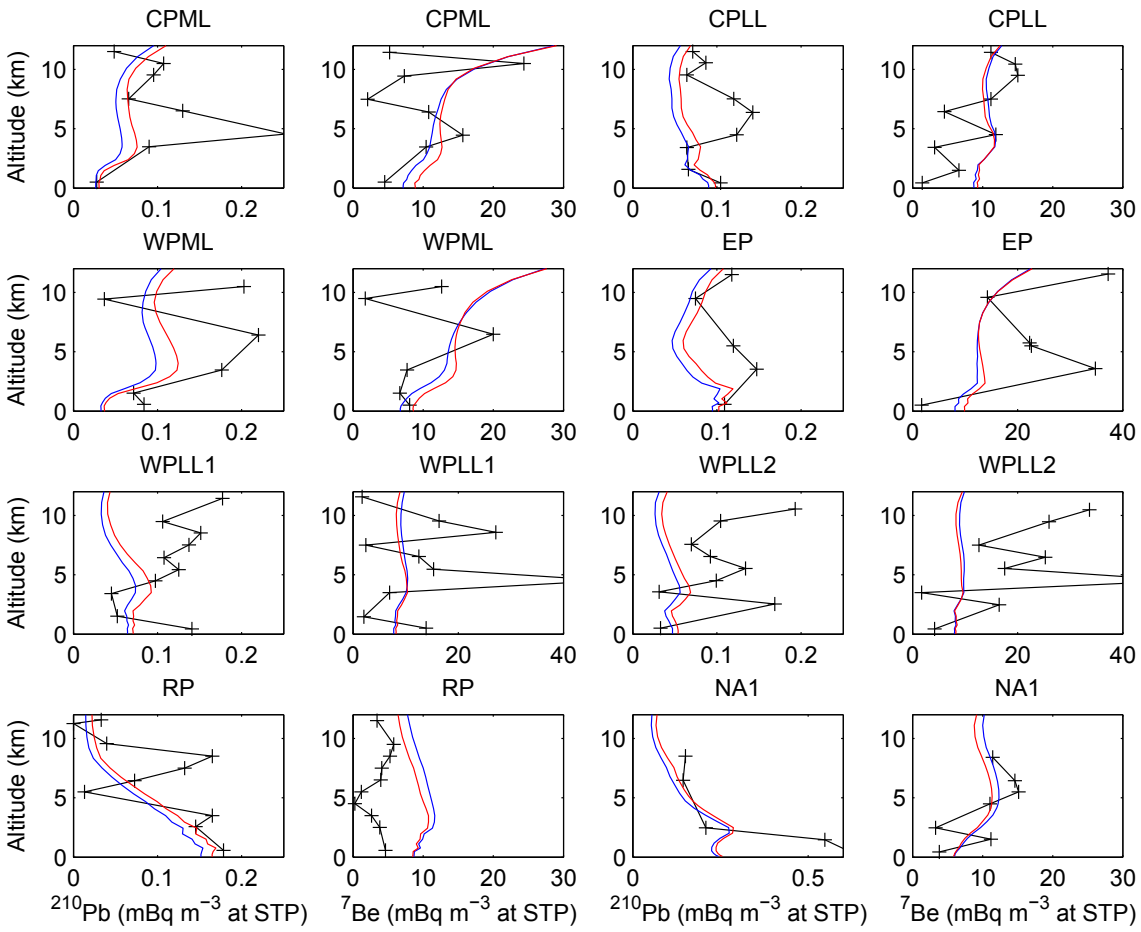

Figure 3.17: Vertical profiles of ^{210}Pb and ^{7}Be concentration (mBq m^{-3} at STP) observed by PEM-Tropics A and PEM-West B aircraft campaigns and for the same regions of the Pacific described in detail in Liu et al. [2001] and compared with simulations CTL and DIAG-FULL. PEM-Tropics A: NASA Pacific Exploratory Mission includes CPML: Central Pacific mid-latitude, WPML: West Pacific mid-latitude, CPLL: Central Pacific low latitude, WPLL: West Pacific low latitude, EP: East Pacific. PEM-West B: NASA Pacific Exploratory Mission in the western Pacific includes RP: remote Pacific, NA1: near Asia. Red: DIAG-FULL simulation, Blue: CTL simulation, Black: Observations.

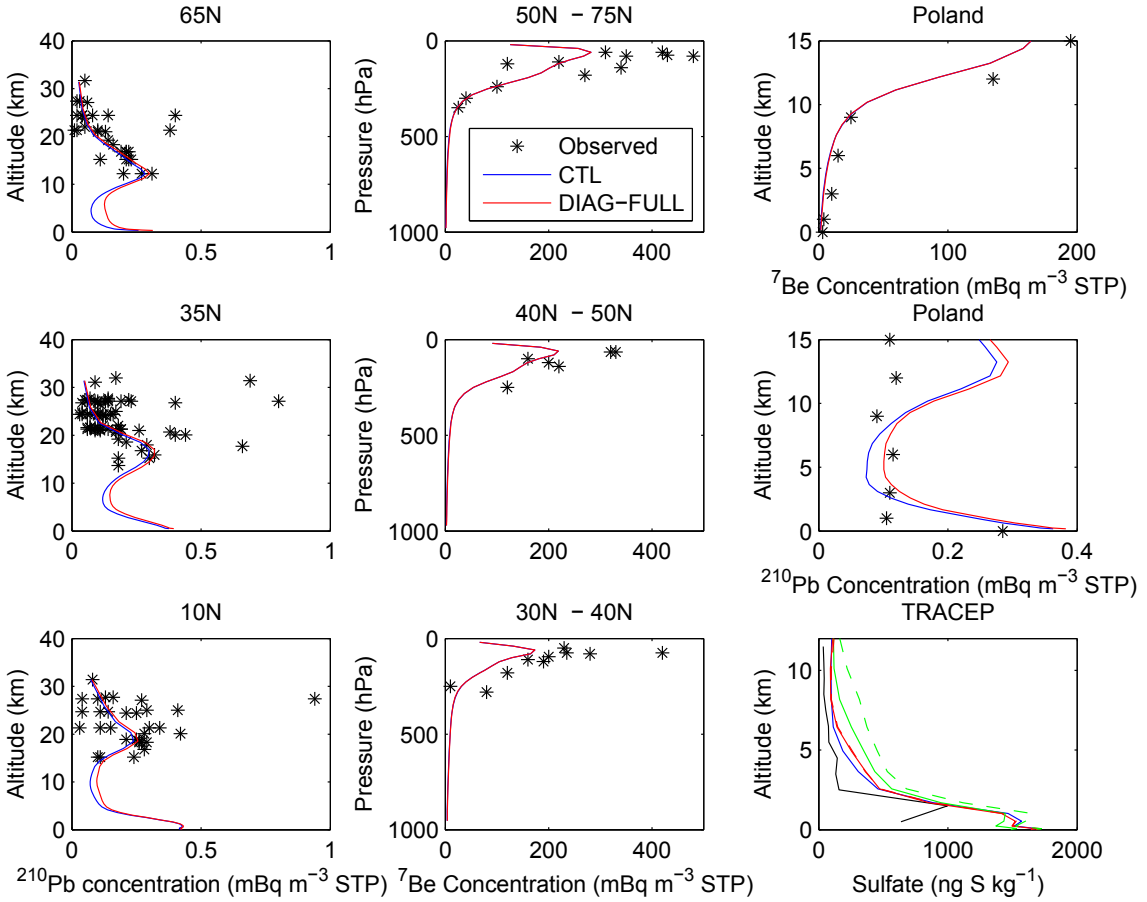

Figure 3.18: Vertical profiles of ^{210}Pb and ^{7}Be concentration (mBq m^{-3} at STP) observed by aircraft campaigns from the Environment Measurements Laboratory (EML) High Altitude Sampling Program (HASP) are shown in the two left columns, and the mean of the multi-year (1987-1998) dataset of Kownacka [2002] is shown in the right column. Modeled concentrations are zonal means for the two left columns, and for the grid box over Poland for the panels labeled Poland. The bottom right panel shows sulfate (ng kg^{-1}) observations from the TRACEP campaign (http://www-gte.larc.nasa.gov/) for March 2001 and for the region between 120 to 140 °E, and 20 to 35 °N. For TRACEP panel only: Green: PROG-AP, Dashed: DIAG-FULL-noimp and PROG-AP-noimp. Note: if DIAG-FULL overlaps CTL, only red is shown; for TRACEP, DIAG-FULL-noimp nearly overlaps DIAG-FULL.

shows a comparison with sulfate data from the TRACEP campaign of 2001. Sulfate concentrations are increased by about 50% for the PROG-AP, as compared to CTL simulation, for altitudes near 5 km. This is a smaller change than was found for black carbon profiles. While this change does not appear to be in better agreement with the observations, this does not necessarily indicate a problem with the scavenging parameterizations since SO_2 concentrations (not shown) were also similarly high in our model for this same comparison. We must be careful not to over interpret results from comparison to aircraft campaigns since the spatial and temporal averaging differs between the model and observations. However, these comparisons do illustrate that the new diagnostic scavenging parameterization for stratiform clouds works quite reasonably, and particularly at mid- and high latitudes does produce results that agree equally or better with many of the observed middle troposphere profiles.

3.6 Summary and Conclusions

A cloud nucleation scavenging scheme that diagnoses scavenging ratios for aerosol mass and number distributions based on cloud droplet and ice crystal number concentrations has been coupled with a physically detailed size-dependent in-cloud impaction scavenging parameterization, and implemented for stratiform clouds in the ECHAM5-HAM model. In the global and annual mean, the aerosol mass scavenged in stratiform clouds was found to be primarily (>90%) scavenged by nucleation processes, except for dust (50%). The aerosol number scavenged was found to be primarily (>90%) attributed to impaction processes. Scavenging in clouds with temperatures below 273 K accounted for more than 99% of this number scavenging. The majority of the aerosol number resides in the nucleation mode size range, which is too small to be scavenged by cloud nucleation processes, and is most abundant in the colder regions of the middle and upper troposphere.

Predicted aerosol concentrations, burdens and deposition have been compared between simulations that implemented the new diagnostic scheme, the prescribed scavenging fractions of the standard ECHAM5-HAM, and the prognostic aerosol cloud processing approach of Hoose et al. [2008a,b]. The prescribed fractions approach was

the least computationally expensive, but was not as physically detailed as the diagnostic and prognostic schemes, and was not able to represent the variability of scavenged fractions, particularly for submicron size particles and for mixed and ice phase clouds. As a result, the diagnostic and prognostic schemes are recommended as preferable to the prescribed fraction scheme. The global and annual mass burdens increased by up to 30% and 15%, for sea salt and dust, respectively, and the accumulation mode number burden increased by about 50%, for the prognostic scheme relative to the diagnostic scheme. Aerosol mass concentrations in the middle troposphere were increased, by up to one order of magnitude for black carbon, for the diagnostic and prognostic schemes compared to the prescribed scavenging fraction approach. Thus, uncertainties in the parameterization of in-cloud scavenging can lead to significant differences in predicted middle troposphere aerosol vertical profiles, particularly for mixed and ice phase clouds. Additionally, we recommend that the next generation of aerosol microphysical models should give careful attention to the representation of impaction processes, particularly in mixed and ice phase clouds, and for dust at all cloud temperatures. Different impaction parameterizations changed the global and annual mean stratiform dust mass removal attributed to impaction by more than two orders of magnitude, which illustrates the considerable uncertainty related to in-cloud impaction scavenging. For the prognostic scheme, exclusion of parameterized impaction increased the the global, annual accumulation mode number burden by about 60%.

In comparison with observations, the prescribed scavenging ratio scheme of the standard ECHAM5-HAM under-estimated black carbon profiles observed from aircraft by up to two orders of magnitude. The revised diagnostic and prognostic scavenging schemes improved the agreement to within one order of magnitude. This strengthens our recommendation of the diagnostic and prognostic schemes as preferable to the prescribed scavenging ratio approach. In comparison with observed profiles of ^{210}Pb, the new diagnostic scheme increased ^{210}Pb concentration by up to 30% in the middle troposphere, which improved the agreement for several mid- and high latitude sites. Comparing with observations of sulfate and ^{210}Pb wet deposition, the new diagnostic scheme was found to perform similarly to the prescribed scavenging

coefficient approach of Stier et al. [2005]. This was not unexpected since the majority of aerosol mass resides in the lower troposphere where warm clouds are most frequent. Our results show that the in-cloud scavenging parameterizations are quite similar for warm phase clouds, and for the scavenging of the accumulation and coarse aerosol modes that contain the majority of the mass. The diagnostic scheme increased the number of grid points within 25% of the observed aerosol optical depth over the oceans by 20%, as compared to the CTL simulation that also over-predicted aerosol optical depth over the oceans. For these comparisons, we have used a new aerosol optical depth climatology (2001–2006) produced from a combination of MODIS, MISR, and AERONET observations.

The prognostic aerosol cloud processing scheme used for this study does require 10 additional tracers, and thus diagnostic scavenging schemes can be desirable in global models due their relative simplicity. However, prognostic aerosol processing schemes, such that of Hoose et al. [2008a,b] are beneficial, and future work should be directed towards extending this prognostic approach to convective clouds, particularly since convective scavenging does account for about 50% of global wet scavenging. We also recommend that the more physically detailed impaction scavenging parameterization of the diagnostic scheme should be coupled with the prognostic cloud processing scheme. Since the global annual mean sulfate mass burdens increased by 10% for the diagnostic scheme when the mass and number nucleation scavenging ratios were equated, as opposed to determined separately, we recommend that the prognostic scheme should be developed to implement separate nucleation scavenging ratios for aerosol number and mass.

Finally, in a more general sense future work should be directed towards examining the influence of these uncertainties in the parameterization of in-cloud scavenging on the aerosol direct and indirect effects upon the climate system, particularly given the sensitivity of the predicted middle and upper tropospheric aerosol concentrations to the in-cloud scavenging parameterization. Additionally, efforts should be ongoing to improve understanding of the impaction scavenging process, particularly in clouds with temperatures below 273 K. This is relevant since aerosol number scavenging in stratiform clouds was found to be primarily attributed to the impaction process in

mixed and ice phase clouds, and dust mass scavenging in stratiform clouds was found to be attributed equally to nucleation and impaction scavenging processes.

3.7 Acknowledgements

The authors are grateful to the National Science and Engineering Research Council of Canada and Killam Trusts Foundation of Canada for financial support. We thank D. Koch, and the following groups associated with providing aircraft data: NOAA at UC Boulder (David Fahey), University of Tokyo (Y. Kondo), and University of Hawaii (T. Clarke). Thanks also to CSCS for computing time.

Chapter 4

Aerosol Processing in Convective and Stratiform Clouds in ECHAM5-HAM

B. Croft, U. Lohmann, R. V. Martin, C. Hoose, and P. Stier

Publication Status: Under preparation, and not yet submitted.
All text, figures, tables, and presented results were contributed by the first author, B. Croft, with the exception of observational data (sources are referenced in the text).

4.1 Abstract

A physically detailed representation of aerosol processing by convective clouds is introduced into the ECHAM5-HAM model, and coupled with a stratiform aerosol processing scheme. Based on the modeled cloud microphysics, this scheme explicitly represents the processes of nucleation and collision scavenging that incorporate aerosols into cloud droplets and crystals, aerosol-aerosol coagulation within the droplets and crystals, as well as evaporation and precipitation processes that remove aerosols from the in-droplet and in-crystal phases. In the global and annual mean, an aerosol undergoes 0.4 to 1 cloud cycles before being removed in our simulations. The number of cycles is greater (1 to 3 times) for smaller aerosols, such as sulfate and carbonaceous aerosols. Considering the global and annual mean evaporation and source rates, convective and stratiform clouds contribute about equally to the global, annual mean aerosol processing. Aerosol concentrations, burdens, and optical depth are strongly sensitive to the representation of cloud processing in ECHAM5-HAM, and increase by a factor of 3-5 for the coupled convective-stratiform scheme. Relative to satellite observations of aerosol optical depth, these increases are excessive by at least a factor of 2. The global, annual mean aerosol optical depth is also highly sensitive to the representation of sea salt emissions, and in-cloud impaction scavenging for these

aerosol processing simulations. Revisions to these later two processes yield a global, annual optical depth that is about 0.9 of the satellite retrieval for the aerosol processing simulations. However, the role of impaction scavenging could be over-estimated if nucleation scavenging is under-estimated in our model. Particularly, the method for apportioning the number of activated aerosols between the soluble/internally mixed modes should be re-examined in future studies since the nucleation scavenging for the accumulation and coarse modes could be under-estimated. Global and annual mean aerosol wet deposition is attributed primarily to stratiform (about 70-80%), as opposed to convective precipitation. The majority of this wet deposition is related to scavenging in the warm, and mixed phase clouds, about 70% and 30%, respectively. The observed marine boundary layer accumulation mode size distribution is more closely represented with the implementation of the coupled convective-stratiform aerosol processing scheme as compared to the standard ECHAM5-HAM, or with the stratiform aerosol processing alone. Vertically integrated aerosol size distributions for the coupled aerosol processing scheme agree more closely with AERONET observations than for the standard ECHAM5-HAM. However, the volume median accumulation mode wet radius is slightly over-predicted for all simulations.

4.2 Introduction

Aerosols have important impacts on the Earth's global climate system: 1) directly since they absorb and reflect radiation, and 2) indirectly since they modify cloud properties by acting as cloud condensation and ice nuclei [Twomey, 1991, Charlson et al., 1992, Lohmann and Feichter, 2005]. Conversely, clouds also modify aerosol concentrations, size distributions, and hygroscopicity [Hoose et al., 2008a,b, Croft et al., 2010]. Global climate models (GCMs) and chemical transport models (CTMs) must represent these processes correctly in order to predict accurate three-dimensional aerosol distributions. However, the Intergovernmental Panel on Climate Change [Forster et al., 2007] has identified that the full range of processes related to the modification of cloud properties by aerosols are not well understood. They are a key uncertainty in our understanding of climate change.

This study focuses on the physical processing of aerosols by both stratiform and

convective clouds. We consider how the explicit representation of these processes in a GCM can change the predicted aerosol size distributions and burdens, which in turn influence cloud properties. Recently, Hoose et al. [2008a,b] implemented a stratiform aerosol processing scheme in the ECHAM5-HAM model, but that study did not consider convective clouds. Hoose et al. [2008a] showed that the predicted global and annual mean number of accumulation mode aerosols was enhanced by about two-fold following the explicit representation of cloud processing in stratiform clouds. Since Lohmann [2008] introduced a double-moment convective cloud microphysics scheme in the ECHAM5-HAM GCM, we can now extend the cloud processing approach of Hoose et al. [2008a,b] to convective clouds using this model. In this study, we examine the relative importance of convective and stratiform clouds in the processing of aerosols from a global perspective.

Aerosol cloud processing refers to a set of processes by which aerosols are taken up into, or formed in cloud droplets and ice crystals, transferred between droplets and crystals, and ultimately either released back to the atmosphere by evaporation of clouds and precipitation, or removed from the atmosphere by precipitation. A larger fraction of the cloud droplets and ice crystals evaporate as opposed to forming precipitation. Pruppacher and Jaenicke [1995] estimated that an aerosol sampled in a location remote to the source has undergone three cloud cycles. Our study will use the ECHAM5-HAM GCM to quantify the annual and global mean cloud cycling of aerosols.

Aerosols are taken up into clouds either 1) by acting as cloud condensation and ice nuclei, or 2) by colliding with droplets and crystals. Thus, each droplet or crystal may take up more than one interstitial aerosol particle. When the droplets or crystals evaporate, assuming each droplet or crystal releases only one internally mixed aerosol, the resultant aerosols can be larger in size, less numerous, and insoluble aerosols can be coated with a soluble layer. Crumeyrolle et al. [2008] presented observations of ratios of cloud condensation nuclei (CCN) to condensation nuclei (CN) and showed that following the passage of a convective system, the CCN/CN ratio was increased, despite the overall reduction in CN. Thus, cloud processing internally mixes aerosols, and increases the relative number of aerosols that are able to act as cloud condensation

or ice nuclei.

Global models account for the influences of clouds on aerosol size distributions with varying approaches. Most global models include some representation of the processes of sulfate formation within cloud droplets [Barth et al., 2000, Adams and Seinfeld, 2002, Park et al., 2005, Stier et al., 2005, Gong et al., 2006, Roelefs et al., 2006]. The mass produced in the aqueous phase is typically treated as additional mass in the accumulation or coarse modes. The formation of organic aerosol, although likely an important source, is not well represented in the current generation of global models [Blando and Turpin, 2000, Kanakidou et al., 2005, Kroll and Seinfeld, 2008, Hallquist et al., 2009]. The number of global models that treat in-cloud aerosols as additional tracers is limited and includes, the Hadley Center climate model (HADAM4) [Jones et al., 2001], the Goddard Institute for Space Studies (GISS) ModelE [Koch et al., 2006], the Model for Integrated Research on Atmospheric Global Exchanges (MIRAGE) modeling system [Easter et al., 2004], and the ECHAM5-HAM GCM [Hoose et al., 2008a,b].

The ECHAM5-HAM GCM stratiform aerosol processing scheme [Hoose et al., 2008b] is unique in that aerosol mass in the liquid and ice hydrometeors is considered separately. Also, the influence of aerosol processing on aerosol size is treated explicitly since the scheme is coupled to the Hamburg Aerosol Module (HAM) scheme of Stier et al. [2005]. In this model, cloud droplet number concentration depends on the number and size of the available aerosol particles, and heterogeneous freezing is parameterized as a function of aerosol chemical composition and mixing state [Lohmann et al., 2007, 2008, Lohmann, 2008]. The double-moment convective cloud microphysics scheme in the ECHAM5-HAM model used for this study considers both the liquid and ice phase. Likewise our convective aerosol processing scheme includes an explicit representation of the aerosol mass in both liquid and ice hydrometeors, and considers the influence of convective cloud processing on aerosol size. Section 4.3 gives an overview of our model including the convective aerosol processing scheme. Section 4.4 summarizes the results from global simulations, and examines the impacts of aerosol processing on three-dimensional aerosol distributions, as well as mass and

number burdens, and aerosol optical depth. Section 4.5 presents comparisons with observations, including size distributions from a sun photometer network (AERONET). Section 4.6 gives the summary and outlook.

4.3 Model Description

The global climate model (GCM) used in this study is the ECHAM5, which is the fifth generation atmospheric general circulation model (GCM) developed at the Max-Planck Institute for Meteorology [Roeckner et al., 2003], and evolved from the model of the European Centre for Medium Range Weather Forecasting (ECMWF). The model solves prognostic equations for vorticity, divergence, temperature and surface pressure using spheric harmonics with triangular truncation. Water vapor, cloud liquid and ice water are transported using a semi-Lagrangian scheme [Lin and Rood, 1996]. The solar radiation scheme has 6 spectral bands [Cagnazzo et al., 2007] and the infrared has 16 spectral bands [Mlawer et al., 1997, Morcrette et al., 1998].

The GCM is coupled to the Hamburg Aerosol Model (HAM), which is described in detail in Stier et al. [2005]. The five aerosol species (sulfate, black carbon, particulate organic matter, sea salt and dust) are represented by seven log-normal modes: 4 internally mixed/soluble modes (nucleation (NS), Aitken (KS), accumulation (AS), and coarse (CS)), and 3 insoluble modes (Aitken (KI), accumulation (AI), and coarse (CI)). The count median radius for each mode is calculated from the aerosol mass and number concentrations of each mode, which are allowed to vary independently, and with a fixed standard deviation for each mode. Aerosol mass and number are transferred from the insoluble modes to the internally mixed/soluble modes depending on the processes of sulfate condensation, and coagulation with other internally mixed/soluble aerosols. Table 4.1 illustrates the modal set-up. The natural emissions of sea salt, dust, and DMS (dimethyl sulfide) from the oceans are calculated on-line, based on the meteorology of the model. Emissions for all other aerosol species are taken from the AEROCOM emission inventory, and are representative for the year 2000 [Dentener et al., 2006b]. The aerosol emissions and the removal processes of sedimentation, and dry deposition are described in detail in Stier et al. [2005].

For this study, the below-cloud scavenging parameterization of Croft et al. [2009]

Table 4.1: The modal structure of the Hamburg Aerosol Module (HAM). N_i is the aerosol number of the mode i, and M_i^j is the mass of the j^{th} compound in mode i. The ranges for $\overline{r}$ are the aerosol sizes included in each respective mode.

Modes $\overline{r}$ [μm]	Soluble/Mixed	Insoluble
Nucleation		
$\overline{r}$ 0.005	N_1,M_1^{SU}	
Aitken		
$0.005 < \overline{r} \leq 0.05$	N_2,M_2^{SU},M_2^{BC},M_2^{POM}	N_5,M_5^{BC},M_5^{POM}
Accumulation		
$0.05 < \overline{r} \leq 0.5$	N_3,M_3^{SU},M_3^{BC},M_3^{POM},M_3^{SS},M_3^{DU}	N_6,M_6^{DU}
Accumulation		
$0.5 < \overline{r}$	N_4,M_4^{SU},M_4^{BC},M_4^{POM},M_4^{SS},M_4^{DU}	N_7,M_7^{DU}

has been implemented for all simulations. This physically detailed below-cloud impaction scavenging parameterization uses look-up tables to select scavenging coefficients that represent the collection of aerosols by rain and snow below clouds based on aerosol size and precipitation rates. This scheme gives more vigorous below-cloud scavenging than for the prescribed coefficient scheme of the standard ECHAM5-HAM model. One additional modification to the standard model is the use of a kappa-Köhler water uptake scheme to represent aerosol wet size for all our simulations. This follows the approach of Petters and Kreidenweis [2007]. Growth factors are in a look-up table as a function of the relative humidity, particle size, a composite hygroscopicity parameter (kappa), and temperature.

Additionally, for this study we have implemented the prognostic equations for cloud liquid and ice water, mass and number for both stratiform and convective clouds following Lohmann et al. [2007], and Lohmann [2008], and the cirrus scheme of Lohmann and Kärcher [2002]. Cloud water detrainment in the upper part of the convective updrafts is used as a source term in the stratiform cloud water equations. Convective clouds and transport are based on the mass-flux scheme of Tiedtke [1989] with modifications following Nordeng [1994]. All results presented in this study are from a one year simulation, following a three months spin-up period, and are nudged to the meteorological conditions of the year 2001. We chose to use the nudging

technique to keep the sea salt and dust emissions the same between simulations.

4.3.1 Convective Aerosol Processing Scheme

The new convective aerosol processing scheme explicitly represents the following mass transfer processes: 1) aerosol uptake into cloud droplets and ice crystals by both nucleation and collision processes, 2) aerosol transfer from droplets to crystals by freezing, 3) aerosol release from droplets by evaporation (including the Bergeron-Findeisen process), from crystals by sublimation, and from precipitation due to below-cloud evaporation, and 4) aerosol removal from the atmosphere by wet deposition. In our model, the lifetime of the convective clouds is one time-step (30 minutes). This may be a reasonable approximation since the life cycle of shallow cumulus and cumulonimbus clouds is about 30-60 minutes [Gambheer and Bhat, 2000, Zhao and Austin, 2005]. However, meso-scale convective systems can persist for longer (about one day) [Chen and Houze, 1997], but those clouds do not dominate the global population of convective clouds. Additionally, we account for longer lived convective clouds through the process of detrainment. The convective microphysics in the version of ECHAM5-HAM that we used for our simulations explicitly includes the detrainment of the cloud droplet and ice crystal number concentration from convective clouds as a source for stratiform clouds. As described in Lohmann [2008], when the clouds are detraining, and the cloud droplet or ice crystal number concentration from the convective clouds exceeds the respective number concentration in stratiform clouds, then the difference is added to the respective number concentration for the stratiform clouds.

We account for aerosol release to the atmosphere by droplet evaporation, and crystal sublimation as the convective clouds collapse after each time-step. The in-droplet and in-crystal aerosol masses are released to either of the three soluble/internally mixed aerosol modes (Aitken, accumulation, and coarse). The convective in-droplet and in-crystal aerosol masses for the five aerosol species are treated as ten additional temporary variables, which are not carried between model time-steps since the lifetime of the convective clouds is one time-step. The microphysics inside convective clouds are only calculated in the rising updrafts. Therefore, we consider only the aerosol mass that is in the convective updrafts for the convective aerosol processing

Table 4.2: In-cloud impaction scavenging kernels (m^3 s^{-1}) for aerosol-droplet, and aerosol-ice crystal collisions for each of the seven log-normal modes of the ECHAM5-HAM, following Hoose et al. [2008a,b] and assuming monodisperse droplets and crystals of radius 10 μm, and 15 μm, respectively. Last column shows enhanced scavenging kernels for evaporating droplets from a sensitivity test of Hoose et al. [2008a].

Mode	Droplets	Crystals	Droplets (sensitivity test)
Nucleation Soluble (NS)	2.5 x 10^{-12}	5.0 x 10^{-11}	3.0 x 10^{-12}
Aitken Soluble (KS)	2.5 x 10^{-12}	5.0 x 10^{-11}	3.0 x 10^{-12}
Accumulation Soluble (AS)	2.0 x 10^{-14}	2.0 x 10^{-12}	4.0 x 10^{-10}
Coarse Soluble (CS)	0.0	2.0 x 10^{-13}	2.0 x 10^{-10}
Aitken Insoluble (KI)	2.5 x 10^{-12}	5.0 x 10^{-11}	3.0 x 10^{-12}
Accumulation Insoluble (AI)	2.0 x 10^{-14}	2.0 x 10^{-12}	4.0 x 10^{-10}
Coarse Insoluble (CI)	0.0	2.0 x 10^{-13}	2.0 x 10^{-10}

scheme.

For the convective clouds, the activation of aerosols follows the Ghan et al. [1993] scheme. The number of activated aerosols $N_{\mathrm{act,Ghan}}$ is given by

$$N_{\mathrm{act,Ghan}} = \frac{\omega N_{>25nm}}{\omega + \beta N_{>25nm}} \tag{4.1}$$

and

$$\omega = \bar{\omega} + 0.7\sqrt{\mathrm{TKE}} + 2\sqrt{\mathrm{CAPE}}\,. \tag{4.2}$$

ω is the updraft velocity, $\bar{\omega}$ is the large-scale vertical velocity, TKE is the turbulent kinetic energy, CAPE is the convective available potential energy, β is 0.0034 $\mathrm{cm^4\,s^{-1}}$, and $\mathrm{N}_{>25nm}$ is the total number of soluble/internally mixed aerosols with wet radii >25 nm. This is similar to the treatment of aerosol activation in stratiform clouds except that the term for CAPE has been added following Lohmann [2008]. Also, for stratiform clouds only soluble/internally mixed aerosols larger than 35 nm participate in the activation. For the convective clouds, updraft velocities are larger, and so smaller aerosols may potentially be activated. The total number of activated aerosols is apportioned between the modes based on the fractional contribution of each mode to the total number of soluble/internally mixed aerosols larger than 25 and 35 nm, for the convective and stratiform clouds, respectively.

For the convective cloud microphysics scheme, ice crystals are formed only by the freezing of cloud droplets. We include heterogeneous contact and immersion

freezing in our model. Supercooled cloud droplets can exist down to temperatures of -35 °C in the model. This is similar to the treatment for stratiform clouds as described in Lohmann et al. [2007, 2008]. When the convective cloud droplets freeze, the convective in-droplet aerosol mass is transferred to the in-crystal aerosol mass variables. The melting of ice crystals to form droplets is not included for convective clouds due to the short lifetime of the convective clouds. Aerosol mass is also taken up into the convective droplets and crystals by the process of collisions between aerosols and the cloud hydrometeors. The collection kernels of Hoose et al. [2008b] are used to represent the collection rates. These are summarized in Table 4.2. We remove a calculated fraction of the aerosol mass from the droplets and crystals to account for precipitation scavenging based on the rates of autoconversion, accretion and aggregation. Following these processes, the remainder of the in-droplet and in-crystal aerosol mass is released to the atmosphere by evaporation or sublimation. We assume that each droplet (crystal) that evaporates (sublimates) releases one aerosol particle. Depending on the size of the released aerosols, this aerosol mass and number is added to either of the three largest soluble/internally mixed aerosol modes (KS, AS, CS).

In summary, the aerosol mass transfer processes related to cloud droplets for the convective aerosol processing scheme are

$$\begin{aligned}\frac{dm_{x,CDCV}}{dt} &= \sum_{j=1}^{4} \frac{m_{x,j}}{N_j} \frac{N_{act,j}}{\sum_{k=1}^{4} N_{act,k}} \overline{Q}_{nuc} \\ &\quad - \frac{m_{x,CDCV}}{N_l} (\overline{Q}_{frz} + \overline{Q}_{BFevap}) + \sum_{j=1}^{7} \frac{m_{x,j}}{N_j} \overline{Q}_{coll,j} \\ &\quad - \frac{m_{x,CDCV}}{q_l} \overline{Q}_{rain} - \frac{m_{x,CDCV}}{N_l} \overline{Q}_{evap} \end{aligned} \tag{4.3}$$

where $m_{x,CDCV}$ is the aerosol mass for each of the aerosol species x = SO4, BC, POM, SS, DU contained in the convective cloud droplets. $\overline{Q}_{nuc}$ is the rate of formation of convective cloud droplets by nucleation, $\overline{Q}_{frz}$ is the rate of droplet freezing, $\overline{Q}_{BFevap}$ is the rate of cloud droplet evaporation due to the Bergeron-Findeisen process, $\overline{Q}_{rain}$ is the rate of rain formation, and $\overline{Q}_{coll,j}$ is the rate that droplets take up aerosol mass by collision processes. $\overline{Q}_{evap}$ is the cloud evaporation rate. At each

time-step, we assume that the convective clouds evaporate to release all in-droplet and in-crystal mass after all of the other processes are taken into account. N_j is the aerosol number, and the index j runs from 1 to 7 for the modes NS, KS, AS, CS, KI, AI, and CI. $N_{act,j}$ is the number of activated aerosols for each of the soluble/internally mixed modes, and $\sum_{k=1}^{4} N_{act,k}$ is the number of activated aerosols summed over all of the soluble/internally mixed modes. q_l is the cloud liquid water content and N_l is the cloud droplet number concentration. This is quite similar to the stratiform aerosol cloud processing scheme of Hoose et al. [2008a,b]. However, unlike for the convective scheme, the stratiform in-droplet and in-crystal aerosol masses are treated as additional prognostic tracers that are carried between model time-steps, and the additional processes of transport, and melting are included. This treatment is possible since the stratiform cloud droplet number and liquid and ice water content are prognostic species in the model, unlike for convective clouds. Also, our model does not yet account for the in-cloud production of sulfate for convective clouds due to the short time-scale, whereas this process is included for stratiform clouds.

The processes related to ice crystals for the convective aerosol processing scheme are

$$\frac{dm_{x,ICCV}}{dt} = \frac{m_{x,ICCV}}{N_l}\overline{Q}_{frz} + \sum_{j=1}^{7} \frac{m_{x,j}}{N_j}\overline{Q}_{colli,j} - \frac{m_{x,ICCV}}{q_i}\overline{Q}_{snow} - \frac{m_{x,ICCV}}{N_i}\overline{Q}_{sub} \quad (4.4)$$

where $m_{x,ICCV}$ is the aerosol mass for each of the aerosol species x = SO4, BC, POM, SS, DU contained in the convective ice crystals. Q_{snow} is the rate of snow formation, $\overline{Q}_{colli,j}$ is the rate that crystals take up aerosol mass by collision processes, and $\overline{Q}_{sub}$ is the rate of sublimation. q_i is the cloud ice water content and N_i the ice crystal number concentration. Since the convective clouds collapse after each time-step, $\frac{dm_{x,CDCV}}{dt}$ and $\frac{dm_{x,ICCV}}{dt}$ equal zero in our model.

A detailed description of the stratiform aerosol processing scheme is given in Hoose et al. [2008a,b]. We have used this scheme for the stratiform clouds with one modification. In the original Hoose et al. [2008b] scheme, the nucleation rate terms included those droplets and crystals that originated from convective anvil detrainment. For

our simulations we have treated the detrainment rate as a separate term for the stratiform in-droplet and in-crystal tracers. Thus, we can explicitly diagnose the influence of detrainment on the stratiform in-droplet and in-crystal aerosol masses.

4.3.2 Summary of Simulations

Table 4.3 summarizes the simulations that were conducted for this study. All simulations are conducted with the ECHAM5-HAM GCM, and implement the double-moment cloud microphysics for both stratiform and convective clouds as presented by Lohmann et al. [2007], and Lohmann [2008]. The model is tuned to have top of atmosphere radiation balance for simulation NOAP. There is no re-tuning for any of the subsequent simulations in order to isolate the influence of our revisions. Simulation NOAP is a control simulation with neither the stratiform, nor the convective aerosol processing included. Simulation SAP has only the stratiform aerosol processing of Hoose et al. [2008a,b]. Simulation CVAP+SAP includes the new convective aerosol processing scheme, as well as the stratiform aerosol processing.

We present two additional sensitivity simulations. Previous evaluations of the stratiform aerosol processing scheme of ECHAM5-HAM versus AERONET have revealed large biases over the ocean sites [Hoose et al., 2008a, Croft et al., 2010]. Simulation CVAP+SAP+ss is the same as CVAP+SAP but includes a revised sea salt parameterization following Jaeglé et al. [2010]. This revision is also used for simulation CVAP+SAP+ss+imp. For these simulations, the sea salt source function in units of particles m^{-2} s^{-1} μm^{-1} is given as

$$\frac{dF}{dr_{80}} = (0.3 + 0.1T - 0.0076T^2 + 0.00021T^3)1.373u_{10m}^{3.41}r_{80}^{-A}(1 + 0.057r_{80}^{3.45})10^{1.607e^{-B^2}} \tag{4.5}$$

where T is the sea surface temperature in °C, u_{10m} is the 10 m wind speed, r_{80} is the particle radius at 80% relative humidity, and A and B are given below.

$$A = 4.7(1 + \theta r_{80})^{-0.017r_{80}^{1.44}} \tag{4.6}$$

and

$$B = \frac{0.433 - log_{10}(r_{80})}{0.433} \tag{4.7}$$

where θ is an adjustable parameter, which is assumed to be 30, following Gong et al. [2003]. For the other simulations, the sea salt source function follows that described in Schultz et al. [2004]. The notable difference between the source functions for simulations CVAP+SAP+ss, and CVAP+SAP+ss+imp relative to the other simulations is that the global and annual mean number of emitted accumulation and coarse mode aerosols is reduced by factors of 0.65 and 0.07, respectively. Additionally, the temperature dependence of sea salt emissions is included. This results in lower sea salt emissions for lower sea surface temperatures, by up to 30%.

Simulation CVAP+SAP+ss+imp includes a change to the assumptions about in-cloud impaction scavenging. The aerosol-droplet collection kernels of Hoose et al. [2008b] are relatively low as compared to the collection kernels presented in Croft et al. [2010]. Croft et al. [2010] assumed that the cloud droplets follow a gamma distribution, as opposed to being monodisperse, and did not neglect the influence of particle inertia on impaction scavenging. This gave non-zero impaction scavenging kernels for the coarse mode. For the simulation CVAP+SAP+ss+imp, we use enhanced collection kernels for cloud droplets. These values are taken from a sensitivity test of Hoose et al. [2008a] for evaporating droplets, and are shown in Table 4.2. Wang et al. [2010] showed for below-cloud impaction scavenging, there are considerable uncertainties related the parameterization of impaction scavenging processes. Our sensitivity simulation allows us to examine how the global aerosol burdens, concentrations and size distributions are influenced by the assumptions about the in-cloud impaction scavenging processes.

4.4 Results of Global Simulations

4.4.1 Aerosol Mass Transfer Processes

Figures 4.1 - 4.5 show the zonal and annual mean mass transfer rates, into and out of the interstitial, in-droplet, and in-crystal phases, for each of the five aerosol species for the simulation CVAP+SAP+ss. The results for simulation CVAP+SAP are very similar (not shown). A similar analysis was presented by Hoose et al. [2008a], but for stratiform clouds only. These figures highlight the importance of evaporation

Table 4.3: The simulations presented in this study are summarized in this table.

Simulation	Description
NOAP	Control simulation of ECHAM5-HAM GCM without aerosol processing
SAP	Stratiform aerosol processing of Hoose et al. [2008a,b] implemented
CVAP+SAP	Convective aerosol processing coupled with the stratiform processing
CVAP+SAP+ss	Same as CVAP+SAP but with revised sea salt emissions following Jaeglé et al. [2010]
CVAP+SAP+ss+imp	Same as CVAP+SAP+ss but with revised assumptions about impaction scavenging

processes related to both clouds and precipitation. For all aerosol species the zonal mean evaporation rates in the tropics and mid-latitudes exceed the wet deposition rates, by up to an order of magnitude. The only exception is for convective in-crystal particulate organic matter.

Similar to the finding of Hoose et al. [2008a], for sulfate (Fig. 4.1) the rate of aerosol release to the interstitial phase by stratiform cloud evaporation exceeds the combined rate of emission and interstitial production by up to a factor of 3 for the mid-latitude Northern Hemisphere. At those same latitudes, sulfate production rates in stratiform cloud droplets exceed the rate of uptake by both nucleation and collision processes by up to a factor of three. For simulation CVAP+SAP+ss, droplet nucleation is the dominant process for taking aerosol mass into convective cloud droplets, by up to an order of magnitude. Sulfate mass leaves droplets by either wet deposition or cloud/precipitation evaporation. For both stratiform and convective clouds, the zonal and annual mean evaporation rates exceed the wet deposition rates, by up to five times for the convective droplets. For all aerosol species, uptake into ice crystals is primarily by collisions, exceeding freezing by an order of magnitude. Freezing of droplets is relatively more important for dust and sea salt in convective clouds but is still not more than half of the collision uptake rate. This differs from the findings of Hoose et al. [2008a] that aerosol uptake into stratiform crystals by collision processes was a relatively minor mass transfer process. However, for our simulations we have

used a more recent ECHAM5-HAM model version coupled with the cirrus scheme of Lohmann and Kärcher [2002], Lohmann et al. [2008], which contributes to this difference. For our simulations, detrainment contributes negligible amounts to the uptake of aerosol mass into stratiform droplets and crystals.

Figures 4.2 and 4.3 show that for black carbon (BC) and particulate organic matter (POM), the rates of aerosol mass uptake into droplets for collision processes about equal those for nucleation processes. Carbonaceous aerosols can be smaller, and exist partially in the insoluble aerosol modes, which makes uptake by nucleation processes relatively less important than for the larger and more soluble aerosols. Carbonaceous aerosols, similar to dust, have a considerable portion of their total emissions in the tropics where convective clouds are more prevalent. As a result, the uptake rates of these aerosols into stratiform and convective cloud droplets are roughly equivalent, unlike for sulfate and sea salt that have a convective uptake rate that is roughly half of the stratiform uptake. Unlike the other aerosols species, for the carbonaceous aerosols, the rates of aerosol release by evaporation from convective clouds in the tropics exceed those for stratiform clouds by up to a factor of three, and about equal the rate of emissions. Recent work by Heald et al. [2010] suggests that organic aerosol emissions are likely under-estimated. Implementation of an enhanced organic source, particularly for secondary production, could change these budgets. If the mid-latitude organics source was increased, then the relative importance of stratiform processing of organics would be increased as compared to our current simulations.

Figures 4.2 and 4.3 also show that for carbonaceous aerosols the transfer rates into, and out of the in-crystal phase are larger for the stratiform as compared to the convective clouds. For these aerosols, the uptake into the stratiform in-crystal phase relative to the stratiform in-droplet phase is the largest among all aerosol species, but uptake into the crystal phase is still only half of that for the in-droplet phase.

Fig. 4.4 shows the mass transfer rates for dust for the simulation CVAP+SAP+ss. Dust emissions are characterized by strong emission peaks in narrow latitude bands. Below-cloud scavenging is relatively more important for removal of dust from the interstitial phase as opposed to uptake into clouds, by more than a factor of five at northern mid-latitudes. Nucleation is the dominant process for transfer of aerosol

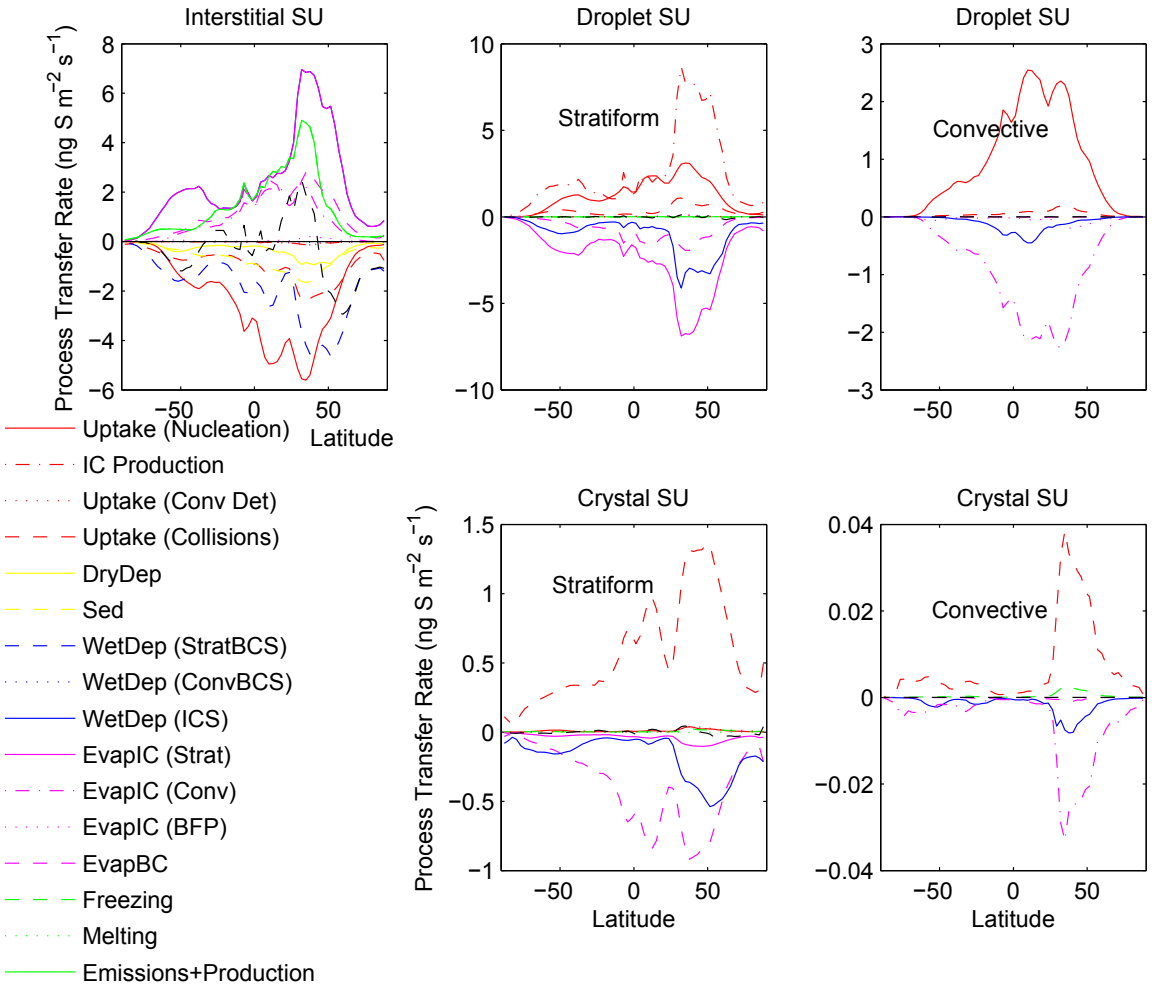

Figure 4.1: The zonal and annual mean sulfate (SU) mass transfer rates (ng S m^{-2} s^{-1}) into (positive) and out of (negative) the interstitial, in-droplet and in-crystal phases for both stratiform and convective clouds for the simulation CVAP+SAP+ss. See Table 4.3 for a description of the simulations. Note: Black dashed line is residual.

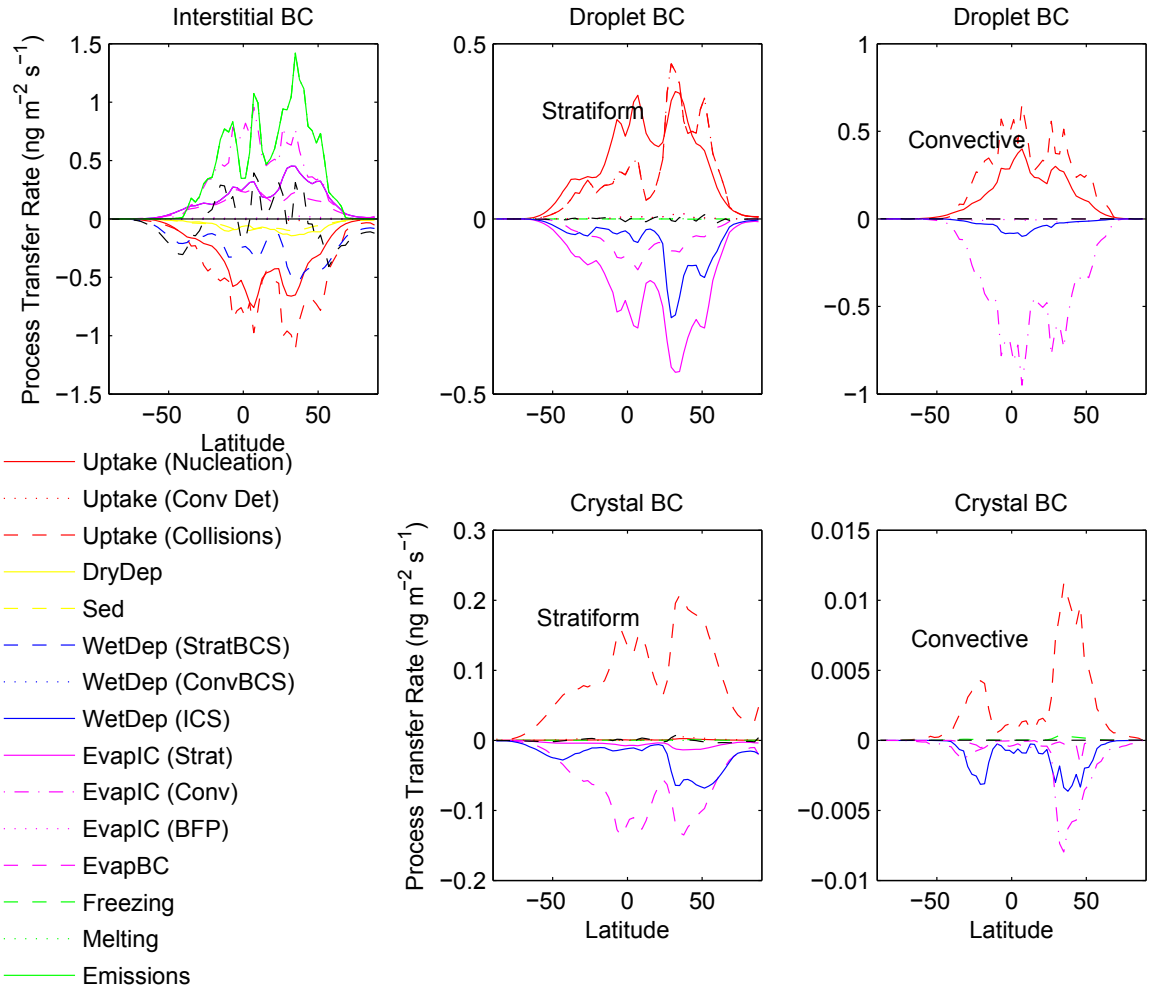

Figure 4.2: The zonal and annual mean black carbon (BC) mass transfer rates (ng m^{-2} s^{-1}) into (positive) and out of (negative) the interstitial, in-droplet and in-crystal phases for both stratiform and convective clouds for the simulation CVAP+SAP+ss. Note: Black dashed line is residual.

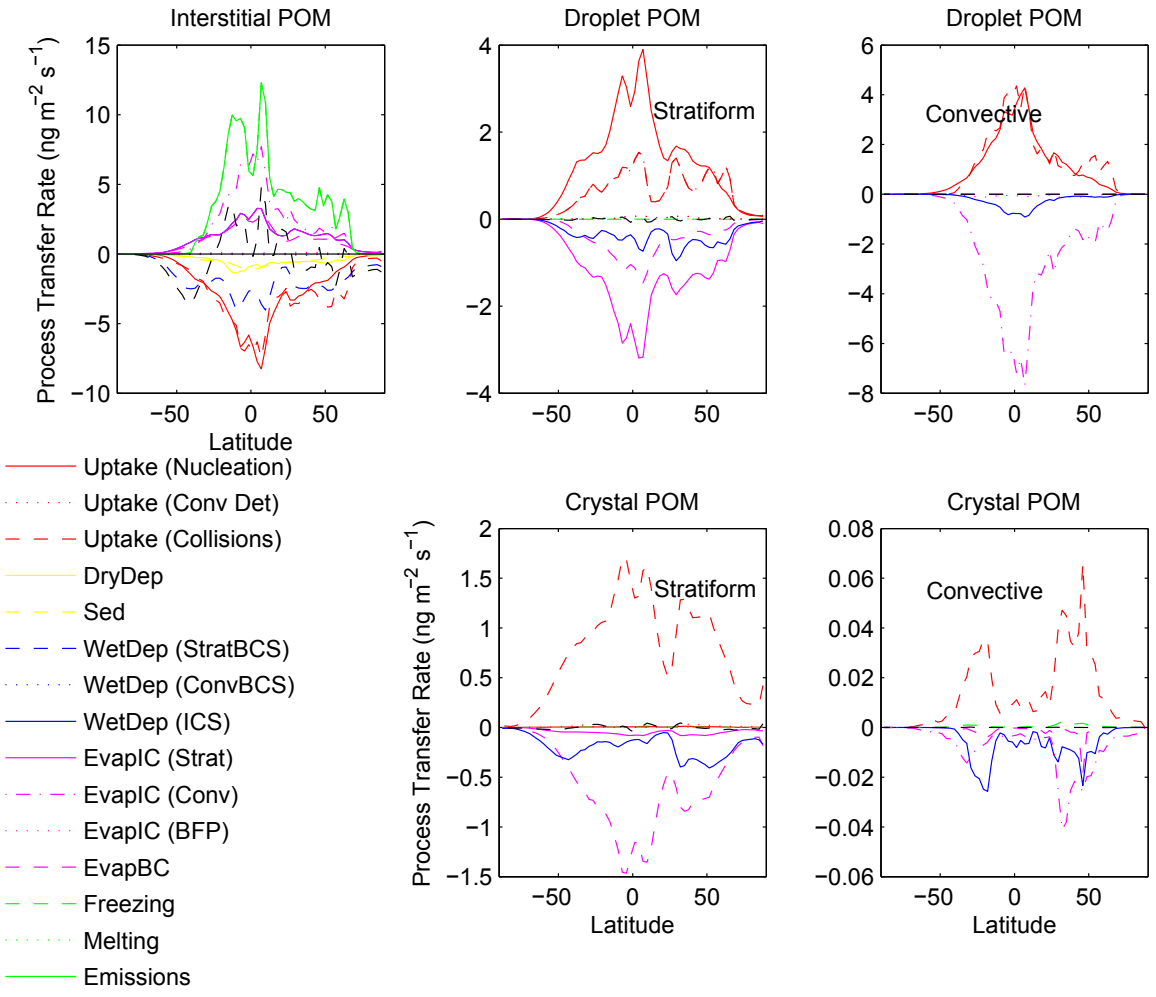

Figure 4.3: The zonal and annual mean particulate organic matter (POM) mass transfer rates (ng m^{-2} s^{-1}) into (positive) and out of (negative) the interstitial, in-droplet and in-crystal phases for both stratiform and convective clouds for the simulation CVAP+SAP+ss. Note: Black dashed line is residual.

mass into the droplets for simulation CVAP+SAP+ss, but impaction scavenging might be underestimated by using the zero collection kernels of Hoose et al. [2008b] for the coarse mode. Rates of release from droplets by evaporation exceed rates of wet deposition by a factor of at least five in the tropics for dust. Similar to the other aerosol species, rates of wet deposition associated with the in-crystal phase roughly equal evaporation rates poleward of 50 °N and 50 °S, but elsewhere evaporation rates dominate by up to an order of magnitude.

Sea salt mass transfer rates are shown in Fig. 4.5 for the simulation CVAP+SAP+ss. Sea salt uptake into droplets is greatest in the mid-latitude Southern Hemisphere. Stratiform uptake exceeds convective uptake by a factor of about 1.5 in this region. However, in the tropics uptake by convective droplets exceeds stratiform droplets by a factor of two. Wet deposition from the in-droplet phase is largest for the Southern Hemisphere mid-latitudes, but is only about one quarter of the evaporation rate. Results for simulation CVAP+SAP are similar, but the mass uptake into the droplets is relatively greater (by about a factor of 2) in the tropics, and lower by about 25% over the southern oceans for simulation CVAP+SAP+ss due to the temperature dependence of the revised sea-salt emissions.

Similar results for these mass transfer rates are found for simulation CVAP+SAP+ss+imp (not shown), except that for this simulation the aerosol mass uptake into cloud droplets is dominated by collision processes, which disagrees with previous work by Jacobson [2003] and Croft et al. [2010]. Implementation of a more physically detailed representation of the uptake by collision processes, which depends on the cloud droplet radii, as well as the count median aerosol radii will likely change this result. Thus, our results for simulation CVAP+SAP+ss+imp should be viewed as an upper limit for the representation of aerosol uptake into cloud droplets by collision processes.

Figure 4.6 shows vertical profiles of the zonal and annual mean fraction of the total in-cloud sulfate mass that is contained in the stratiform and convective cloud droplets. These scavenged fractions are generally largest in the lower troposphere, and at the latitudes between 50 °N and 50 °S where warm phase clouds exist. This pattern is in agreement with the prescribed in-cloud scavenging fractions of Stier

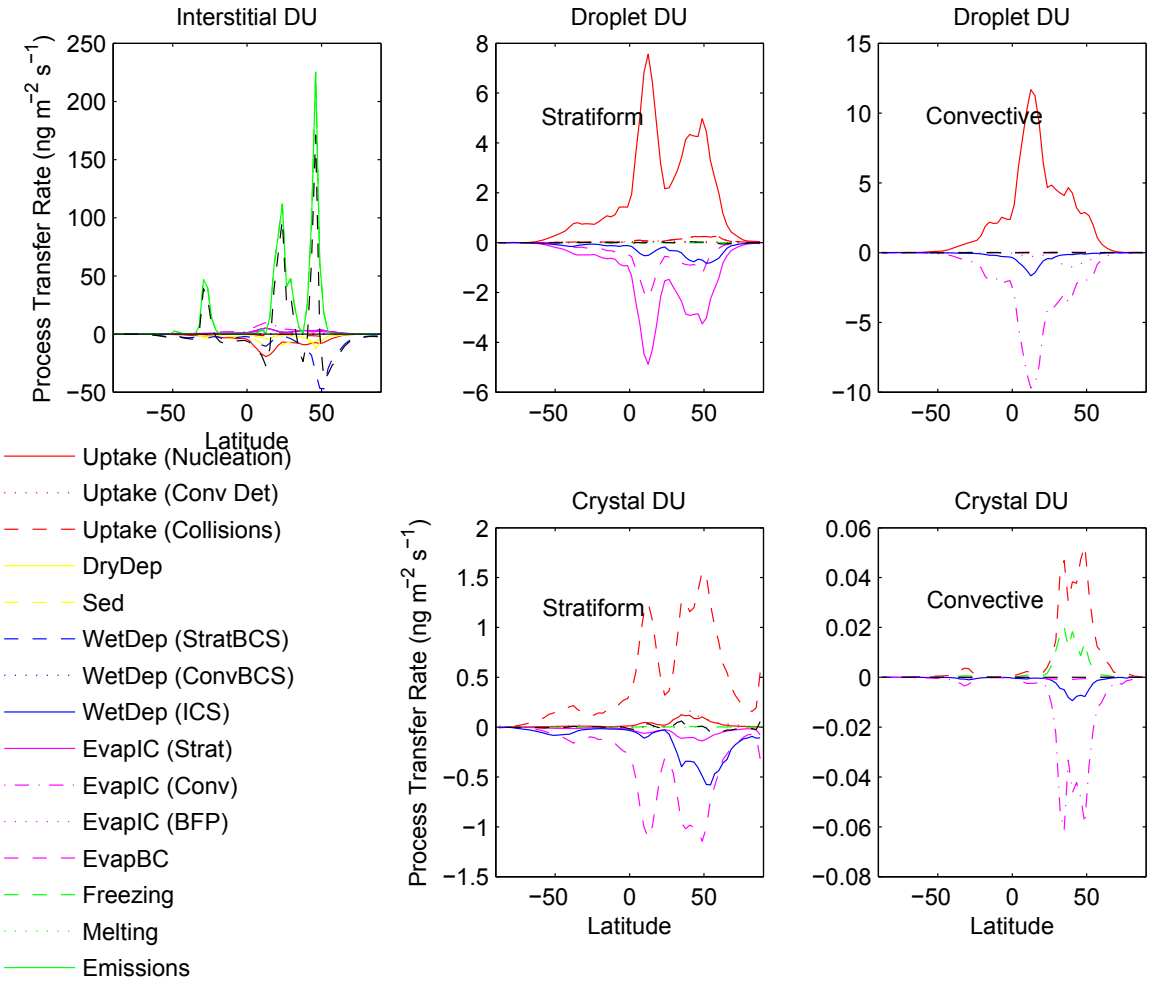

Figure 4.4: The zonal and annual mean dust (DU) mass transfer rates (ng m^{-2} s^{-1}) into (positive) and out of (negative) the interstitial, in-droplet and in-crystal phases for both stratiform and convective clouds for the simulation CVAP+SAP+ss. Note: Black dashed line is residual.

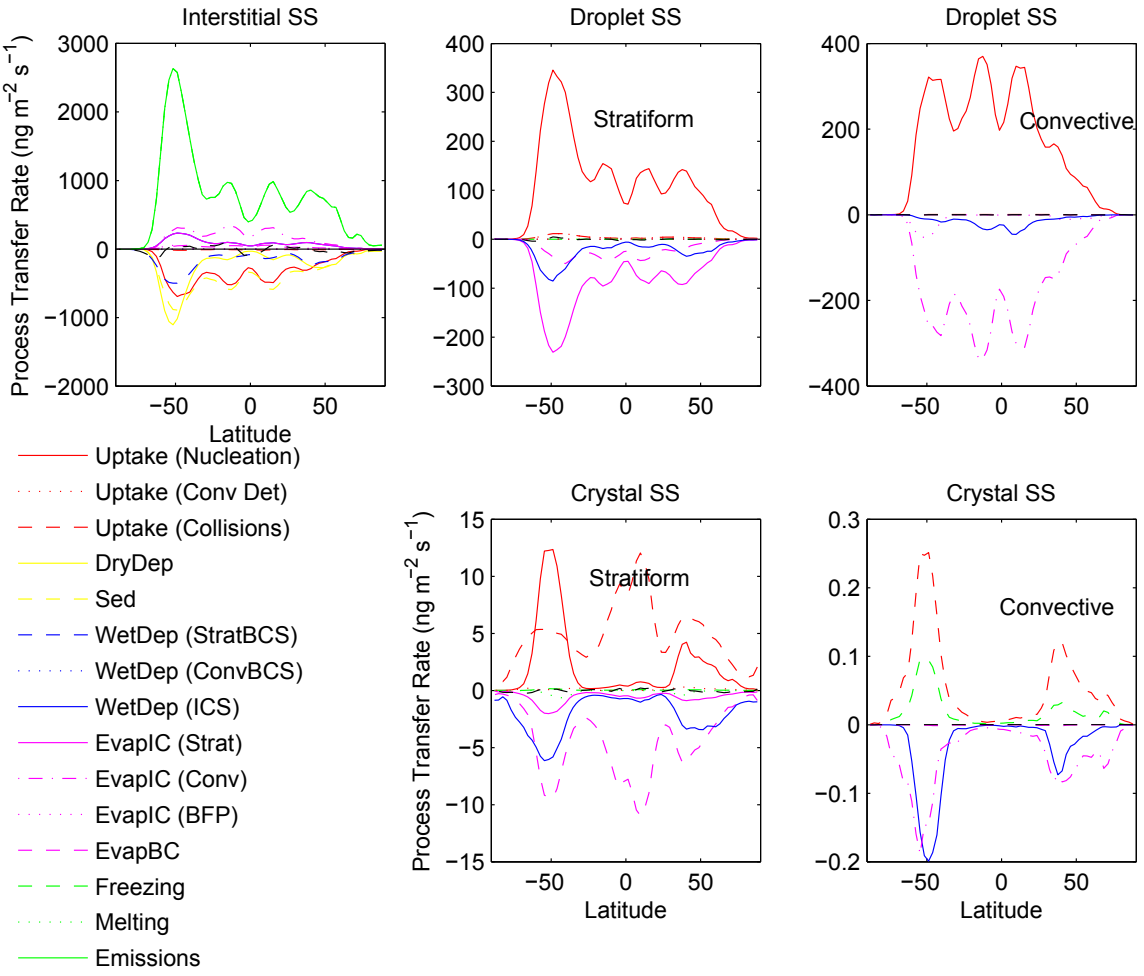

Figure 4.5: The zonal and annual mean sea salt (SS) mass transfer rates (ng S m^{-2} s^{-1}) into (positive) and out of (negative) the interstitial, in-droplet and in-crystal phases for both stratiform and convective clouds for the simulation CVAP+SAP+ss. Note: Black dashed line is residual.

et al. [2005]. For simulation CVAP+SAP+ss the convective scavenged fractions for warm clouds are generally 0.35 or less, whereas for stratiform clouds these fractions are up to 0.85. The results for simulation CVAP+SAP are very similar (not shown). These scavenging ratios are lower than the prescribed fractions of Stier et al. [2005]. Future work should examine the source for this bias. There should be a re-evaluation of the nucleation scavenging scheme, particularly the method of apportioning the number of activated aerosols between the soluble/internally mixed modes, which may bias the nucleation scavenging to be too low for the accumulation and coarse modes and too high for the Aitken mode. The enhanced impaction scavenging for simulation CVAP+SAP+ss+imp, increases the convective scavenged fractions to above 0.9 throughout much of the lower tropical and mid-latitude troposphere. However, the role of impaction scavenging might be over-estimated if the nucleation scavenging is biased low by the current methodology.

Figure 4.6 also shows vertical profiles of the zonal and annual mean stratiform and convective cloud fraction. The convective cloud fractions are greatest in the lower troposphere between 50 °N and 50 °S (but only about 0.01), whereas the stratiform cloud fractions are greatest at higher latitudes, and also in the upper troposphere (and up to 0.4). Interestingly, for stratiform clouds, the maxima for the cloud fraction are not coincident with the maxima for the scavenged fractions, which are essentially temperature dependent. However, for convective clouds, these maxima are coincident, showing the significance of processing of sulfate by convective clouds. We do not show these figures for the other aerosol species as the results are similar.

Figure 4.7 is similar to Fig. 4.6, but shows the scavenged mass fractions for sulfate in ice crystals. For stratiform clouds, the fraction of in-cloud sulfate mass that is scavenged into the crystals is greater throughout the troposphere between 50 °N and 50 °S (about 0.65) and also in the upper troposphere. However for convective clouds, the scavenged fraction maxima are in the middle troposphere. For simulations CVAP+SAP+ss and CVAP+SAP+ss+imp, the maximum convective scavenged mass fractions are about 0.1 and 0.3, respectively. Similar results were found for the other aerosol species (not shown here).

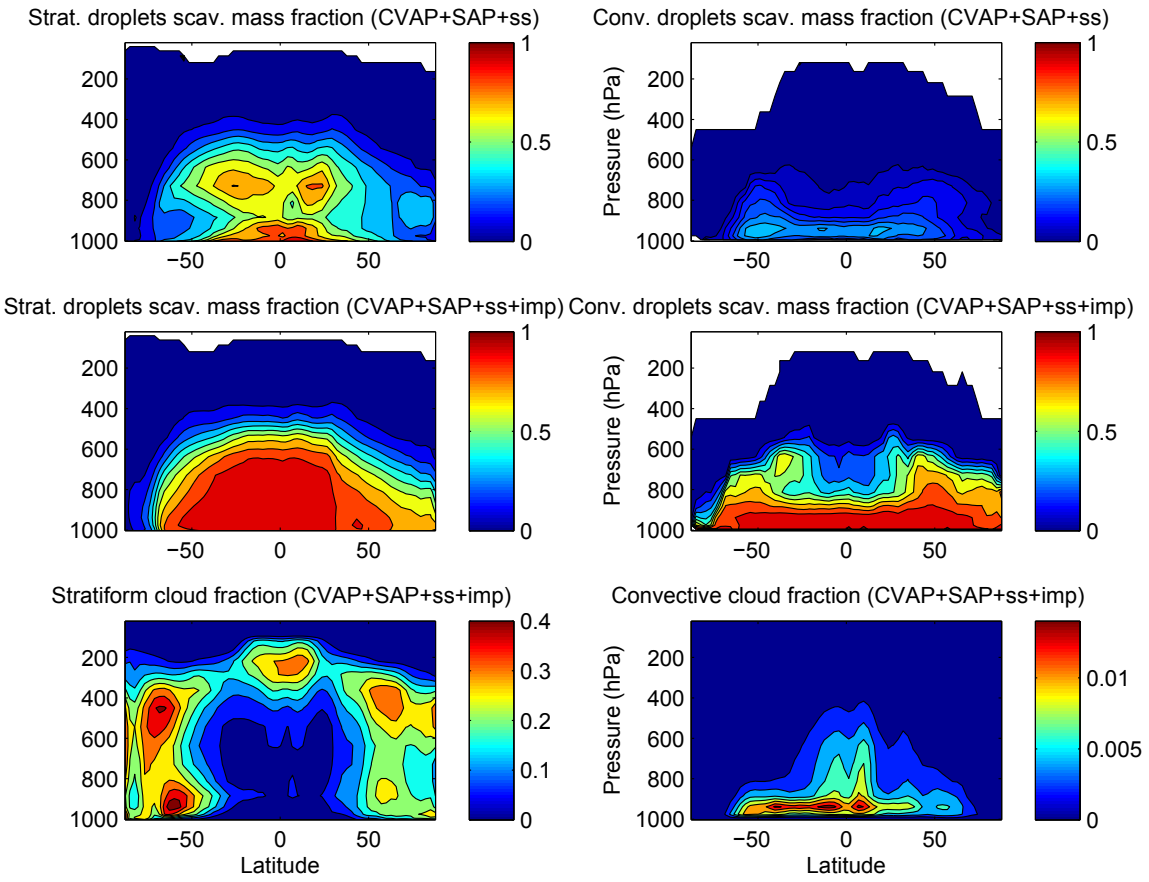

Figure 4.6: The zonal and annual mean fraction of in-cloud sulfate mass scavenged into the stratiform (Strat.) and convective (Conv.) cloud droplets for the simulations CVAP+SAP+ss and CVAP+SAP+ss+imp. The bottom row shows the zonal and annual mean stratiform and convective cloud fraction.

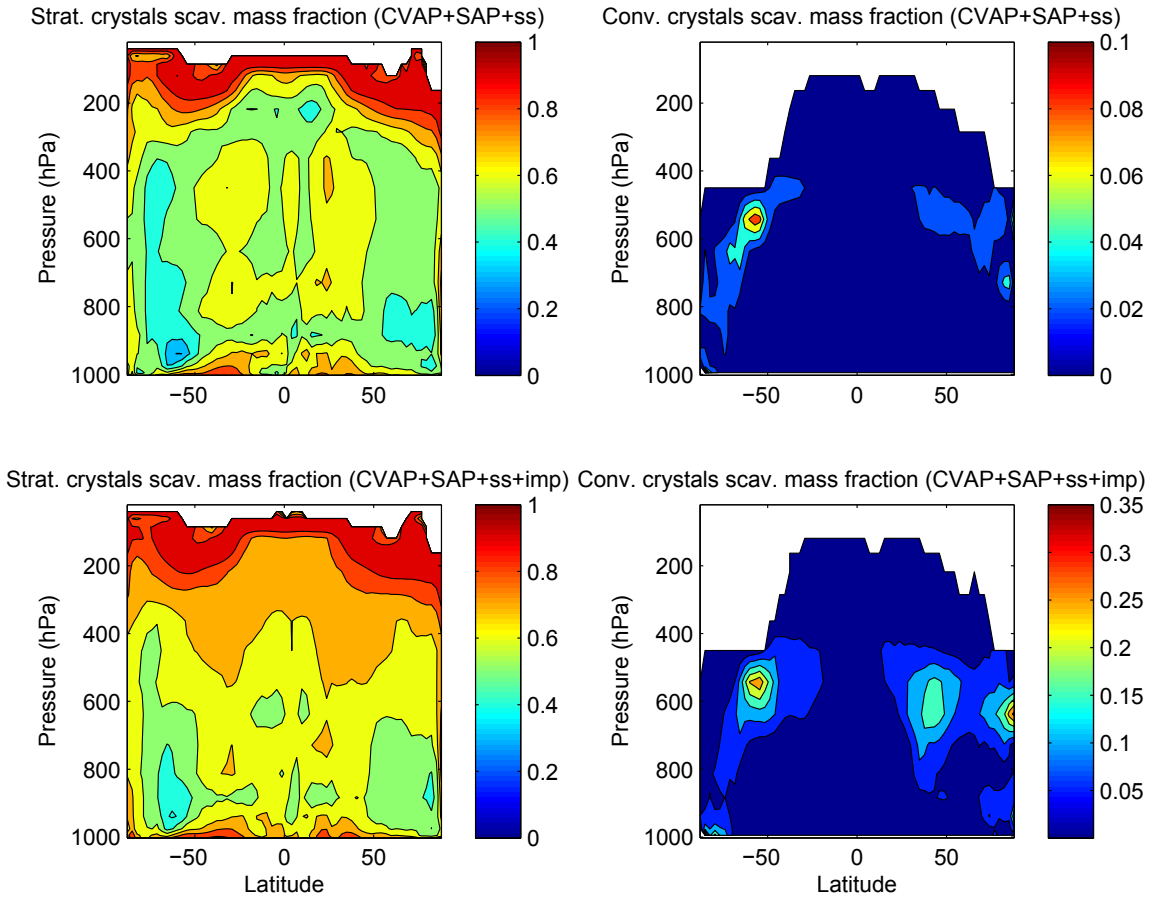

Figure 4.7: The zonal and annual mean fraction of in-cloud sulfate mass scavenged into the stratiform (Strat.) and convective (Conv.) ice crystals for the simulations CVAP+SAP+ss and CVAP+SAP+ss+imp.

4.4.2 Aerosol Mass Burdens, Concentrations and AOD

Table 4.4 shows the annual and global mean aerosol mass burdens and lifetimes for the five aerosol species, as well as the aerosol optical depth at 550 nm, for the five simulations. Aerosols burdens are enhanced by a factor of 3 to 5 when an explicit representation of aerosol processing is introduced in our model (simulation CVAP+SAP relative to NOAP). This is similar to the finding of Hoose et al. [2008a] for stratiform aerosol processing, but is of a greater magnitude since we include both stratiform and convective aerosol processing. This enhancement occurs since we now explicitly represent the processes of aerosol-aerosol coagulation in droplets and crystals, followed by cloud/precipitation evaporation, which releases aerosols to the atmosphere. Also, we have explicitly linked the uptake of aerosols into droplets and crystals to the cloud droplet and ice crystal number concentrations. This approach is quite different from the simulation NOAP, which uses the prescribed fractions of Stier et al. [2005] to represent the uptake of aerosols into droplets and crystals, and does not include size-dependent release by evaporation.

For simulation CVAP+SAP relative to NOAP, the annual and global mean aerosol optical depth (AOD) has increased by 5-fold. This occurs since the aerosol-aerosol coagulation within the cloud droplets and ice crystals produces accumulation mode aerosols that are released by cloud evaporation, and then contribute strongly to AOD. Relative to the annual and global mean observed AOD (0.17) from the MODIS/MISR/AERONET dataset of van Donkelaar et al. [2010], the global and annual mean AOD for simulation CVAP+SAP is a significant over-prediction, by more than a factor of 3. Simulation NOAP under-estimates the global, annual mean AOD by a factor of two. This AOD value is lower relative to other standard ECHAM5-HAM simulations by Stier et al. [2005], and Hoose et al. [2008a] since we have implemented a more vigorous below-cloud scavenging scheme, and new aerosol water uptake scheme, which gives lower AODs, particularly over the oceans. However, the AOD for simulation CVAP+SAP is definitely excessive. Revisions to the sea salt parameterization (emission of fewer accumulation mode aerosols) for simulation CVAP+SAP+ss yield an AOD increase by a factor of about 2.5 relative to simulation NOAP, thus an important correction. Revisions to the parameterization of impaction for simulation

CVAP+SAP+ss+imp yield an AOD under-prediction by a factor of 0.9 relative to the satellite retrieval. Given that recent work by Heald et al. [2010] suggests that our source of organic aerosols might be under-estimated by a factor of two, AOD under-estimation is not unexpected. The aerosol lifetimes are on the order of a few days for the simulation CVAP+SAP+ss+imp, which is an increase of about 10% relative to simulation NOAP, but a decrease by a factor of 2-3 relative to simulation CVAP+SAP. Thus, predicted aerosol burdens and AOD are strongly sensitive to the representation of aerosol processing, as well as the representation of impaction scavenging and sea salt emissions in our model.

The clear-sky AODs are also shown in Table 4.4. We require the entire GCM grid-box column to be clear for this calculation. While satellite retrievals are for clear-sky conditions, the spatial extent of the clear sky could only be on the order of some tens of kilometers, as opposed on the order of a few hundred kilometers for our GCM clear-sky results. Thus, we expect the satellite retrieval of AOD should lie between the GCM AOD and CS-AOD values.

We find a relatively greater increase in the aerosol burdens for the implementation of coupled convective and stratiform aerosol processing (simulation CVAP+SAP) as compared to the stratiform aerosol processing only (simulation SAP). Several factors contribute to this. Firstly, cloud evaporation is more important for convective clouds than for stratiform clouds. The rates of aerosol release from cloud droplets due to evaporation for convective clouds often exceed or about equal that for stratiform clouds at the tropical latitudes (see Figs. 4.1 - 4.5). Additionally, if we implement stratiform aerosol processing alone, the convective wet removal of aerosols can increase and moderate the burden increase. However, if both stratiform and convective aerosol cloud processing are explicitly represented, the aerosol scavenging and burdens are very dependent on cloud microphysical processes. Convective wet deposition is more constrained by the cloud microphysics and can not increase to compensate for the decreased stratiform wet deposition. This point is examined further in a following subsection, which shows the wet deposition budgets.

Simulation CVAP+SAP+ss+imp demonstrates that the parameterizations of in-cloud collision scavenging does strongly influence the predicted burdens, lifetimes,

Table 4.4: Global and annual mean aerosol burdens (Tg, except Tg S for sulfate), lifetimes (days) in brackets after the burdens, all-sky aerosol optical depth (AOD) at 550 nm, and clear-sky aerosol optical depth (CS-AOD) at 550 nm, for the five simulations presented in Table 4.3.

	NOAP	SAP	CVAP +SAP	CVAP +SAP +ss	CVAP +SAP +ss+imp
SO4	0.741 (3.6)	0.974 (4.8)	2.32 (11.2)	2.04 (9.9)	0.78 (3.9)
BC	0.113 (5.4)	0.136 (6.4)	0.312 (14.8)	0.292 (13.8)	0.127 (6.0)
POM	0.986 (5.4)	1.17 (6.4)	3.09 (17.1)	2.89 (15.9)	1.19 (6.6)
DU	2.88 (3.4)	3.37 (3.9)	6.01 (7.4)	5.15 (6.3)	3.25 (3.8)
SS	8.49 (0.58)	12.4 (0.85)	41.0 (2.8)	48.3 (1.3)	17.0 (0.5)
AOD	0.091	0.205	0.492	0.240	0.154
CS-AOD	0.088	0.170	0.420	0.389	0.164

and optical depth for our model. There are reductions between 2 to 3-fold for these quantities with more vigourous impaction scavenging of the accumulation and coarse modes. The original impaction scavenging kernels of Hoose et al. [2008b] were based on the work of Young [1974], which ignored the influence of inertial impaction. Thus, the impaction scavenging for the accumulation and coarse modes is likely underestimated for the simulations SAP, CVAP+SAP, and CVAP+SAP+ss. Based on the work of Schlamp et al. [1976], Lin and Lee [1975], and Klett and Davis [1973], we know that droplets of radius between 10 to 50 μm have a collision efficiency for super-micron size collision partners that can be about 0.1. Despite the low fall speeds for droplets of this size, there are non-negligible collection kernels for collisions between droplets, and accumulation and coarse mode aerosols, particularly under the assumption that the droplets will have a size distribution [Croft et al., 2010].

The annual and zonal mean vertical profile of the aerosol mass mixing ratios for the five aerosol species is shown in Fig. 4.8. Similar to the findings presented in Hoose et al. [2008a], and Croft et al. [2010], we find that for the aerosol processing simulation CVAP+SAP+ss relative to NOAP, the mass mixing ratios for all aerosol species are increased by up to 5-fold, particularly in the regions of mixed and ice phase clouds, poleward of 50 °N and 50 °S, and in the upper troposphere. This mass

increase may be associated with an under-estimation of the nucleation scavenging, particularly for aerosol species that have considerable mass in the soluble/internally mixed accumulation and coarse modes, such as sea salt. The current method of apportioning of the number of activated aerosols between the three largest soluble modes may bias the nucleation scavenging to be under-estimated for the coarse and accumulation modes, and over-estimated for the Aitken mode. Thus, the high sea salt mass mixing ratios shown in the middle and upper troposphere in Fig. 4.8 could be an artifact of this bias. The results for simulation CVAP+SAP are very similar (not shown). With the revisions for simulation CVAP+SAP+ss+imp, the concentration increase is still focused on the same regions, but is about 50 to 100% relative to simulation NOAP. In comparison with Fig. 4.6, we see that these regions are about coincident with the regions of maximum stratiform cloud cover.

4.4.3 Aerosol Cycling Through Clouds

Table 4.5 summarizes the annual and global mean rates of uptake of aerosol mass into cloud hydrometeors (droplets and crystals), and rates of release of aerosol mass due to evaporation of cloud hydrometeors and precipitation. For this table, all rates are summed over the five aerosol species. Considering simulation CVAP+SAP, the ratio of total evaporation to uptake is higher for convective clouds than for stratiform clouds, 0.94 and 0.84, respectively. Below-cloud evaporation contributes strongly to the total evaporation (about 10-25%). Changing the assumptions about in-cloud impaction scavenging reduces the total evaporation to uptake ratio to 0.80 for simulation CVAP+SAP+ss+imp. This occurs since the wet deposition of aerosols is increased for the simulation CVAP+SAP+ss+imp. This is examined further in a following section, which presents the wet deposition budgets. This sensitivity to the parameterization of in-cloud impaction scavenging indicates the importance of developing physically detailed representations of size-dependent impaction scavenging in models that explicitly represent the nucleation scavenging processes.

Similar to Hoose et al. [2008a] and Pruppacher and Jaenicke [1995], we consider the ratio of the rate of release of aerosol mass by evaporation to the source rate as an indicator of the number of times that an aerosol sampled remote to source has cycled

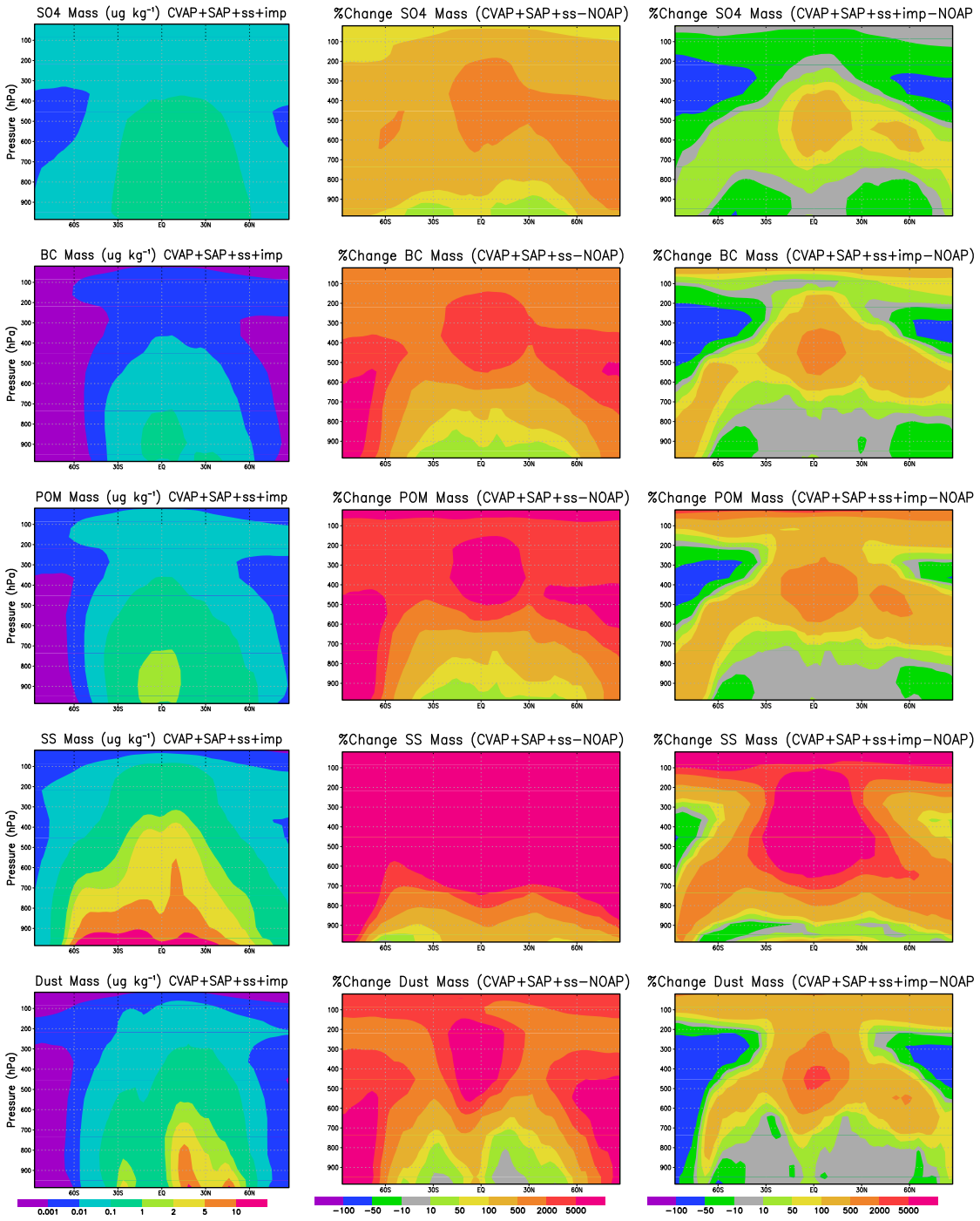

Figure 4.8: The zonal and annual mean sulfate (SO4), black carbon (BC), particulate organic matter (POM), sea salt (SS), and dust (DU) mass mixing ratios (μg kg^{-1}, except μg S kg^{-1} for sulfate) for the simulation CVAP+SAP+ss+imp, and the percent change in these masses for the simulations CVAP+SAP+ss and CVAP+SAP+ss+imp as compared to the simulation NOAP.

Table 4.5: Annual and global mean rates of aerosol emission (source), uptake and evaporation (Tg yr $^{-1}$) for stratiform clouds for the simulation SAP, and for both stratiform and convective clouds for the simulations CVAP+SAP, CVAP+SAP+ss, and CVAP+SAP+ss+imp. All clouds refers to the summation of the rates for both stratiform and convective clouds. Evap/Uptake is the ratio of the summed evaporation rates, in-cloud (IC) and below-cloud (BC), to the uptake rate. The below-cloud evaporation rate includes only aerosol that was in precipitation due to in-cloud scavenging processes, excluding aerosol in precipitation due to below-cloud scavenging. Evap/Source is the ratio of the summed evaporation to the emission rate and gives the number of times an aerosol, sampled remote to source, has cycled through clouds. Rates are summed over the five aerosol species.

	Stratiform (SAP)	Stratiform (CVAP +SAP)	Convective (CVAP +SAP)	All clouds (CVAP +SAP +ss)	All clouds (CVAP +SAP +ss+imp)
Source	5790.	5790.	5790.	14100.	14100
Uptake	1450.	2480.	2140.	5940.	18800
Evap(IC)	990.	1630.	2010.	4700.	13500
Evap(BC)	206.	442.	0.40	564.	1560
Evap/Uptake	0.82	0.84	0.94	0.89	0.80
Evap/Source	0.21	0.36	0.35	0.37	1.07

through clouds in an annual and global mean sense. For simulations CVAP+SAP+ss and CVAP+SAP+ss+imp, the number of cycles is 0.4 and 1., respectively. The estimate of Hoose et al. [2008a] was 0.53, considering stratiform clouds only. We attribute about equal contributions from stratiform and convective clouds to this cycling. Pruppacher and Jaenicke [1995] estimated 3 cloud cycles. However, as reviewed by Hoose et al. [2008a], the Pruppacher and Jaenicke [1995] model had excessive global cloud liquid water content, and was a simpler calculation. These factors contribute to the difference relative to our simulations.

The results presented in Table 4.5 are strongly dominated by sea salt, which constitutes at least 95% of the total aerosol mass in our simulations. Table 4.6 presents similar annual and global mean results for simulations CVAP+SAP+ss and CVAP+SAP+ss+imp, considering each aerosol species separately. The aerosol species that exist in the smaller modes, sulfate, black carbon, and particulate organic

Table 4.6: Annual and global emission (Source), uptake and evaporation rates (Tg yr^{-1}, except Tg S yr^{-1} for sulfate) and the ratio of the rates of evaporation to uptake, and evaporation to source as described in the previous table, for each of the five aerosol species and for the simulations CVAP+SAP+ss+imp, and CVAP+SAP+ss in brackets. Results shown include both stratiform and convective clouds.

	SO4	BC	POM	DU	SS
Source	74.3 (74.1)	7.7 (7.7)	66.1 (66.1)	315. (297.)	13600. (13600.)
Uptake	193. (107.)	27.8 (13.2)	249. (100.)	430. (92.5)	17900 (5670.)
Evap(IC)	101. (61.3)	17.9 (9.04)	157. (65.4)	249. (63.8)	12900. (4380.)
Evap(BC)	47.0 (21.9)	5.15 (2.13)	50.6 (20.1)	92.9 (15.5)	1360. (504.)
Evap/Uptake	0.77 (0.78)	0.83 (0.85)	0.83 (0.86)	0.80 (0.86)	0.80 (0.86)
Evap/Source	2.0 (1.1)	3.0 (1.5)	3.1 (1.3)	1.1 (0.27)	1.1 (0.36)

matter are found to cycle through clouds more times (between 1 - 3 times for simulations CVAP+SAP+ss and CVAP+SAP+ss+imp). Dust and sea salt had the smallest number of cycles through clouds, between 0.3 and 1. for simulations CVAP+SAP+ss, and CVAP+SAP+ss+imp, respectively. Both dust and sea salt have a large fraction of removal from the atmosphere by dry deposition and sedimentation processes, as opposed to wet scavenging. As a result, the cloud cycling for dust and sea salt is lower than for the other aerosol species. Table 4.6 shows that the global and annual mean ratio of evaporation to uptake is lowest for sulfate, 0.77. The in-cloud production of sulfate is included in the uptake rate for this species. This contributes to the relatively higher uptake rate as compared to the evaporation rate for sulfate. For the other aerosol species, the ratio of evaporation to uptake is above 0.8. The number of cloud cycles is greater by about a factor of about two for simulation CVAP+SAP+ss+imp relative to CVAP+SAP+ss. This is due to the increased aerosol uptake rates due to more vigorous in-cloud impaction scavenging.

4.4.4 Aerosol Number

The annual mean geographic distributions of the number burdens for the four insoluble/internally mixed modes, comparing the simulations CVAP+SAP+ss and CVAP+SAP+ss+imp with the NOAP simulation, are shown in Fig. 4.9. The number of soluble/internally mixed accumulation mode aerosols is increased by up to 2-5 times

for the simulation CVAP+SAP+ss compared to NOAP. This increase is greatest in the mid-latitudes and poleward. The number of soluble/internally mixed Aitken and nucleation mode aerosols is reduced by about 0.1 for the simulation CVAP+SAP+ss as compared to NOAP. The aerosol processing simulations explicitly represent aerosol-aerosol coagulation within the cloud droplets and crystals, followed by evaporation, which releases larger aerosols to the atmosphere. The increased available surface area of the accumulation and coarse modes favors condensation of sulfate as opposed to nucleation of new particles. For the CVAP+SAP+ss+imp simulation, the accumulation mode number burden is increased by only up to 2-fold, primarily over the oceans.

Table 4.7 summarizes the annual and global mean aerosol number burdens for the aerosol modes of our model. The number of soluble/internally mixed accumulation mode aerosols is climatologically relevant since aerosols in this size range dominate the modification of the radiation budget and cloud properties. The global and annual mean number of accumulation mode aerosols is enhanced by about 2.5 times for the simulations CVAP+SAP, and CVAP+SAP+ss compared to the NOAP simulation. Conversely, there is a reduction in the number of nucleation (by 80%) and soluble Aitken mode aerosols (by 90%) for the simulation CVAP+SAP relative to simulation NOAP. Nucleation of new particles is not favored by the enhanced surface area in the larger aerosol modes. For the simulation CVAP+SAP+ss+imp, the number of accumulation mode aerosols is enhanced by about 10% relative to the simulation NOAP. These results indicate that the prediction of the number of accumulation mode aerosols is strongly dependent on the representation of aerosol processing by clouds, but also on the representation of in-cloud impaction scavenging and the sea salt emissions.

4.4.5 Wet Deposition

Figure 4.10 shows the geographic distribution of the annual mean aerosol wet deposition and precipitation, and the changes for the simulations CVAP+SAP+ss and CVAP+SAP+ss+imp relative to the NOAP simulation. The results for simulation CVAP+SAP (not shown) are very similar to the results for simulation CVAP+SAP+ss. However, the changes for simulation CVAP+SAP relative to NOAP are greater by

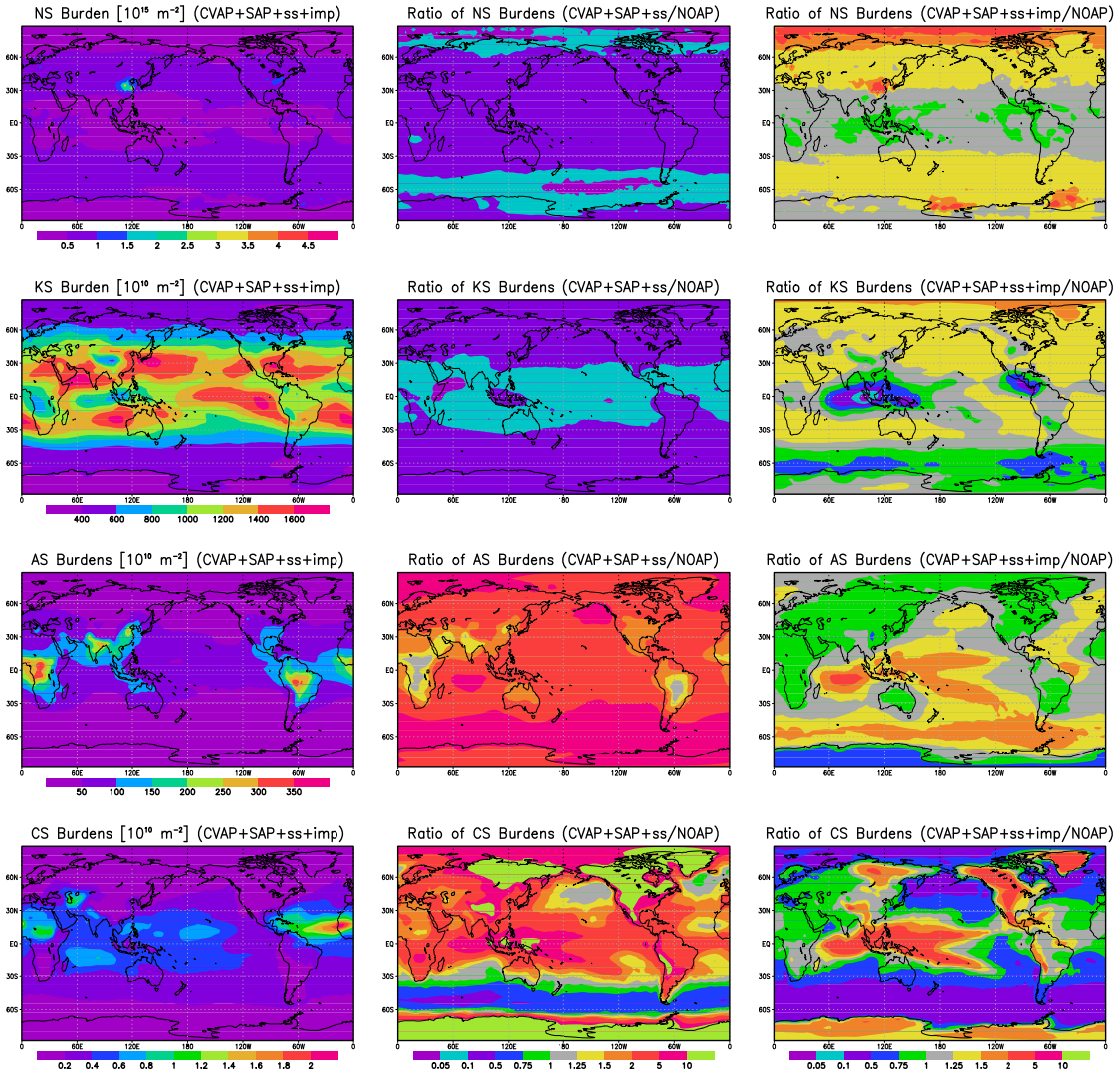

Figure 4.9: The geographic distribution of annual mean number burdens (10^{10} m^{-2}) for the four soluble/internally mixed modes: nucleation (NS), Aitken (KS), accumulation (AS), and coarse (CS) for the simulation CVAP+SAP+ss+imp, and the ratio of the number burdens for simulations CVAP+SAP+ss and CVAP+SAP+ss+imp relative to simulation NOAP.

Table 4.7: Global and annual mean number burdens (10^{10} m^{-2}) for the five simulations and for the seven aerosol modes. CD and IC refer to the stratiform in-droplet and in-crystal modes. Acronyms are defined in Table 4.2.

Number	NS	KS	AS	CS	KI	AI	CI	CD	IC
NOAP	47900.	1040.	59.8	0.39	6.9	0.027	0.057		
SAP	50200.	817.	90.3	0.40	5.5	0.047	0.081	5.45	0.49
CVAP+SAP	8740.	125.	169.	1.5	8.2	0.055	0.12	8.56	0.68
CVAP+SAP+ss	8720.	120.	153.	0.79	8.2	0.055	0.12	6.14	0.62
CVAP+SAP +ss+imp	58000.	1000.	66.2	0.33	6.6	0.024	0.051	2.49	0.42

10-20%, with the greatest differences for sea salt. Wet deposition is reduced closer to the source regions (50% for CVAP+SAP+ss, and 10-25% by CVAP+SAP+ss+imp) . Wet deposition is increased in the regions more remote to the sources (up to 4-fold for CVAP+SAP+ss, and 10-50% for CVAP+SAP+ss+imp). The longer aerosol lifetimes for simulation CVAP+SAP+ss allow aerosol transport to more remote regions before deposition. The geographic distribution of the annual mean precipitation shows that the precipitation maxima occur at the tropical latitudes and over the oceans, which are not exactly co-incident with the maxima for the aerosol wet deposition.

For the simulation SAP relative to the NOAP simulation, the global and annual mean stratiform wet deposition is reduced between 20 - 40% for all aerosol species. However, the convective wet deposition increases by a comparable amount such that the total wet deposition is quite similar between the simulations SAP and NOAP. For simulation CVAP+SAP, the global and annual mean convective wet deposition decreases by about 90% relative to simulations NOAP and SAP for all aerosol species because simulations NOAP and SAP use the prescribed scavenging fractions of Stier et al. [2005]. Simulation CVAP+SAP+ss+imp suggests that global and annual wet deposition of aerosols is dominated by stratiform cloud scavenging, which accounts for 65 - 80% of the total wet deposition, depending on the aerosol species. This is in agreement with the findings of Fang et al. [submitted], that stratiform wet deposition makes the dominant contribution to the global, annual mean aerosol wet deposition. However, this contrasts with the results for simulation SAP, which attributes the global, annual mean aerosol wet deposition about equally between stratiform and

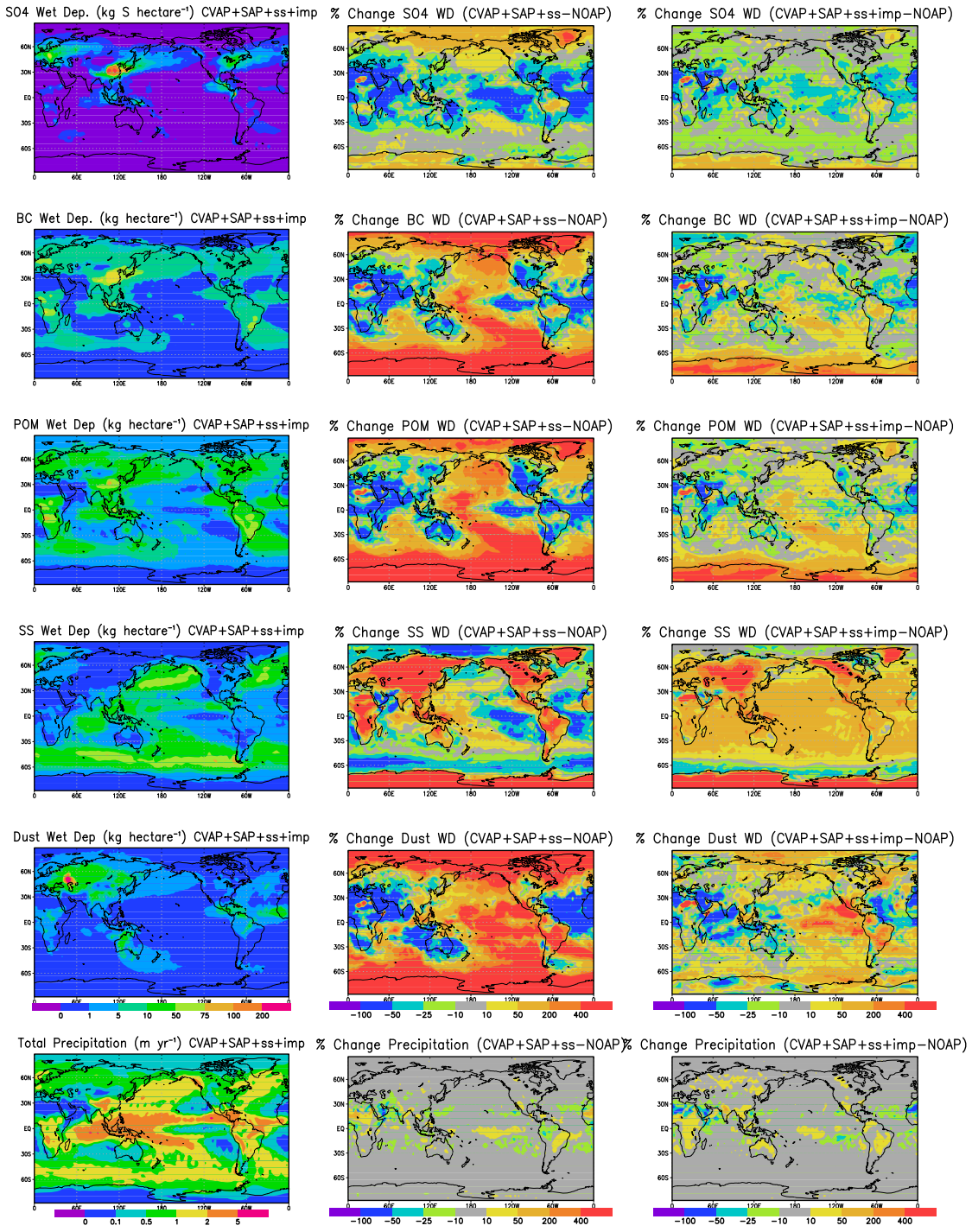

Figure 4.10: The geographic distribution of sulfate (SO4), black carbon (BC), particulate organic matter (POM), sea salt (SS) and dust annual mean wet deposition (kg hectare^{-1}, except kg S hectare^{-1} for sulfate), and total annual precipitation (m) for the CVAP+SAP+ss+imp simulation, and the percent change for the simulations CVAP+SAP+ss and CVAP+SAP+ss+imp as compared to the NOAP simulation.

convective clouds. For the interested reader, these deposition budgets are summarized in Tables A.1 - A.5.

The predicted wet deposition depends strongly on the parameterization of in-cloud impaction scavenging, which is associated with uncertainty for several reasons. Firstly, this is a strongly size-dependent process, and collection kernels can change over several orders of magnitude with quite small changes in the size of the collision partners. Secondly, as clouds evaporate, thermophoretic processes associated with lowering relative humidity enhance the collection of interstitial aerosol by droplets and crystals in a complex manner that is not straightforward to represent in a global model. Using the enhanced collection kernels for simulation CVAP+SAP+ss+imp, increases the uptake of aerosols by convective clouds, and increases the convective wet deposition between 3 to 5-fold relative to simulation CVAP+SAP+ss. However, this sensitivity to the parameterization of impaction scavenging may also arise due to an under-estimation of the nucleation scavenging in our model. This could be related to biases associated with the current method of apportioning of the number of activated aerosols between the three largest soluble modes, which could lead to over-estimation of the nucleation scavenging for the Aitken mode and under-estimation for the accumulation and coarse modes.

Warm phase scavenging dominates the removal of aerosols for both convective and stratiform clouds for our simulations. Considering stratiform and convective clouds together, warm phase in-cloud scavenging account for about 70% of the total aerosol removal attributed to in-cloud scavenging processes in the annual and global mean. Mixed phase in-cloud scavenging accounts for between 25 to 30% of the total aerosol removal attributed to in-cloud scavenging. For simulation CVAP+SAP+ss, the less vigourous impaction scavenging scavenging gives lower in-cloud scavenging rates, by a factor of 2-3 for warm and mixed phase clouds relative to simulation CVAP+SAP+ss+imp. Since the reductions are greatest for the convective clouds, this reduces the contribution of convective wet scavenging to annual and global mean wet deposition to about 10%.

4.5 Comparison with Observations

4.5.1 Cloud Properties

Table 4.8 summarizes the annual and global cloud properties for the five simulations. Figure 4.11 shows the annual and zonal mean distribution of the cloud properties. The liquid water path (LWP) is largest (91.6 g m^{-2}) for the CVAP+SAP simulation, which had the largest aerosol burdens, and smallest for simulation CVAP+SAP+ss+imp (34.9 g m^{-2}). Observations from Greenwald et al. [1993], Weng and Grody [1994], and Ferraro et al. [1996] give the LWP as 49-84 g m^{-2}. The latitudinal distribution of the LWP for all simulations agrees well with the observations, except for an over-estimation, about two-fold, over the southern mid-latitude oceans, which is corrected for simulation CVAP+SAP+ss+imp. This over-estimation is greatest for the simulations CVAP+SAP and CVAP+SAP+ss. The modeled global and annual cloud droplet number concentration agrees within a factor of two with the estimate of Han et al. [1998], and the latitudinal distribution is well represented, except over the southern oceans. The modeled annual global mean ice water path (IWP) is low (about 8 g m^{-2}) relative to the estimate from ISCCP data of Storelvmo et al. [2008] (29 g m^{-2}), and from CloudSat data of Austin et al. [2009] (75 g m^{-2}). This is also evident in Fig. 4.11.

The simulated cloud cover is slightly lower (56%) than the range estimated by Rossow and Schiffer [1999] from ISCCP (62-67%). The annual and global shortwave and longwave cloud forcing (SCF and LCF) has been estimated by Kiehl and Trenberth [1997] as -50 and +30 W m^{-2}, as shown in Table 4.8. Our simulations have a low LCF (about 26 W m^{-2}), which is expected since the modeled IWP is low. The SCF is also low (-40 to -45 W m^{-2}) for our simulations, which is also expected since the modeled cloud cover is low (55-58%). The observed latitudinal distribution of SCF and LCF from ERBE are in close agreement with our model.

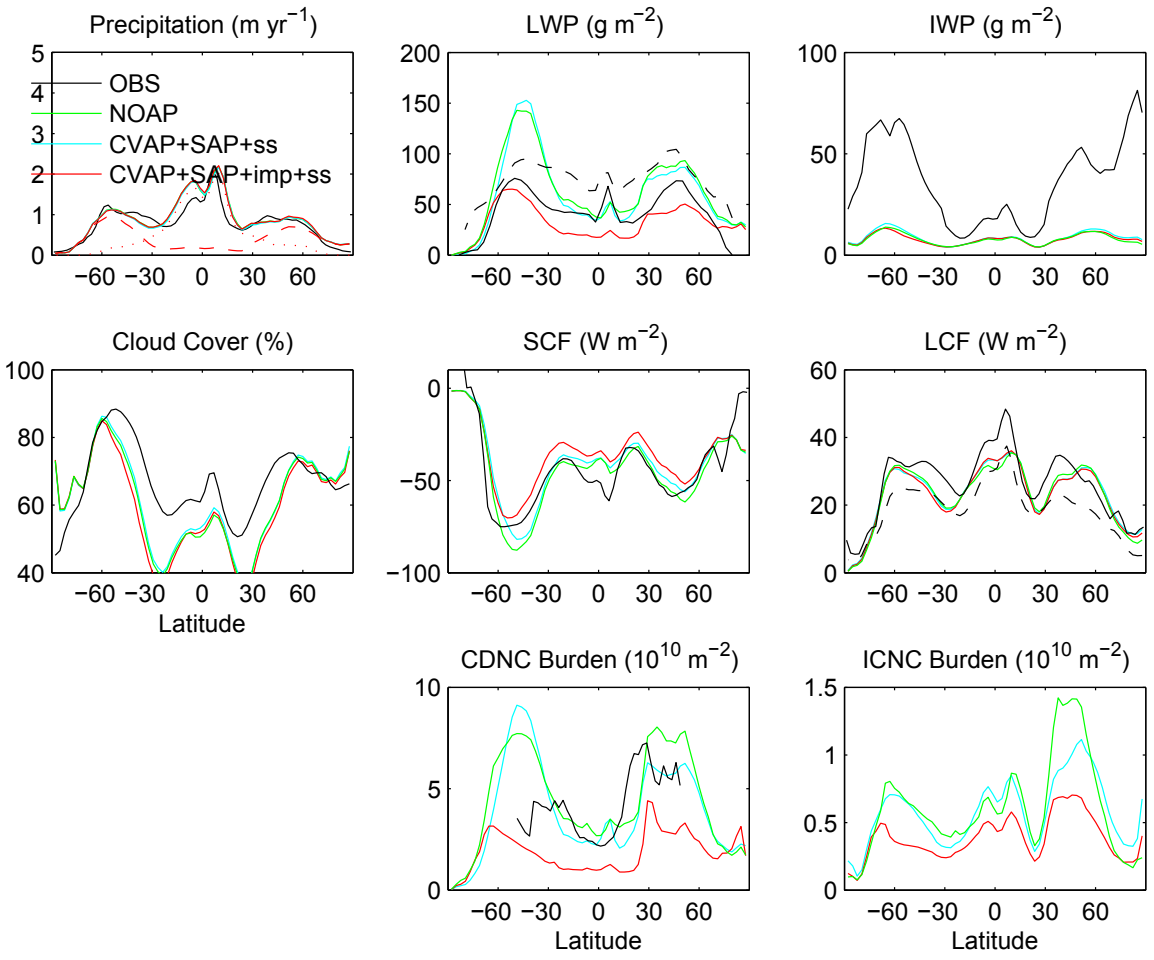

Figure 4.11: The annual and zonal mean precipitation, mean liquid water path (LWP), ice water path (IWP), cloud cover (CC), short wave cloud forcing (SCF), long wave cloud forcing (LCF), vertically integrated in-cloud droplet number concentration (CDNC) and vertically integrated ice crystal number concentration (ICNC) for the NOAP, CVAP+SAP+ss and CVAP+SAP+ss+imp simulations and observations. The sources of the observations are described in Table 4.8. For precipitation, dashed line:stratiform, dotted line:convective. For LWP observations, solid black: Weng and Grody [1994], dashed black: Greenwald et al. [1993]. For LCF, solid black: ERBE, dashed black: TOVS data. The SCF is from ERBE data.

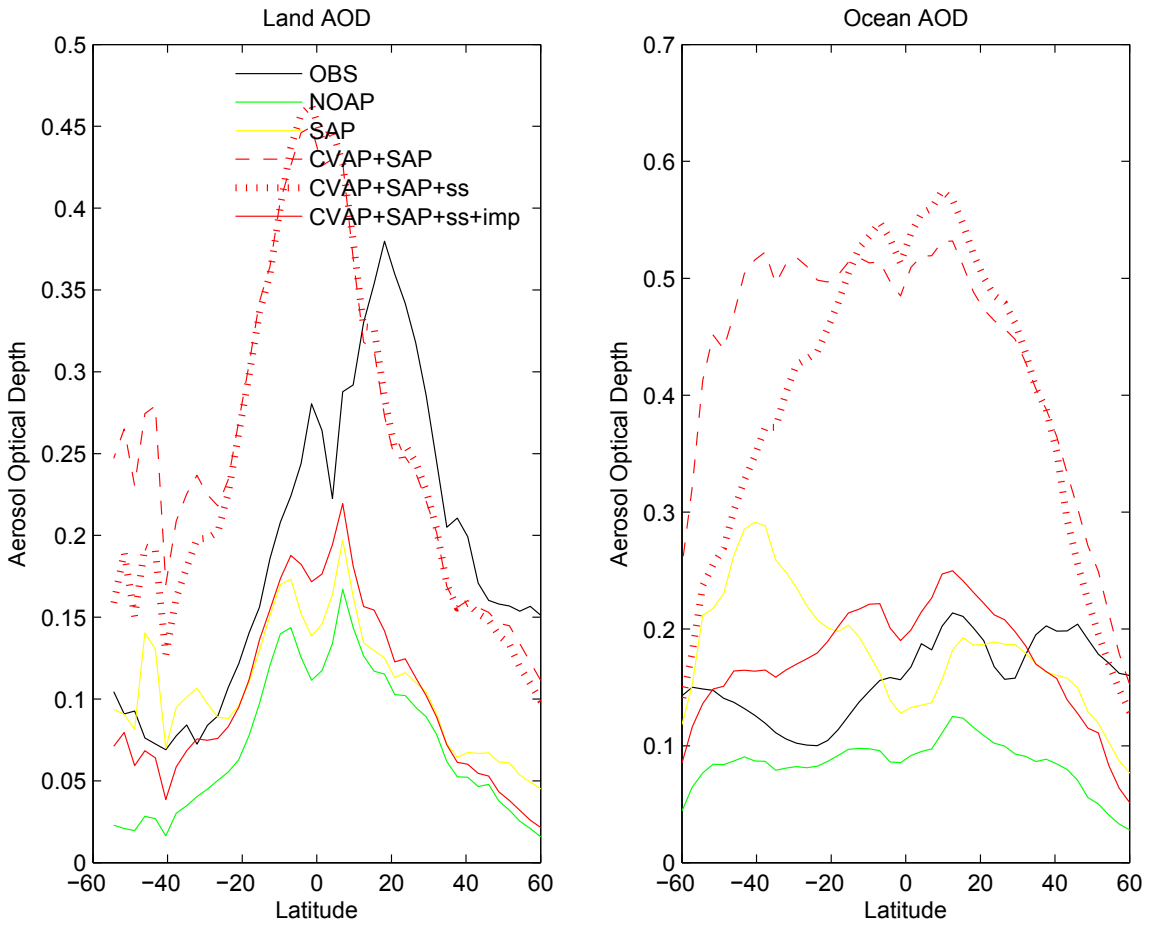

Figure 4.12: The annual and zonal mean clear-sky aerosol optical depth at 550 nm over land and over the oceans for the simulations NOAP, SAP, CVAP+SAP, CVAP+SAP+ss and CVAP+SAP+ss+imp and observations from MODIS, MISR and AERONET compiled by van Donkelaar et al. [2010].

Table 4.8: Annual and global mean liquid water path (LWP in g m^{-2}), ice water path (IWP in g m^{-2}), cloud cover (CC in percent), precipitation (mm day $^{-1}$), vertically integrated cloud droplet number concentration (N_d in 10^{10} m^{-2}), vertically integrated ice crystal number concentration (N_i in 10^{10} m^{-2}), and top of the atmosphere shortwave cloud forcing (SCF in W m^{-2}), and longwave cloud forcing (LCF in W m^{-2}). LWP observations are from SSM/I [Greenwald et al., 1993, Weng and Grody, 1994, Ferraro et al., 1996]. IWP has been derived from ISCCP [Storelvmo et al., 2008] . Total cloud cover is from ISCCP [Rossow and Schiffer, 1999], and total precipitation is from the Global Precipitation Data Set. Observations of N_d are from ISCCP [Han et al., 1998]. SCF and LCF observations are from Kiehl and Trenberth [1997].

	LWP	IWP	CC	Precip	N_d	N_i	SCF	LCF
OBS	49–84	29	62–67	2.64–2.7	4		-50	30
MODIS/TOVS	94–109		65–67					
NOAP	77.1	7.57	56.3	2.91	4.86	0.67	-48.2	26.1
SAP	67.8	7.92	56.5	2.91	3.87	0.48	-44.2	26.1
CVAP+SAP	91.6	8.13	58.2	2.85	5.97	0.67	-46.7	26.3
CVAP+SAP +ss	65.5	8.04	57.3	2.86	4.28	0.61	-44.6	26.2
CVAP+SAP +ss+imp	34.9	7.51	55.0	2.91	1.84	0.41	-38.9	25.9

4.5.2 Aerosol Optical Depth

Figure 4.12 shows the annual and zonal mean clear-sky aerosol optical depth (AOD) at 550 nm for the five simulations and satellite observations from the 6-year climatology (2001-2006) dataset compiled by van Donkelaar et al. [2010]. A land-ocean mask has been applied to extract AOD over land and ocean separately. Simulation NOAP under-predicts the observations by about a factor of 2. These AODs are lower than for simulations by Stier et al. [2005] since we have implemented the more vigourous below-cloud scavenging scheme of Croft et al. [2009], and a also a revised aerosol water uptake scheme following Petters and Kreidenweis [2007]. The inclusion of aerosol processing in our model increases the AOD to give better agreement with the observations. The simulation CVAP+SAP+ss+imp agrees closest with the observations for the Southern Hemisphere land, and also agrees closest with oceans observations relative to the other aerosol processing simulations. Simulation CVAP+SAP+ss+imp appears to under-predict the Northern Hemisphere dust maximum, but is in closer

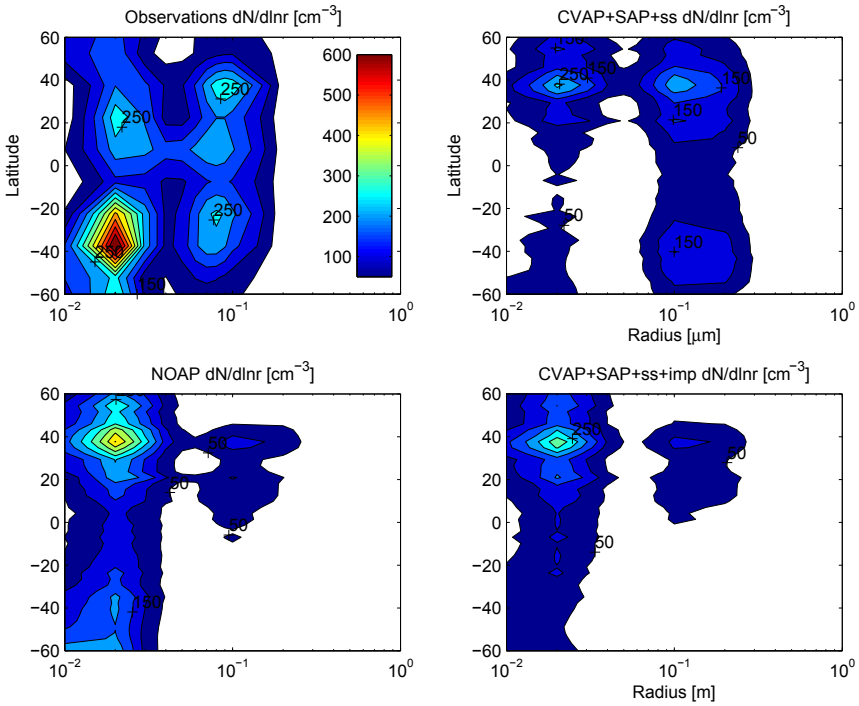

Figure 4.13: The zonal mean aerosol size distributions in the marine boundary layer for the simulations NOAP, SAP, CVAP+SAP, CVAP+SAP+ss, and CVAP+SAP+ss+imp and the observations of Heintzenberg et al. [2000], and similar to Hoose et al. [2008a].

agreement with the observations than for simulations NOAP and SAP.

4.5.3 Marine Boundary Layer Size Distributions

A comparison with the observed marine boundary layer aerosol size distributions of Heintzenberg et al. [2000] is shown in Figure 4.13. A similar comparison was shown by Hoose et al. [2008a] to demonstrate the increase in the number of accumulation mode aerosols with the implementation of a stratiform aerosol processing scheme. The implementation of convective aerosol processing does also influence the marine boundary layer size distributions. The agreement with the observed accumulation mode size distribution is best for the CVAP+SAP+ss simulation. The Aitken mode is under-predicted for all of our simulations, but agrees closest with the NOAP simulation. Aerosol processing reduces the Aitken mode since those aerosols coagulate with other aerosols in the stratiform and convective droplets, and are released by

droplet evaporation as larger aerosols. Future work to improve the boundary layer nucleation scheme and implementation of sea salt emissions into the Aitken mode in the model should help to reduce this under-prediction of the Aitken mode. This could also help improve the agreement for the simulation CVAP+SAP+ss+imp.

4.5.4 AERONET Size Distributions

Figures 4.14 shows the regional mean vertically integrated volume size distributions for 48 Aerosol Robotic Network (AERONET) sites for the year 2001 and for the simulations NOAP, SAP, CVAP+SAP+ss, and CVAP+SAP+ss+imp. AERONET is a world-wide network of automated ground-based sun photometers [Holben et al., 1998]. For the interested reader, a site-by-site comparison for these 48 sites is shown in Figs. B.1 - B.3. The retrieved aerosol optical parameters are used to derive vertically integrated aerosol size distributions. We have calculated these size distributions for our simulations following Hoose et al. [2008a].

$$\frac{dV(r)}{d\ln r} = \sum_k \Big(\sum_{j=1}^{7} \frac{4\pi}{3} r^3 \frac{N_{j,k}}{\sqrt{2\pi}\ln\sigma_j} \exp\Big(- \frac{2(r - r_{wet,j,k})^2}{\ln^2 \sigma_j} \Big) \Big) \frac{\Delta p_k}{g \rho_{air,k}} \tag{4.8}$$

where the index k runs over all vertical levels. $N_{j,k}$ is the aerosol number concentration of mode j and level k, $r_{wet,j,k}$ is the count median wet radius of mode j and level k, σ_j is the standard deviation of the lognormal distribution of the jth mode, Δp_k is the pressure difference between adjacent layers, g is the acceleration due to gravity, and $\rho_{air,k}$ is the air density.

The volume median accumulation mode wet radius is over-estimated in all simulations relative to the observations. Figure 4.13 also shows that the count median radius for the accumulation mode was over-estimated in the marine boundary layer. However, the modeled volume median coarse mode wet radius agrees closely with the AERONET observations in all simulations, except for the ocean sites. Applying separate scavenging fractions for the aerosol mass and number distributions could help to reduce the volume median accumulation mode radius, as was shown by Croft et al. [2010]. For all regions excepting those near the oceans, the volume of accumulation and coarse mode particles is under-estimated for the NOAP simulation. The

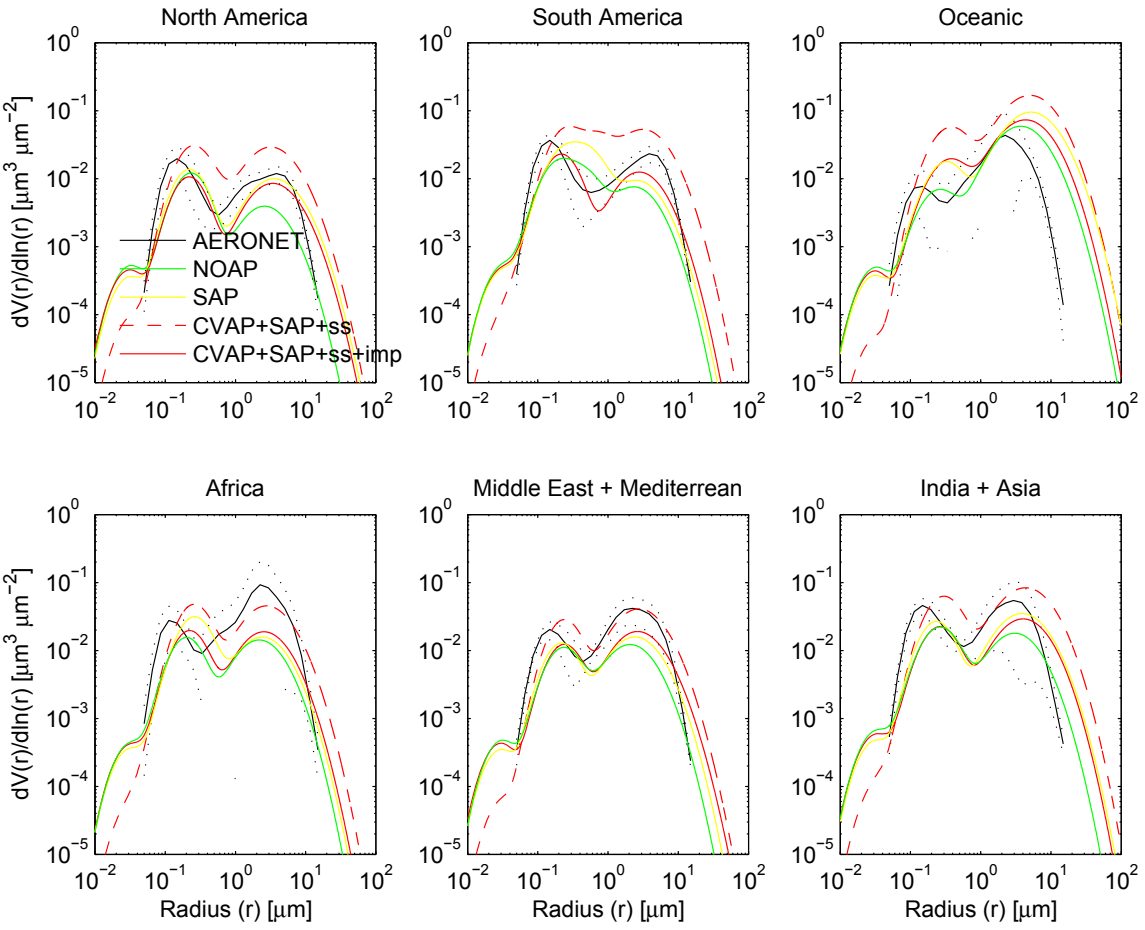

Figure 4.14: The annual and regional mean vertically integrated aerosol volume size distributions (dV(r)/dlnr in μm^{-3} μm^{-2}) for the simulations NOAP, SAP, CVAP+SAP+ss and CVAP+SAP+ss+imp and AERONET observations, compiling the site results from Figs. B.1 - B.3. The sites included in the regions are as follows: North America: All sites from Fig. B.1 except Guadaloup; South America: First 2 rows of Fig. B.2 and Mexico City. Oceanic: Remainder of Fig. B.2 and Guadaloup; Africa: First row of Fig. B.3 and Skukuza and Thala; Mediterranean and Middle East: third row of Fig. B.3 and El Arenosillo and IMC Oristano; India and Asia: Last row of Fig. B.3. The black dots are one standard deviation for the observations.

simulations CVAP+SAP+ss and CVAP+SAP+ss+imp agree more closely with the observations than for the NOAP and SAP simulations.

For the ocean sites, the coarse mode volume is over-estimated. For simulation CVAP+SAP (not shown), the over-estimation was severe, by almost two orders of magnitude relative to the observations. However, the revised sea salt emissions, and

in-cloud impaction for simulation CVAP+SAP+ss+imp give similar agreement as for simulation NOAP. As noted by Hoose et al. [2008a], assumptions about the emitted size of the sea salt particles in ECHAM5-HAM strongly influences these comparisons. Further improvements are still needed in this regard.

4.6 Summary and Outlook

A convective aerosol processing scheme has been coupled with the stratiform aerosol processing scheme of Hoose et al. [2008b] and implemented in the ECHAM5-HAM GCM. We found that aerosol cycling through convective clouds contributes significantly to global aerosol processing. For our simulations, in a global and annual mean sense, an aerosol cycled through clouds 0.4 to 1 times prior to removal from the atmosphere. Stratiform and convective clouds contributed about equally to this cycling. For our model, this estimate was shown to depend strongly on the assumptions about the rates that aerosol mass was taken up into cloud hydrometeors by collision processes and on the sea salt emissions parameterization. However, the nucleation scavenging for the accumulation and coarse modes may be under-estimated by our model as a result of the current method of apportioning of the number of activated aerosols between the three largest soluble/internally mixed modes. Thus, the role of impaction scavenging could be over-estimated for these simulations. Our estimate is lower than the previous estimate of Pruppacher and Jaenicke [1995] (3 cycles). However, as noted by Hoose et al. [2008a], the Pruppacher and Jaenicke [1995] estimate might be biased high due to an overestimate in the global liquid water path. For our simulations, the number of cycles through clouds was greater (1-3 cycles) for aerosol species that exist in the smaller size modes (sulfate, black carbon and particulate organic matter) as opposed to dust and sea salt (about 0.4-1 cycles).

The annual and global mean aerosol optical depth (AOD) was under-estimated by a factor of two for our standard model relative to satellite retrievals. The AOD was found to be strongly sensitive to the representation of aerosol processing by clouds. With the implementation of the convective-stratiform aerosol processing scheme, the global, annual mean AOD was overestimated by a factor of about three. The aerosol processing scheme represented the processes of aerosol-aerosol coagulation within

cloud droplets and crystals, followed by release by evaporation of clouds and precipitation. This particularly enhanced the number of accumulation mode aerosols (by a factor of about 2.5 for our simulations), which in turn enhanced the AOD. For these aerosol processing simulations the global, annual AOD was also highly sensitive to the sea salt emissions and in-cloud impaction scavenging parameterizations. Revisions to these latter two parameterizations yielded a global annual mean AOD for the aerosol processing simulation that was 0.9 of the satellite retrieval. The remaining AOD under-estimation was primarily over land, suggesting possible missing aerosol sources such as for organics.

Considering the sensitivity of our results to the representation of aerosol uptake into cloud droplets and crystals by impaction scavenging, we recommend future work to couple a more physically detailed size-dependent representation of collision scavenging, with the aerosol processing scheme. Future work should also examine the parameterization of nucleation scavenging for our model since the apportioning of the number of activated aerosols between the modes based on the fractional contribution of each mode to the total number of soluble/internally mixed aerosols larger than 25 and 35 nm for convective and stratiform clouds, respectively, could introduce biases. Particularly, the nucleation scavenging could be over-estimated for the Aitken mode and under-estimated for the accumulation and coarse modes. This bias could be greatest in regions of the middle troposphere where Aitken mode aerosols are most numerous. Additional work should also be directed towards making laboratory and field measurements of the collection rate of aerosols by cloud droplets and crystals for the size ranges typically found in the atmosphere. Particularly, thermophoretic, electric and turbulent forces can modify this collection, and should be incorporated in global models in a more physically detailed manner. Our results indicated that evaporation processes (and thus thermophoretic effects) are very important for clouds. The global and annual mean rate of aerosol mass release attributed to evaporation of both clouds and precipitation was about 0.8 of the rate of aerosol mass uptake, slightly lower than the Pruppacher and Jaenicke [1995] estimate of 0.91.

We conducted an analysis of the rates of aerosol mass transfer between the in-droplet, in-crystal and interstitial phases for our global simulations of coupled convective and stratiform aerosol processing. The rate of aerosol mass uptake into droplets by collision processes was about equal to the rate for nucleation processes for the carbonaceous aerosols. Collision processes dominated over nucleation for the rates of uptake into ice crystals for all aerosol species. For stratiform clouds, below-cloud evaporation of precipitation accounted for 10 to 25% of the total aerosol release by evaporation, whereas for convective clouds this fraction was less than 5%. Particularly for stratiform clouds, a more physical size-dependent treatment of below-cloud evaporation should be developed by coupling with the prognostic rain scheme of Posselt and Lohmann [2008]. Our results suggest this coupling is less important for convective clouds. Additionally, since convective clouds can have lifespans longer than the 30 minute time-step for our simulations, future work should examine the sensitivity of the modeled evaporation rates, and number of aerosol cloud cycles to the assumed time-step.

For the coupled stratiform-convective aerosol processing scheme, convective wet deposition was found to make a relatively smaller contribution to annual and global mean aerosol wet deposition (about 30%). Assuming less vigourous in-cloud collision scavenging of aerosols decreased the contribution of convective wet deposition to about 10% of the annual and global mean wet deposition.

Comparison with observations demonstrated that the coupled convective and stratiform aerosol processing scheme enhanced the number of accumulation mode aerosols in the marine boundary layer to give closer agreement with observations as compared to a simulation with no aerosol processing. Comparisons with Aerosol Robotic Network (AERONET) size distributions showed that the median wet radius of the accumulation mode was slightly overestimated for our simulations relative to the observations. The model agreed closely with the observations for the median coarse mode wet radius for all sites, except over the oceans. The volume of accumulation and coarse mode aerosols was enhanced and simulated best relative to the AERONET retrieval for simulations with the coupled convective and stratiform aerosol processing scheme.

4.7 Acknowledgements

The authors thank Lyatt Jaeglé, Sylvaine Ferrachat, Philipp Reuter, and Luis Ladino for helpful discussions. We thank Declan O'Donnell for his help with providing the kappa-Köhler water uptake scheme. We also thank Aaron van Donkelaar for providing AOD data, and the AERONET Principal Investigators and their staff for establishing and maintaining the 48 sites used in this investigation.

Chapter 5

Conclusion

5.1 Summary of this Present Work

Clouds influence aerosol distributions by 1) wet scavenging and subsequent deposition to the earth's surface and 2) processing and subsequent release to the atmosphere by evaporation processes. In this study, physically detailed size-dependent representations of below-cloud and in-cloud scavenging have been introduced into the ECHAM5-HAM global climate model. As well, the stratiform cloud aerosol processing scheme of Hoose et al. [2008a,b] was extended to convective clouds. Below-cloud impaction scavenging was found to contribute strongly to the global and annual mean mass deposition for sulfate (14%), black carbon (13%), particulate organic matter (10%), sea salt (23%) and dust (24%). Look-up tables were prepared that provide size-dependent below-cloud scavenging coefficients for both rain and snow. The tables were a compilation of work by Grover and Pruppacher [1977], Wang et al. [1978], Hall [1980]. For rain, the tables are a function of aerosol median radius for the lognormal mass and number distributions, and the rainfall rate. Separate coefficients were used to scavenge the mass and number distributions. For snow, the look-up tables are a function of the aerosol median radius and a fixed size for the snow was assumed. The predicted below-cloud scavenging was found to depend strongly on assumptions about the size distribution function for the rainfall. Assuming a distribution function for the raindrops as opposed to assuming monodisperse raindrops reduced the predicted global and annual sea salt burden by about 15%.

In the second part of this study, a size-dependent representation of in-cloud scavenging was introduced into the ECHAM5 HAM GCM. This included both nucleation and impaction scavenging. The representation of in-cloud scavenging was shown to strongly control predicted vertical profiles of aerosol mass mixing ratios. For the middle troposphere, the black carbon concentrations changed by more than one order of

magnitude. The in-cloud scavenging for mixed and ice phase clouds was found to be less vigorous for the more physically detailed parameterization as compared to the prescribed fractions of Stier et al. [2005]. The more physically detailed scheme gave closer agreement with vertical profiles of aerosol concentrations from recent aircraft campaigns.

In the final part of this study, a convective aerosol processing scheme was developed as a companion to the Hoose et al. [2008a,b] stratiform aerosol processing scheme. Considering stratiform and convective clouds together, an aerosol remote to source was found to cycle through clouds about 0.4 to 1 times prior to removal from the atmosphere. The modeled global and annual mean aerosol optical depth, and the predicted number of accumulation mode aerosols were found to depend strongly on the representation of aerosol processing by stratiform and convective clouds, and on the parameterizations for sea salt emissions, and in-cloud impaction scavenging. With the implementation of the convective-stratiform aerosol processing scheme, the global, annual mean AOD was overestimated by a factor of about 3 relative to satellite observations. Revisions to the sea salt emissions and parameterization of in-cloud impaction yielded an annual, global mean optical depth that was 0.9 of the satellite retrieval. This sensitivity to impaction scavenging could be over-estimated for our model since the nucleation scavenging of the accumulation and coarse modes could be under-estimated by the current methodology for apportioning the number of activated aerosols between the three largest soluble/internally mixed modes. Convective wet deposition was found to account for about 30% of the global and annual mean aerosol wet deposition. The remainder is attributed to stratiform wet deposition. Better agreement with AERONET size distributions was found with the implementation of the coupled stratiform-convective aerosol processing scheme as compared to the standard model without aerosol processing.

5.2 Outlook

5.2.1 Below-Cloud Scavenging by Rain

Following publication of this study on below-cloud scavenging, Wang et al. [2010] published an uncertainty assessment for current below-cloud scavenging by rain parameterizations. Our new parameterization was included in these comparisons. Wang et al. [2010] agreed with the result of this project that assumptions about the representation of the size-dependence of this process can strongly control predicted aerosol concentrations. This also motivates the need for ongoing field and laboratory studies coupled with modeling studies to validate that this process is represented correctly in global models for the full spectrum of collision partner sizes, and conditions of electric charge, turbulence and relative humidity.

5.2.2 Below-Cloud Scavenging by Snow

For this study, the assumption was made that the snow crystals were monodisperse. Future studies are needed to introduce a representation of different snow crystal habits and examine the influence that assumptions about snow crystal habit and size can have on the predicted scavenging. As well on-going field and laboratory are needed to provide a solid database on the scavenging efficiency of snow of various sizes and habits. For both snow and rain, there should be further investigations of the coalescence efficiency as a function of aerosol hygroscopicity and size.

5.2.3 In-Cloud Impaction Scavenging

There have been numerous theoretical studies on the collision efficiency for various size hydrometeors and aerosols. However, the available laboratory studies are a patchwork of collision partners sizes. Ongoing research is need to fill in the gaps. Particularly, laboratory studies are needed to measure collision efficiencies for the full spectrum of atmospheric aerosol sizes coupled with the full-spectrum of cloud droplet sizes, and under varying, and carefully controlled conditions of relative humidity, turbulence and electric charge. Recent work by Ladino et al. [submitted] is contributing towards

extending the laboratory data available in this field. There is also a need for laboratory and field studies on the collision efficiency for aerosol and ice crystal collisions for the full spectrum of collision partner sizes. Field studies by Baumgardner et al. [2008] showed that aerosol-ice crystal impaction was an important process for the incorporation of aerosols into crystals. This current work also found that collisions dominate over the nucleation processes for the rate of aerosol uptake into ice crystals, which motivates the need for ongoing laboratory and field investigations to increase understanding of this process.

5.2.4 Aerosol Processing

For the ECHAM5-HAM model, future work should include coupling a size-dependent representation of collision scavenging in clouds with the aerosol processing schemes. Also, the representation of nucleation scavenging should be re-examined. Particularly there should be a re-examination of the methodology for apportioning the number of activated aerosols between the modes based on the fractional contribution of each mode to the total number of soluble/internally mixed aerosols larger than 25 and 35 nm for convective and stratiform clouds, respectively. The current methodology could bias the nucleation scavenging to be over-estimated for the soluble/internally mixed Aitken mode, and under-estimated for the soluble/internally mixed accumulation and coarse modes, particularly for regions of the middle troposphere where Aitken mode aerosols are most numerous. The nucleation scavenging scheme should also be developed to include separate scavenging fractions for the aerosol mass and number distributions for the case of aerosol processing. This study found that convective clouds contribute rather comparably with stratiform clouds to the global mean processing of aerosols. This motivates the need for ongoing field studies coupled with modeling work related to aerosol processing by convective clouds. Additionally, since convective clouds can have lifespans longer than the 30 minute time-step for our simulations, future work should examine the sensitivity of the modeled evaporation rates, and number of aerosol cloud cycles to the assumed time-step. This was not possible to test for our simulations since low-resolution simulations with the GCM are subject to deteriorating meteorology.

5.2.5 Improving Aerosol Representation in ECHAM5-HAM

This study found that the aerosol optical depth over the oceans was highly sensitive to the sea salt emissions parameterizations for the aerosol processing simulations. A preliminary revision was made to the sea salt emissions scheme. Future work should be directed towards evaluating and refining the implementation of this temperature-dependent scheme. Additionally, comparison with marine boundary layer observations showed that the number of Aitken mode aerosols was under-estimated. Consideration should be given to the implementation of sea salt emission for this size range. Aerosol optical depth was under-estimated over the land. This may reflect missing aerosol sources such as for organics, nitrate, ammonium and convective in-cloud production of sulfate. Future work should be directed towards examining the representation of these sources in the ECHAM5-HAM.

Bibliography

W. A. Abdou, D. J. Diner, J. V. Matonchik, C. J. Bruegge, R. A. Kahn, B. J. Gaitley, K. A. Crean, L. A. Remer, and B. Holben. Comparison of coincident Multiangle Imaging SpectroRadiometer aerosol optical depths over land and ocean scenes containing Aerosol Robotic Network sites. *J. Geophys. Res.*, 110: doi:10.1029/2004JD004693, 2005.

P. J. Adams and J. H. Seinfeld. Predicting global aerosol size distributions in general circulation models. *J. Geophys. Res.*, 107:doi:10.1029/2001JD001010, 2002.

B. A. Albrecht. Aerosols, cloud microphysics, and fractional cloudiness. *Science*, 245: 1227 – 1230, 1989.

R. J. Andres and A. D. Kasgnoc. A time-averaged inventory of subaerial volcanic sulfur emissions. *J. Geophys. Res.*, 103:25 251 – 25 261, 1998.

C. Andronache. Estimated variability of below-cloud aerosol removal by rainfall for observed aerosol size distributions. *Atmos. Chem. Phys.*, 3:131 – 143, 2003.

C. Andronache, T. Groenholm, L. Laasko, V. Phillips, and A. Venalainen. Scavenging of ultrafine particles by rainfall at a boreal site: Observations and model estimations. *Atmos. Chem. Phys.*, 6:4739 – 4754, 2006.

R. T. Austin, A. J. Heymsfield, and G. L. Stephens. Retrieval of ice cloud microphysical parameters using the CloudSat millimeter-wave radar and temperature. *J. Geophys. Res.*, 114:doi:10.1029/2008JD010049, 2009.

M. Barth, P. J. Rasch, J. T. Kiehl, C. M. Benkovitz, and S. E. Schwartz. Sulfur chemistry in the NCAR CCM: Description, evaluation, features and sensitivity to aqueous chemistry. *J. Geophys. Res.*, 105:1387 – 1415, 2000.

D. Baumgardner, R. Subramanian, C. Twohy, J. Stith, and G. Kok. Scavenging of black carbon by ice crystals over the Northern Pacific. *Geophys. Res Lett.*, 35: doi:10.1029/2008GL035764, 2008.

K. V. Beard. Terminal velocity and shape of cloud and precipitation drops aloft. *J. Atmos. Sci.*, 33:851 – 864, 1976.

K. V. Beard and H. R. Pruppacher. A determination of the terminal velocity and drag of small water drops by means of a wind tunnel. *J. Atmos. Sci.*, 26:1066 – 1072, 1969.

D. A. Bell and C. P. R. Saunders. An experimental study of aerosol scavenging by hexagonal plate ice crystals. *Atmos. Res.*, 38:9 – 19, 1995.

J. D. Blando and B. J. Turpin. Secondary organic aerosol formation in cloud and fog droplets: a literature evaluation of plausibility. *Atmos. Environ.*, 34:1623 – 1632, 2000.

T. C. Bond, D. G. Streets, K. F. Yarber, S. M. Nelson, J.-H. Woo, and Z. Klimont. A technology-based global inventory of black and organic carbon emissions from combustion. *J. Geophys. Res.*, 109:doi:10.1029/2003JDO03697, 2004.

R. D. Borys, D. H. Lownthal, S. A. Cohn, and W. O. J. Brown. Mountaintop and radar measurements of anthropogenic aerosol effects on snow growth and snowfall rate. *Geophys. Res. Lett.*, 30:doi:10.1029/2002GL016855, 2003.

R. Brost, J. Feichter, and M. Heimann. Three-dimensional simulation of ^{7}Be in a global climate model. *J. Geophys. Res.*, 96, D12:22 423 – 22445, 1991.

C. Cagnazzo, E. Manzini, M. A. Giorgetta, P. M. De F. Forster, and J. J. Morcrette. Impact of an improved radiation scheme in the MAECHAM5 general circulation model. *Atmos. Chem. Phys.*, 7:2503 – 2515, 2007.

R. J. Charlson, S. E. Schwartz, J. M. Hales, R. D. Cess, J. A. Coakley, J. E. Hansen, and D. J. Hofmann. Climate forcing by anthropogenic aerosols. *J. Geophys. Res.*, 255:423 – 430, 1992.

S. S. Chen and R. A. Houze. Diurnal variation and life-cycle of deep convective systems over the tropical pacific warm pool. *Q. J. R. Meteorol. Soc.*, 123:357 – 388, 1997.

M. Chin, R. B. Rood, S.-J. Lin, J.-F. Muller, and A. M. Thompson. Atmospheric sulfur cycle in the global model GOCART: Model description and global properties. *J. Geophys. Res.*, 105:24 661 – 24 687, 2000.

P. Chylek and J. Wong. Effect of absorbing aerosols on global radiation budget. *Geophys. Res. Lett.*, 22:929 – 931, 1995.

J. Cofala, M. Amann, and R. Mechler. Scenarios of world anthropogenic emissions of air pollutants and methane up to 2030, tech. rep., International Institute for Applied Systems Analysis (IIASA), laxenburg, austria, available from http://www.iiasa.ac.at/rains/global_ emiss/global_ emiss.html. 2005.

W. Cotton, R. Tripoli, R. Rauber, and E. Mulvihill. Numerical simulation of the effects of varying ice crystal nucleation rates and aggregation processes in orographic snowfall. *J. Clim. and Appl. Meteorol.*, 25:1658 – 1680, 1986.

B. Croft, U. Lohmann, R. V. Martin, P. Stier, S. Wurzler, J. Feichter, C. Hoose, U. Heikkilä, A. van Donkelaar, and S. Ferrachat. Influences of in-cloud aerosol scavenging parameterizations on aerosol concentrations and wet deposition in ECHAM5-HAM. *Atmos. Phys. Chem.*, 10:1511 – 1543, 2010.

B. Croft, U. Lohmann, R. V. Martin, P. Stier, S. Wurzler, J. Feichter, R. Posselt, and S. Ferrachat. Aerosol size-dependent below-cloud scavenging by rain and snow in the ECHAM5-HAM. *Atmos. Chem. Phys.*, 9:4653 – 4675, 2009.

S. Crumeyrolle, L. Gomes, P. Tulet, A. Matsuki, A. Schwarzenboeck, and K. Crahan. Increase of the aerosol hygroscopicity by cloud processing in a mesoscale convective system: A case study from the amma campaign. *Atmos. Chem. Phys.*, 8:6907 – 6924, 2008.

F. Dentener, J. Drevet, J. F. Lamarque, I. Bey, B.Eickhout, A. M. Fiore, D. Haiglustaine, L. W. Horowitz, M. Krol, U. C. Lawrence, C. Galy-Lacaux, S. Rast, D. Shindell, D. Stevenson, T. Van Noije, C. Atherton, N. Bell, D. Bergman, T. Butler, J. Cofala, B. Colins, R. Doherty, K. Ellingsen, J. Galloway, M. Gauss, V. Montanaro, J. F. Müller, G. Pitari, J. Rodriguez, M. Sanderson, F. Solomon, S. Strahan, M. Schultz, K. Sudo, S. Szopa, and O. Wild. Nitrogen and sulfur deposition on regional and global scales: A multimodel evaluation. *Global Biogeochem. Cycles*, 20:GB4003,doi:10.1029/2005GB002672, 2006a.

F. Dentener, S. Kinne, T. Bond, O. Boucher, J. Cofala, S. Generoso, P. Ginoux, S. Gong, J. Hoelzemann, A. Ito, L. Marelli, J. E. Penner, J.-P. Putaud, C. Textor, M. Schulz, G. R. van der Werf, and J. Wilson. Emissions of primary aerosol and precursor gases in the years 2000 and 1750: Prescribed data-sets for AeroCom. *Atmos. Phys. Chem.*, 6:4321 – 4344, 2006b.

A. L. Dick. A simple model for air/snow fractionation of aerosol components over the Antarctic Peninsula. *J. Atmos. Chem.*, 11:179 – 196, 1990.

K. Diehl and S. Wurzler. Heterogeneous drop freezing in the immersion mode: Model calculations considering soluble and insoluble particles in drops. *J. Atmos. Sci.*, 61:2063 – 2072, 2004.

D. D. Diner, B. H. Braswell, R. Davies, N. Gobron, J. Hu, Y. Jin, R. A. Kahn, Y. Knyazikhin, N. Loeb, J.-P. Muller, A. W. Nolin, B. Pinty, C. B. Schaaf, G. Seiz, and J. Stroeve. The value of multiangle measurements for retrieving structurally and radiatively consistent properties of cloud, aerosols and surfaces. *Remote Sensing the Environment*, 97:495 – 518, 2005.

R. C. Easter, S. J. Ghan, Y. Zhang, R. D. Saylor, E. G. Chapman, N. S. Laulainen, H. Abdul-Razzak, L. R. Leung, X. Bian, and R. A. Zaveri. Mirage: Model description and evaluation of aerosols and trace gases. *J. Geophys. Res.*, 106:20 311 – 20 332, 2004.

A. M. L. Ekman, C. Weng, J. Ström, and R. Krejci. Explicit simulation of aerosol physics in a cloud-resolving model: Aerosol transport and processing in the free troposphere. *J. Atmos. Sci.*, 63:682 – 696, 2006.

Y. Fang, A. Fiore, L. Horowitz, A. Gnandesikan, I. Held, G. Chen, G. Vecchi, and H. Levy. The impacts of changing transport and precipitation on pollutant distribution in a future climate. *J. Geophys. Res.*, submitted.

J. Feichter, R. A. Brost, and M. Heimann. Three-dimensional modeling of the concentration and deposition of ^{210}Pb aerosols. *J. Geophys. Res.*, 96:22 447 – 22 460, 1991.

J. Feichter, E. Kjellstrom, H. Rodhe, F. Dentener, J. Lelieveld, and G.-J. Roelofs. Simulation of the tropospheric sulfur cycle in a global climate model. *Atmos. Environ.*, 30:1693 – 1707, 1996.

J. Feng. A size-resolved model for below-cloud scavenging of aerosols by snowfall. *J. Geophys. Res.*, 114:doi:10.1029/2008JD011012, 2009.

R. Ferraro, F. Weng, N. Grody, and A. Basist. An eight year (1987-1994) time series of rainfall, clouds, water vapor, snow-cover, and sea-ice derived from SSM/I measurements. *B. Am. Meteorol. Soc.*, 77:891 – 905, 1996.

P. Forster, V. Ramaswamy, P. Artaxo, T. Berntsen, R. Betts, D.W. Fahey, J. Haywood, J. Lean, D.C. Lowe, G. Myhre, J. Nganga, R. Prinn, G. Raga, M. Schulz, and R. Van Dorland. Changes in atmospheric constituents and radiative forcing. In Climate Change 2007: The physical science basis. Contribution of working group I to the fourth assessment report of the Intergovernmental Panel on Climate Change, [S. Solomon, D. Qin, M. Manning, Z. Chen, M. Marquis, K. B. Averyt, M. Tignor and H. L. Miller (eds.)]. Cambridge University Press. pages 129 –234, 2007.

A. V. Gambheer and G. S. Bhat. Life cycle characteristics of deep cloud systems over the Indian region using INSAT-1B pixel data. *Mon. Wea. Rev.*, 128:4071 – 4083, 2000.

F. H. Garner and D. A. Lihou. *DECHEMA Monographien*, 55:155, 1965.

S. J. Ghan, C. C. Chuang, and J. E. Penner. A parameterization of cloud droplet nucleation. Part I: Single aerosol type. *Atmos. Res.*, 30:198 – 221, 1993.

S. J. Ghan and R.C. Easter. Impact of cloud-borne aerosol representation on aerosol direct and indirect effects. *Atmos. Chem. Phys.*, 6:4163 – 4174, 2006.

S. L. Gong, L. A. Barrie, and J.-P. Blanchet. Modeling sea-salt aerosols in the atmosphere: 1. Model development. *J. Geophys. Res.*, 102:3805–3818, 1997.

S. L. Gong, L. A. Barrie, J.-P. Blanchet, K. vonSalzen, U. Lohmann, G. Lesins, L. Spacek, L. M. Zhang, E. Girard, H. Lin, R. Leaitch, H. Leighton, P. Chylek, and P. Huang. Canadian aerosol module: A size-segregated simulation of atmospheric aerosol processes for climate and air quality models: 1. Module developments. *J. Geophys. Res.*, 108:doi:10.1029/2001JD002002, 2003.

W. Gong, A. P. Dastoor, V. S. Bouchet, S. Gong, P. A. Makar, M. D. Moran, B. Pabla, S. Menard, L.-P. Crevier, S. Cousineau, and S. Venkatesh. Cloud processing of gases and aerosols in a regional air quality model (AURAMS). *Atmos. Res.*, 82:248 – 275, 2006.

S. Greenfield. Rain scavenging of radioactive particulate matter from the atmosphere. *J. Meteorol.*, 14:115 – 125, 1957.

T. J. Greenwald, G. L. Stephens, T. H. Vonder Haar, and D. L. Jackson. A physical retrieval of cloud liquid water over the global oceans using Special Sensor Microwave/Imager (SSM/I) observations. *J. Geophys. Res.*, 98:18 471 – 18 488, 1993.

S. N. Grover and H. R. Pruppacher. A numerical determination of the efficiency with which spherical aerosol particles collide with spherical water drops due to inertial impaction and phoretic and electric forces. *J. Atmos. Sci.*, 34:1655 – 1663, 1977.

A. Guenther, C. N. Hewitt, D. Erickson, R. Fall, C. Geron, T. Greadel, P. Harley, L. Klinger, M. Lerdau, W. A. McKay, T. Pierce, B. Scholes, R. Steinbrecher, R. Tallamraju, J. Taylor, and P. Zimmerman. A global model of natural volatile organic compound emissions. *J. Geophys. Res.*, 100:8873–8892, 1995.

R. Gunn and G. D. Kinzer. The terminal velocity of fall for water droplets in stagnant air. *J. Meteorol.*, 6:243–248, 1949.

W. D. Hall. A detailed microphysical model within a two-dimensional dynamic framework: Model description and preliminary results. *J. Atmos. Sci.*, 37:2486 – 2507, 1980.

M. Hallquist, J. C. Wenger, U. Baltensperger, Y. Rudich, D. Simpson, M. Claeys, J. Dommen, N. M. Donahue, C. George, A. H. Goldstein, J. F. Hamilton, H. Herrmann, T. Hoffmann, Y. Iinuma, M. Jang, M. E. Jenkin, J. L. Jimenez, A. Kiendler-Scharr, W. Maenhaut, G. McFiggans, T. F. Mentel, A. Monod, A. S. H. Prevot, J. H. Seinfeld amd J. D. Surratt, R. Szmigielski, and J. Wildt. The formation, properties and impact of secondary organic aerosol: Current and emerging issues. *Atmos. Chem. Phys.*, 9:5155 – 5236, 2009.

M. M. Halmer, H.-U. Schmincke, and H.-F. Graf. The annual volcanic gas input into the atmosphere, in particular into the stratosphere: A global data set for the past 100 years. *Journal of Volcanology and Geothermal Research*, 115:511 – 528, 2002.

Q. Han, W. B. Rossow, J. Chou, and R. Welch. Global variation of column droplet concentration in low-level clouds. *Geophys. Res Lett.*, 25:1419 – 1422, 1998.

J. Hansen, L. Nazarenko, R. Reudy, M. Sato, J. Willis, A. Del Genio, D. Koch, A. Lacis, K. Lo, S. Menon, T. Novakov, J. Perlwitz, G. Russell, G. A. Schmidt, and

N. Tausnev. Earth's energy imbalance: Confirmation and implications. *Science*, 308:1431 – 1435, 2005.

C. L. Heald, D. A. Ridley, S. M. Kriedenweis, and E. E. Drury. Satellite observations cap the atmospheric organic aerosol budget. *Geophys. Res. Lett.*, 37, L24808: doi:10.1029/2010GL045095, 2010.

U. Heikkilä. Modeling of the atmospheric transport of the cosmogenic radionuclides 10Be and 7Be using the ECHAM5-HAM General Circulation Model, PhD thesis, Dissertation ETH no. 17516, available from http://e-collection.ethbib.ethz.ch. 2007.

U. Heikkilä, J. Beer, and J. Feichter. Modeling cosmogenic radionuclides ^{10}Be and ^{7}Be during the Maunder Minimum using the ECHAM5-HAM General Circulation Model. *Atmos. Chem. Phys.*, 8:2797 – 2809, 2008.

U. Heikkilä, J. Beer, and J. Feichter. Meridional transport and deposition of atmospheric ^{10}Be. *Atmos. Chem. Phys.*, 9:515 – 527, 2009.

J. Heintzenberg, D. C. Covert, and R. van Dingenen. Size distributions and chemical composition of marine aerosols: A composition and review. *Tellus*, 52B:1104 – 1122, 2000.

J. S. Henzing, D. J. L. Olivie, and P. F. J. Van Velthoven. A parameterization of size resolved below cloud scavenging of aerosols by rain. *Atmos. Chem. Phys.*, 6:3363 – 3375, 2006.

B. N. Holben, T. F. Eck, I. Slutsker, D. Tanre, J. P. Buis, A. Setzer, E. Vermote, J. A. Reagan, Y. J. Kaufman, T. Nakajima, F. Lavenu, I. Jankowiak, and A. Smirnov. Aeronet - a federated instrument network and data archive for aerosol characterization. *Remote Sensing the Environment*, 66:1 –16, 1998.

C. Hoose, U. Lohmann, R. Bennartz, B. Croft, and G. Lesins. Global simulations of aerosol processing in clouds. *Atmos. Chem Phys.*, 8:6939 – 6963, 2008a.

C. Hoose, U. Lohmann, P. Stier, B. Verheggen, and E. Weingartner. Aerosol processing in mixed-phase clouds in ECHAM5-HAM: Model description and comparison to obserations. *J. Geophys. Res.*, 113:doi:10.1029/2007JD009251, 2008b.

M. Z Jacobson. Development of mixed-phase clouds from multiple aerosol size distributions and the effect of the clouds on aerosol removal. *J. Geophys. Res.*, 108: doi:10.1029/2002JD002691, 2003.

L. Jaeglé, P. K. Quinn, T. Bates, B. Alexander, and J.-T. Lin. Global distribution of sea salt aerosols: New constraints from in situ and remote sensing observations. *Atmos. Chem. Phys. Discuss.*, 10:25 687 – 25 742, 2010.

H. Jiang, H. Xue, A. Teller, G. Feingold, and Z. Levin. Aerosol effects on the lifetime of shallow cumulus. *Geophys. Res. Lett.*, 33:doi:10.1029/2006GL026024, 2006.

A. Jones, D. L. Roberts, M. J. Woodage, and C. E. Johnson. Indirect sulfate aerosol forcing in a climate model with an interactive sulphur cycle. *J. Geophys. Res.*, 106: 20 293 – 20 310, 2001.

J. Joss and A. Waldvogel. Raindrop size distribution and sampling size errors. *J. Atmos. Sci.*, 26:566 – 569, 1969.

C. H. Jung and K. W. Lee. Filtration of fine particles by multiple liquid drop and gas bubble systems. *Aeros. Sci. and Tech.*, 29:389 – 401, 1998.

M. Kanakidou, J. H. Seinfeld, S. N. Pandis, I. Barnes, F. J. Dentener, M. C. Facchini, R. Van Dingenen, B. Ervens, A. Nenes, C. J. Nielsen, E. Swietlicki, J. P. Putaud, Y. Balkanski, S. Fuzzi, J. Horth, G. K. Moortgat, R. Winterhalter, C. E. L. Myhre, K. Tsigaridis, E. Vignati, E. G. Stephanou, and J. Wilson. Organic aerosol and global climate modelling: A review. *Atmos. Chem and Phys.*, 5:1053 – 1123, 2005.

A. Kettle and M. Andreae. Flux of the dimethylsulfide from the oceans: A comparison of updated data sets and flux models. *J. Geophys. Res.*, 105:26 793 – 26 808, 2000.

A. P. Khain, D. Rosenfeld, and A. Pokrovsky. Simulating convective clouds with sustained supercooled liquid water down to -37.5 C using a spectral microphysics model. *Geophys. Res. Lett.*, 28:3887 – 3890, 2001.

A. P. Khain, D. Rosenfeld, and A. Pokrovsky. Aerosol impacts on the dynamics and microphysics of deeep convective clouds. *Q. J. R. Meteorol. Soc.*, 131:2639 – 2663, 2005.

J. T. Kiehl and K. Trenberth. Earth's annual global mean energy budget. *B. Amer. Meteorol. Soc.*, 78:197 – 208, 1997.

S. Kinne. Remote sensing data combinations - superior global maps for aerosol optical depth, in: Satellite aerosol remote sensing over land, editted by: A. A. kokhanovsky and G. De Leeuw, Springer. 2009.

J. D. Klett and M. H. Davis. Theoretical collision efficiencies of cloud droplets at small reynolds numbers. *J. Atmos. Sci.*, 30:107 – 117, 1973.

D. Koch, D. Jacob, and W. Graustein. Vertical transport of tropospheric aerosols as indicated by ^{7}Be and ^{210}Pb in a chemical tracer model. *J. Geophys. Res.*, 101, D13: 18 651 – 18 666, 1996.

D. Koch, G. A. Schmidt, and C. Field. Sulfur, sea salt and radionuclide aerosols in GISS ModelE. *J. Geopys. Res.*, 111, D06206:doi:10.1029/2004JD005550, 2006.

D. Koch, M. Schultz, S. Kinne, T. C. Bond, Y. Balkanski, S. Bauer, T. Bernsten, O. Boucher, M. Chin, A. Clarke, N. De Luca, F. Dentener, T. Diehl, O. Dubovik, R. Easter, D. W. Fahey, J. Feichter, D. Fillmore, S. Freitag, S. Ghan, P. Ginoux, S. Gong, L. Horowitz, T. Iversen, A. Kirkevag, Z. Klimont, Y. Kondo, M. Krol, X. Lui, C. McNaughton, R. Miller, V. Montanaro, N. Moteki, G. Myhre, J. E. Penner, Ja. Perlwitz, G. Pitari, S. Reddy, L. Sahu, H. Sakamoto, G. Schuster, J. P. Schwartz, O. Seland, J. R. Spackman, P. Stier, N. Takegawa, T. Takemura, C. Textor, J. A. van Aardenne, and Y. Zhoa. Evaluation of black carbon estimations in global aerosol models. *Atmos. Chem. Phys.*, 9:9001 – 2026, 2009.

D. Koch, M. Schultz, S. Kinne, T. C. Bond, Y. Balkanski, S. Bauer, T. Bernsten, O. Boucher, M. Chin, A. Clarke, N. De Luca, F. Dentener, T. Diehl, O. Dubovik, R. Easter, D. W. Fahey, J. Feichter, D. Fillmore, S. Freitag, S. Ghan, P. Ginoux, S. Gong, L. Horowitz, T. Iversen, A. Kirkevag, Z. Klimont, Y. Kondo, M. Krol, X. Lui, C. McNaughton, R. Miller, V. Montanaro, N. Moteki, G. Myhre, J. E. Penner, Ja. Perlwitz, G. Pitari, S. Reddy, L. Sahu, H. Sakamoto, G. Schuster, J. P. Schwartz, O. Seland, J. R. Spackman, P. Stier, N. Takegawa, T. Takemura, C. Textor, J. A. van Aardenne, and Y. Zhoa. Corrigendum to evaluation of black carbon estimations in global aerosol models. *Atmos. Chem. Phys.*, 10:79 – 81, 2010.

H. Köhler. The nucleus in and the growth of hygroscpic droplets. *Trans. Farad. Soc.*, 32:1152 – 1161, 1936.

L. Kownacka. Vertical distributions of beryllium-7 and lead-210 in the tropospheric and lower stratospheric air. *Nukleonika*, 47:79 – 82, 2002.

J. H. Kroll and J. H. Seinfeld. Chemistry of secondary aerosol: Formation and evolution of low-volatility organics in the atmosphere. *Atmos. Environ.*, 42:3593 – 3624, 2008.

L. Ladino, O. Stetzer, B. Hattendorf, D. Günther, B. Croft, and U. Lohmann. Experimental study of collection efficiencies between submicron aerosols and cloud droplets. *J. Atmos. Sci.*, submitted.

R. C. Levy, L. A. Remer, S. Mattoo, E. F. Vermote, and Y. J. Kaufman. Second-generation operational algorithm: Retrieval of aerosol properties over land from inversion of Moderate Resolution Imaging Spectroradiometer spectral reflectance. *J. Geophys. Res.*, 112, D13211:doi:10.1029/2006JD007811, 2007.

C. L. Lin and S.C. Lee. Collision efficiency of water drops in the atmosphere. *J. Atmos. Sci.*, 32:1412 – 1418, 1975.

H. Lin and W. R. Leaitch. Development of an in-cloud aerosol activation parameterization for cliamte modelling, in: Proceedings of the WMO workshop on measurement of cloud properties for forecasts of weather, air quality and climate, World Meteorol. Organ., Geneva. pages pp. 328 – 335, 1997.

S. J. Lin and R. B. Rood. Multidimensional flux form semi-lagrangian transport. *Mon. Wea. Rev.*, 124:2046 – 2068, 1996.

H. Liu, D. J. Jacob, I. Bey, and R. M. Yantosca. Constraints from 210Pb and 7Be on wet deposition and transport in a global three-dimensional chemical tracer model driven by assimilated meteorolgical fields. *J. Geophys. Res.*, 106:12109 – 12128, 2001.

U. Lohmann. A glaciation indirect effect caused by soot aerosols. *Geophys. Res. Lett.*, 29:doi:10.1029/2001GL014357, 2002.

U. Lohmann. Global anthropogenic aerosol effects on convective clouds in ECHAM5-HAM. *Atmos. Chem. Phys.*, 8:2115 – 2131, 2008.

U. Lohmann and K. Diehl. Sensitivity studies of the importance of dust ice nuclei for the indirect aerosol effect on stratiform mixed-phase clouds. *J. Atmos. Sci.*, 63:968 – 982, 2006.

U. Lohmann and J. Feichter. Global indirect aerosol effects: A review. *Atmos. Chem and Phys.*, 5:715 – 737, 2005.

U. Lohmann and B. Kärcher. First interactive simulations of cirrus clouds formed by homogeneous freezing in the ECHAM general circulation model. *J. Geophys. Res.*, 107, D(10), 4105:doi:10.1029/2001JD000767, 2002.

U. Lohmann, P. Spichtinger, S. Jess, T. Peter, and H. Smit. Cirrus cloud formation and ice supersaturated regions in a global climate model. *Environ. Res. Lett.*, 3: doi:10.1088/1748–9326/3/4/045022, 2008.

U. Lohmann, P. Stier, C. Hoose, S. Ferrachat, S. Kloster, E. Roeckner, and J. Zhang. Cloud microphysics and aerosol indirect effects in the global climate model ECHAM5-HAM. *Atmos. Chem. Phys.*, 7:3425 – 3446, 2007.

J. S. Marshall and W. M. Palmer. The distribution of raindrops with size. *J. Meteorol.*, 5:165 – 166, 1948.

J. J. Martin, P. K. Wang, and H. R. Pruppacher. A theoretical determination of the efficiency with which aerosol particles are collected by simple ice crystal plates. *J. Atmos. Sci.*, 37:1628 – 1638, 1980.

J. V. Martonchik, D. J. Diner, K. A. Crean, and M. A. Bull. Regional aerosol retrieval results from MISR. *IEEE Transactions on Geoscience and Remote Sensing*, 40:1520 – 1531, 2002.

J. Masarik and J. Beer. Simulation of particle fluxes and cosmogenic nuclide production in the earth's atmosphere. *J. Geophys. Res.*, 104:12 099 – 12 111, 1999.

N. L. Miller and P. K. Wang. Theoretical determination of the efficiency of aerosol particle collection by falling columnar ice crystals. *J. Atmos. Sci.*, 46:1656 – 1663, 1989.

N. L. Miller and P. K. Wang. A theoretical determination of the collection rates of aerosol particles by falling ice crystal plates and columns. *Atmos. Environ.*, 25A: 2593 – 2606, 1991.

E. J. Mlawer, S. J. Taubman, P. D. Brown, M. J. Iacono, and S. A. Clough. Radiative transfer for inhomogeneous atmosphere: RRTM, a validated correlated-k model for the longwave. *J. Geophys. Res.*, 102:16 663 – 16 682, 1997.

J.-J. Morcrette, S. A. Clough, E. J. Mlawer, and M. J. Iacono. Impact of a validated radiative transfer scheme, RRTM, on the ECMWF model cliamte and 10-day forecasts, ECMWF, Reading, UK, technical memorandum 252 edn. 1998.

M. Murakami, K. Kikuchi, and C. Magono. Experiments on aerosol scavenging by natural snow crystals: Part I: Collection efficiency of uncharged snow crystals for micron and sub-micron particles. *J. Meterol. Soc. Japan*, 63:119 – 121, 1985.

P. Nightingale, G. Malin, C. Law, A. Watson, P. Liss, M. Liddicoat, J. Boutin, and R. Upstill-Goaddard. In situ evaluation of air-sea gas exchange parameterizations using novel conservative and volatile tracers. *Global Biogeochem. Cycles*, 14:373 – 387, 2000.

T. E. Nordeng. Extended versions of the convective parameterization scheme at ECWMF and their impact on the mean and transient activity of the model in the tropics, ECMWF, Reading, UK, technical memorandum 206 edn. 1994.

R. J. Park, D. J. Jacob, P. I. Palmer, A. D. Clarke, R. J. Weber, M. A. Zondlo, F. L. Eisele, A. R. Bandy, D. C. Thornton, G. W. Sachse, and T. C. Bond. Satellite observations cap the atmospheric organic aerosol budget. *J. Geophys. Res.*, 110, D11205:doi:10.1029/2004JD005432, 2005.

M. Petters and S. Kreidenweis. A single parameter representation of hygroscopic growth and cloud condensation nucleus activity. *Atmos. Chem and Phys.*, 7:1961 – 1971, 2007.

M. Pham, J.-F. Muller, G. Brasseur, C. Granier, and G. Megie. A three-dimensional study of the tropospheric sulfur cycle. *J. Geophys. Res.*, 100:26 061 – 26 092, 1995.

R. L. Pitter. Scavenging efficiency of electrostatically charged thin ice plates and spherical aerosol particles. *J. Atmos. Sci.*, 34:1797 – 1800, 1977.

R. Posselt and U. Lohmann. Introduction of prognostic rain in ECHAM5: Design and single column model simulations. *Atmos. Phys. Chem.*, 8:2949 – 2963, 2008.

H. R. Pruppacher and R. Jaenicke. The processing of water vapor and aerosol by atmospheric clouds, a global estimate. *Atmos. Res.*, 38:283 – 295, 1995.

H. R. Pruppacher and J. D. Klett. Microphysics of clouds and precipitation. *Kluwer Academic Publishers*, Dordrecht, Boston, London, 1997.

V. Ramanthan, R. Cess, E. Harrison, P. Minnis, B. Barkstrom, E. Ahmad, and D. Hartmann. Cloud-radiative forcing and climate: Results from the earth radiation budget experiment. *Science*, 243:57 – 63, 1989.

P. J. Rasch, J. Feitcher, J. Law, N. Mahowald, J. Penner, C. Benkovitz, C. Genthon, C. Giannakopoulos, P. Kasibhatla, D. Koch, H. Levy, T. Maki, M. Prather, D. L. Roberts, G.-J. Roelefs, D. Stevenson, Z. Stockwell, S. Taguchi, M. Kritz, M. Chipperfield, D. Baldocchi, P. McMurry, L. Barry, Y. Balkanski, R. Chatfield, E. Kjellstrom, M. Lawrence, H. N. Lee, J. Lelieveld, K. J. Noone, J. Seinfeld, G. Stenchikov, S. Schwartz, C. Walcek, and D. Williamson. A comparison of scavenging and deposition processes in global models: Results from the WCRP Cambridge Workshop of 1995. *Tellus*, 52B:1025 – 1056, 2000.

L. A. Remer, Y. J. Kaufman, D. Tanre, S. Mattoo, D. A. Chu, J. V. Martins, R.-R. Li, C. Ichoku, R. C. Levy, R. G. Kleidman, T. F. Eck, E. Vermote, and B. N. Holben. The MODIS aerosol algorithm, products and validation. *J. Atmos. Sci.*, 62:947 – 973, 2005.

E. Roeckner, G. Baeuml, L. Bonventura, R. Brokopf, M. Esch, M. Giorgetta, S. Hagemann, I. Kirchner, L. Kornblueh, E. Manzini, A. Rhodin, U. Schlese, U. Schilzweida, and A. Tompkins. The atmospheric general circulation model ECHAM5. Part I: Model description, Report 349, Max Planck Institute for Meteorology, Hamburg, Germany, available from http://www.mpimet.mpg.de. 2003.

G. J. Roelefs, P. Stier, J. Feichter, E. Vignati, and J. Wilson. Aerosol activation and cloud processing in the global aerosol-climate model ECHAM5-HAM. *Atmos. Chem. Phys.*, 6:2389 – 2399, 2006.

D. Rosenfeld and W. L. Woodley. Deep convective clouds with sustained supercooled liquid water down to -37.5 C. *Nature*, 405:440 – 442, 2000.

W. B. Rossow and R. A. Schiffer. Advances in understanding clouds from ISCCP. *B. Am. Meteorol. Soc.*, 80:2261 – 2287, 1999.

D. P. Sauter and P. K. Wang. An experimental study of the scavenging of aerosol particles by natural snow crystals. *J. Atmos. Sci.*, 46:1650 – 1655, 1989.

R. J. Schlamp, S. N. Grover, and H. R. Pruppacher. A numerical investigation of the effect of electric charges and vertical external electric fields on the collision efficiency of cloud drops. *J. Atmos. Sci.*, 33:1747 –1755, 1976.

M. Schultz, G. deLeeuw, and Y. Balkanski. Emission of atmospheric trace compounds, chap. Sea-salt aerosol source functions and emissions, pp333-359, ed. Kluwer. 2004.

J. H. Seinfeld and S. N. Pandis. Atmospheric chemistry and physics. *Wiley, New York*, 1998.

W. G. N. Slinn. Precipitation scavenging in atmospheric science and power production, Ch. 11, editted by D. Randerson, Tech. Inf. Cent., Off. of Sci. and Techn. Inf., Dep. of Energy, Washington, D. C. pages 466 – 532, 1984.

S. Solomon, D. Qin, M. Manning, R.B. Alley, T. Berntsen, N.L. Bindoff, Z. Chen, A. Chidthaisong, J.M. Gregory, G.C. Hegerl, M. Heimann, B. Hewitson, B.J. Hoskins, F. Joos, J. Jouzel, V. Kattsov, U. Lohmann, T. Matsuno, M. Molina, N. Nicholls, J. Overpeck, G. Raga, V. Ramaswamy, J. Ren, M. Rusticucci, R. Somerville, T.F. Stocker, P. Whetton, R.A. Wood, and D. Wratt. Technical summary. in: Climate change 2007: The physical science basis. Contribution of Working Group I to the fourth assessment report of the Intergovernmental Panel on Climate Change [S. Solomon, D. Qin, M. Manning, Z. Chen, M. Marquis, K. B. Averyt, M. Tignor and H. L. Miller (eds.)]. Cambridge University Press. 2007.

N. Song and D. Lamb. Experimental investigations of ice in supercooled clouds: Part II: Scavenging of an insoluble aerosol. *J. Atmos. Sci.*, 51:104 – 116, 1994.

P. Spichtinger and K. M. Gierens. Modelling of cirrus clouds - part 1a: Model description and validation. *Atmos. Chem. Phys.*, 9:685 – 706, 2009.

P. Stier, J. Feichter, S. Kinne, S. Kloster, E. Vignati, J. Wilson, L. Ganzeveld, I. Tegen, M. Werner, Y. Balkanski, M. Schultz, O. Boucher, A. Minikin, and A. Petzold. The aerosol-climate model ECHAM5-HAM. *Atmos. Chem. Phys.*, 5:1125 – 1156, 2005.

T. Storelvmo, J.-E. Kristjansson, and U. Lohmann. Aerosol influences on mixed-phase cloud in CAM-Oslo. *J. Atmos. Sci.*, 60:3214 – 3230, 2008.

T. Takemura, T. Nakajima, O. Dubovik, B. N. Holben, and S. Kinne. Single scattering albedo and radiative forcing of various aerosol species with a global three-dimensional model. *J. Clim.*, 15:333 – 352, 2002.

I. Tegen, S. P. Harrison, K. Kohfeld, I. C. Prentice, M. Coe, and M. Heimann. Impact of vegetation and preferential source areas on global dust aerosol: Results from a model study. *J. Geophys. Res.*, 107:4576 – 4597, 2002.

C. Textor, M. Schulz, S. Guibert, S. Kinne, Y. Balkanski, S. Bauer, T. Berntsen, T. Berglen, O. Boucher, M. Chin, F. Dentener, R. Easter, D. Fillmore, S. Ghan, P. Ginoux, S. Gong, A. Grini, J. Hendricks, L. Horowitz, P. Huang, I. Isaksen, T. Iversen, S. Kloster, D. Koch, A. Kirkevag, J. E. Kristjansson, M. Krol, A. Lauer,

J.F. Lamarque, X. Liu, V. Montanaro, G. Myhre, J. Penner, G. Pitari, S. Reddy, Ø. Seland, P. Stier, T. Takemura, , and X. Tie. Analysis and quantification of the diversities of aerosol life cycles within AeroCom. *Atmos. Chem. Phys.*, 6:1777 – 1813, 2006.

X. Tie, S. Madronich, S. Walters, D. P. Edwards, P. Ginoux, N. Mahowald, R. Y. Zhang, C. Lou, and G. Brasseur. Assessment of the global impact of aerosols on tropospheric oxidants. *J. Geophys. Res.*, 110, D03204:doi:10.1029/2004JD005359, 2005.

M. Tiedtke. A comprehensive mass flux scheme for cumulus parameterization in large scale model. *Mon. Wea. Rev.*, 117:1779 – 1800, 1989.

B. A. Tinsley, L. Zhou, and A. Plemmons. Changes in scavenging of particles by droplets due to weak electrification in clouds. *Atmos. Res.*, 79:266 – 295, 2006.

H. Tost, P. Jockel, A. Kerkweg, R. Sander, and J. Lelieveld. Technical note: A new comprehensive scavenging submodel for global atmospheric chemistry models. *Atmos. Chem. Phys.*, 6:565 – 574, 2006.

K. E. Trenberth, J. T. Fasullo, and J. Kiehl. Earth's global energy budget. *B. Am. Meteorol. Soc.*, doi:10.1175/2008BAMS2634.1:311 – 323, 2009.

S. Twomey. Aerosol, clouds, and radiation. *Atmos. Environ.*, 25A:2435 – 2442, 1991.

G. R. van der Werf, J. T. Randerson, G. J. Collatz, and L. Giglio. Carbon emissions from fires in tropical and subtropical ecosystems. *Global Change Biology*, 9:547–562, 2003.

A. van Donkelaar, R. V. Martin, M. Brauer, R. Kahn, R. Levy, C. Verduzco, and P. Villeneuve. Global estimates of exposure to fine particulate matter concentrations from satellite-based aerosol optical depth. *Environ. Health Perspec.*, 118(6): doi:10.1289/ehp.0901623, 2010.

E. Vignati, J. Wilson, and P. Stier. An efficient size-resolved aerosol microphysics module for large-scale aerosol transport models. *J. Geophys. Res.*, 109: doi:10.1029/2003JD004485, 2004.

O. Vohl, S. Mitra, S. Wurzler, and H. R. Prupppacher. A wind tunnel study on the effects of turbulence on the growth of cloud drops by collision and coalescence. *J. Atmos. Sci.*, 56:4088 – 4099, 1999.

P. K. Wang, S. N. Grover, and H. R. Pruppacher. On the effect of electric charges on the scavenging of aerosol particles by clouds and small raindrops. *J. Atmos. Sci.*, 35:1735 – 1743, 1978.

P. K. Wang and H. Lin. Comparison of model results of collection efficiency of aerosol particles by individual water droplets and ice crystals in a subsaturated atmosphere. *Atmos. Res.*, 38:381 – 390, 1995.

X. Wang, L. Zhang, and M. D. Moran. Uncertainty assessment of current size-resolved parameterizations for below-cloud particle scavenging by rain. *Atmos. Phys. Chem.*, 10:5685 – 5705, 2010.

F. Weng and N. C. Grody. Retrieval of cloud liquid water using the Special Sensor Microwave Imager (SSM/I). *J. Geophys. Res.*, 99:25 535 – 25 551, 1994.

S. Wurzler, T. G. Reisin, and Z. Levin. Modification of mineral dust particles by cloud processing and subsequent effects on drop size distributions. *J. Geophys. Res.*, 105:4501 – 4512, 2000.

K. C. Young. The role of contact nucleation in ice phase initiation in clouds. *J. Atmos. Sci.*, 31:768 – 776, 1974.

K. C. Young. Microphysical processes in clouds. *Oxford University Press*, New York, Oxford, 1993.

M. Zhao and P. H. Austin. Life cycle of numerically simulated shallow cumulus clouds. Part I: Transport. *J. Atmos. Sci*, 62:1269 – 1290, 2005.

Appendix A

A.1 Wet Deposition Budgets

The following tables present the deposition budgets related to simulations included in Chapter 4. Descriptions of the simulations are given in Table 4.3.

Table A.1: Annual and global mean deposition of sulfate (Tg S yr^{-1}) due to the processes of in-cloud scavenging (ICS) for warm (T>273.15 K), mixed (238.15<T≤273.15 K), and ice phase (T≤238.15 K) clouds, and below-cloud scavenging (BCS) for stratiform (Strat.) and convective (Conv.) clouds, and dry deposition and sedimentation for the five simulations presented in Table 4.3. Wet Dep. is the total wet deposition, summing ICS and BCS for stratiform and convective clouds separately.

Sulfate	NOAP	SAP	CVAP +SAP	CVAP +SAP +ss	CVAP +SAP +ss+imp
Stratiform clouds					
Warm ICS	23.5	11.0	13.5	12.7	21.8
Mixed ICS	14.2	5.28	5.86	5.67	12.1
Ice ICS	0.17	0.78	2.00	1.78	0.65
Convective clouds					
Warm ICS	13.7	17.4	2.06	2.06	8.1
Mixed ICS	11.3	13.4	0.27	0.25	1.57
Ice ICS	0.48	0.54	negl.	negl.	negl.
Total ICS	63.4	48.8	24.2	22.5	44.2
Strat. BCS	8.26	17.3	37.3	33.0	15.5
Conv. BCS	0.03	0.06	0.15	0.14	0.10
Total BCS	8.28	17.4	37.5	33.1	15.6
Strat. Wet Dep.	46.1	34.4	58.7	53.2	50.1
Conv. Wet Dep.	25.5	31.4	2.5	2.45	9.8
Dry Deposition	2.07	3.27	4.43	5.92	4.21
Sedimentation	1.18	4.85	8.92	13.1	9.79

Table A.2: Annual and global mean deposition of black carbon (Tg yr^{-1}) due to the processes of in-cloud scavenging (ICS) for warm (T>273.15 K), mixed (238.15<T≤273.15 K), and ice phase (T≤238.15 K) clouds, and below-cloud scavenging (BCS) for stratiform (Strat.) and convective (Conv.) clouds, and dry deposition and sedimentation for the five simulations presented in Table 4.3. Wet Dep. is the total wet deposition, summing ICS and BCS for stratiform and convective clouds separately.

Black Carbon	NOAP	SAP	CVAP +SAP	CVAP +SAP +ss	CVAP +SAP +ss+imp
Stratiform clouds					
Warm ICS	1.81	0.58	0.86	0.81	1.88
Mixed ICS	1.09	0.23	0.34	0.32	0.93
Ice ICS	0.01	0.09	0.30	0.27	0.07
Convective clouds					
Warm ICS	1.62	2.20	0.43	0.44	1.32
Mixed ICS	1.69	2.00	0.08	0.08	0.38
Ice ICS	0.08	0.09	negl.	negl.	negl.
Total ICS	6.30	5.22	2.06	1.92	4.58
Strat. BCS	0.79	1.63	4.12	3.8	1.72
Conv. BCS	negl.	negl.	0.01	0.01	negl.
Total BCS	0.79	1.63	4.13	3.87	1.72
Strat. Wet Dep.	3.7	2.5	5.6	5.2	4.6
Conv. Wet Dep.	3.4	4.3	0.52	0.53	1.7
Dry Deposition	0.72	0.77	0.94	1.03	0.95
Sedimentation	0.02	0.24	0.60	0.90	0.78

Table A.3: Annual and global mean deposition of particulate organic matter (Tg yr^{-1}) due to the processes of in-cloud scavenging (ICS) for warm (T>273.15 K), mixed (238.15<T≤273.15 K), and ice phase (T≤238.15 K) clouds, and below-cloud scavenging (BCS) for stratiform (Strat.) and convective (Conv.) clouds, and dry deposition and sedimentation for the five simulations presented in Table 4.3. Wet Dep. is the total wet deposition, summing ICS and BCS for stratiform and convective clouds separately.

Organic Matter	NOAP	SAP	CVAP +SAP	CVAP +SAP +ss	CVAP +SAP +ss+imp
Stratiform clouds					
Warm ICS	13.8	2.80	5.51	5.04	14.7
Mixed ICS	5.99	0.88	1.86	1.70	5.85
Ice ICS	0.05	0.63	2.67	2.42	0.58
Convective clouds					
Warm ICS	18.8	25.6	3.85	3.99	14.9
Mixed ICS	17.2	19.6	0.60	0.59	3.54
Ice ICS	0.85	0.90	negl.	negl.	negl.
Total ICS	56.7	50.5	15.0	13.7	39.6
Strat. BCS	5.26	10.7	37.0	34.7	14.7
Conv. BCS	0.02	0.04	0.14	0.14	0.11
Total BCS	5.28	10.8	37.1	34.8	14.8
Strat. Wet Dep.	25.1	15.0	47.0	43.9	35.8
Conv. Wet Dep.	36.9	46.1	4.6	4.7	18.6
Dry Deposition	6.02	6.37	8.04	8.78	8.16
Sedimentation	0.19	1.62	5.31	8.16	6.82

Table A.4: Annual and global mean deposition of dust (Tg yr^{-1}) due to the processes of in-cloud scavenging (ICS) for warm (T>273.15 K), mixed (238.15<T≤273.15 K), and ice phase (T≤238.15 K) clouds, and below-cloud scavenging (BCS) for stratiform (Strat.) and convective (Conv.) clouds, and dry deposition and sedimentation for the five simulations presented in Table 4.3. Wet Dep. is the total wet deposition, summing ICS and BCS for stratiform and convective clouds separately.

Dust	NOAP	SAP	CVAP +SAP	CVAP +SAP +ss	CVAP +SAP +ss+imp
Stratiform clouds					
Warm ICS	18.3	1.65	3.82	2.71	27.0
Mixed ICS	25.8	1.52	1.99	1.68	24.5
Ice ICS	0.19	0.48	1.70	1.39	1.21
Convective clouds					
Warm ICS	30.8	38.0	4.76	4.10	24.6
Mixed ICS	35.3	39.9	0.58	0.51	6.11
Ice ICS	1.74	1.87	negl.	negl.	negl.
Total ICS	112.	83.6	13.3	10.4	83.4
Strat. BCS	64.7	85.1	126.	114.	70.8
Conv. BCS	1.0	1.0	1.2	1.2	1.1
Total BCS	65.7	86.1	127.	115.	71.9
Strat. Wet Dep.	109.	88.8	134.	120.	124.
Conv. Wet Dep.	68.8	80.8	6.5	5.8	31.8
Dry Deposition	21.1	22.5	25.1	27.9	26.4
Sedimentation	114.	121.	131.	144.	133.

Table A.5: Annual and global mean deposition of sea salt (Tg yr^{-1}) due to the processes of in-cloud scavenging (ICS) for warm (T>273.15 K), mixed (238.15<T≤273.15 K), and ice phase (T≤238.15 K) clouds, and below-cloud scavenging (BCS) for stratiform (Strat.) and convective (Conv.) clouds, and dry deposition and sedimentation for the five simulations presented in Table 4.3. Wet Dep. is the total wet deposition, summing ICS and BCS for stratiform and convective clouds separately.

Sea Salt	NOAP	SAP	CVAP +SAP	CVAP +SAP +ss	CVAP +SAP +ss+imp
Stratiform clouds					
Warm ICS	711.	206.	279.	293.	1120.
Mixed ICS	544.	96.2	111.	88.7	654.
Ice ICS	0.18	2.05	18.4	15.8	11.9
Convective clouds					
Warm ICS	742.	908.	94.0	239.	1450.
Mixed ICS	562.	676.	13.1	24.2	349.
Ice ICS	4.92	5.46	negl.	negl.	negl.
Total ICS	2560.	1900.	525.	661.	3590.
Strat. BCS	963.	1300.	2160.	2630.	1800.
Conv. BCS	6.2	6.5	11.1	18.2	14.1
Total BCS	969.	1310.	2170.	2650.	1810.
Strat. Wet Dep.	2220.	1600.	2570.	3030.	3590.
Conv. Wet Dep.	1320.	1600.	118.	281.	1810.
Dry Deposition	819.	949.	1060.	3530.	2500.
Sedimentation	1090.	1260.	1570.	6790.	5710.

Appendix B

B.1 Comparison with AERONET Size Distributions

The following figures show aerosol size distributions for 48 AERONET sites for the year 2001, and for four simulations described in Table 4.3.

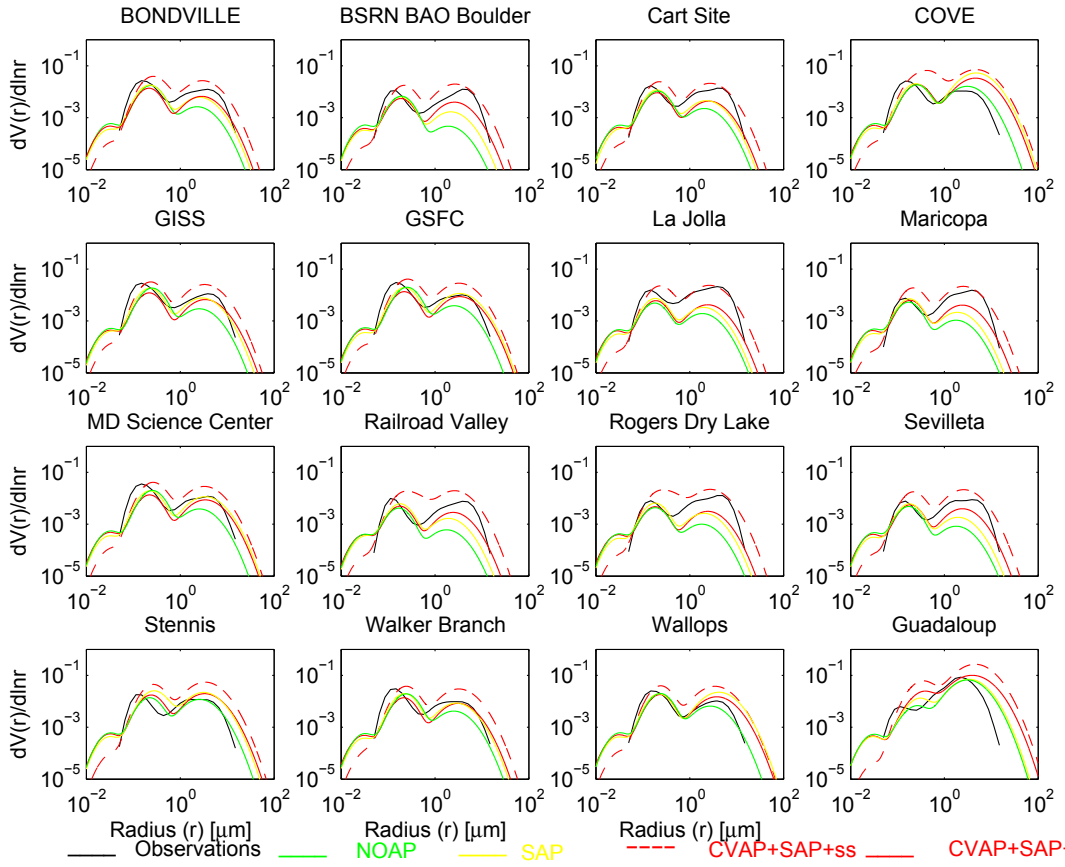

Figure B.1: The annual mean vertically integrated aerosol volume size distributions (dV(r)/dlnr in μm^{-3} μm^{-2}) for North American sites for the simulations NOAP, SAP, CVAP+SAP+ss and CVAP+SAP+ss+imp and AERONET observations.

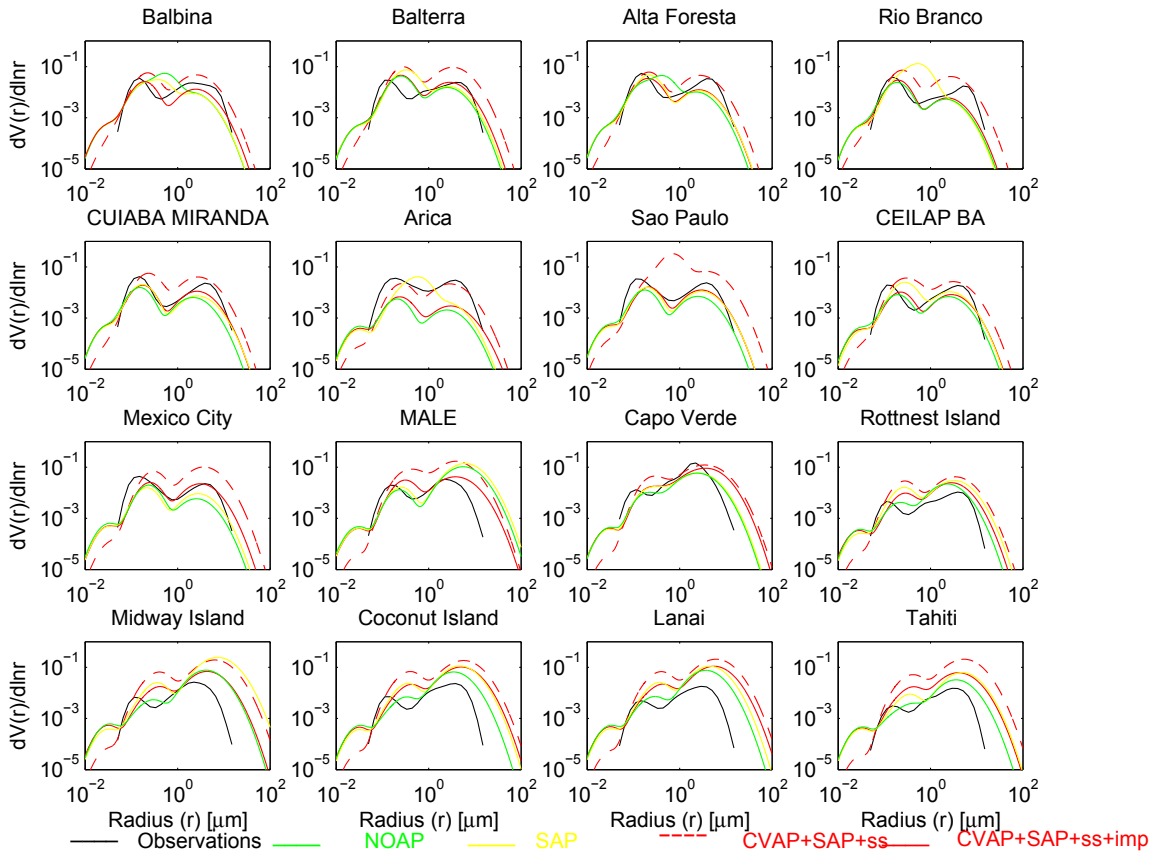

Figure B.2: The annual mean vertically integrated aerosol volume size distributions (dV(r)/dlnr in μm^{-3} μm^{-2}) for South American and oceanic sites for the simulations NOAP, SAP, CVAP+SAP+ss and CVAP+SAP+ss+imp and AERONET observations.

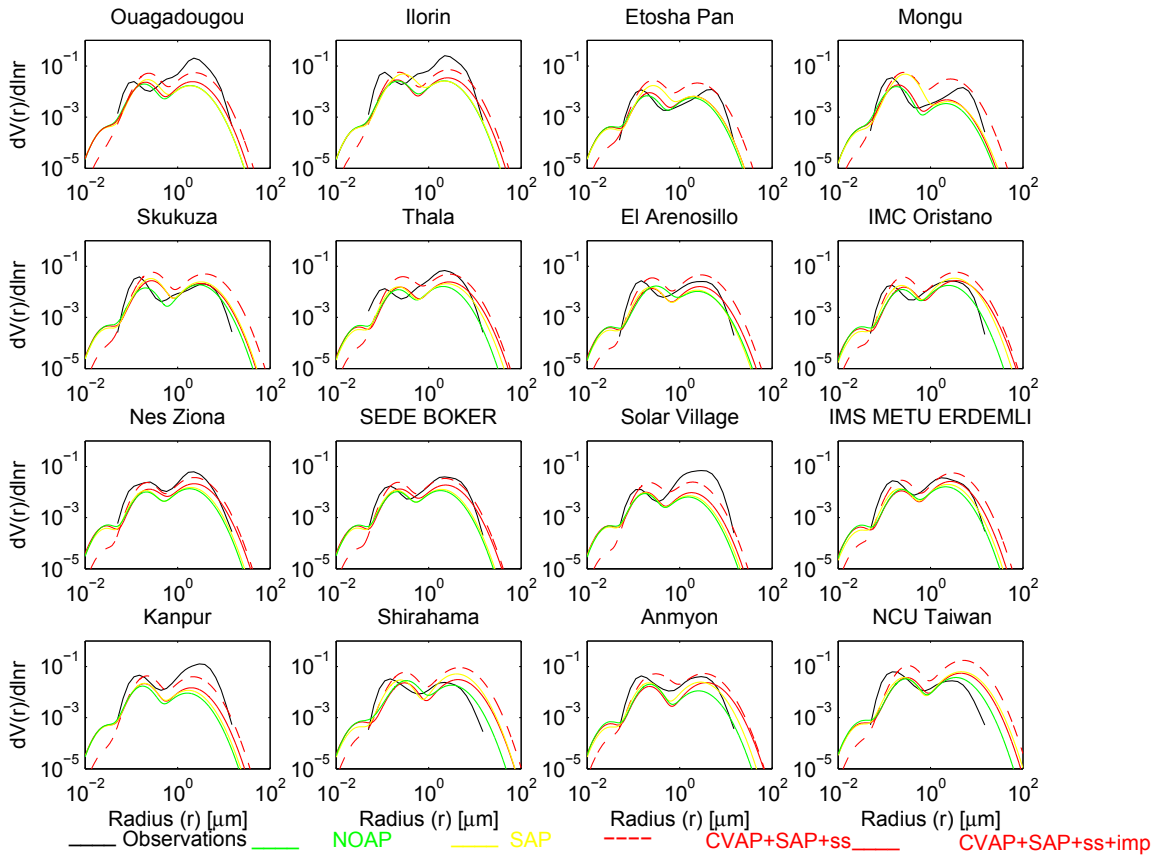

Figure B.3: The annual mean vertically integrated aerosol volume size distributions (dV(r)/dlnr in μm^{-3} μm^{-2}) for African, Mediterranean, Middle East and Asian sites for the simulations NOAP, SAP, CVAP+SAP+ss and CVAP+SAP+ss+imp and AERONET observations.

Appendix C

C.1 Copyright Information

Chapters 2 and 3 of this thesis contain articles published in the journal Atmospheric Chemistry and Physics. The author retains the copyright for these publications. Further information can be found at http://www.atmospheric-chemistry-and-physics.net/general_information/license_and_copyright.html.